UNIVERSITÉ DE STRASBOURG

ÉCOLE DOCTORALE MSII (ED N°269)

laboratoire des sciences de l'ingénieur, de l'informatique

et de l'imagerie (ICUBE)-UMR 7357

THÈSE présentée par :

Xiaofeng GAO

soutenue le : **6 Mars 2017**

pour obtenir le grade de : **Docteur de l'université de Strasbourg**

Discipline/ Spécialité : Mécanique/ Génie Civil

Modèle pour la prévision de la résistance nominale des matériaux quasi-fragiles. Application à la modélisation de l'endommagement et de la rupture des enrobés bitumineux sous sollicitations de fatigue par la méthode des éléments discrets.

THÈSE dirigée par :

M. CHAZALLON Cyrille	Professeur, INSA de Strasbourg
M. DESCANTES Yannick	Chargé de recherches (HDR), IFSTTAR

RAPPORTEURS :

M. RAGUENEAU Frederic	Professeur, ENS Cachan
M. ROUX Jean-Nöel	IPEF-DR (HDR), IFSTTAR

AUTRES MEMBRES DU JURY :

M. DAOUADJI Ali	Professeur, INSA Lyon
M. KOVAL Georg	Maître de conférences, INSA de Strasbourg

UNIVERSITY OF STRASBOURG

Modelling of nominal strength prediction for quasi-brittle materials. Application to discrete element modelling of damage and fracture of asphalt concrete under fatigue loading.

by

Xiaofeng GAO

A thesis submitted in partial fulfillment for the
degree of Doctor of Philosophy

in the
Doctoral School of MSII

March 2017

Acknowledgments

My deepest gratitude goes first and foremost to my advisers, Georg KOVAL, thesis director Cyrille CHAZALLON, and co-director Yannick DESCANTES, who provided helpful advice, and continuous encouragement and support. I am very grateful to Georg KOVAL for his instructive advice and useful suggestions to improve my thesis. Besides my advisers, I would like to thank the rest of my thesis committee: Frederic RAGUENEAU, Jean-Nöel ROUX, and Ali DAOUADJI, for their encouragement and insightful comments.

I would like to thank my colleagues in the Group of Civil Engineering and Energy at INSA Strasbourg, Bernard MIGAULT, Saïda MOUHOUBI, Hossein NOWAMOOZ, Juan Carlos QUEZADA GUAJARDO, and Lucile GONDOR, for their hospitality and friendship during my time as a Ph.D. student. Special thanks to my fellow Ph.D. students, Xuan Nam HO, Ioana Maria ARSENIE, Quoc Tuan TRINH, Kai LI, Andrea THEMELI, Peng JING, Loba SAGNOL, Guixian LIU, Anicet DANSOU, Fujiao TANG, and Laura GAILLARD, for all the great moments we shared.

I am also grateful to the China Scholarship Council (CSC) who provided me with a full scholarship for three-and-a-half years that guaranteed the smooth completion of my thesis.

Finally I wish to thank my family and my wife for their endless and unconditional encouragement and support.

Résumé étendu

Contexte

Les matériaux quasi-fragiles, comme les bétons hydrauliques ou bitumineux, les roches et certains types de céramiques, sont largement utilisés dans la construction moderne. La prédiction de comportement en fatigue et en rupture de ces matériaux est essentielle à la conception et à l'entretien des structures. La gestion d'un projet demande naturellement, le développement d'outils théoriques et numériques efficaces.

De nombreux résultats expérimentaux démontrent que la rupture quasi-fragile dépend de la taille, c'est-à-dire, qu'elle dépend de la taille physique de la structure, de la taille des défauts existants, en plus de leur forme (fissures, vides, rainures, etc.). La conception d'une structure réelle est basée sur les propriétés mécaniques obtenues expérimentalement avec des spécimens relativement petits. Par conséquent, les effets de la taille doivent être pris en compte pour des prédictions réalistes de la résistance des grandes structures telles que les grands éléments en béton, ou même des glaciers. La théorie des distances critiques, les approches basées sur le champ de contraintes élastiques, les approches basées sur la mécanique de la rupture et les modèles combinant les contraintes et l'énergie, incorporent une dimension pour caractériser les matériaux. Cette longueur (dite critique), qui dépend globalement des propriétés du matériau, telles que la résistance et la ténacité, associe un comportement non local à la rupture. Pour certains géo-matériaux (béton, béton bitumineux, maçonnerie...), la longueur critique peut atteindre quelques centimètres, ce qui est dans l'ordre de grandeur de la dimension des spécimens expérimentaux, ou encore de l'épaisseur des couches supérieures de chaussées et des dalles en béton, par exemple. Par conséquent, de tels modèles ne peuvent pas être appliqués directement dans de nombreux cas pratiques.

Dans le cas de chargement de fatigue (cycle en forces ou déplacements imposés, ou en température...) les efforts qui se développent au sein de la structure sont bien en deçà de la résistance ultime des matériaux ou de la limite d'élasticité. Cependant, ils sont responsables de la dégradation continue de la rigidité et de la propagation des fissures, ce qui conduit finalement à la défaillance de la structure. Au début de la vie d'une structure, le matériau qui la compose ne présente que des défauts internes (microfissures, vides, discontinuités...). En raison du chargement cyclique (normalement de faible intensité, mais de longue durée), ces petits défauts ont tendance à croître en taille et en quantité, ce qui endommage le matériau, réduisant ainsi sa rigidité. Avec un nombre relativement élevé de cycles, les micro défauts se relient et deviennent des fissures, qui précèdent la rupture. D'un point de vue théorique, les deux mécanismes sont traités différemment. La fracture est habituellement décrite localement, avec la propagation de fissures définie par la valeur du facteur d'intensité de contraintes en pointe de fissure, alors que l'endommagement est habituellement associé à des approches non locales. Certains modèles fusionnent les deux approches avec la représentation des fissures comme des zones fortement endommagées. Cependant, cette stratégie est habituellement sensible aux effets de discrétisation, ce qui peut générer des réponses non physiques des modèles.

Dans ce travail, la modélisation de l'apparition des fissures et leurs propagations en chargement monotone est d'abord étudiée. Les prédictions du modèle de rupture sont comparées à des résultats expérimentaux de la littérature pour divers spécimens (intacts ou pré-fissurés) constitués de différents matériaux et de différentes tailles. Des échantillons présentant des défauts initiaux en forme de V et en forme de trou illustrent les capacités de la formulation. Ensuite, l'endommagement et la fissuration induite par des chargements cycliques en fatigue sont discutés. Un modèle local en éléments discrets est alors développé, qui permet de coupler les deux mécanismes (endommagement et fissuration). Les prédictions numériques sont comparées aux résultats théoriques et expérimentaux. À la fin, des applications associées au comportement du béton bitumineux, présentent l'effet de renfort par des grilles en fibres de verre.

Plan du Mémoire

Le contexte et les objectifs de la thèse étant fixés, ce mémoire est découpé en sept chapitres :

Le chapitre 1, "Introduction", présente les objectifs, la portée de l'étude, et les grandes lignes de la thèse.

Le chapitre 2, "Revue de la littérature", contient quatre parties. La première partie résume brièvement les théories fondamentales de la mécanique de la rupture. La deuxième partie présente la dépendance de la résistance nominale des matériaux quasi-fragiles par rapport à la taille physique de la structure, la taille des défauts (fissures, vides...) et leur forme (rainure, trous...), ainsi que l'analyse des modèles utilisés pour caractériser ces effets. La troisième partie compare un modèle d'endommagement continu avec un modèle de propagation de fissures par fatigue pour un béton bitumineux. Enfin, la quatrième partie présente la méthode aux éléments discrets et introduit les définitions de déformation et de contraintes pour un motif hexagonal de particules.

Le chapitre 3, "Résistance nominale des structures fissurées", présente un modèle de rupture capable d'analyser efficacement les effets de la taille sur la base de l'information locale du taux de restitution d'énergie en pointe de fissure et son évolution durant la propagation de celle-là. La dérivée du taux de restitution d'énergie est introduite pour caractériser le mécanisme de résistance, qui domine la rupture en absence de fissures ou lorsque elles sont petites. Avec le critère d'énergie classique pour le mécanisme énergétique, un modèle asymptotique est établi pour caractériser l'ensemble du processus de défaillance (initiation et propagation de fissures). Une expression pour des échantillons géométriquement similaires est directement établie, ce qui permet de comparer le modèle proposé avec les résultats expérimentaux présentés dans la littérature (ex.: essais de flexion trois points de poutres pré-fissurés) et d'autres modèles capables de caractériser les effets de la taille.

Le chapitre 4, "Généralisation du modèle de rupture quasi-fragile", introduit une généralisation du modèle de rupture locale présenté dans le chapitre précédent, basée sur les quantités locales évaluées en pointe de fissure. Le modèle généralisé permet une analyse de la rupture des structures présentant des défauts plus complexes. Les prévisions de la résistance nominale données par le modèle proposé sont comparées aux résultats expérimentaux de la littérature pour différents échantillons (intacts ou pré-fissurés), constitués de différents matériaux, et de différentes tailles. Des échantillons présentant des défauts initiaux en forme de V et en forme de trou sont étudiés et modélisés.

Le chapitre 5, "Modélisation de l'endommagement et fissuration du béton bitumineux", développe un modèle local en éléments discrets qui permet de coupler les deux mécanismes (endommagement et fissuration). Les résultats numériques sont comparés à des essais de fatigue de poutres en flexion 4 points.

Le chapitre 6, " Application au béton bitumineux renforcé par des grilles en fibre de verre", utilise les modèles proposés pour l'étude des effets des renforts par grille en fibre de verre dans la résistance et la durée de vie des structures des chaussées. La capacité de la grille en fibre de verre à ralentir l'ouverture de fissures transversales en conditions de déformation imposée est étudiée. Ces résultats en conditions monotones sont associés à l'évaluation de l'effet des renforts dans la durée de vie en fatigue, notamment en fonction de la quantité de fibres.

Le chapitre 7, “Conclusions et perspectives”, contient un résumé des conclusions de cette étude et traite des travaux futurs envisageables.

Le mémoire se termine avec trois annexes. L'annexe A présente une comparaison des différentes formules de facteur de correction géométrique pour le taux de restitution d'énergie des poutres en flexion trois points. L'annexe B introduit la méthode de fermeture de fissure modifiée, qui sert à calculer le taux de restitution d'énergie numériquement. L'annexe C présente l'algorithme de calcul de la méthode des éléments discrets.

Résistance nominale de structures fissurées

La résistance nominale des structures constituées de matériaux quasi-fragiles est généralement liée à la taille physique de la structure (effet de taille) et la taille des fissures existantes (effet de bord). Dans cette partie, un modèle de rupture capable de prendre en compte ces deux effets à partir du taux de restitution d'énergie en pointe de fissure et son évolution durant la propagation de celle-là est établie :

$$\sigma_N = \frac{1.12 f_t}{H(\alpha)} \left(1 + \frac{a_e}{a_t}\right)^{-1/2}, \tag{1}$$

où σ_N est la résistance nominale, f_t est la résistance en traction du matériau, $H(\alpha)$ est un facteur de correction géométrique pour la dérivée du taux de restitution d'énergie (Équation 3.9, α est le ratio entre la taille de la fissure a et la hauteur de la poutre h, a_e est la longueur de fissure équivalente (Équation 3.13) et a_t est la longueur de fissure de transition (Équation 2.21).

Une expression pour des spécimens géométriquement similaires est directement établie :

$$\sigma_N = \frac{1.12 f_t}{H(\alpha)} \left(1 + \frac{h}{h_t}\right)^{-1/2}, \tag{2}$$

où h_t est la longueur de transition de la poutre (Équation 3.19).

Afin de valider le modèle proposé, trois séries de résultats expérimentaux ont été utilisées à partir de recherches existantes sur le calcaire, le béton et la pâte de ciment durci. La Figure 1 (Figure 3.23) montre les prédictions de la charge de rupture en fonction de la hauteur de la poutre h en comparaison avec les prédictions de la loi de l"effet de la taille (Équation 2.41), les prévisions du modèle d'effet de bord (Équation 3.21) et les résultats des essais des échantillons de pâte de ciment durcie. Les résultats indiquent que les prédictions des résistance nominale obtenues à partir du modèle proposé concordent très bien avec les résultats expérimentaux.

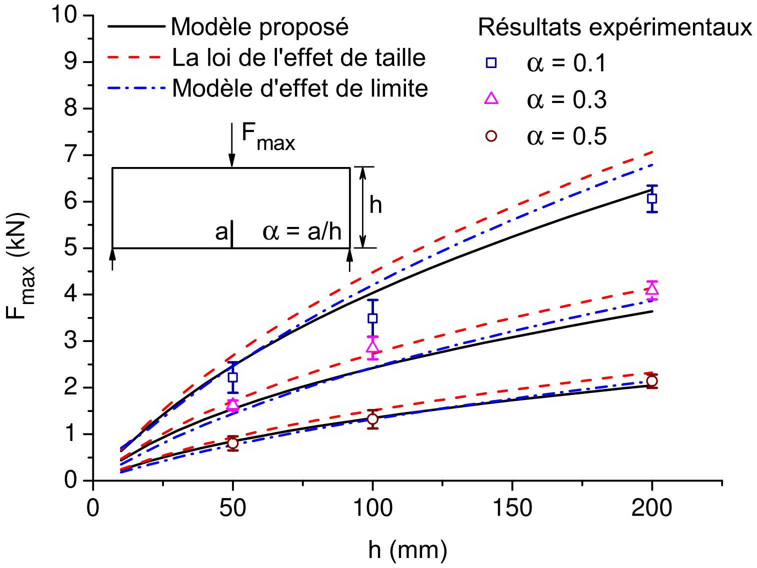

Figure 1: Prédictions du modèle de la charge de rupture F_{max} par rapport à la hauteur de la poutre h en comparaison avec les prédictions de la loi de l'effet de la taille, les prévisions du modèle d'effet de bord, et les résultats des essais des échantillons de pâte de ciment durcie.

Généralisation du modèle de rupture quasi-fragile

La caractérisation locale du processus de rupture, présentée dans le chapitre précèdent à partir des quantités évaluées en pointe de fissure, demande une fine description de la transition entre les mécanismes de résistance et celui de propagation de fissures. L'utilisation d'un paramètre supplémentaire r dans le modèle (c'est-à-dire, en plus de la résistance en traction et de la ténacité) permet l'analyse de la rupture pour des structures présentant des défauts plus complexes qu'une fissure. Le modèle généralisé s'écrit de la façon suivante :

$$\left(\frac{G}{G_c}\right)^r + \left(\frac{G'}{\bar{G}_c}\right)^r = 1, \tag{3}$$

où G est le taux de restitution d'énergie, G_c est l'énergie de rupture, G' est la dérivée du taux de restitution par rapport à la taille de la fissure a, and $\bar{G}_c$ est la valeur critique de la dérivée du taux de restitution d'énergie.

Les prédictions du modèle de rupture sont comparées à des résultats expérimentaux de la littérature pour divers spécimens (intacts ou pré-fissurés) constitués de différents matériaux etde différentes tailles. Des échantillons présentant des défauts initiaux en forme de V et en forme de trou (Figure 2) illustrent les capacités de la formulation.

Modélisation de l'endommagement et fissuration du béton bitumineux

Les processus de défaillance par fatigue de certains géomatériaux (comme le béton bitumineux) sont responsables de la plupart des dysfonctionnements des chaussées, soumises à des chargements répétés (véhicules, température...). Le modèle d'endommagement de Bodin a été implanté dans le code aux éléments discrets et comparé à la prédiction théorique et montre un bon accord dans des conditions de contraintes homogènes. Une comparaison des approches non locales et locales appliquées au test de flexion à quatre points indique les limites de chaque cas. La plupart des approches non locales peuvent produire une réponse raisonnable à l'échelle de l'échantillon, résultant d'un comportement à l'échelle du matériau qui est irréaliste. D'autre part, une approche purement locale présente une cinématique de rupture plus cohérente, mais fortement affectée par des effets de maillage.

Afin de réduire cette limitation des approches locales, un schéma numérique simple couplant endommagement et fissuration dans un modèle par éléments discrets est proposé. L'association de ces différentes formulations mécaniques permet de bien reproduire le comportement expérimental : avant l'apparition de fissures par

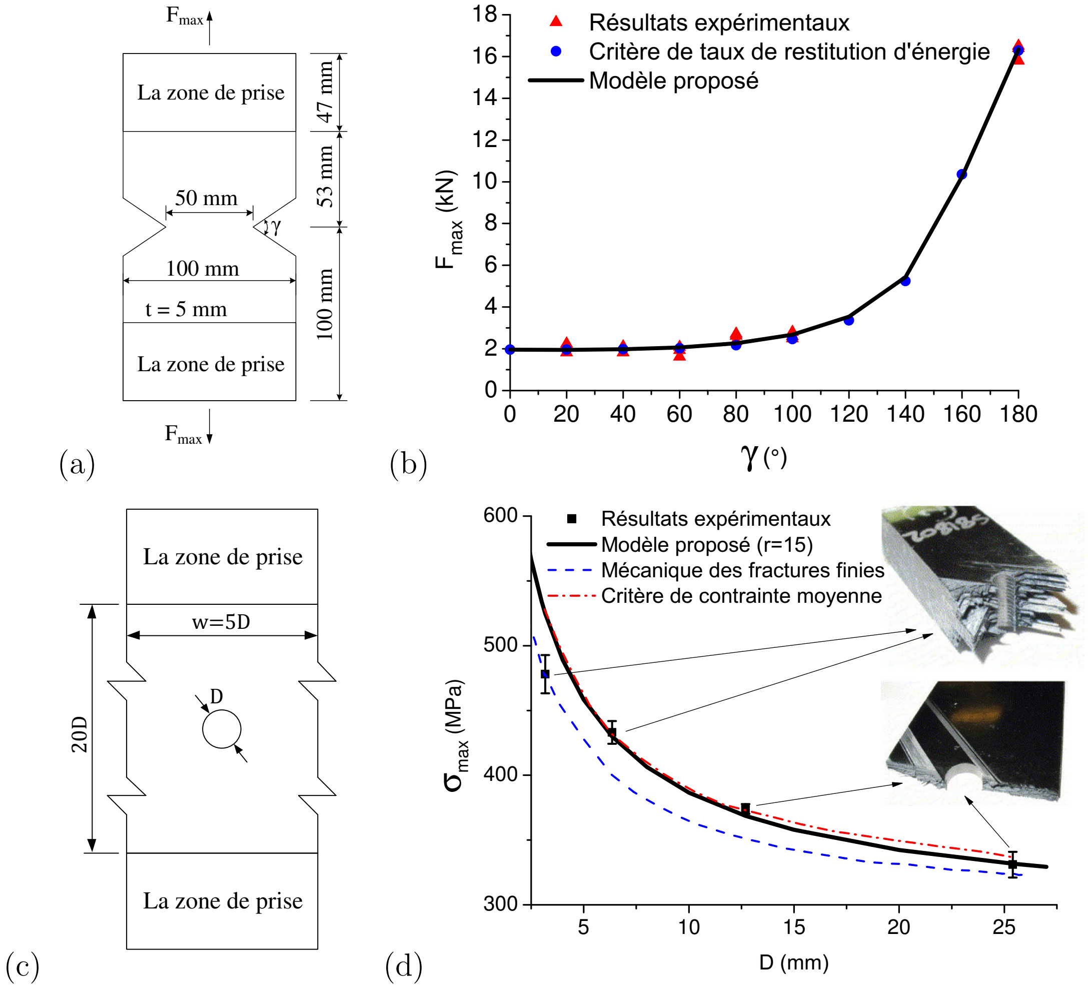

Figure 2: (a) Géométrie des échantillons avec des défauts initiaux en forme de V. (b) Charges de rupture F_{max} pour différents angles d'ouverture d'encoche γ. (c) Géométrie des plaques avec trous circulaires. (d) Prévision de la contrainte de rupture pour différents diamètres D. Comparaison des résultats experimentaux avec des modèles.

le modèle d'endommagement ; pendant l'apparition et propagation des fissures par le modèle de fissuration. Des inconvénients importants de chaque approche sont ainsi évités, tels que les effets de discrétisation, comme le montre le comportement convergeant des résultats ; et des résultats non physiques des modèles de croissance des fissures pour de très courtes ou tout simplement d'absence de fissures. Les résultats numériques sont comparés aux prédictions théoriques de la mécanique de la rupture et aux résultats expérimentaux de la littérature. La Figure 3 montre un exemple de la distribution d'endommagement et de la propagation des fissures d'une plaque pré-fissurée avec une longueur de fissure initiale $a_0 = 5\,mm$ après 166 cycles de charge de fatigue. L'augmentation du nombre de cycles, provoque l'évolution de la zone d'endommagement élevé due à l'extension de la fissure de fatigue, comme le montre la Figure 4. La taille de la zone de processus de fracture semble dépendre de la taille de la fissure.

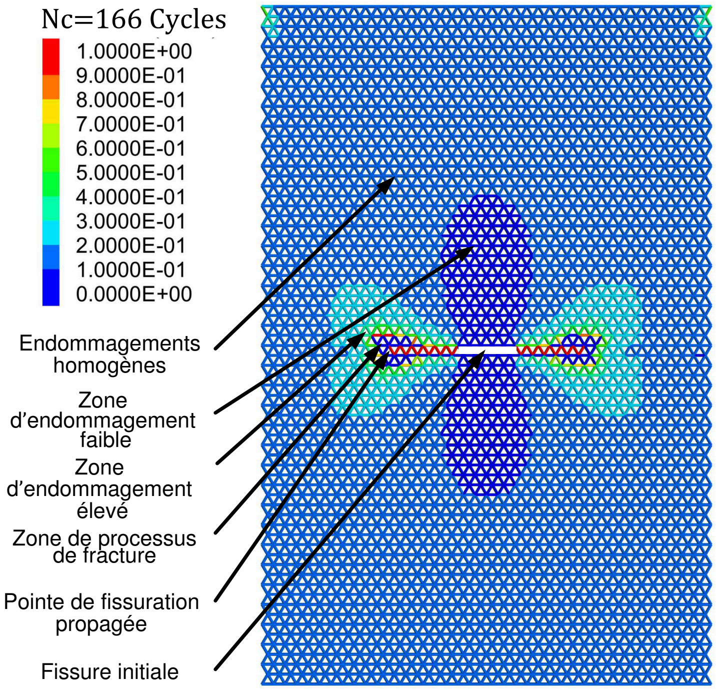

Figure 3: Distribution de l'endommagement et de la propagation des fissures d'une plaque pré-fissurée avec une longueur de fissure initiale $a_0 = 5\,mm$ après 166 cycles de charge de fatigue.

Application au béton bitumineux renforcé par des grilles en fibre de verre

Dans cette partie, on étudie l'effet du renfort des couches bitumineuses par des grilles en fibre de verre sur l'initiation et propagation de fissures. Les structures renforcées sont analysés par un modèle bidimensionnel. On considère les fissures dans différentes couches de béton bitumineux (représentées dans la Figure 5), qui représentent soit une nouvelle chaussée intacte, soit une chaussée fissuré qui reçoit un renfort et une nouvelle couche de béton bitumineux. L'effet

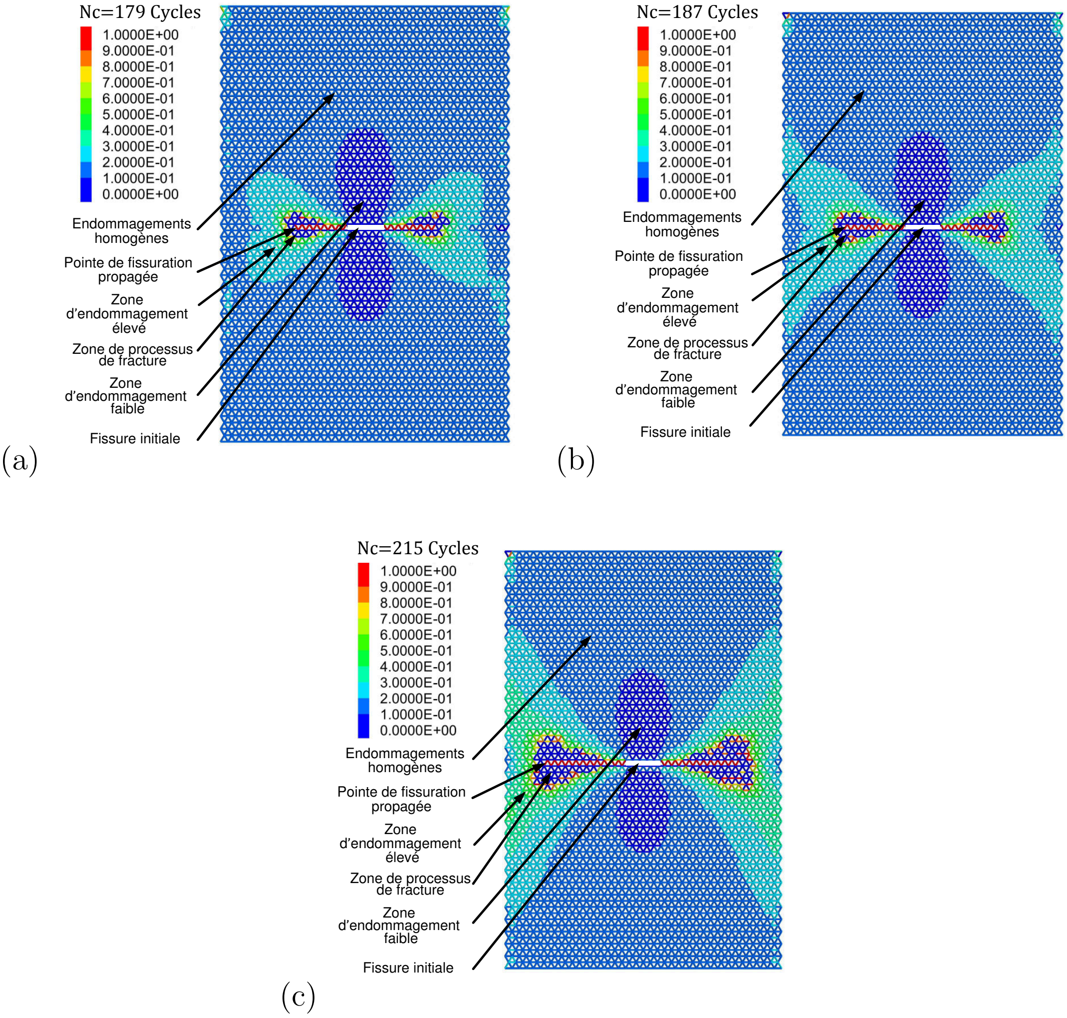

(a) (b) (c)

Figure 4: Distribution de l'endommagement et de la propagation des fissures d'une plaque pré-fissurée avec une longueur de fissure initiale $a_0 = 5\,mm$ après (a) 179, (b) 187 and (c) 215 cycles de charge de fatigue.

de la quantité de fibres sur la résistance nominale du matériau renforcé est ensuite analysé sur la base du modèle de rupture proposé dans le Chapitre 4. Le facteur de correction géométrique pour la dérivée du taux de restitution H est tracé par rapport aux quantités de fibres $S_f E_f / E_{ac}$ pour les différents cas dans la Figure 6. On a observé un faible effet des fibres vis-à-vis de l'initiation des fissures alors que les fissures sont loin du renfort. Cependant, l'effet protecteur des renforts est évident lorsque les fissures traversent la grille de fibre de verre.

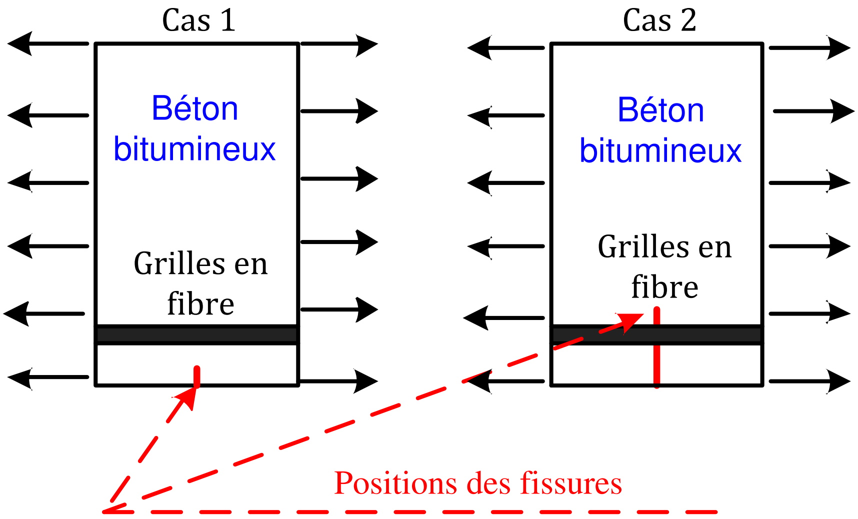

Figure 5: Déclenchement par fissuration à partir de la limite inférieure de la deuxième couche de béton bitumineux (cas 1) et du fond de la première couche de béton bitumineux (cas 2).

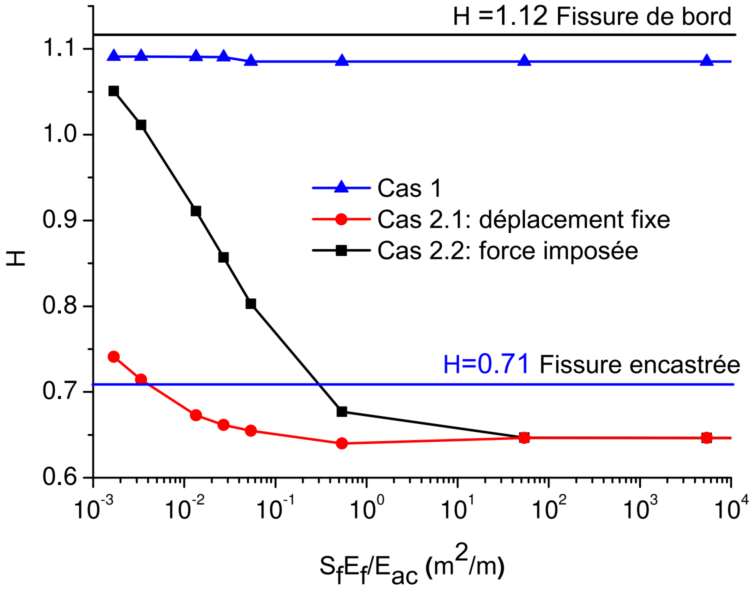

Figure 6: Facteur de correction géométrique H par rapport à la quantité de fibres $S_f E_f / E_{ac}$ pour différents cas.

Conclusions et perspectives

Dans le cadre d'une meilleure estimation de la durée de vie et de la capacité des structures à supporter des charges, la modélisation de l'apparition des fissures et leur propagation en chargement monotone est d'abord étudiée. Une expression permetant l'analyse des effets de taille basée sur des quantités localement définies (à partir du taux de restitution d'energie en pointe de fissure) pour des spécimens préfissurés est initiallement établie. Ceci a permis des comparaisons avec des résultats expérimentaux issus de la littérature (flexion de poutres geometriquement similaires à trois points) et d'autres modèles. L'utilisation d'un paramètre supplémentaire dans le modèle a rendu l'analyse de la rupture pour des structures présentant des défauts plus complexes (cavités, encoches...) possible. Les prédictions du modèle de rupture ont été comparées à des résultats expérimentaux de la littérature pour divers spécimens (intacts ou pré-fissurés) constitués de différents matériaux et de différentes tailles. Des échantillons présentant des défauts initiaux en forme de V et en forme de trou ont été traités avec des résultats consistants. Ensuite, l'endommagement et la fissuration induite par des chargements cycliques en fatigue sont discutés. Un modèle local en éléments discrets est développé afin de coupler les deux mécanismes. Les prédictions numériques sont comparées aux résultats théoriques et expérimentaux de la litérature. À la fin, des applications associées au comportement du béton bitumineux et l'effet des renforts par des grilles en fibres de verres sont analysés plus en détail.

Les modèles théoriques et numériques proposés permettent de prédire efficacement la résistance nominale et la durée de vie en fatigue des matériaux quasi-fragiles au niveau local. D'un point de vue théorique, les modèles proposés présentent de nombreuses extensions possibles. Le modèle de rupture monotone peut être simplement adapté au mode mixte à partir de la définition de la direction de l'initiation ou de l'extension d'une fissure. Une version tridimensionnelle du modèle de fatigue peut être obtenue par au moins deux façons. La première est de continuer avec une approche par éléments discrets. Néanmoins, une distribution aléatoire des particules peut diminuer le temps de calcul nécessaire, moyennant une procédure de calibration des paramètres. La seconde est d'adapter la formulation à un code aux éléments finis, considérant que toute la théorie utilisée est fondée sur la mécanique des milieux continus.

Principales publications

CONFERENCES

1. X. Gao, G. Koval, and C. Chazallon. Effect of fiber grid reinforcement on crack initiation and propagation in asphalt concrete. In 8th RILEM International Conference on Mechanisms of Cracking and Debonding in Pavements, pages 55-60. Springer, 2016.

2. X. Gao, G. Koval, and C. Chazallon. A discrete element model for damage and fracture of geomaterials under fatigue loading. 8th International Conference on Micromechanics of Granular Media. (Powders and Grains 2017, accepté, 4 pages).

PAPERS

1. X. Gao, G. Koval, and C. Chazallon. Energetical formulation of size effect law for quasi-brittle fracture. Engineering Fracture Mechanics, 2017. http://dx.doi.org/10.1016/j.engfracmech.2017.02.001. (en publication, 14 pages)

2. X. Gao, G. Koval, and C. Chazallon. A size and boundary effects model for quasi-brittle fracture. Materials, 9(12):1-20, 2016.

Contents

List of Figures

List of Tables

Chapter 1

Introduction

Contents

This work was undertaken at the National Institute of Applied Sciences of Strasbourg (INSA de Strasbourg), in the Engineering Science, Computer Science and Imaging Laboratory (ICUBE, UMR7357). Firstly, the general background and motivation of the thesis are given in this chapter. Then, the objectives and research scope are discussed. Finally, an outline of the remainder of the thesis is presented.

1.1 General background and motivation

Quasi-brittle materials (measurable plastic deformation before failure), such as hydraulic or asphalt concretes, rocks, and certain types of ceramics, are widely used in modern construction. The prediction of the fatigue life and fracture of structures composed of these materials is essential to their design and maintenance. The high complexity of the material properties requires the development of theoretical and numerical tools in order to achieve effective structures.

Numerous experimental results have shown that quasi-brittle rupture is size dependent, i.e., it depends on the physical size of the structure, the size of existing defects (cracks, voids, etc.) and their shape (notches, holes, etc.). The design of a real structure is based on material properties obtained for much smaller experimental specimens. Hence, size effects must be taken into account for realistic predictions of the strength of big structures such as large concrete elements, nuclear facilities, large load-bearing parts of aircraft, and floating sea ice carrying loads. Existing non-local critical distance theories, including elastic stress field based models, fracture mechanics based models, and combined stress and energy models, are associated with a length scale parameter. This length scale depends globally on material properties such as strength and toughness . For some geomaterials (concrete, asphalt concrete, masonry, etc.), the critical length can reach the scale of centimeters; which is comparable to the size of experimental specimens or the thickness of upper pavement layers, for example. Consequently, such models cannot be directly applied in many practical cases.

Under fatigue loading (cyclical loads or temperature cycling) the applied efforts are far below the ultimate strength of the materials, but are responsible for the continuous degradation of the stiffness and propagation of cracks, etc., which finally result in the failure of the structure. At the beginning of the lifetime of a structure, the material contains only intrinsic defects (microcracks, voids, etc.). Due to the effect of cyclic loading, these small defects tend to grow in size and number, damaging the material and reducing its stiffness. With a relatively high number of cycles, these growing microcracks become large cracks, which determine the fracture behavior. From a theoretical point of view, the two mechanisms are treated differently. Fracture is usually described locally, with the propagation of cracks defined by the range of the stress intensity factor at the crack tip, while damage is usually associated with non-local approaches. Most of the existing models merge both approaches with the representation of cracks as highly damaged zones. However, this strategy is usually sensitive to discretization effects, which may generate non-physical responses of the models.

1.2 Objectives and scope

The main purpose of this study was to merge local and non-local aspects of the rupture of quasi-brittle materials into simple local approaches. The following objectives are considered:

1. Development of an energetic size effect model, which allows a local definition of the monotonic rupture of pre-cracked structures.

2. Generalization of the local model for more complex defects such as holes and V-notches.

3. Combine damage with crack propagation under fatigue loading and propose a

local model developed in a discrete element environment.

4. Application of the models for the analysis of asphalt concrete behavior.

1.3 Outline of the thesis

This thesis is organized in seven chapters:

Chapter 1, “Introduction”, presents the objectives, scope of the study, and outline of the thesis.

Chapter 2, “Literature review”, contains four parts. The first part briefly summarizes basic theories of fracture mechanics. The second part introduces the nominal strength dependency of quasi-brittle materials on the physical size of the structure, the size of existing defects (cracks, voids, etc.) and their shape (notches, holes, etc.), and reviews models used to characterize these effects. The third part compares a continuum damage model with a fatigue crack growth model for asphalt concrete. Finally, the fourth part presents a discrete element method and introduces the definitions of strain and stress in the close-packed assembly.

Chapter 3, “Nominal strength of cracked structures”, presents a local failure model which is able to effectively analyze the size and boundary effects based on the local information of energy release rate and its derivative at the crack tip. The derivative of the energy release rate is introduced to predict the nominal strength for the strength mechanism, which dominates the rupture in the absence of cracks or when only short cracks are present. Along with the classical energy criterion for the energy mechanism, an asymptotic model is established to characterize the entire failure process (crack initiation and crack propagation). An expression for geometrically similar specimens is directly established, which allows comparison of the proposed model with experimental results presented in the literature (e.g. cracked three point bending tests of concrete, limestone and hardened cement paste beams) and other models that are capable of characterizing size and boundary effects.

Chapter 4, “Generalization of the quasi-brittle rupture model”, discusses a generalization of the local failure model presented in the previous chapter, based on the local quantities evaluated at the crack tip. The generalized model allows rupture analysis of structures with more complex defects. The nominal strength predictions given by the proposed model are compared with experimental results from the literature for various specimens (intact or pre-cracked) made of different materials and in different sizes. The comparison with samples with initial V-shaped and hole-shaped defects demonstrate the capabilities of the model.

Chapter 5, "Modelling of damage and fracture of asphalt concrete", develops a local model in discrete elements that couples two different failure mechanisms (damage and fatigue crack growth). The numerical results are compared with the results of four point bending beam fatigue tests.

Chapter 6, "Application to fiber glass reinforced asphalt concrete", uses the proposed models to the study of the effects of fiber glass reinforcement on the strength of pavement materials. The capacity of the fiber glass grid to avoid the opening of transverse cracks under imposed deformations is studied. These results derived under monotonic conditions are compared to those measuring the effect of the reinforcement on the fatigue lifetime, in particular according to the quantity of fibers.

Chapter 7, "Conclusions and perspectives", contains a summary of the findings of this study and discusses potential future work.

Three appendices are included to provide supplementary information. Appendix A presents a comparison of the different empirical geometrical correction factor formulas for the energy release rate of the cracked three point bending beams with different span to height ratios. Appendix B introduces the modified crack closure method, which can be used to calculate the energy release rate and its derivative of the structure with complex geometry and/or boundary conditions. Appendix C presents the algorithm of discrete element method calculation.

Chapter 2

Literature review

Contents

2.1 Introduction

The fundamental aspects of linear elastic fracture mechanics (LEFM) have been extensively applied to the analysis of structures with sufficiently large cracks. The mixed mode crack propagation criteria, including the maximum tensile stress criterion, minimum energy density criterion, and maximum energy release rate criterion, are well developed for predicting the fracture load and extension angle for large crack propagation.

Based on the LEFM fracture criteria, predictions of the nominal strength of quasi-brittle materials with sufficiently large cracks can be easily achieved. However, when the size of the crack or the crack-like defect is not large enough or visually identifiable (intermediate defects), the crack initiation and propagation from the defect is not dominated by LEFM. These intermediate states, including the rupture of small cracked specimens or structures with defects others than cracks (heterogeneities, complex shaped notches, etc.), are very common in modern structures. Therefore, it is very important to study the dependence of the nominal strength on the defect size.

Experimental studies have shown that the nominal strength of quasi-brittle materials is not just defect size and shape dependent, but also specimen size dependent. This means that on a small scale the nominal strengths obey the strength theory, characterized by the material strength, and on a large scale follow LEFM, characterized by the toughness. It is very important to consider this phenomenon in structural failure analysis, because real structures made from the same materials, but with different sizes, can show very different properties. Many specimen size based models have been developed to consider such behavior.

In addition to predictions of the nominal strength, the damage evolution and fatigue crack propagation of the material are also significant in structural failure analysis. For example, fatigue cracking is the most common failure observed for asphalt pavements due to repeated traffic loading, which could decrease the service life of the structure. In order to predict the lifetime of damage evolution, fatigue crack initiation, and small and large fatigue crack propagation, some continuum damage models and fatigue crack propagation models have been developed . These models have been validated by experimental results and some have been implemented as numerical codes, using finite element (FEM), discrete element (DEM), or boundary element methods . Among all the numerical methods, DEM is attractive for simulating crack propagation, since it can accurately simulate the contact problem (crack opening and closing) and can manage composite materials.

In this literature review chapter, the theory of fracture mechanics is briefly introduced in the first part. Then experimental evidence of the size effect related to the physical size of the structure, the size of existing defects and their shape, and the existing analytic models are reviewed. In the third part, damage and fracture models for damage evolution and fatigue crack propagation, respectively, are explored. Finally, the advantages and disadvantages of the most common numerical methods are discussed, and the stress and strain definitions in the discrete element method are presented.

2.2 Basic knowledge of fracture mechanics

A better understanding of structural failure is a very important issue for modern construction. The failure of structures can have various forms, where excessive permanent deformation and material fracture are the most common. The former has been studied and applied to structural designs for more than a century, and can be viewed as an extension of elasticity for characterizing the mechanical behavior beyond yielding. The latter is usually related to the strength of the material, which can cause crack initiation and propagation in the material.

Classical phenomenological approaches were used for strength prediction of solid materials before the inception of fracture mechanics, which assumes the materials to be free of cracks or crack-like defects. Classical approaches can generally predict the failure of engineering materials with acceptable accuracy when the stress field is relatively uniform. However, they are not capable of predicting the strength in the presence of high stress gradients caused by a crack or crack-like defects. Therefore, fracture mechanics was developed, where the major objective is to study the load-carrying capacity of structures in the presence of intrinsic defects.

2.2.1 History

Fracture mechanics is a relatively young scientific branch of solid mechanics, which concerns the failure of materials caused by crack initiation and propagation. The beginning of fracture mechanics is usually associated with the pioneering work of Griffith on brittle fracture of glass [1]. Griffith used an energy balance approach to determine the strength of cracked solids, which assumes the work done during crack growth must be equal to the surface energy stored in the newly created surfaces. He thus introduced a variable (later called the energy release rate) for characterizing the fracture failure; the critical energy release rate is a material constant.

Although Griffith presented the basic energy concept of fracture mechanics in 1920, it was only after the 1950s that fracture mechanics was accepted as an engineering science with successful practical applications. This was mainly as a result of the work of Irwin [2], who defined the stress intensity factors , and derived the relationship between the energy release rate, G, and the stress intensity factor, K. Based on this relationship, Irwin proposed using K as a fracture parameter, which is a more direct approach.

Between 1960 and 1980, fracture mechanics proved to be a great scientific success, including the emergence of nonlinear fracture mechanics that allowed better consideration of the behavior of nonlinear elastic materials or elastic-plastic materials. Many studies were published during this time, including the theoretical concept of the J-integral, which was developed in 1967 by Cherepanov [3] and independently in 1968 by Rice [4]. The latter generalized the energy release rate concept to describe deformation plasticity and found that G can be represented by a line integral, the so called path-independent J-integral. The J-integral method reduces to the Griffith theory for linear-elastic behavior. All theoretical developments made at this time were used to determine the exact form of singularity and asymptotic crack tip fields necessary for the analysis and interpretation of experimental results. Furthermore, such methods provide exact solutions to many problems with simple geometries, and can therefore be applied when approaching more complex problems.

In recent years, LEFM has been applied to many new materials, such as nonhomogeneous and anisotropic fiber-reinforced composites [5]. In addition, a new form of fracture model called the cohesive zone model (CZM) has evolved from LEFM [6], and many research groups have reported successful results using this approach [7]. The stress singularity is avoided in CZM, and material failure is controlled by quantities such as displacements and stresses, which are consistent with the usual strength of materials theory.

2.2.2 Basic modes of fracture

A crack in a solid consists of disjointed upper and lower crack surfaces, which are the dominating influence on the stress distribution near the crack tip. There are three different ways to load a plate containing a crack, and each load orientation has its own designation. The problems associated with these different loading configurations can be divided into three basic types. Each type associates with a local mode of deformation as presented in Figure 2.1. These basic fracture modes are called Mode I, Mode II, and Mode III, respectively, and any fracture mode in a cracked body may be viewed as a superposition of these basic modes.

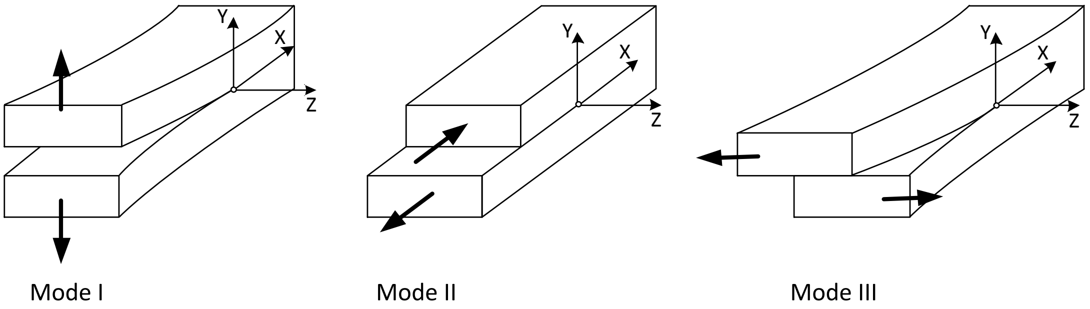

Figure 2.1: Schematic of the basic fracture modes (Modified from [8]).

The three basic fracture modes are defined as follows:

(1) Mode I (Opening Mode): The two crack surfaces have the displacement only in Y direction. They move away symmetrically with respect to the XZ plane, which is the crack plane.

(2) Mode II (Sliding Mode): The two crack surfaces have the displacement only in X direction. They slide against each other along directions perpendicular to the crack front but in the same plane (XZ plane).

(3) Mode III (Tearing Mode): The two crack surfaces have the displacement only in Z direction. They tear over each other in the directions parallel to the crack front but in the same plane (XZ plane).

2.2.3 The elastic stress field around a crack tip

Among various mathematical methods in plane elasticity, the Westergaard function method [9, 10] is more convenient than the other methods for discussing the basic crack problems, which is used to find the elasticity solutions for an infinite plane with a center crack under uniform tension (mode I), in-plane shear (mode II), and anti-plane shear loading (mode III), respectively. The Westergaard solutions are given below for each of the three modes in relation to the coordinate system shown in Figure 2.2. The origins of the coordinate system (r, θ) and (X, Y) are located at the crack tip, K terms are the stress intensity factor for each mode, E is the Young's modulus, ν is Poisson ratio, shear modulus $\mu = E/[2(1+\nu)]$, $\kappa = 3 - 4\nu$ for plane strain and $\kappa = (3-\nu)/(1+\nu)$ for plane stress.

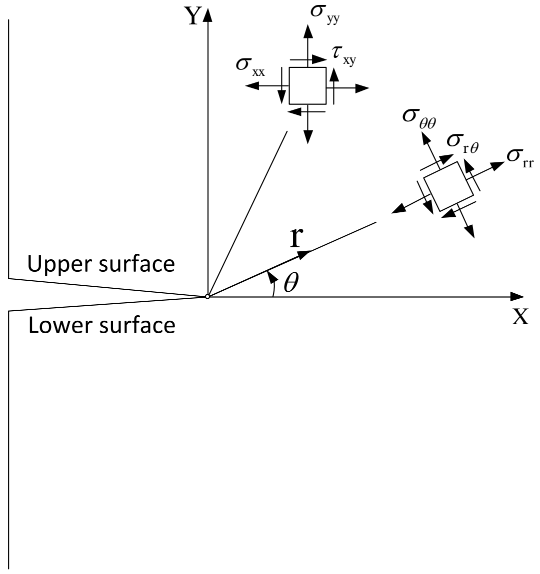

Figure 2.2: The rectangular and polar coordinate components of stress field around the crack tip (Modified from [8]).

A center cracked infinite plate subjected to mode I loading (uniform tension) is presented in Figure 2.3. The stress and displacement fields given by the Westergaard Function Method in polar coordinate system are given by:

$$\sigma_{rr} = \frac{K_I}{\sqrt{2\pi r}} \cos\frac{\theta}{2}\left(1 + \sin^2\frac{\theta}{2}\right) \tag{2.1}$$

$$\sigma_{\theta\theta} = \frac{K_I}{\sqrt{2\pi r}} \cos^2\frac{\theta}{2} \tag{2.2}$$

$$\sigma_{r\theta} = \frac{K_I}{\sqrt{2\pi r}} \sin\frac{\theta}{2} \cos^2\frac{\theta}{2} \tag{2.3}$$

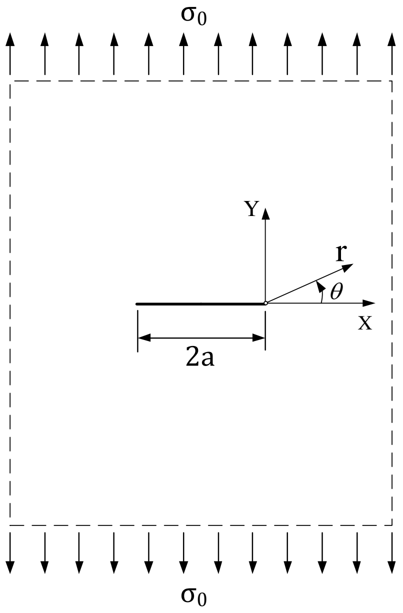

Figure 2.3: A center cracked infinite plate subjected to mode I loading.

$$u_r = \frac{K_I}{8\mu\pi}\sqrt{2\pi r}\left[(2\kappa - 1)\cos\frac{\theta}{2} - \cos\frac{3\theta}{2}\right] \tag{2.4}$$

$$u_\theta = \frac{K_I}{8\mu\pi}\sqrt{2\pi r}\left[(2\kappa + 1)\sin\frac{\theta}{2} - \sin\frac{3\theta}{2}\right] \tag{2.5}$$

Figure 2.4 shows a center cracked infinite plate subjected to mode II loading (in-plane shear). In polar coordinate system, the stress and displacement fields are given by the Westergaard Function Method as follows:

$$\sigma_{rr} = \frac{K_{II}}{\sqrt{2\pi r}}\sin\frac{\theta}{2}\left(1 - 3\sin^2\frac{\theta}{2}\right) \tag{2.6}$$

$$\sigma_{\theta\theta} = \frac{K_{II}}{\sqrt{2\pi r}} - 3\sin\frac{\theta}{2}\cos^2\frac{\theta}{2} \tag{2.7}$$

$$\sigma_{r\theta} = \frac{K_{II}}{\sqrt{2\pi r}}\cos\frac{\theta}{2}\left(1 - 3\sin^2\frac{\theta}{2}\right) \tag{2.8}$$

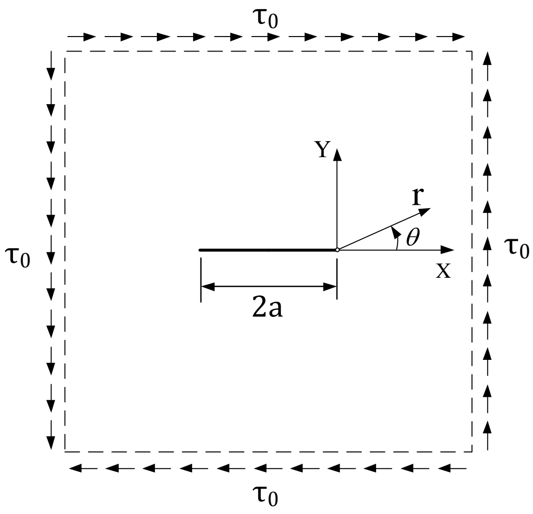

Figure 2.4: A center cracked infinite plate subjected to mode II loading.

$$u_r = \frac{K_{II}}{8\mu\pi}\sqrt{2\pi r}\left[-(2\kappa-1)\sin\frac{\theta}{2}+\sin\frac{3\theta}{2}\right] \tag{2.9}$$

$$u_\theta = \frac{K_{II}}{8\mu\pi}\sqrt{2\pi r}\left[-(2\kappa+1)\cos\frac{\theta}{2}+3\cos\frac{3\theta}{2}\right] \tag{2.10}$$

Mode III is a tearing mode (see Figure 2.5). The two crack surfaces have the displacement only in Z direction:

$$u_z = \frac{K_{III}}{\mu\pi}\sqrt{2\pi r}\sin\frac{\theta}{2} \tag{2.11}$$

The stress fields in polar coordinate systems are:

$$\sigma_{rz} = \frac{K_{III}}{\sqrt{2\pi r}}\sin\frac{\theta}{2} \tag{2.12}$$

$$\sigma_{\theta z} = \frac{K_{III}}{\sqrt{2\pi r}}\cos\frac{\theta}{2} \tag{2.13}$$

Equation 2.1 to 2.13 present the stress and displacement fields of the three basic modes, solved by Westergaard Function Method. Any fracture mode in a cracked

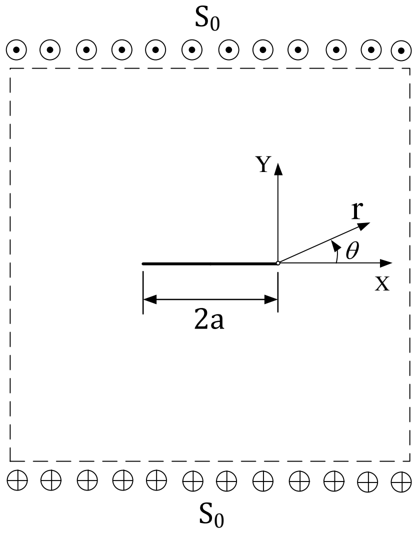

Figure 2.5: A center cracked infinite plate subjected to mode III loading.

body may be viewed as a superposition of these basic modes. Hence, the expressions of stress and displacement fields near the crack tip in mixed mode can be easily obtained.

2.2.4 Energy release rate

The near-tip stress field method and energy method are two basic methods of linear elastic fracture mechanics. In the near-tip stress field method, crack growth is dominated by the local stress field around the crack tip, which is characterized by the stress intensity factor K. Fracture occurs when the stress intensity factor reaches its critical value K_c (fracture toughness). In the energy method, the fracture behavior of a material is described by the energy variation of the cracked system during crack extension, which is characterized by the energy release rate G. Fracture occurs when the energy release rate reaches its critical value G_c (fracture energy). For linear elastic materials, the energy and the stress field approaches can be considered equivalent.

2.2.4.1 The concept of energy release rate

The energy release rate is the energy dissipated during fracture per unit of newly created fracture surface area. According to Griffith's original concept [1], the work done during a crack extension must be equal to the surface energy stored in the newly created surfaces. Hence, the energy release rate is defined as follows:

$$G = -\frac{\partial(U - V)}{\partial Q}, \tag{2.14}$$

where U is the potential energy available for crack growth, V is the work associated with any external forces acting, and Q is the extended crack area for 3D problems and crack length for 2D problems.

2.2.4.2 The relation between G and K by crack closure method

For linear elastic materials, the energy and the stress field approaches can be considered equivalent, therefore, there exists a unique relation between the energy release rate G and the stress intensity factor K. This relationship can be established by Crack Closure Method (CCM). CCM assumes that the energy released during crack extension is equal to the work done in closing the opened surfaces. Consider a plate in model I, Figure 2.6 shows its singular stress field in y direction along x axis, and the displacement field after an infinitesimal crack extension of da.

The singular stress distribution can be written as follows (Equation 2.2 with $r = x$ and $\theta = 0°$):

$$\sigma_{yy} = \frac{K_I(a)}{\sqrt{2\pi x}} \tag{2.15}$$

The surface displacement after an infinitesimal extension of da can be simplified from Equation 2.5 and written as:

$$u_y = \frac{\kappa + 1}{4\mu\pi} K_I(a + da)\sqrt{2\pi(da - x)} \tag{2.16}$$

The energy released during the extension can be computed by the integral of stress and displacement over 0 to da. And energy release rate is the released

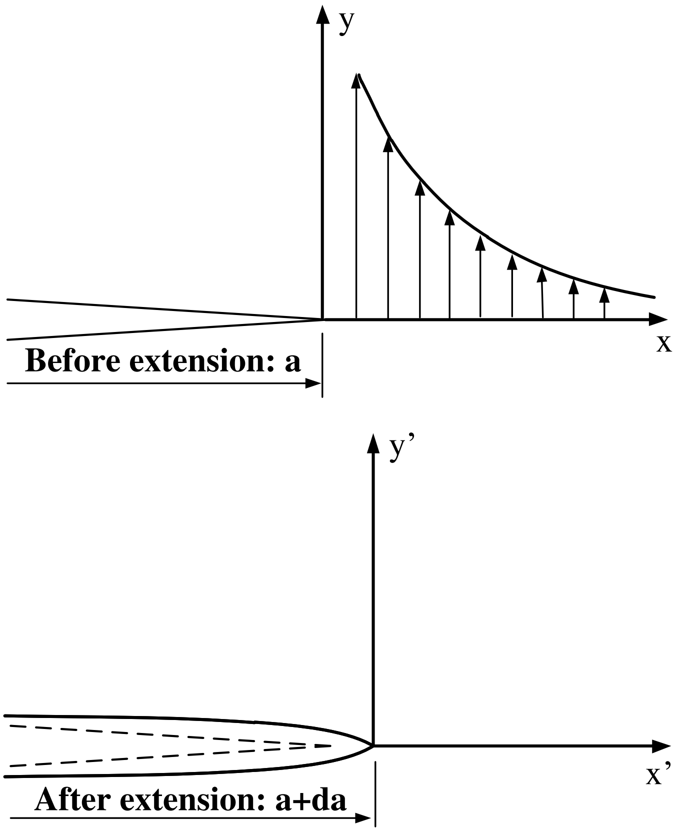

Figure 2.6: Stress distribution before extension and surface opening after extension.

energy of unit surface. Assuming $K_I(a+da) = K_I(a)$, the relation of G_I and K_I can be computed as follows:

$$G_I = \frac{2}{da}\int_0^{da}\frac{1}{2}\sigma_{yy}u_y dx = \frac{\kappa+1}{8\mu}K_I^2 \tag{2.17}$$

For plane stress condition, this expression can be simplified as $G_I = K_I^2/E$. Following the same procedure and assuming the infinitesimal extension da is always in the original direction of the main crack, the similar relation of G and K can be found for mode II and mode III, respectively:

$$G_{II} = \frac{\kappa+1}{8\mu}K_{II}^2, \tag{2.18}$$

$$G_{III} = \frac{1}{2\mu} K_{III}^2, \tag{2.19}$$

2.2.5 Mixed mode crack propagation criteria

It involves two aspects to predict the crack propagation, including when the crack would propagate, and along which direction. For mode I failure, it is known that the crack would propagate in its original direction, and the critical moment for the crack starts to propagate when the stress intensity factor K and energy release rate G reach their critical values. However, for mixed mode crack propagation, the crack would no longer propagate in its original direction, because K_{II} also plays a role in crack growth (see Figure 2.7). Therefore, in order to study the crack propagation of mixed mode, the appropriate fracture criteria need to be established.

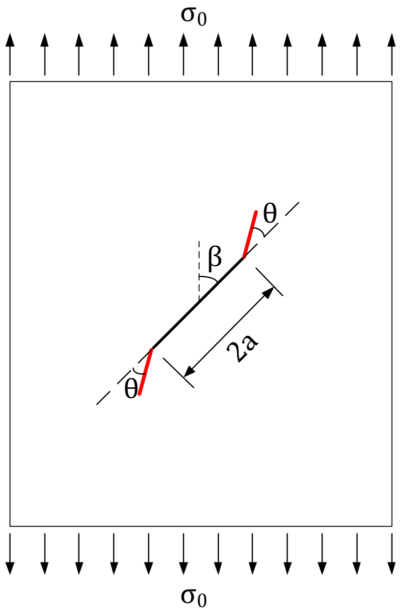

Figure 2.7: A plate containing an inclined crack under uniform tensile loading (mixed mode).

Erdogan and Sih [11] proposed a maximum tensile stress criterion for mixed mode fracture. The criterion assumes that crack extension occurs in the direction at which the circumferential stress takes the maximum with respect to near the crack tip, and fracture takes place when maximum tensile stress is equal to the stress that leads to Mode I fracture. Sih [12] proposed a mixed mode fracture criterion based on the strain energy density concept. The fundamental hypotheses of the strain energy density are the crack will extend in the direction of the minimum strain energy density; and the crack extension occurs when the minimum strain energy density factor reaches its critical value S_{cr}. The maximum energy release rate criterion is an extension of the Griffith fracture theory in that the crack will grow in the direction along which the maximum potential energy is released. In this study, only mode I crack propagation will be studied for simplicity.

2.2.6 Summary

The fracture mechanics is developed to study the load-carrying capacity of structures in the presence of initial defects with high stress gradients. In this section, the fundamental aspects of the linear elastic fracture mechanics are presented.

2.3 Nominal strength - size effects in quasi-brittle fracture

2.3.1 Overview

For the fracture of quasi-brittle materials like concretes, rocks, fiber composites, some types of ceramics, sea ice etc., two main failure criterion are generally taken into account. The former one is stress criterion, assumes that failure happens if the stress σ reaches the tensile strength f_t. This criterion can predict good nominal strength (defined as the mean stress at failure plane) for crack-free bodies, but provides a null failure stress for a body containing a crack, because the stress is singular in front of the crack tip. The latter one is the energy criterion (LEFM fracture criterion), which assumes failure takes place if the energy release rate G equals the fracture energy G_c. The energy criterion works for structures with sufficiently large cracks, but provides an infinite failure load for a crack-free body, because the energy release rate being zero in absence of a crack. Therefore, the above mentioned criteria work only for the extreme cases (i.e. no crack or large crack), but are no longer valid for short and intermediate cracks.

Figure 2.8 shows a center cracked infinite plate subjected to the failure stress σ_{max}. The failure stress σ_{max} according to the energy criterion is dependent on the crack length, which equals to $\sigma_{max} = \sqrt{G_c E/\pi a}$. For a small crack length a, one may obtain $\sigma_{max} > f_t$, which is unrealistic becasue the failure stress cannot be higher than the material tensile strength f_t. The combination of the f_t and fracture energy G_c yields Irwin's [2] characteristic length:

$$l_{ch} = \frac{G_c E}{f_t^2} = \frac{K_c^2}{f_t^2}. \tag{2.20}$$

where E is Young's modulus, K_c is the fracture toughness. Based on a length scale usually proportional to Irwin's characteristic length l_{ch}, several non-local failure criteria have been proposed in the literature [13–16], for the purpose of giving a better prediction of the nominal strength for quasi-brittle materials.

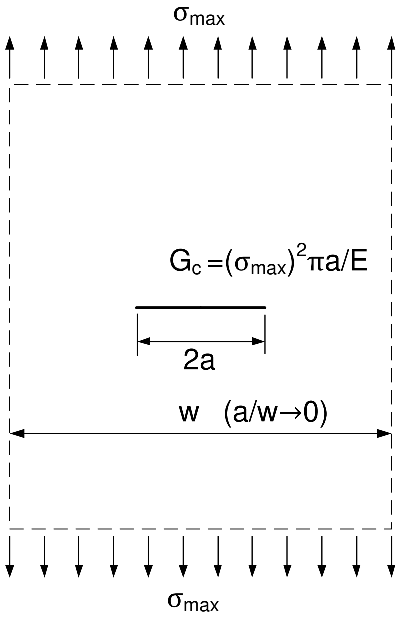

Figure 2.8: Center cracked infinite plate subjected to the failure stress σ_{max}.

The difficulties of nominal strength predictions for quasi-brittle materials is not only the invalidation of conventional stress and energetic criteria for short and intermediate cracks, but also the dependencies of nominal strength on the physical sizes of the specimens and defect types (v-notches, holes etc.), which have been proved by plenty of experiment results. The influences of crack sizes, specimen sizes and defect types on the nominal strength can be summarized as the size effects.

In this section, the experimental evidences (from the literature) of size effects induced by crack size, specimen size and defect type will be reviewed. Then the nominal strength prediction models, including the non-local Theories of Critical Distance (TCDs), and the asymptotic approaches are studied to better understand the advantages and limitations of the existing models.

2.3.2 Size effect induced by defect size at constant specimen size

Figure 2.9 shows typical test results measuring the nominal strength of specimen of silicon carbide (SiC) containing different crack sizes and the model predictions [15]. The model predictions given along with the experimental results will be discussed in detail in Sections 2.3.5, 2.3.6 and 2.3.7. The energy criterion of LEFM works for sufficiently large crack, while the tensile strength seems to be the failure stress when the crack length is below $0.001\,mm$. Between these two conditions, both stress criterion and energy criterion are not applicable. The stress criterion would provide a null strength due to the stress singularity at the crack tip, while the energy criterion would give a unreal nominal strength, which is higher than the material tensile strength. The test results shown in Figure 2.9 indicate that the nominal strength transits smoothly from the tensile strength to LEFM. The intersection of the LEFM line and the line corresponding to the tensile strength is defined as the transition crack length, which can be calculated by the following expression [17]:

$$a_t = \frac{G_c E}{\left(1.12 f_t\right)^2 \pi} = \frac{l_{ch}}{1.12^2 \pi}. \tag{2.21}$$

The transition crack length a_t is proportional to Irwin's characteristic length l_{ch}. Therefore, it is also a material dependent parameter relating to toughness G_c and tensile strength f_t. It should be noticed that SiC is a brittle material with a small value of a_t. Quasi-brittle materials commonly have larger values of a_t, which can be around 40 mm for concrete material. The example of SiC is taken here to illustrate the influence of crack length on the nominal strength, which is the same for brittle and quasi-brittle materials.

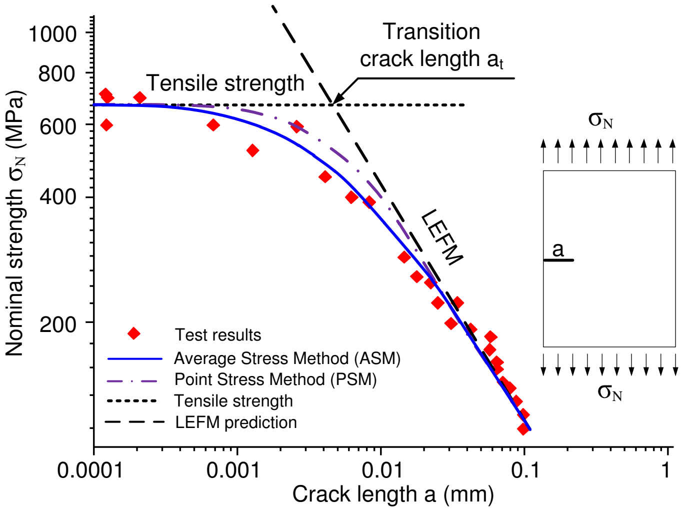

Figure 2.9: Test results and model predictions of nominal strengths versus crack length in SiC (Modifed from [15]).

2.3.3 Size effect induced by specimen size

Bažant *et al.* [18,19] carried out a series of experiments with Cracked Three Point Bending (C-TPB) specimen with similar geometry, to investigate the size effects in geometrically similar concrete specimens. The specimens have the same crack to height ratio $\alpha = 0.33$, the same span to beam height ratio $S/h = 4$ (h varies from $38.1\,mm$ to $533.4\,mm$) and a fixed thickness $t = 25.4\,mm$ (shown in 2.10a). The test results and model predictions of nominal strength for different specimen sizes are plotted in 2.10b, shows a decrease of nominal strength as the increase of specimen size.

2.3.4 Size effect induced by different type of defects

2.3.4.1 Nominal strength dependence on the v-notch opening angle at constant specimen size

The tests of Nominal strength dependence on the v-notch opening angle at constant specimen size have performed by many reserchers [20–22]. Figure 2.11a shows an example of v-notched three point bending beam with notch opening angle γ. The ratio of nominal strength $\sigma_N(\gamma)/\sigma_N(\gamma = \pi)$ with respect to different notch opening angles is plotted in Figure 2.11b [20], where $\sigma_N(\gamma = \pi)$ is

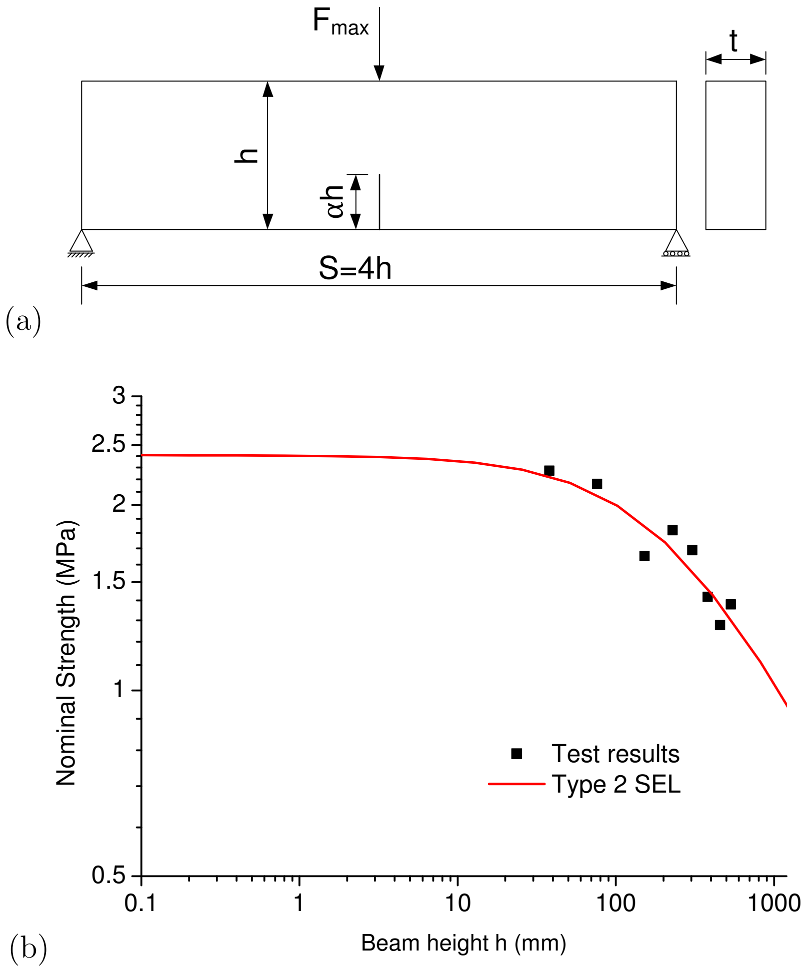

Figure 2.10: (a) Cracked three point bending beam and (b) Test results and model predictions of nominal strength σ_N for different specimen sizes [18, 19].

material tensile strength f_t. For $\gamma = 0°$, the v-notch becomes a crack, therefore, the failure behavior is dominated purely by fracture mechanics. As the increase of γ, the nominal strength would increase accordingly and transit smoothly to be dominated by material tensile strength. When $\gamma = 180°$, the v-notch becomes a straight edge, where fracture mechanics doesn't work because of the zero energy release rate for un-notched sample, and therefore $\sigma_N(\gamma = \pi) = f_t$. To sum up, the nominal strength of the v-notched three point bending beam specimen with constant size is dependent on the v-notch opening angle, which transits smoothly from LEFM dominant to material strength dominant.

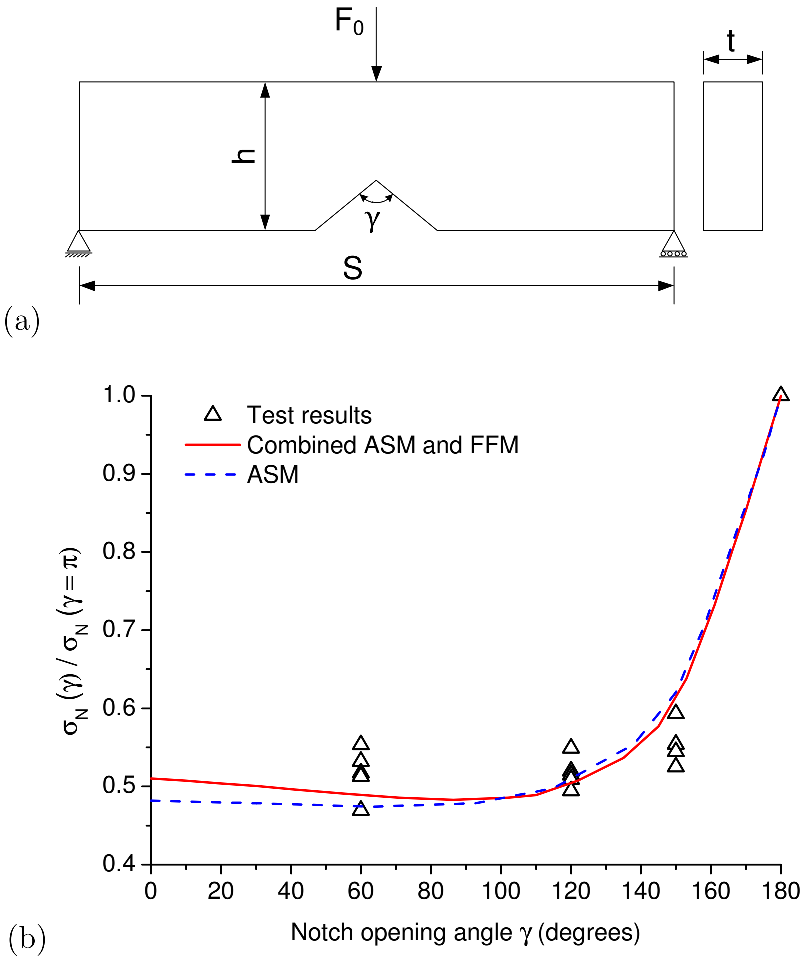

Figure 2.11: (a) V-notched three point bending beam and (b) Test results and model predictions of nominal strength ratio $\sigma_N(\gamma)/\sigma_N(\gamma = \pi)$ for different notch opening angles γ [20].

2.3.4.2 Nominal strength dependence on the specimen size of open hole plate specimen

Camanho *et al.* [23] performed open-hole tensile tests using the $[90/0/\pm 45]_{3s}$ lay-up IM7-8552 in carbon epoxy. Specimens presenting the same aspect ratio based on the hole diameters D ($2.0\,mm$, $4.0\,mm$, $6.0\,mm$, $8.0\,mm$ and $10.0\,mm$) were adopted (for widths $w = 6D$, as shown in Figure 2.12a).

The nominal strength dependence on the specimen size of open hole plate specimen is presented in Figure 2.12b), shows a decrease of nominal strength as the increase of specimen size (proportional to hole diameter). For plates with circular holes, although the stress concentration factor (the ratio of the highest stress σ_{max} to a reference stress σ_0 of the gross cross-section) is 3, which is independent with the hole diameter (specimen size), the nominal strength of the open-hole is $f_t/3$ only for sufficiently large specimen sizes. As the decrease of hole diameter, the nominal strength will increase and tend to the material tensile strength f_t (hole size being smaller or in the same magnitude of material's micro defect size).

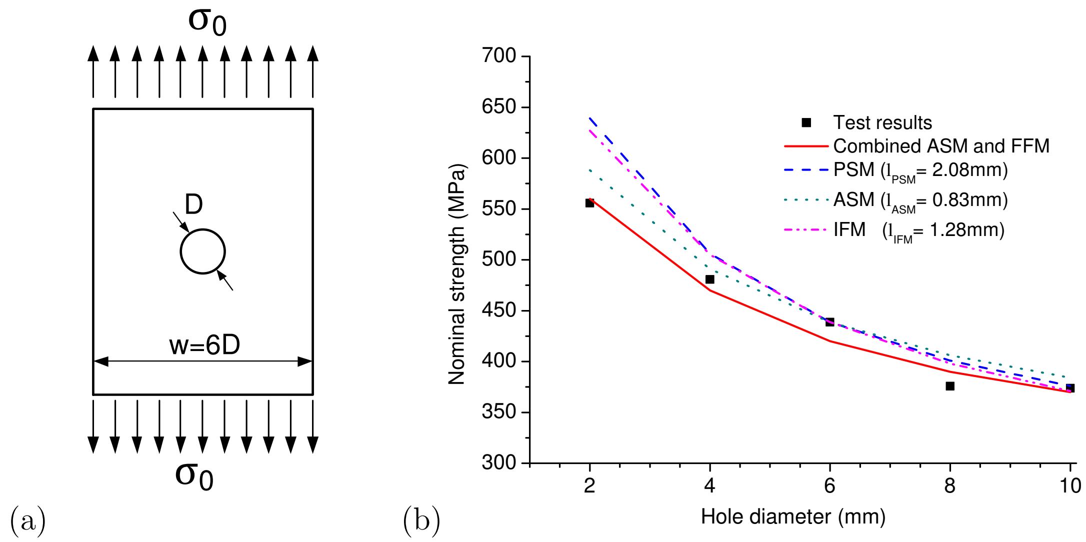

(a) (b)

Figure 2.12: (a) Geometry of the plates with open holes and (b) Test results and model predictions of nominal strength for various hole diameters D [24].

2.3.4.3 Notion of crack band

The transition from the crack initiation (dominated by the strength of the material) and its propagation (described by fracture mechanics) can be analyzed conceptually by the notion of crack band (defined by its thickness T) as proposed in [25–27]; high-stress gradients (at the vicinity of a crack, for example) induce small values of T, whereas in homogeneous stress, T contain all the sample (Figure 2.13).

2.3.5 Theories of critical distance (TCDs)

In order to reproduce the observed size effects, several elastic stress field based models, fracture mechanics based models, combined stress and energy models,

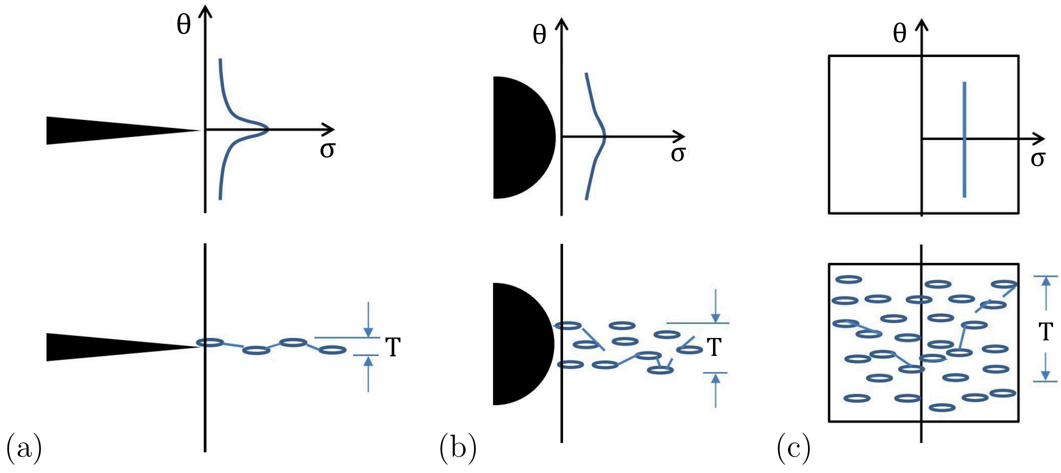

Figure 2.13: Crack band T according to the stress gradient: (a) under high gradient, near a crack, (b) under low gradient, near a geometric defect, and (c) under absence of gradient, in uniform stress. Figure present in reference [28], modified from Zhang and Li [27].

and asymptotic approaches have been established by the researchers. The first three models are classified as Theories of Critical Distance (TCDs), because they are associated to a length scale usually proportional to characteristic length l_{ch}. This length scale is needed because of the singular stress state near the crack tip, which makes a pure evaluation of the stress is useless when predicting the nominal strength.

Based on the stress criterion, TCDs were initially proposed in 1930's by Neuber [29] and Peterson [30], using a punctual evaluation of the stress at a certain distance from the crack tip (PSM: Point Stress Method) and the average of the stress over a certain length (ASM: Average stress Method) respectively to analyze the failure of metallic structures. After that, TCDs have been developed to a group of methods which have certain features in common, that is, principally the use of a characteristic material length parameter, which is proportional to the material characteristic length l_{ch} (Equation 2.20) [15]. In recent years, TCDs have gained popularity, due to the easiness of the elastic stress field computation by finite element method. TCDs have been employed for different materials, such as ceramics [31], polymers [32], composites [33], etc.

According to Taylor [15] and Maimi [16], TCDs can be classified in three categories: the elastic stress field based models, the fracture mechanics based models, and the combined stress and energy models. The elastic stress field based models, such as PSM and ASM, only use the elastic stress field to predict the nominal strength, while the fracture mechanics based models usually use only the energy criterion of LEFM. The combined stress and energy models couple both criteria to predict the nominal strength.

2.3.5.1 Elastic stress field based models of TCDs

(a) Point Stress Method (PSM): Point stress method is the simplest form of the TCDs. It assumes that failure will occur when the stress at a distance l_{PSM} from the notch tip is equal to material tensile strength f_t. The PSM can be written as:

$$\sigma(l_{PSM}) = f_t \tag{2.22}$$

Consider a center cracked infinite plate subjected to pure tensile stress σ_0 (See Figure 2.3), the full expression of stress field ahead of the crack tip for any crack length a (Westergaard's solution) in rectangular coordinate system is:

$$\sigma(x) = \sigma_0 \left[1 - \left(\frac{a}{a+x}\right)^2\right]^{-1/2}. \tag{2.23}$$

When $a \gg x$, this expression is reduced to $\sigma(x) = \sigma_0\sqrt{a/(2x)}$. Recall the definition of mode I stress intensity factor $K_I = \sigma_0\sqrt{\pi a}$, the expression of stress field will be the same as the one presented in Section 2.2.3, which is:

$$\sigma(x) = \frac{K_I}{\sqrt{2\pi x}}. \tag{2.24}$$

The material length scale parameter l_{PSM} is obtained when $K = K_c$ and $\sigma(x) = f_t$:

$$l_{PSM} = \frac{1}{2\pi}\left(\frac{K_c}{f_t}\right)^2 = \frac{l_{ch}}{2\pi}. \tag{2.25}$$

According to PSM, the nominal strength of middle cracked plate with any crack length a can be solved using 2.23 as:

$$\sigma_N = f_t \left[1 - \left(\frac{a}{a + l_{PSM}} \right)^2 \right]^{1/2}. \tag{2.26}$$

When $a = 0$, $\sigma_N = f_t$, as the increase of a, the nominal strength σ_N would decrease and after a certain crack length, the failure of the structure is dominated mainly by LEFM.

For other defect types, such as v-notched specimens, specimens with circular holes, once the stress distribution is known, the nominal strength then can be easily predicted by PSM. Figure 2.9 shows the nominal strength of cracked plate predicted by PSM and compared with the test results, indicates that the PSM can capture the transition effectively and give the predictions in good agreement with the test results for any crack length. In term of open hole tests shown in Figure 2.12, PSM can also give the acceptable predictions of nominal strengths for various hole diameters. However, it should be pointed out that, in order to fit the test results, l_{PSM} is calculated from the test results of the specimen with a $6\,mm$ diameter hole, instead of calculating from the material parameters [24].

(b) Average Stress Method (ASM): Average stress method uses the average stress over some distance l_{ASM} starting at $x = 0$. The ASM criterion can be written as:

$$\frac{1}{l_{ASM}} \int_0^{l_{ASM}} \sigma(x) dx = f_t \tag{2.27}$$

Substituting Equation 2.24 into Equation 2.27 when $K_I = K_c$, the ASM length scale l_{ASM} can be solved as $l_{ASM} = 2l_{ch}/\pi$, which is $4 \times l_{PSM}$.

In order to generalize ASM criterion to any crack length a, the full stress filed of Equation 2.23 should be substituted into ASM criterion (Equation 2.27). Hence, the nominal strength of the center cracked plate can be solved as:

$$\sigma_N = f_t \sqrt{\frac{l_{ASM}}{2a + l_{ASM}}}. \tag{2.28}$$

For long cracks subjected to tensile loading, the predictions given by PSM and ASM would be identical. When the crack length is in the same magnitude of transition crack length a_t, shown in Figure 2.9, PSM and ASM give the predictions of nominal strength with small differences. Figure 2.11b and Figure 2.12b show respectively, the nominal strength predictions given by the ASM, for v-notched beams and plates with circular holes, which show good agreements with the test results.

(c) Area Stress Method and Volume Stress Method: These two methods average the stresses over some area or some volume around the tip of defect, and their critical value is tensile strength f_t. The predictions of these two methods are dependent on the shape of the area or volume chosen to calculate the mean stress. These two methods are also able to predict the nominal strength for various defect types, however, in contrast to PSM and ASM, they are more difficult to be implemented and cannot provide the higher accuracy [15].

2.3.5.2 Fracture mechanics based models

(a) Imaginary Crack Models (ICM): This model was firstly developed independently by Waddoups *et al.* [34] for the static failure analysis of composite materials, and by El Haddad *et al.*, for the fatigue analysis of short cracks [35]. ICM predicts the failure by introducing a sharp crack with length l_{ICM} at the root of the defect and applying LEFM. The length of the crack l_{ICM} is assumed to be a material constant. The critical stress intensity factor of the introduced crack is fracture toughness K_c.

Consider a plate under tensile stress σ_0, and contains a crack of length a. Applying ICM, the stress intensity factor at the imaginary crack tip is:

$$K = A(\alpha)\sigma_0\sqrt{\pi(a + l_{ICM})}, \tag{2.29}$$

where $A(\alpha)$ is the geometrical correction factor dependent on the crack to width ratio $\alpha = a/w$, $A(\alpha) = 1$ and $A(\alpha) = 1.12$ respectively for a center crack and edge crack, when $\alpha \to 0$. The empirical equations of $A(\alpha)$ with high accuracy for different structures can be found in [36]. For $a \gg l_{ICM}$, the length of l_{ICM} has a negligible effect on K, hence, failure is dominated by LEFM. For another extreme case, when $a = 0$, in order to obtain the material tensile strength f_t as the failure stress, the following equation must be satisfied:

$$K_c = A(\alpha = 0)f_t\sqrt{\pi l_{ICM}}. \tag{2.30}$$

Therefore, the length of l_{ICM} can be solved as:

$$l_{ICM} = \frac{1}{\pi}\left[\frac{K_c}{A(\alpha=0)f_t}\right]^2 = \frac{l_{ch}}{A^2(\alpha=0)\pi}. \tag{2.31}$$

By relating Equations 2.29 and 2.30, the nominal strength for any crack length a can be obtained:

$$\sigma_N = \frac{f_t A(\alpha=0)}{A(\alpha)}\sqrt{\frac{l_{ICM}}{a+l_{ICM}}}. \tag{2.32}$$

It is noticed that the nominal strength predicted by ICM (Equation 2.32) is identical with the ASM (Equation 2.28), for the case of $A(\alpha=0) = A(\alpha) = 1$ ($l_{ICM} = 1/2l_{ASM}$). An application shown in Figure 2.12 indicates that ICM is capable of characterizing the size effect.

(b) Finite Fracture Mechanics (FFM): The finite fracture mechanics method (FFM) [14,37] computes the mean energy release rate necessary for a crack growth at a distance l_{FFM}. Failure will occur if there is sufficient energy available to allow this finite amount of crack growth. The value of l_{FFM} is a material constant, which equals to $2l_{ch}/\pi$. FFM model can be expressed in two ways, either in terms of the strain energy release rate:

$$\int_a^{a+l_{FFM}} G da = G_c l_{FFM}, \tag{2.33}$$

or in terms of the stress intensity:

$$\int_a^{a+l_{FFM}} K^2 da = K_c^2 l_{FFM}. \tag{2.34}$$

For a center crack in a infinite plate subjected to tensile loading ($A(\alpha) = 1$), the nominal strength given by FFM can be expressed as:

$$\sigma_N = K_c\sqrt{\frac{2}{\pi(2a+l_{FFM})}}. \tag{2.35}$$

When $a \gg l_{FFM}$, $Kc \approx \sigma_N\sqrt{\pi a}$, being identical as the predictions of LEFM. On the other hand, when $a = 0$, the length scale in FFM l_{FFM} can be solved as:

$$l_{FFM} = \frac{2}{\pi}\frac{K_c^2}{f_t^2} = \frac{2l_{ch}}{\pi}, \tag{2.36}$$

which is equal to l_{ASM}.

2.3.5.3 Combined stress and energy models

The combined stress and energy models assume that failure is reached when stress and energy criteria are fulfilled simultaneously. To enforce the accomplishment of both criteria at the same time, it is required to consider the characteristic material length as variable [16].

(a) Combined PSM and FFM (Leguillon's model [13,38]): Leguillon proposed a criterion to predict the crack initiation in a v-notch tip, assuming that when fracture occurs the energy criterion and stress criterion are fulfilled simultaneously, even if one often hides the other. An increment length l_0 depending on the material properties and the notch opening angles is determined to ensure that the two criteria hold true, then the failure load can be calculated by either the stress criterion or the energy criterion.

(b) Combined ASM and FFM (Coupled Finite Fracture Mechanics [14, 24]): In Coupled Finite Fracture Mechanics (CFFM), the value of the finite crack extension l_{CFFM} is determined by the fulfillment of both the stress and energy criteria:

$$\begin{aligned} &\int_a^{a+l_{CFFM}} \sigma_y(x)dx = f_t \times l_{CFFM}, \\ &\int_a^{a+l_{CFFM}} K^2 dx = K_c^2 \times l_{CFFM}. \end{aligned} \tag{2.37}$$

The two unknowns values in Equation 2.37, including the failure load σ_{max}, and the finite crack extension l_{CFFM}, can be solved when the stress distribution and stress intensity factor expression are known. Two applications of CFFM are presented in 2.11b and 2.12b. The better nominal strengths are obtained than the other models, for v-notched beam and holed plate subjected to tension.

2.3.6 Boundary Effect Model (BEM)

2.3.6.1 Boundary effect on fracture of a large plate with an edge crack

The Hu-Duan Boundary Effect Model (BEM) [17,39,40] attributes the size effect on structural strength to the interaction between the Fracture Process Zone (FPZ) and the structural boundary. Figure 2.14a shows a plate with an edge crack. The nominal strength σ_N is defined without considering the presence of the crack, while σ_n represents the stress for peak load at the crack tip under the hypothesis of a linear stress distribution across the ligament, without considering the stress concentration and singularity at the crack tip. The relationship of σ_N and σ_n is $\sigma_N = B(\alpha)\sigma_n$. $B(\alpha)$ is a non-dimensional factor depending on the crack to width ratio α $(\alpha = a/w)$, $B(\alpha) = (1-\alpha)^2/(1+2\alpha)$ for single edged cracked plate, and $B(\alpha) = (1-\alpha)^2$ for cracked three point bending specimen.

When the crack length $a \to 0$, the nominal strength σ_N is considered to approach the material tensile strength f_t, and when a and $(W-a)$ are sufficiently large, the nominal strength is dominated by LEFM. Hence, Hu and Duan proposed the following expression to describe the dependence of specimen strength σ_N on the crack length a for a large plate with an edge crack:

$$\sigma_N = f_t \left[1 + \left(\frac{a}{a_t}\right)\right]^{-1/2}, \tag{2.38}$$

where a_t is the transition crack size (Equation 2.21. For the large plate case, the crack size a represents the distance of the crack-tip to the specimen front free surface. Eq. 2.38 indicates that when the distance of the crack-tip to the front boundary is comparable to a_t, the specimen strength will be subjected to the boundary effect. When the crack-tip is very far away from the front boundary, the LEFM criterion prevails and the specimen strength is mainly determined by its toughness G_c (see Figure 2.14b) [17].

2.3.6.2 Boundary effect on fracture of a finite width plate with an edge crack

Equation 2.38 is developed for an large plate with an edge crack. while for a finite width plate with an edge crack, $B(\alpha) \approx 1$ is no longer valid for any crack

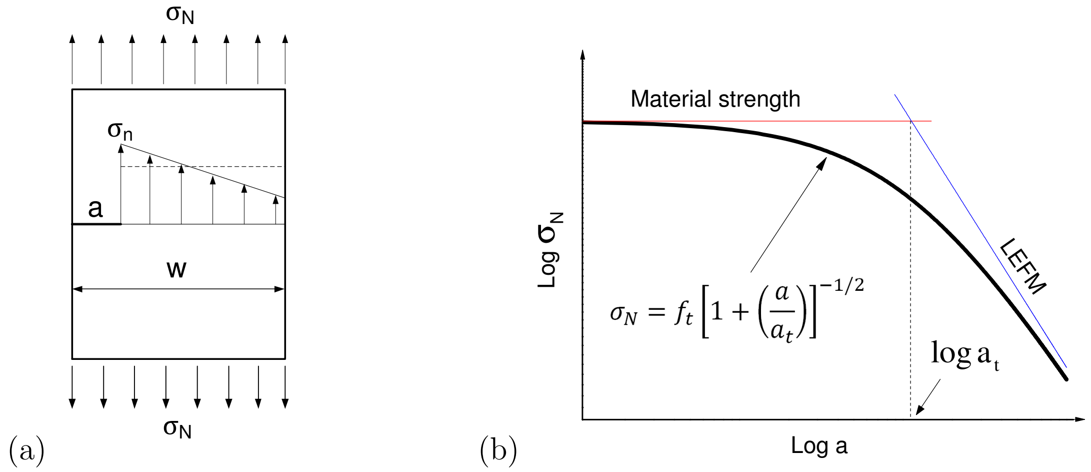

Figure 2.14: (a) An edge crack in a plate and (b) its nominal strength σ_N as a function of crack length a (modified from [17]).

size. In order to extend Equation 2.38 to the cracked finite width plate, Hu and Duan introduced the following modification of Equation 2.38:

$$\sigma_N = B(\alpha) f_t \left[1 + \left(\frac{a_{e1}}{a_t}\right)\right]^{-1/2}, \tag{2.39}$$

where $B(\alpha) = (1-\alpha)^2/(1+2\alpha)$ for single edged cracked plate, a_{e1} is referred to as the equivalent crack length, and its value depends on specimen geometry and crack length, which reads:

$$a_{e1} = \left[\frac{B(\alpha) \times A(\alpha)}{1.12}\right]^2. \tag{2.40}$$

Equation 2.39 can be used to predict the nominal strengths of finite or infinite width specimen containing different crack sizes. The applications of BEM can be found in [17, 39, 40].

2.3.7 Size Effect Law (SEL)

2.3.7.1 Type 2 Size Effect Law

On a small scale, quasi-brittle materials obey the strength theory that is characterized by the material strength f_t, while on a large scale, they conform to

Linear Elastic Fracture Mechanics (LEFM) and are characterized by the fracture energy G_c. The combination of f_t and G_c yields Irwin's [2] characteristic length $l_{ch} = G_c E / f_t^2$, where E is the Young's modulus, and divides the small and large scales [41]. Based on an approximate energy release analysis, SEL was derived for geometrically similar specimens (Figure 2.15a) in 1984 [42] and reformulated in 1991 [43]. For type 2 failures, which are occurring when there is a notch or large stress-free crack formed before reaching the maximum lading, the law reads:

$$\sigma_N = \hat{B} f_t \left(1 + \frac{h}{h_0}\right)^{-1/2}, \tag{2.41}$$

where $\hat{B}$ is a positive dimensionless constant depending on the geometry of the structure; f_t is the material tensile strength; h_0 is a constant proportional to Irwin's characteristic length l_{ch}, at which the failure laws based on material strength and LEFM intersect, as shown in Figure 2.15b. h_0 and $\hat{B}$ characterize the structure geometry.

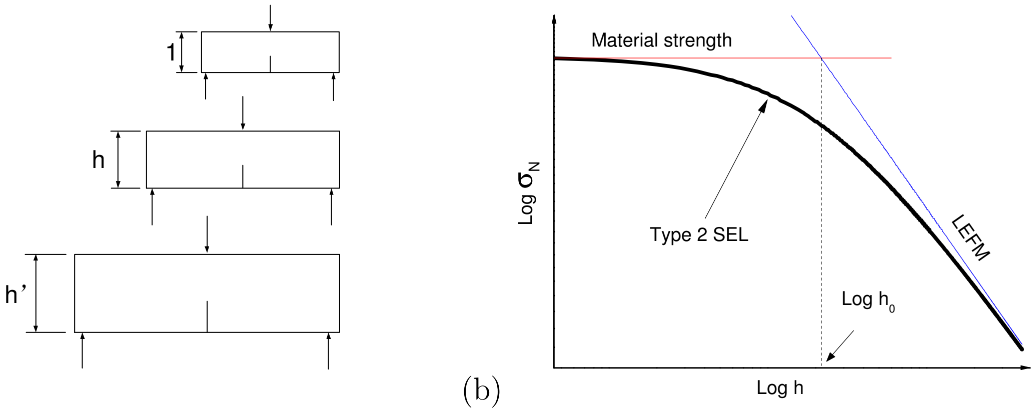

(a) (b)

Figure 2.15: (a) Similar cracked structures and (b) SEL bridging the failure mechanisms of material strength and LEFM.

2.3.7.2 Type 1 Size Effect Law

Since Type 2 SEL is not valid when crack to height ratio α tends to 0, the Type 1 SEL [44] was proposed after Type 2 SEL, and applied to structures failing at crack initiation from a smooth surface. The Type 1 SEL reads [45]:

$$\sigma_N = f_{r,\infty} \left(1 + \frac{r h_b}{h + l_p} \right)^{1/r}, \tag{2.42}$$

where $f_{r,\infty}$, h_b, l_p, and r are constants of the model whose values need to be determined empirically.

2.3.7.3 Universal Size Effect Law (USEL)

Type 1 SEL is developed for failures at crack initiation from a smooth surface, and Type 2 SEL is for failures starting from a deep notch or crack. In order to describe the continuous transition between these two types of size effects, the Universal Size Effect Law (USEL) was firstly defined by Bažant [46], and then improved by Bažant and Yu [47]. USEL has been validated by the various experimental results, shows to fit the test results quite well [48].

2.3.8 Summary

The experimental evidences of size effects induced by defect size at constant specimen size and induced by specimen size have been reviewed in this section. The non-local models for nominal strength predictions, which are associated with a length scale usually proportional to material characteristic length l_{ch} is then studied. TCDs are capable of predicting the nominal strength in good agreement with the test results. However, for certain building materials (such as concrete), the value of the characteristic length scale can become too large compared to the specimen size (sometimes even exceeding it), which makes the direct implementation of these approaches impossible [15]. The asymptotic approaches, such as Hu-Duan's Boundary effect model, and Bažant's Size Effect Law, are all able to characterize the size effect induced by the defect size and specimen size. The detailed comparison of these two models can be found in [45, 47, 49].

2.4 Damage and fatigue crack growth

2.4.1 Overview

Fatigue is the weakening of a material caused by repeatedly applied loads (moving forces, cycles of temperature, etc.). The intensity of the applied loads are usually far below the strength of the material, but it is responsible by the degradation of the mechanical behavior of the material. Most laboratory fatigue tests consist of applying constant amplitude sinusoidal displacement or force at the boundary of an asphalt concrete sample. During the tests, the variation in global stiffness is monitored. Figure 2.16 shows the stiffness degradation during a fatigue bending test. The global stiffness is calculated by the ratio of the force to the displacement amplitude, which decreases following three stages as shown in Figure 2.16: stage I is characterized by a rapid decrease in the stiffness and the nucleation of micro cracks. It is followed by stage II that corresponds to a quasi-linear decay in stiffness. During this phase the changing stiffness stabilizes and there dissemination and distribution of micro cracks in the whole volume. Fracture occurs during stage III, due to damage acceleration and to ultimately to the propagation of macro cracks.

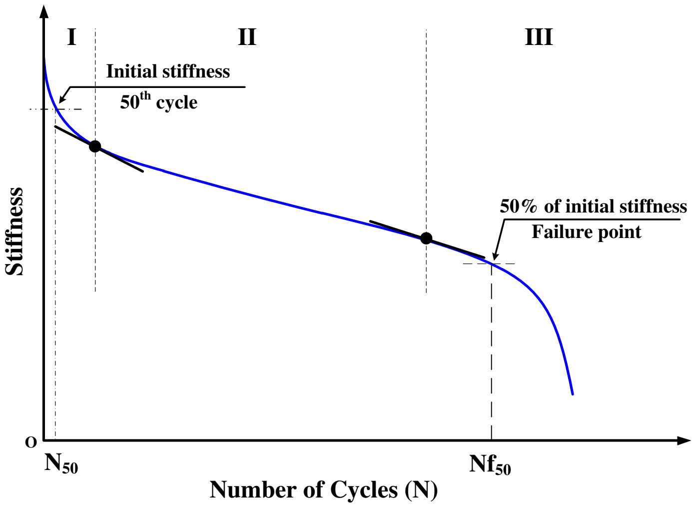

Figure 2.16: Evolution of stiffness during typical fatigue test.

Fatigue life is very important for the structure design, which is the number of stress cycles of a specified character that a specimen sustains before failure of a specified nature occurs. Its prediction is still an empirical science rather than a theoretical one [50]. Considering the duration of fatigue life, the cyclic behavior can be classified as High Cycle Fatigue (HCF) and Low Cycle Fatigue (LCF). For HCF, where stress is low and deformation is primarily elastic. The performance of the material is commonly characterized by an Stress-cycle curve (S-N curve or Wöhler curve). For LCF the stress is high enough for plastic deformation to occur, hence, the fatigue life is much lower.

The continuum damage model (CDM) is capable of predicting the fatigue life of the asphalt concrete samples; however, CDM neglects the existence of large cracks in the damaged material. In reality, the macro cracks can be observed during the end of stage II and stage III, which indicate that the continuum damage model is not appropriate to describe all the stages of fatigue life. On the other hand, the fatigue crack growth model, such as Paris' law, can predict the fatigue life of the structure with sufficiently large crack, but fails to capture the regime of crack initiation and small crack propagation.

It is still difficult today to capture all of the stages with one single fatigue model. In other words, the fatigue life prediction of all the stages might be inaccurate and need to be better understood. In this section, continuum damage models (usually more adapted for stages I, II) are presented. Then, fatigue crack growth modelling is introduced in order to better represent stage III.

2.4.2 Continuum damage models (CDMs)

CDMs are capable of predicting the fatigue life of the specimen without large cracks. During the fatigue tests, as the material is deformed, the initiation, growth and coalescence of micro defects decrease the stiffness (degradation of material properties), which is represented by the growth of the damage variable D. D is a scalar ranges from 0 to 1. For the virgin, undamaged material, D is 0. While D = 1 corresponds to a completely damaged with zero stiffness. The stress strain relation can be written as Equation 2.43:

$$\sigma_{ij} = C_{ijkl}\varepsilon_{kl} = (1 - D)C^0_{ijkl}\varepsilon_{kl}, \tag{2.43}$$

where σ_{ij} and ε_{kl} are the elastic stress and strain tensor components, $= C_{ijkl}$ and C^0_{ijkl} are damaged and initial (elastic) secant stiffness of the material. C^0_{ijkl} is a function of Young's modulus E and Poisson ratio ν.

Several stress and strain based continuum damage models have been established by the researchers, including the models established by Castro and Sanchez [51], Di Benedetto [52], Lee [53], Bodin et al. [54, 55]. All the models are capable of predicting the fatigue life of asphalt concrete. However, the damage evolution law for D and stress, strain adopted in the damage models might be different. In this study, the local version of continuum damage model proposed by Bodin *et al.* will be utilized, which is widely used for asphalt mixtures [54, 56, 57].

2.4.2.1 Bodin's model

Bodin et al. proposed an elastic isotropic continuum damage model for fatigue, which characterizes the decrease in stiffness with cyclic loading. The damage growth criterion is based on a modified Rankine criterion with zero threshold damage growth. Evolution of damage (local version of the model) is controlled by the strain state of the material by a scalar equivalent strain, which can be written as follows:

$$\tilde{\varepsilon} = \sqrt{\sum_{i=1}^{i=3} \left(\frac{\langle \sigma_i \rangle_+}{E(1-D)} \right)^2} \tag{2.44}$$

In the nonlocal version of Bodin's model, the "local" equivalent strain $\tilde{\varepsilon}$, is replaced by its weighted average strain. The expressions for weighted average strain calculation can be found in [54, 55, 58].

The rate of damage growth is defined as a function of local equivalent strain rate:

$$\dot{D} = f(D)\tilde{\varepsilon}^{\beta} \left\langle \dot{\tilde{\varepsilon}} \right\rangle, \tag{2.45}$$

where $f(D)$ is function of damage. The exponent β is a material parameter, which relates to the slope (equals to$-1-\beta$) of S-N curve in the log-log diagram.

The function of damage $f(D)$ given by Paas [59] can capture two regimes shown in Figure 2.16 very well:

$$f(D) = CD^{\alpha}. \tag{2.46}$$

The occurrence of the third stage, with significant acceleration of damage growth, cannot be described properly by Equation 2.46. Therefore, Bodin proposed a new damage function (Equation 2.47) [54] which can describe all of the three stage law:

$$f(D) = \frac{\alpha_2}{\alpha_1 \alpha_3} \left(\frac{D}{\alpha_2} \right)^{1-\alpha_3} \exp \left(\frac{D}{\alpha_2} \right)^{\alpha_3} \tag{2.47}$$

where α_1 , α_2 , and α_3 are three model parameters. Figure 2.17 shows the effects of these parameters on the damage evolution of a uni-axial fatigue test subjected to sinusoidal displacement cycles with constant amplitude ε.

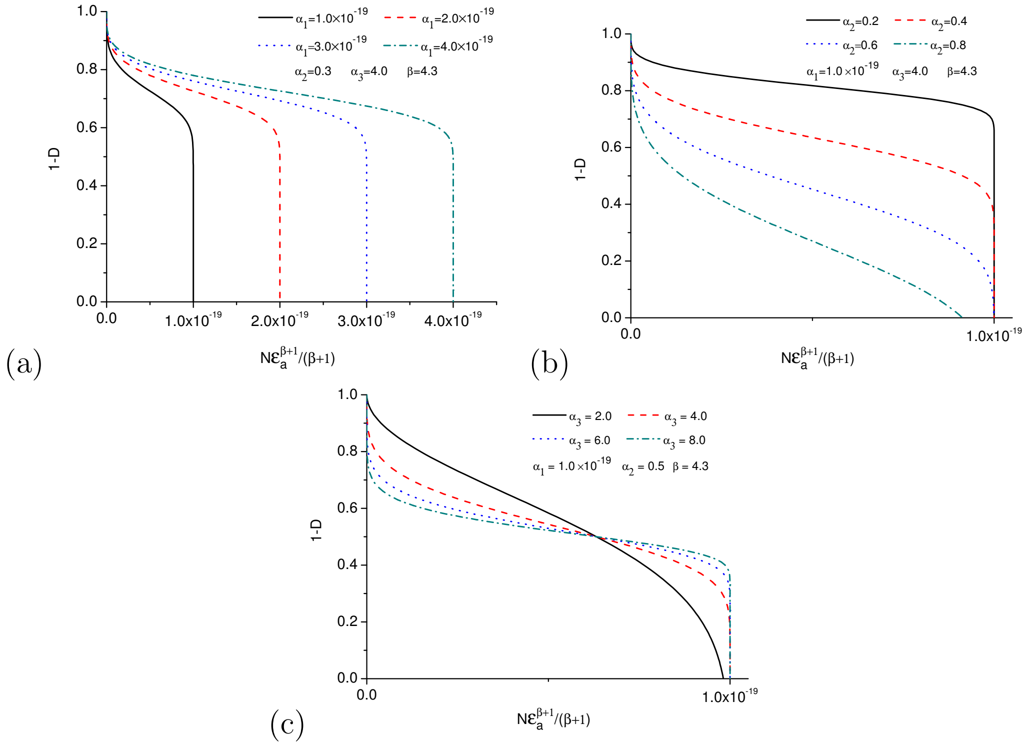

(a) (b) (c)

Figure 2.17: Sensitivity of parameters (a) α_1, (b) α_2 and (c) α_3 in damage model to uni-axial fatigue [54].

2.4.2.2 Numerical calculation of damage increment by cycle

In the case of uni-axial fatigue test, the fatigue life prediction based on Bodin's model can be achieved by a simple integration of Equation 2.45. While for the cases of multi-axial fatigue tests, such as two-point bending (2PB) test and four-point bending (4PB) test, the numerical method is needed to predict the damage evolution and fatigue life of the material. For each cycle, the increment of damage can be calculated based on the equations of the damage model presented in the previous section.

The damage calculation is done using a step by step approach. Consider a local point in the structure subjected to sinusoidal cyclic loading. A loading cycle (cycle N) is discretized in different time intervals as shown in Figure 2.18. Recall the relationship of damage growth rate and local equivalent strain rate:

$$\frac{d(D)}{f(D)} = \tilde{\varepsilon}^{\beta} d\left\langle \tilde{\varepsilon} \right\rangle . \tag{2.48}$$

Only during the time that local equivalent strain is increasing, the damage value of this local point increases too, otherwise, damage remains unchanged. In cycle N, from t_i to t_{i+1}, the local strain varies from $\tilde{\varepsilon}_i$ to $\tilde{\varepsilon}_{i+1}$. By integration of Equation 2.48:

$$\int_{t_i}^{t_{i+1}} \frac{1}{f(D)} dD = \int_{t_i}^{t_{i+1}} \tilde{\varepsilon}^{\beta} d\left\langle \tilde{\varepsilon} \right\rangle , \tag{2.49}$$

one can easily obtain the damage increment from D_i to D_{i+1}. The function of f(D) is given by Paas (Equation 2.46) or Bodin (Equation 2.47).

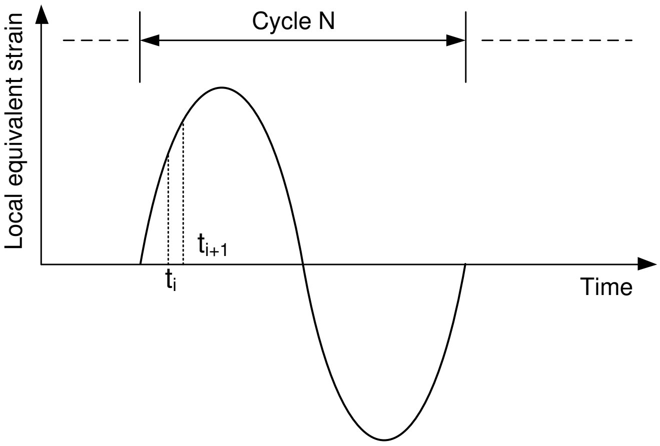

Figure 2.18: Cycle N.

The local equivalent strain can be obtained easily by the numerical methods, such as Finite Element Method and Discrete Element Method, etc. The number of time intervals during one cycle is decided based on the accuracy needed for the calculation.

2.4.2.3 Jump in cycles procedure in fatigue damage modelling

As has been introduced in the previous section, the damage increment by cycle can be calculated based on the evolution of the local equivalent strain, hence technically, the damage at the end of cycle N can be calculated cycle by cycle. However, for high cycle fatigue computations, the fatigue life can be greater than 10^6 cycles. Therefore, it does not seem to be realistic to perform a numerical computation over the entire number of cycles. To avoid the integration of the model on each cycle, the so-called "jump-in-cycle" procedure devised by Lemaitre [60] and improved by Peerlings *et al.* [61] has been implemented in Bodin's work [54, 55].

Consider an initial state defined at the beginning of cycles $N-1$, each point in the material has its damage state $D(N-1)$. After performing one cycle, one can obtain the increment of damage per cycle $dD/dN = M[D(N)]$. Integration of damage growth between cycle N and cycle $N+\Delta N$ is approximated with the help of a trapezoidal rule:

$$D(N+\Delta N) = D(N) + \frac{1}{2}\left\{M[D(N)] + M[D(N+\Delta N)]\right\}\Delta N. \tag{2.50}$$

This integration is implicit as it requires the computation of $M[D(N+\Delta N)]$. This term can be obtained by performing a cycle of cycle $(N+\Delta N-1)$, the damage state at the beginning of cycle $(N+\Delta N-1)$ is predicted by $D^P(N+\Delta N-1) = D(N)+(\Delta N-1)M[D(N)]$ [54]. An alternative way to calculate $M[D(N+\Delta N)]$ is evaluated following Euler forward prediction [55]:

$$M[D(N+\Delta N)] = M[D(N)] + \frac{\partial M}{\partial N}\Delta N. \tag{2.51}$$

In order to limit the error of this jump in cycles procedure, the increment of cycles ΔN should be satisfied $\Delta N = \varphi \times \partial D/\partial M$, φ is a fixed parameter in the computation [54, 55, 61].

2.4.2.4 Non-local damage approaches

Non-local continuum damage is a consistent general concept for macroscopic modelling of failure in quasi-brittle materials. In these approaches, the internal length plays a pivotal role as it controls the size of damage localization zone, and the larger this parameter, the longer the fatigue life of bending beams [54, 62]. Some variables (stress, strain etc.) in the constitutive equation for a point of the continuum are related through spatial averaging integrals to the field of these or other variables in a certain neighborhood of the point [63]. This average of the variables avoids the problems existed in most of the local models when the state of strain is not homogeneous, such as localization of the stresses, mesh effects, and unreal low fatigue life etc.

Bodin's damage model was used for the prediction of fatigue damage of asphalt concrete in the configurations of the tensile compression (T/C) test [54], shear test [54], two-point bending (2PB) test [54–56], and four-point bending (4PB) test [54, 57, 64, 65].

Arsenie [57, 64, 65] performed the 4PB tests of non-reinforced and fiber glass grid reinforced asphalt concrete. Figure 2.19 presents a typical beam specimen subjected to imposed sinusoidal displacement. Based on Bodin's damage model, Arsenie predicted the fatigue lives of non-reinforced and fiber glass reinforced specimens, and compared with the test results, showed good agreements.

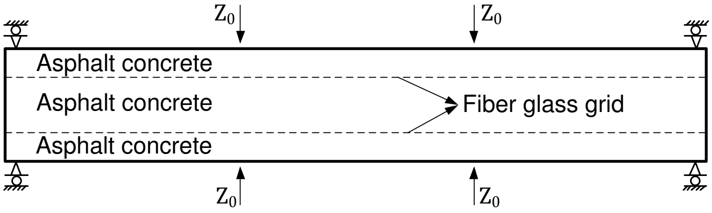

Figure 2.19: Fiber glass grid reinforced four-point bending specimen made of asphalt concrete.

Figure 2.20 shows the final damage distributions in the beam of the non-reinforced and reinforced specimens, respectively. The modelling results showed that at the moment of failure, there exited two symmetric large zones that damage $D = 1$ (red area). For fiber glass grid reinforced specimen, the material damage $D \approx 0$ (blue layer) between the fiber glass gird. With the calibrated material parameters, the good fatigue life can be predicted based on Bodin's damage model, however, the failure pattern is not close to reality, that the cracks should appear instead of two large zones where the materials are nonfunctional.

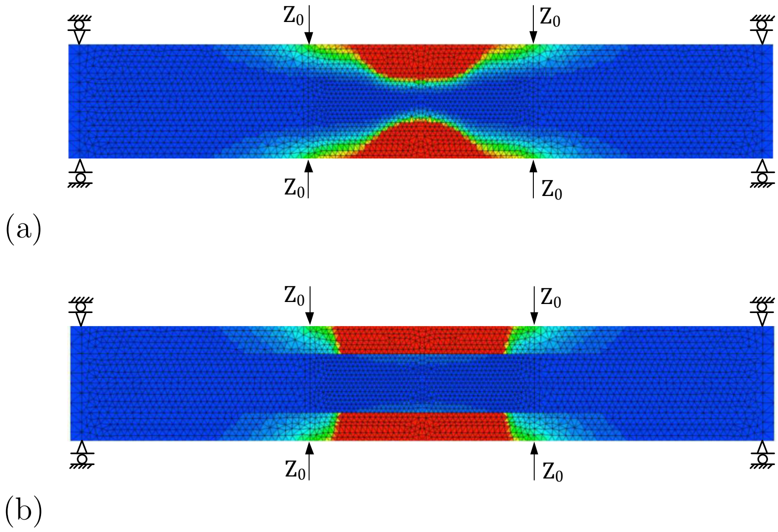

Figure 2.20: Modelling results of damage distributions at failure for (a) non-reinforced and (b) reinforced specimens [57,64,65].

The non-local continuum damage approaches are widely used for the fatigue life predictions, however, it introduces the non-physical effects because of the internal length. In fact, it has been shown for monotonic loads that there is an infinite set of model parameters, with arbitrary values of internal length that can fit a single structural response with the same very good accuracy [66]. In order to obtain a unique set of model parameters, including the internal length, tests on several specimens subjected to different boundary conditions, with different geometries, or size effect tests must be available [55,67]. For the layered structure with different materials, such as the pavement structures, a simple average of the stress or stain in a region defined by the internal length is inappropriate, due to the different damage behaviors and inconsistency of the averaging process.

2.4.3 Fatigue Crack Growth Models (FCGMs)

The existence of cracks can significantly reduce the fatigue life of a component or the whole structure. Some physical evidences are quite intuitive: at higher stresses, a crack tends to propagate “faster” (with respect of the number of cycles); at similar stress levels, a bigger crack tends also to propagate “faster”. The propagation of localized cracks depends on many parameters and is not well characterized by damage models. Fatigue crack growth models (FCGMs) take into account the variation of the stress intensity factor during the cycles to describe the crack propagation [68]. By simplicity, only Paris's law is discussed.

Paris’ law: Fatigue crack growth in a wide variety of brittle and quasi-brittle materials [69–71] is described well by the well-known Paris (or Paris–Ergodan) law [68], which relates the stress intensity factor range ΔK to crack growth rate da/dN_c via a power law, with $\Delta K = K_{max} - K_{min}$. The basic formula reads:

$$\frac{da}{dN_c} = c\Delta K^m, \quad \Delta K > \Delta K_{th}, \; K_{max} < K_c \tag{2.52}$$

where da/dN_c is the crack growth rate, a is the crack length and N_c is the number of load cycles, c and m are material constants. ΔK_{th} and K_c are the fatigue threshold and fracture toughness of the material, respectively. Paris’ law works for sufficiently large cracks, where ΔK is higher than the fatigue threshold ΔK_{th}, and the maximum value of the stress intensity factor K_{max} remains below the material fracture toughness K_c.

2.4.4 Summary

In this section, Bodin’s continuum damage model and the fatigue crack growth model of Paris’ law are reviewed. The continuum damage model is able to predict the fatigue life in good agreement with the test results, however, the numerically obtained failure pattern differs from the experimental observations, and the non-physical effects are introduced because of the internal length. While for Paris’ law, it can predict the rest fatigue life of a specimen containing a sufficiently large crack, but it is inapplicable for the un-cracked specimen or specimen containing small crack with the range of stress intensity factor $\Delta K < \Delta K_{th}$.

2.5 Discrete element modelling of quasi-brittle rupture

2.5.1 Overview

The discrete element method (DEM) was originally developed by Cundall for modeling granular and particulate systems [72]. Nowadays, DEM is becoming widely accepted as an effective method of addressing engineering problems in granular and discontinuous materials, especially in granular flows, powder mechanics, and rock mechanics. The method is based on the use of a numerical scheme in which the interaction of the particles is monitored at every contact and the motion of the particles modeled for every particle.

Both continuous and discrete numerical methods have their own advantages and shortcomings. In contrast to finite element method (FEM), as shown in Figure 2.21a, DEM is particularly attractive for modeling geo-materials due to its ability to construct a mesh that is not completely continuous and homogeneous. Since the mesh is constructed from rigid elements that interact with each other at points of contact, the DEM mesh is able to construct a medium with voids, imperfections, and heterogeneities, which commonly exist in rocks, concretes, asphalt mixtures, and other geo-materials (Figure 2.21b) [73].

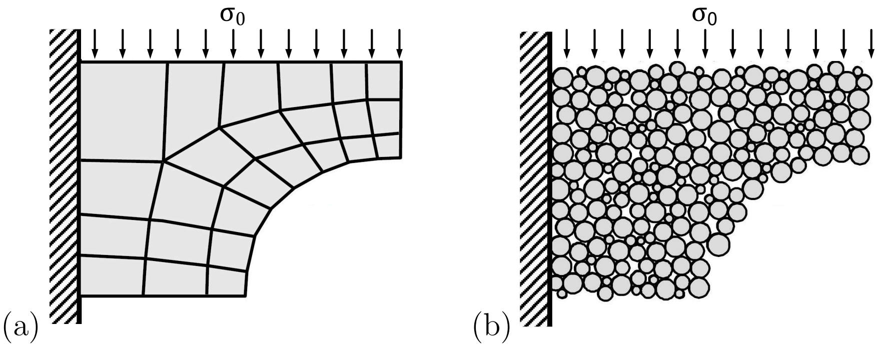

Figure 2.21: (a) Finite element mesh and (b) discrete element mesh [73].

Despite the advantages of DEM, the constitutive parameters for the contacts between the discrete elements, such as stiffness and strength, influence the behavior of the model at the macroscopic scale. These parameters are usually calibrated in order to reproduce experimental results.

Challenges related to calibration between the macro and micro material parameters can be avoided if a close-packed assembly (regular hexagonal packing), as shown in Figure 2.22b, is adopted. The close-packed assembly is composed of particles with identical size. The mechanical properties of the specimen (see Figure 2.22a) depend on the mechanical parameters of the particles. This regular hexagonal packing has been used Le *et al.* [28,74–76] and Liu *et al.* [77] for brittle failure of rocks and crystals.

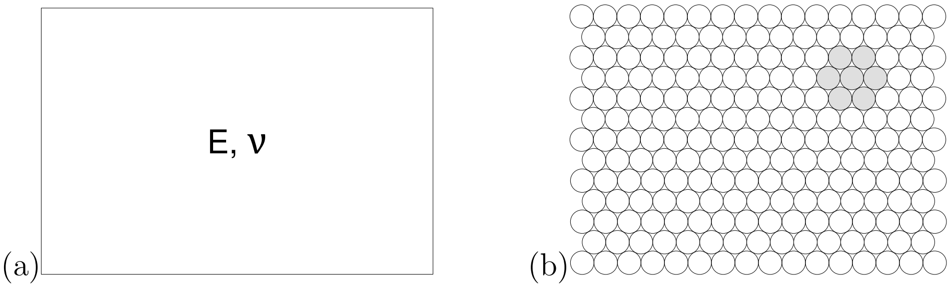

Figure 2.22: Equivalent (a) continuous and (b) discrete medium (close-packed assembly).

2.5.2 Contact model

DEM discretizes a material using elements of simple shapes (circles, spheres, or blocks) that interact with neighboring elements according to laws of interaction that are applied at points of contact. At each time step, the computation of all contact forces is followed by the application of Newton's second law to the particles. Each contact force has normal and tangential components, N and T, respectively (Figure 2.23). The contact behavior follows a standard linear spring and dash-pot model. When the value of the damping parameters, c_n and c_t, are a sufficiently small fraction of $\sqrt{mk_n}$ (where m is the particle mass), the inelastic effect is negligible [28]. In this study, only the elastic contribution of the contact force, the relative displacements, δ_n and δ_t (see Figure 2.23) will be considered.

Young's modulus E, and Poisson ratio ν, are the two elastic constants used to characterize the macroscopic linear elastic behavior of isotropic materials. A direct relationship between these macroscopic parameters and discrete elastic parameters (normal and tangential stiffness, k_n and k_t, respectively) has been established by Taverez [73,74], which for plane stress is as shown in Equation 2.53.

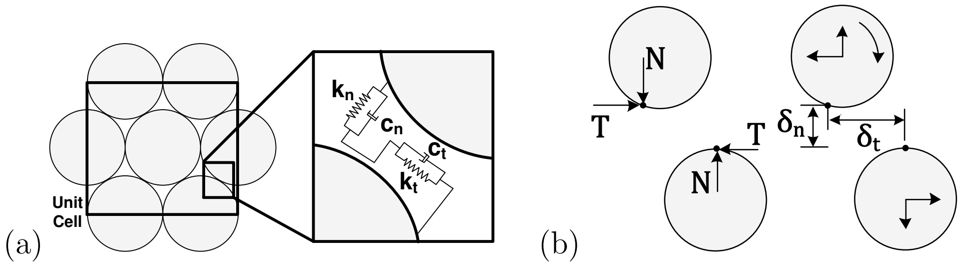

Figure 2.23: (a) Unit cell and (b) contact law (modified from [74]).

$$\begin{cases} k_n = \dfrac{Et}{\sqrt{3}\,(1-\nu)}, \\ \\ k_t = \dfrac{1-3\nu}{1+\nu} k_n = \dfrac{1-3\nu}{\sqrt{3}\,(1-\nu^2)} Et, \end{cases} \tag{2.53}$$

where t is thickness of the discrete element model.

2.5.3 Definition of strain and stress in discrete medium

2.5.3.1 Mean strains and stresses

The mean values of the components of the tensors of stress and strain are based on the behavior of one pair of contacts (ki and kj) associated with three particles (i, j, and k). A local coordinate system (n; t) is defined, where t virtually connects both contacts for which n is an orthogonal axis (see Figure 2.24a). The normal and tangential (relative) displacements associated with contacts ki and kj (δ_{nik} and δ_{tik}, δ_{njk} and δ_{tjk}, respectively, as shown in Figure 2.24a) give rise to mean strain values, $\overline{\varepsilon}_{nn}$ and $\overline{\varepsilon}_{tt}$:

$$\begin{cases} \overline{\varepsilon}_{nn} = \dfrac{1}{4}\left(\delta_{nik}\sqrt{3} + \delta_{njk}\sqrt{3} + \delta_{tik} - \delta_{tjk}\right)\dfrac{2}{\sqrt{3}d}, \\ \\ \overline{\varepsilon}_{tt} = \dfrac{1}{2}\left(\delta_{nik} + \delta_{njk} - \delta_{tik}\sqrt{3} + \delta_{tjk}\sqrt{3}\right)\dfrac{1}{d}, \end{cases} \tag{2.54}$$

The normal and tangential components of each contact (N_{ik} and T_{ik}, N_{jk} and T_{jk}, respectively, as indicated in Figure 2.24b) can be projected over the directions (n; t) giving rise to the resultant forces. Considering of a particle with diameter

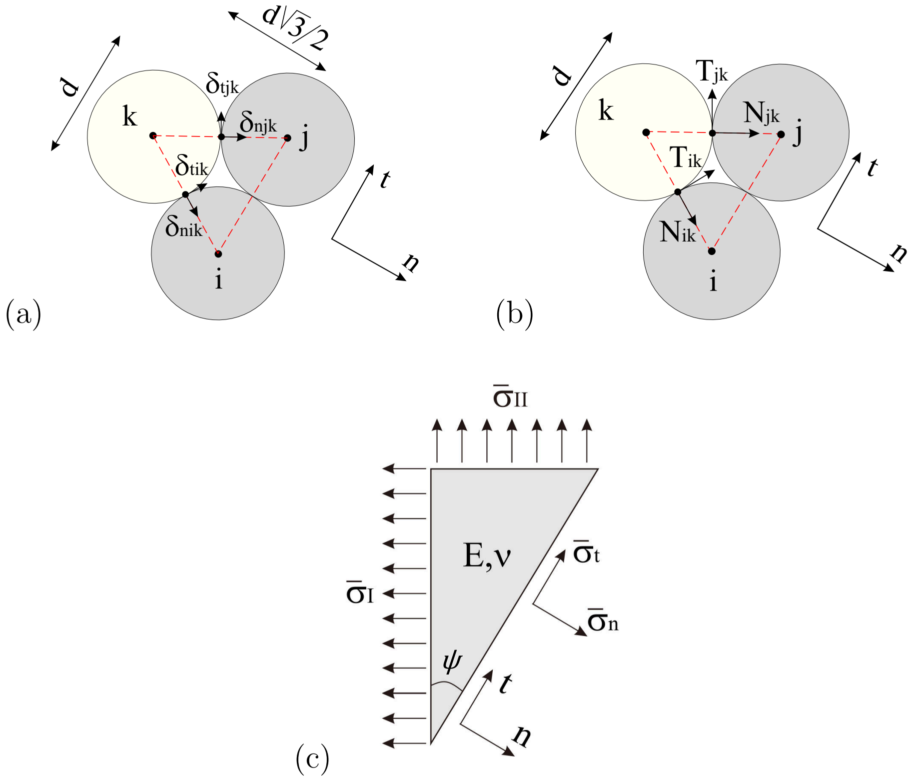

Figure 2.24: (a) Adjacent particles, respective contact displacements and (b) contact forces. (c) Mean stresses and the orientation of their principal values [74].

d and thickness of t ($t = d$), mean stresses (Figure 2.24c) may be associated with these forces:

$$\begin{cases} \overline{\sigma}_n = \left(N_{ik}\sqrt{3} + T_{ik} + N_{jk}\sqrt{3} - T_{jk}\right)/(2dt), \\ \overline{\sigma}_t = \left(-N_{ik} + T_{ik}\sqrt{3} + N_{jk} + T_{jk}\sqrt{3}\right)/(2dt). \end{cases} \tag{2.55}$$

2.5.3.2 Principal stresses

The stress tensor (in two dimensions) can be defined by the values of the principal stresses $\overline{\sigma}_I$ and $\overline{\sigma}_{II}$, and their orientations. Hence ψ is defined as the angle between (n; t) and the coordinate system associated with the principal stresses (Figure 2.24c). Consequently, the principal stresses may be written as:

$$\begin{cases} \overline{\sigma}_I = \overline{\sigma}_n + \overline{\sigma}_t \tan(\psi), \\ \\ \overline{\sigma}_{II} = \overline{\sigma}_n - \overline{\sigma}_t / \tan(\psi). \end{cases} \tag{2.56}$$

The value of ψ is determined based on the information from mean strains and mean stresses at a pair of contacts, which can be written as:

$$\psi = -\frac{1}{2} \arctan\left(\frac{2\overline{\sigma}_t}{A}\right), \tag{2.57}$$

where $A = \frac{E}{1-\nu}(\overline{\varepsilon}_{nn} + \overline{\varepsilon}_{tt}) - 2\overline{\sigma}_n$.

2.5.4 Effective stress intensity factor

According to the maximum tensile stress criterion for mixed mode fracture [11], crack propagation occurs in the direction θ_0, where the circumferential stress $\overline{\sigma}_{\theta\theta}(\theta_0)$ takes the maximum with respect to θ near the crack tip, and fracture occurs when the maximum tensile stress is equal to the stress leading to Mode I fracture. Hence, the maximum circumferential stress $\overline{\sigma}_{\theta\theta}(\theta_0)$ is defined as follows [74]:

$$\begin{cases} \overline{\sigma}_{\theta\theta} = \overline{\sigma}_I,\ if\ \psi \leq \pi/4, \\ \\ \overline{\sigma}_{\theta\theta} = \overline{\sigma}_{II},\ if\ \psi > \pi/4. \end{cases} \tag{2.58}$$

The mean stress over the length of one particle diameter in the direction of θ_0 can be obtained by the integration of the stress field, as shown in Equation 2.2.

$$\overline{\sigma}_{\theta\theta}(\theta_0) = \frac{1}{d}\int_0^d \sigma_{\theta\theta}(r, \theta_0)dr = \frac{1}{d}\int_0^d \frac{K_{\theta\theta}(\theta_0)}{\sqrt{2\pi r}}dr = \sqrt{\frac{2}{\pi d}}K_{\theta\theta}(\theta_0) \tag{2.59}$$

Using the $\overline{\sigma}_{\theta\theta}(\theta_0)$ value obtained from Equation 2.58, the stress intensity factor $K_{\theta\theta}(\theta_0)$ can be calculated using the following expression:

$$K_{\theta\theta}(\theta_0) = \overline{\sigma}_{\theta\theta}(\theta_0)\sqrt{\frac{\pi d}{2}}. \tag{2.60}$$

when $K_{\theta\theta}(\theta_0)$ reaches the material fracture toughness K_c, the contact under the highest tension of the contact pair will be broken, according to LEFM.

2.5.5 Summary

In this section, the discrete element method is reviewed briefly. The definition of strain and stress in the close-packed assembly is introduced, which has been implemented in the discrete element code and will provide the strain values for the fatigue damage calculations, as presented in Section 2.4.2.

2.6 Conclusions of the chapter

The basics of fracture mechanics theory is firstly presented, as it is the basis of this study. Experimental measurements of the nominal strength of quasi-brittle materials indicate that the nominal strength is dependent on the sizes of both the defects and specimens. The existing models aiming to predict size effects in quasi-brittle materials have scope for further improvement as they still have various shortcomings.

The failure process of a structure under fatigue loading is another important aspect of this research work. The review of the continuum damage approach and fatigue crack growth models suggests that it is necessary to develop a more realistic model that can consider both mechanisms. The discrete element method will be adopted in this analysis due to its advantages in comparison with other numerical methods.

Chapter 3

Nominal strength of cracked structures

Contents

3.1 Introduction

Typically, nominal strengths of quasi-brittle materials including concretes, rocks, and some types of ceramics are dependent on specimen size and crack size. A literature review suggests that generally accepted models for nominal strength predictions can capture size effects induced by crack size (which is also defined as boundary effect) and specimen size. Non-local critical distance theories, such as elastic stress field based models, fracture mechanics based models, and combined stress and energy models, are associated with a length scale parameter that can reach the same order of magnitude of the specimen size for some quasi-brittle materials. Therefore, such models are not always applicable.

Asymptotic models, such as Bažant's Size Effect Law and Hu-Duan's Boundary effect model, can also characterize size effects. Size effect models including Bažant's Size Effect Law emphasizes the influence of physical size of the specimen on the nominal strength. However, the dependence of fracture properties on crack length is not emphasized. Each size effect model has at least two experimental parameters that can be adjusted to fit the experimental results, and thus, the models can effectively characterize the transition of quasi-brittle failure from the tensile strength mechanism to the LEFM criterion for geometrically similar specimens. In a different manner, the Boundary Effect Model (BEM) does not consider the physical size of a specimen as the most fundamental measurement. Instead of it, the size effect induced by the crack length is determined by the size of a fully developed fracture process zone, its distance to the front boundary is measured by the crack length, and its distance to the back boundary is measured by the un-cracked ligament. The dependences of fracture behavior on the crack length or ligament, explicitly point out the influence of specimen boundaries on quasi-brittle fracture [17]. The boundary effect model is not restricted to geometrically similar specimens, proving that the size effect induced by crack-length can exist even in large specimens. Based on this, Hu and Duan concluded that the common size effect, associated with geometrically similar specimens, is only a special case of the boundary effect [17]. A model of Universal Size Effect Law proposed later by Bažant and Yu [47] considered that the dependence of the nominal strength of structure on the crack length at constant specimen size is a special case of the Universal Size Effect Law (USEL), and USEL is more realistic than the boundary effect model.

The size effect and boundary effect models can predict effectively the nominal strength for cracked structures made of quasi-brittle materials. However, for size effect models, the model parameters needs to be adjusted to fit the experimental results, instead of being calculated from the material parameters measured from the standard tests. On the other hand, the assumptions in the boundary effect model are debatable, and the application of this model is restricted to a certain crack to width range α [49].

In this chapter, a new crack size based failure model is developed to characterize the boundary and size effects, which works also for the crack to width ratios where Type 2 Size Effect Law and boundary effect model are not recommended. The model parameters can be directly decided by the measured material tensile strength and fracture toughness, or calibrated from the geometrically similar specimen tests, same as the other asymptotic models. The proposed model is compared comprehensively with the Boundary Effect Model, Type 2 Size Effect Law and validated by three sets of experimental results of Cracked Three-Point Bending (C-TPB) beam specimens composed of concrete, limestone, and hardened cement paste.

3.2 Proposed failure model

As widely known, it is not possible to predict the failure of specimens containing a relatively small or intermediate cracks [15, 17] with the local stress criterion and energy criterion. In this section, the derivative of energy release rate G' is introduced to predict the nominal strength given by the strength mechanism. Conversely, the energy criterion is sufficient to provide a good prediction for material ruptures dominated by the energy mechanism. Based on the energy release rate and its derivative, the results indicate that the asymptotic model covers the nominal strength prediction for any crack size. The proposed model is established based on the edge cracked plate and cracked three point bending beam specimen. However, the model could be easily generalized to several other structures and different boundary conditions, such as a center-cracked plate, cracked pure bending specimen, and compact tension test specimen.

3.2.1 Infinite width plate analysis

3.2.1.1 Derivative of energy release rate

With respect to a cracked structure subjected to mode I loading, the energy release rate at the crack tip can be expressed as follows:

$$G = \frac{[A(\alpha)\sigma]^2 \pi a}{E}, \tag{3.1}$$

where α denotes the crack to width ratio a/w for the plate or crack to height ratio a/h for the beam; $A(\alpha)$ denotes the geometrical correction factor for energy release rate that can be calculated analytically or numerically [36]; σ denotes the applied loading; and E denotes the Young's modulus of the material.

With respect to an edge cracked infinite width plate ($\alpha = a/w \to 0$) under uniform tensile stress σ (as shown in Figure 3.1), the energy release rate at the crack tip can be expressed as follows:

$$G = \frac{(1.12\sigma)^2 \pi a}{E}. \tag{3.2}$$

The geometrical correction factor $A(\alpha) \approx 1.12$ for $\alpha \to 0$. For sufficiently large crack sizes, the energy criterion of linear elastic fracture mechanics can provide good nominal strength predictions. However, both stress criterion and energy criterion would fail when the crack size is smaller than the transition crack size a_t as previously demonstrated in Section 2.3.2. The stress criterion provides a null strength due to stress singularity at the crack tip, while the energy criterion provides an unreal nominal strength that is higher than the material tensile strength.

In order to overcome this problem, the non-singular value of the derivative of energy release rate $G' = dG/da$ is adopted in this study, and this can be expressed as follows for an infinite width plate:

$$G' = \frac{dG}{da} = \frac{(1.12\sigma)^2 \pi}{E}. \tag{3.3}$$

The critical value of G' is related to tensile strength f_t of the material and obtained when $\sigma = f_t$. With respect to an infinite plate, $\bar{G}_c$ is defined as follows:

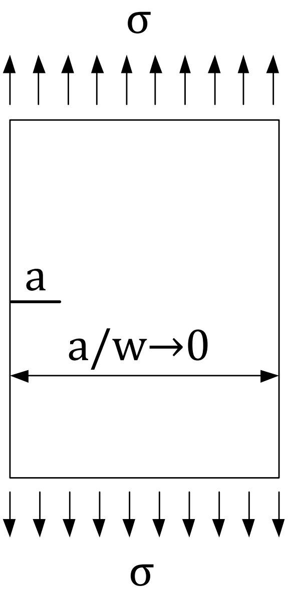

Figure 3.1: Infinite width plate subjected to uniform tensile stress σ.

$$\bar{G_c} = \frac{(1.12 f_t)^2 \pi}{E}. \tag{3.4}$$

By using the derivative of energy release rate G' as the fracture parameter of strength mechanism, for the infinite plate, one can obtain $\sigma_N = f_t$ for any crack size. The real failure behavior is described by both mechanisms. That is, prior to transition crack length a_t, the failure is dominated by the strength mechanism and nominal strength $\sigma_N = f_t$, while for crack length $a > a_t$, the nominal strength decreases following the prediction of linear elastic fracture mechanics. The failure envelop is shown in Figure 3.2, in which the horizontal dotted line is predicted by the strength mechanism (derivative of energy release rate), and the inclined dash line is given by the energy mechanism (energy release rate).

3.2.1.2 Asymptotic model

In order to obtain a smooth transition from one mechanism to another, a simple asymptotic model is proposed as follows:

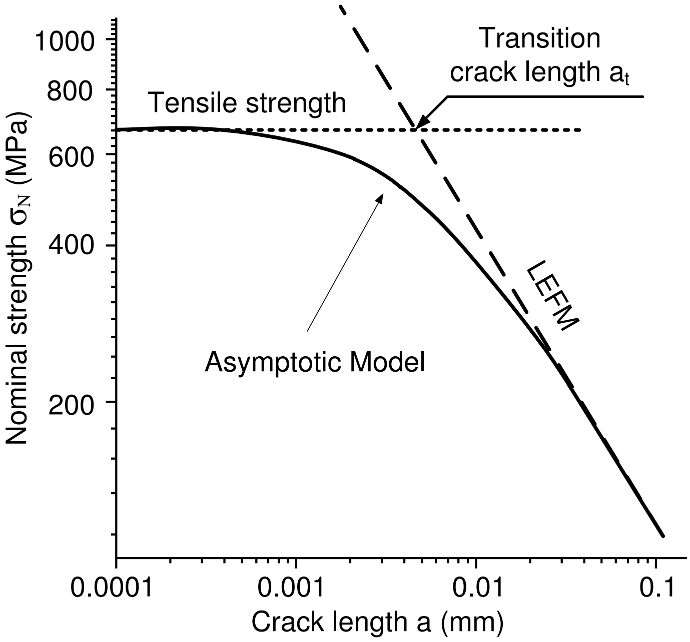

Figure 3.2: Nominal strength predictions given by the energy release rate and its derivative for an infinite plate.

$$\frac{G}{G_c} + \frac{G'}{\bar{G}_c} = 1. \tag{3.5}$$

A smooth transition is obtained from a strength mechanism to an energy mechanism (linear elastic fracture mechanics) as shown in Figure 3.2.

In case of rupture of an infinite width plate, the energy release rate $G = (1.12\sigma_N)^2\pi a/E$, critical energy release rate $G_c = (1.12f_t)^2\pi a_t/E$, the derivative of energy release rate at failure $G' = (1.12\sigma_N)^2\pi/E$, and critical derivative of energy resale rate $\bar{G}_c = (1.12f_t)^2\pi/E$ can be easily obtained. Substituting these expressions into Equation 3.5, one gets:

$$\sigma_N = f_t\left(1+\frac{a}{a_t}\right)^{-1/2}, \tag{3.6}$$

identical to Hu-Duan's Boundary Effect Model for an infinite size plate. The advantage of Equation 3.5 is that basic quantities G and G' are defined locally, at the crack tip.

3.2.2 Finite width plate

3.2.2.1 Derivative of energy release rate

With respect to a single edge cracked finite width plate subjected to mode I loading, the geometrical correction factor $A(\alpha)$ shown in Equation 3.1 is no longer a constant that corresponds to 1.12. The empirical expression of $A(\alpha)$ is given by Tada [36] with an error lower than 0.5% for any crack to width ratio $\alpha = a/w$ as follows:

$$A(\alpha) = \sqrt{\frac{2}{\pi\alpha}\tan\frac{\pi\alpha}{2}} \cdot \frac{0.752 + 2.02\alpha + 0.37\left[1 - \sin(\pi\alpha/2)\right]^3}{\cos(\pi\alpha/2)} \tag{3.7}$$

The product rule is used to find the derivative of the energy release rate with respect to the crack length a. In Equation 3.1, $\sigma^2\pi/E$ is a constant, and the derivative of $A^2(\alpha)a$ corresponds to $A^2(\alpha)+2A(\alpha)A'(\alpha)\alpha' a$, with $\alpha' = 1/w$ ($\alpha' a = \alpha$). Therefore, the derivative of energy release rate with respect to the crack length a can be written as follows:

$$G' = \frac{[H(\alpha)\sigma]^2\pi}{E}, \tag{3.8}$$

where $H(\alpha)$ is defined as the geometrical correction factor for the derivative of the energy release rate G' as follows:

$$H(\alpha) = \sqrt{A^2(\alpha) + 2A(\alpha) \times dA(\alpha)/d\alpha \times \alpha}. \tag{3.9}$$

The evolution of $A(\alpha)$ and $H(\alpha)$ with respect to α is presented in Figure 3.3. When $\alpha < 0.1$, then $A(\alpha) \approx H(\alpha) \approx 1.12$. Both correction factors tend to infinity when α approaches to 1.

The derivative of the energy release rate as shown in Equation 3.8 is proportional to the geometrically corrected stress value $H(\alpha)\sigma$, in which σ is obtained as the stress at the bottom of the mid-span without considering the crack; $H(\alpha)$ can be regarded also as a correction factor, which can take the crack into consideration. The critical value of the derivative of energy release rate $\bar{G}_c$ for the finite plate is obtained when $\sigma \to f_t$ and $a \to 0$. That is, the critical value for the corrected stress $H(\alpha)\sigma$ corresponds to $1.12f_t$.

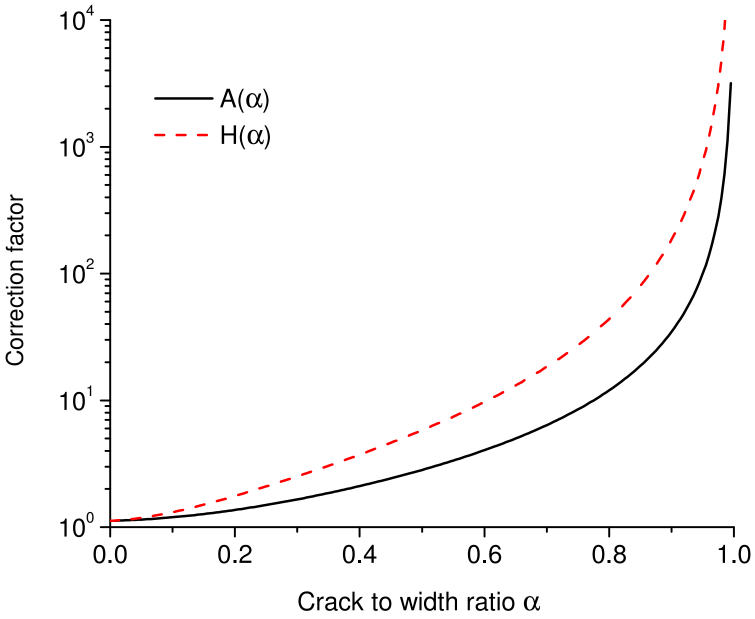

Figure 3.3: Correction factors $A(\alpha)$ and $H(\alpha)$ versus crack to width ratio α.

$$\bar{G_c} = \frac{[H(\alpha \to 0)f_t]^2\pi}{E} \approx \frac{[A(\alpha \to 0)f_t]^2\pi}{E} \approx \frac{(1.12f_t)^2\pi}{E}, \tag{3.10}$$

This is identical to the $\bar{G_c}$ for an infinite width plate. In fact, $\bar{G_c}$ corresponds to a material constant related to the tensile strength f_t and Young's modulus E. This is because when $\alpha \to 0$, for edge cracked structure, $H(\alpha \to 0) \approx A(\alpha \to 0) \approx 1.12$.

Equations 3.8 and 3.10 are related to calculate the nominal strength σ_N based on the derivative of energy release rate G' as follows:

$$\sigma_N = \frac{1.12f_t}{H(\alpha)}. \tag{3.11}$$

In other words, it could be simply considered that failure occurs when the corrected stress value $H(\alpha)\sigma = 1.12f_t$. Hence, the nominal strength σ_N of strength mechanism could be predicted by Equation 3.11. When $\alpha < 0.1$, as shown in Figure 3.3, $H(\alpha) \approx 1.12$, and therefore, $\sigma_N \approx f_t$. It should be noted that $H(\alpha)$ has different expressions for different structures, and this is related to $A(\alpha)$ and could be found analytically or numerically.

3.2.2.2 Asymptotic model

With respect to relatively large cracks, the material rupture is dominated by the energy criterion. Given the definition of $H(\alpha)$, the expression for energy release rate as shown in Equation 3.1 can be written as follows:

$$G = \frac{[A(\alpha)\sigma H(\alpha)/H(\alpha)]^2 \pi a}{E} = \frac{[H(\alpha)\sigma]^2 \pi a_e}{E}, \tag{3.12}$$

where

$$a_e = \frac{A^2(\alpha)}{H^2(\alpha)} a, \tag{3.13}$$

a_e is defined as the equivalent crack length, which depends on the initial crack length a and crack to height ratio α. After introducing the concept of equivalent crack length a_e, the cracked plate with initial crack length a and stress σ (as shown in Figure 3.4a) is equivalent to the plate with crack length a_e and loading $[H(\alpha)/A(\alpha)]\sigma$ (as shown in Figure 3.4b). Hence, the energy release rate at the tip of the equivalent crack is identical to the value of the initial crack.

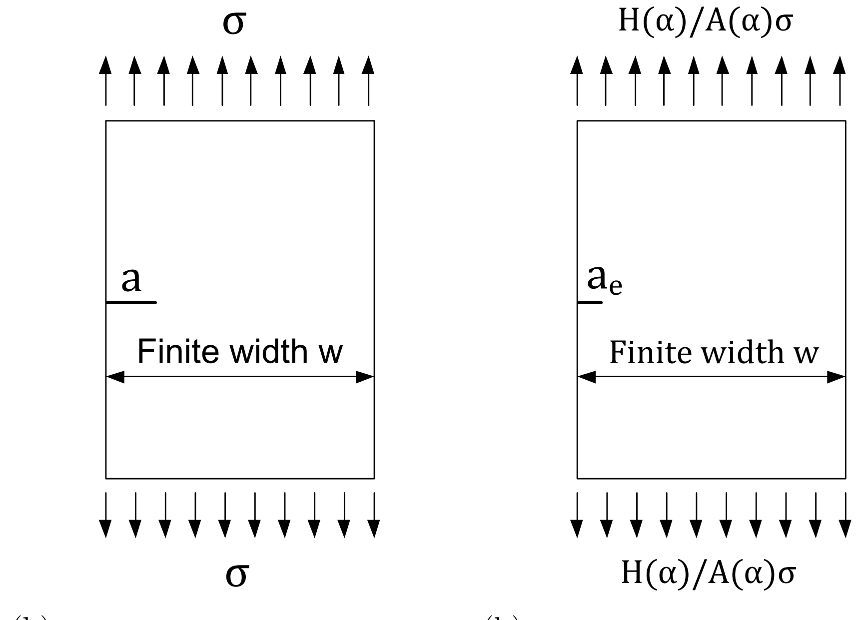

(b) (b)

Figure 3.4: (a) Finite width plate and (b) its equivalent model

Figure 3.5 illustrates the variation of equivalent crack length a_e with respect to real crack length a for a plate with $w = 1m$. a_e tends to 0 when $\alpha \to 0$ and $\alpha \to 1$.

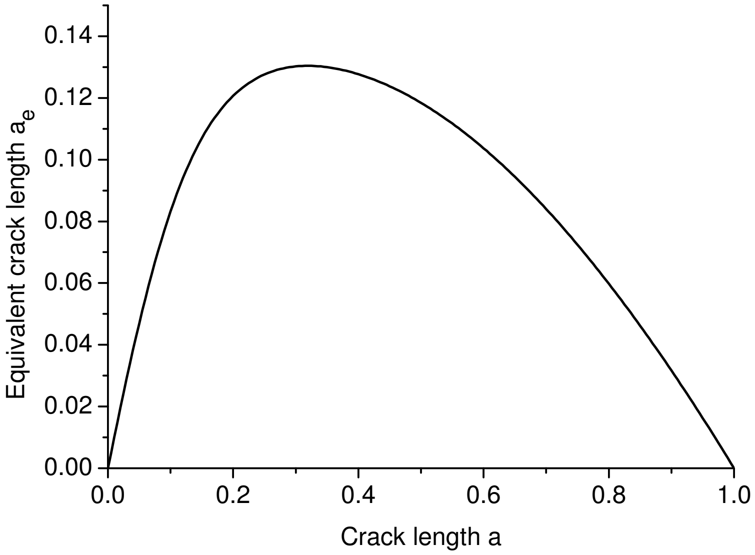

Figure 3.5: Equivalent crack length a_e versus real crack length a for a finite width plate.

The critical energy release rate corresponds to the material toughness G_c. In conjunction with the definition of transition crack length a_t as shown in Equation 2.21, the nominal strength given by the energy criterion can be written as Equation 3.14 given below:

$$\sigma_N = \frac{1.12 f_t}{H(\alpha)} \left(\frac{a_e}{a_t}\right)^{-1/2}. \tag{3.14}$$

It should be noted that Equation 3.11 and Equation 3.14 can be combined together to predict the material rupture from strength mechanism to the energy mechanism. Thus, an asymptotic model for a finite width plate is developed as shown in Equation 3.15:

$$\sigma_N = \frac{1.12 f_t}{H(\alpha)} \left(1 + \frac{a_e}{a_t}\right)^{-1/2}. \tag{3.15}$$

In a manner similar to the Hu-Duan boundary effect model [17], Equation 3.15 is also a crack size based model that estimates the effect of crack length on the nominal strength. Despite the similarity in the shapes, the definitions and expressions of equivalent crack length and geometrical correction factor in Equation 3.15 are fundamentally different from those in the boundary effect model. The differences between the proposed model and the Hu-Duan Boundary Effect Model are presented in Section 3.3.1.

It is interesting to note that the ratio of nominal strength σ_N given by Equation 3.15 and Equation 3.11, tends to 1 for very small and very large crack to width ratios α, as shown in Figure 3.6. This phenomenon indicates that with respect to these two extreme cases, the derivative of the energy release rate G' corresponds to the dominant factor for the rupture. For example, in the edge cracked plate shown in Figure 3.4a for instance when the real crack length approaches to 1, the equivalent crack length a_e in contrast tends to 0. Hence, the contribution of the energy release rate part in Equation 3.15 on the nominal strength σ_N is considerably weaker than the derivative of the energy release rate G' and could be eventually neglected at a certain moment.

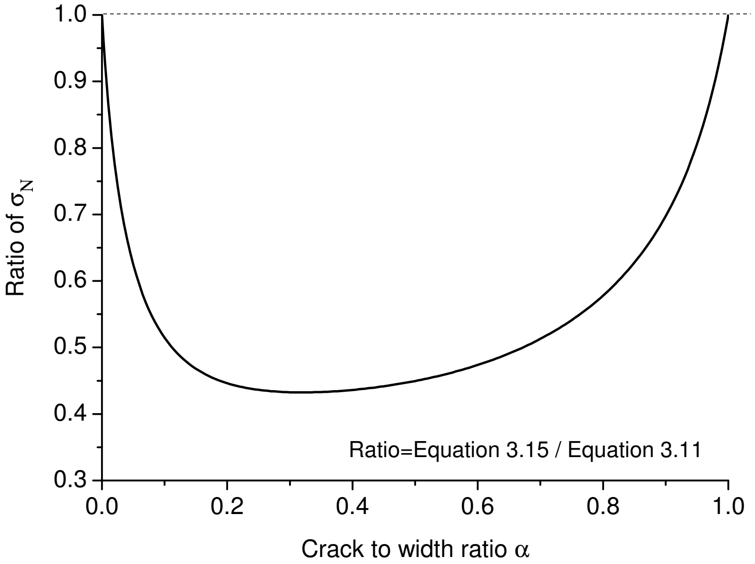

Figure 3.6: Ratio of nominal strength σ_N given by Equation 3.15 and Equation 3.11 versus crack to width ratio α.

Figure 3.7 presents the ratios of nominal strength to tensile strength σ_N/f_t of the single edge cracked plate versus equivalent crack length a_e (plate width $w = 1\,m$). When $\alpha < 0.031$ and $\alpha > 0.901$, the rupture behavior is mainly dominated by the strength mechanism (derivative of energy release rate) that is previously discussed. This phenomenon is attributed to the boundary effect [17] because the distances of the Fracture Process Zone to the left boundary measured by the crack length ($\alpha < 0.031$) and to the right boundary measured by the un-cracked ligament ($\alpha > 0.901$) are too small. Therefore, the fracture behaviors are influenced by the specimen boundaries and dominated by the strength mechanism. When equivalent crack length a_e exceeds the transition crack length a_t, the rupture behavior is mainly dominated by the energy mechanism. $\alpha = 0.32$ corresponds to the strongest contribution of the strength mechanism to the failure of the plate.

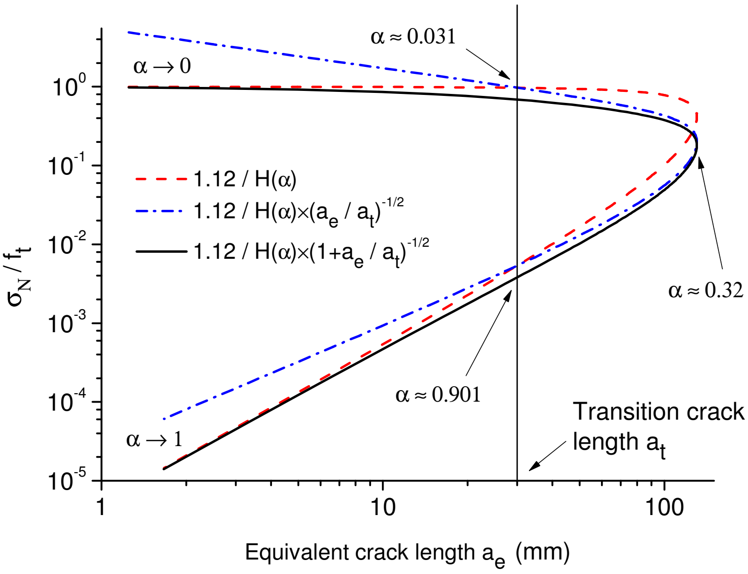

Figure 3.7: Nominal strength to tensile strength ratios relative to equivalent crack length a_e.

3.2.3 Finite size beam

Size effect tests are commonly performed with cracked three point bending specimens with similar geometry (identical span to height ratios). The finite size beam is examined in this section to validate the proposed asymptotic model (Equation 3.15) with test results in extant studies.

With respect to a cracked three point bending beam (Figure 3.8) under loading F with crack to height ratio $\alpha = a/h$, the energy release rate G can be written as Equation 3.1 [36] with $\sigma = 3FS/(2h^2t)$. Additionally, h, S, and t denote the height, span, and thickness of the beam respectively. For the beam with span to height ratio $S/h = 4$, Equation 3.16 results in 0.5% accuracy of G for all crack to height ratios α,

$$A(\alpha) = \frac{1}{\sqrt{\pi}} \frac{1.99 - \alpha(1-\alpha)(2.15 - 3.93\alpha + 2.7\alpha^2)}{(1+2\alpha)(1-\alpha)^{3/2}}, \tag{3.16}$$

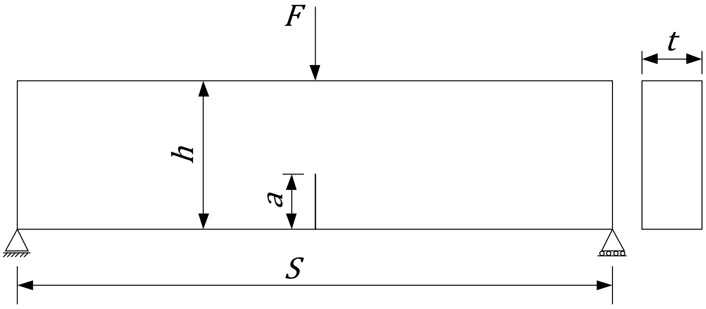

Figure 3.8: Cracked three point bending beam specimen.

In a manner similar to the finite width plate, the derivative of energy release rate with respect to the crack length a can be written as Equation 3.8, with the geometrical correction factor $H(\alpha)$. Figure 3.9 shows the values of two correction factors $A(\alpha)$ and $H(\alpha)$ for G and G' with respect to the crack to height ratio α. When $\alpha < 0.01$, the difference between the two factors is very small, and they all tend to infinity when $\alpha \to 1$.

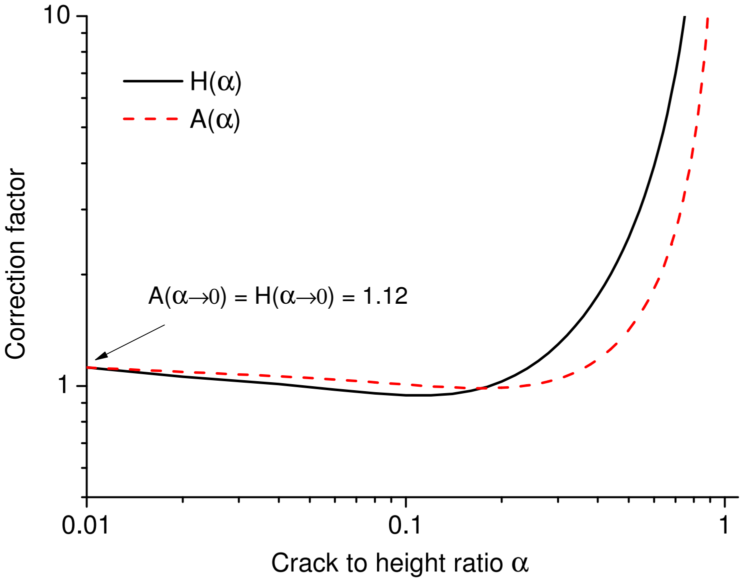

Figure 3.9: Correction factors $A(\alpha)$ and $H(\alpha)$ versus crack to height ratio α.

The critical value of the derivative of energy release rate $\bar{G}_c$ for the cracked three point bending specimen with a span to height ratio corresponding to 4 is identical to that of infinite and finite width plates. This is calculated as follows:

$$\bar{G_c} = \frac{(1.99 f_t/\sqrt{\pi})^2 \pi}{E} \approx \frac{(1.12 f_t)^2 \pi}{E}, \tag{3.17}$$

Hence, the nominal strength σ_N based on the derivative of energy release rate G' can be computed by Equation 3.11. When $\alpha < 0.01$, as shown in Figure 3.9, $H(\alpha) \approx 1.12$, and therefore $\sigma_N \approx f_t$. It should be noted that for the cracked three point bending beam specimen, Equation 3.11 does not provide the nominal strength predictions for intermediate cracks because $H(\alpha)$ experiences a slight decrease before it increases towards to infinity. This lead to unrealistic nominal strength predictions that exceed the material tensile strength by simply using Equation 3.11 for intermediate crack sizes.

With respect to relatively large cracks, the material rupture is dominated by the energy mechanism. Following the introduction of the definition of equivalent crack length a_e, the nominal strength is calculated by Equation 3.14. Figure 3.10 illustrates the variation of equivalent crack length a_e with respect to the real crack length a for the beam with $h = 1\,m$ and $S = 4\,m$. In a manner similar to the case of finite plate, a_e tends to 0 when $\alpha \to 0$ and $\alpha \to 1$.

The asymptotic model for the finite size beam is shown in Equation 3.15 and is identical to that of the finite width beam. Figure 3.11 shows the ratio of nominal strength σ_N as given by Equation 3.15 and Equation 3.11 relative to the crack to height ratio α. This indicates that for two extreme cases, the derivative of energy release rate G' is the dominant factor that lead to the rupture.

Figure 3.12 presents the nominal strength to tensile strength ratios of the cracked beam structure relative to the equivalent crack length a_e (Beam height $h = 1\,m$. The rupture behavior is mainly dominated by the strength mechanism (derivative of energy release rate). When $\alpha < 0.0279$ and $\alpha > 0.909$. This is due to the boundary effects. The rupture behavior is mainly dominated by the energy mechanism when the equivalent crack length a_e exceeds the transition crack length a_t. Additionally, $\alpha = 0.275$ provides the strongest contribution of strength mechanism to the failure of the beam.

The asymptotic model shown in Equation 3.15 is used to predict the failure stress for any crack size (or any crack to height ratio α). This provides a smooth transition from small and intermediate cracks to large cracks. Figure 3.13 presents

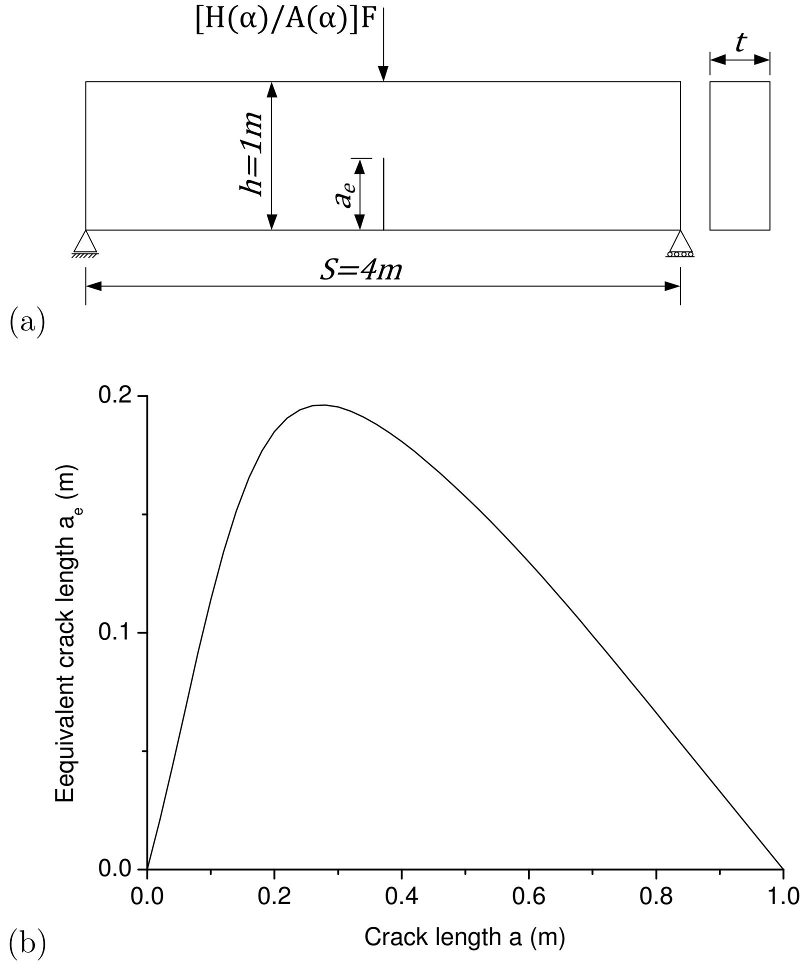

Figure 3.10: (a) Beam with equivalent loading and equivalent crack length a_e and (b) equivalent crack length a_e relative to the real crack length a.

an example of the nominal strength relative to the crack to height ratio α for beam height $h = 0.1\ m, 1\ m, 10\ m, 100\ m$. The nominal strengths could be easily predicted by using Equation 3.15 and the information on the material parameters, including tensile strength $f_t = 3.0\ MPa$, fracture toughness $K_c = \sqrt{G_c E} = 1.0\ MPa\sqrt{m}$, and transition crack length $a_t = 28.2\ mm$. They are plotted in Figure 3.13. With respect to beam height $h = 100\ m$, a smaller crack to height α is necessary to obtain a nominal strength approximately equal to the tensile strength f_t.

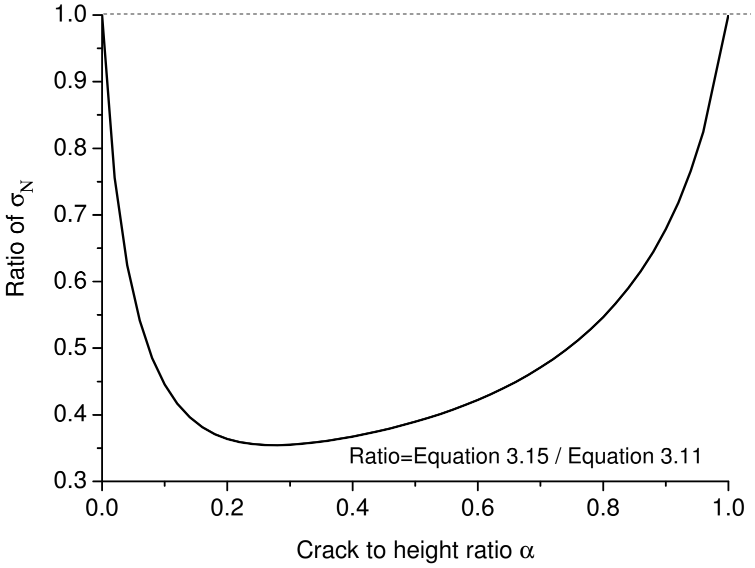

Figure 3.11: Ratio of nominal strength σ_N given by Equation 3.15 and Equation 3.11 relative to the crack to height ratio α.

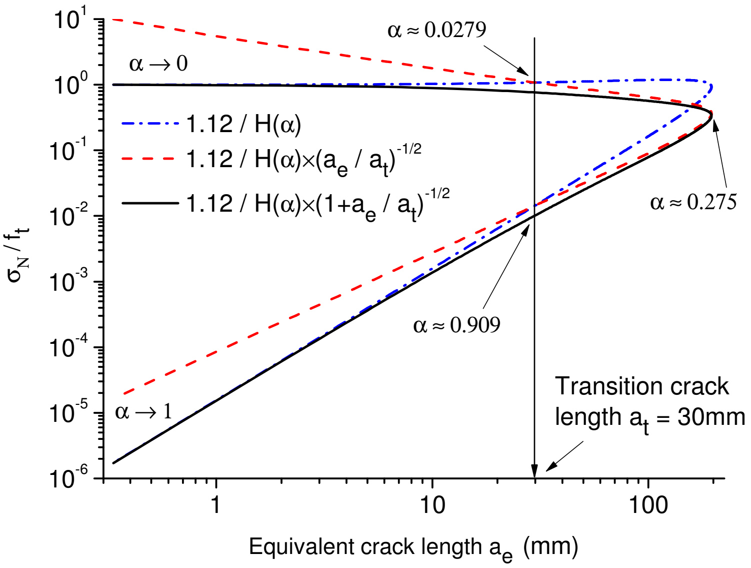

Figure 3.12: Nominal strength to tensile strength ratios relative to the equivalent crack length a_e.

3.2.4 Material parameter identifications

The material parameters may vary for different specimen shapes and sizes due to the size effects. In a manner analogous to SEL, the material and geometrical

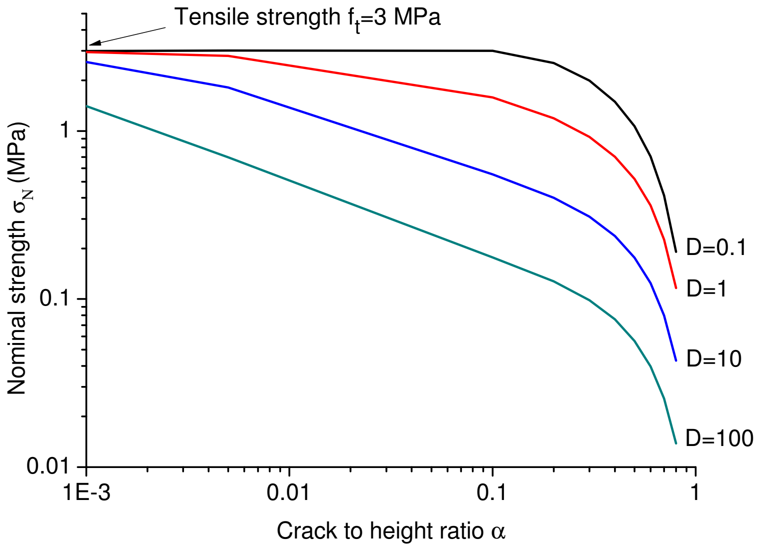

Figure 3.13: Nominal strengths relative to the crack to height ratio α for various beam heights.

information including $H(\alpha)/(1.12f_t)$ and a_t can be identified from the test results (geometrically similar tests) if they are not sufficient or not easy to be calculate. By setting $Y = 1/(\sigma_N^2)$, Equation 3.15 results in a linear regression plot $Y = JX + C$ as shown in Equation 3.18, from which J and C could be identified as the slope and intercept as follows:

$$Y = \frac{1}{\sigma_N^2} = \left[\frac{H(\alpha)}{1.12f_t}\right]^2 \frac{a_e}{a_t} + \left[\frac{H(\alpha)}{1.12f_t}\right]^2, \tag{3.18}$$

with $a_e = X$, $[H(\alpha)/(1.12f_t)]^2/a_t = J$, $[H(\alpha)/(1.12f_t)]^2 = C$

It should be noted that J and C are constants only for geometrically similar specimens (shapes with identical crack to height ratios α), due to the identical correction factor $H(\alpha)$.

3.2.5 Model for geometrically similar specimens

The asymptotic model in Equation 3.15 can predict the nominal strength for different crack sizes, and it has a shape similar to the Type 2 SEL shown in Equation 2.41. Given that $a = \alpha h$, the equivalent crack length a_e in Equation 3.15 can be replaced by $a_e = [A(\alpha)/H(\alpha)]^2 \alpha h$. Thus, a transition beam height h_t can be defined as follows:

$$h_t = \frac{a_t}{\alpha}\left[\frac{H(\alpha)}{A(\alpha)}\right]^2, \tag{3.19}$$

h_t denotes a function of transition crack length a_t and crack to height ratio α that is proportional to the characteristic length l_{ch}. Hence, an asymptotic model for geometrically similar specimens of the proposed model is developed as follows:

$$\sigma_N = \frac{1.12 f_t}{H(\alpha)}\left(1 + \frac{h}{h_t}\right)^{-1/2}, \tag{3.20}$$

Equation 3.20 possesses the same shape as Type 2 SEL. Additionally, h_t and h_0 correspond to the transitional size at which the material strength and LEFM intersect and are all proportional to Irwin's characteristic length l_{ch}. Furthermore, $\hat{B}$ in Equation 2.41 corresponds to a positive dimensionless constant that is based on the geometry of the structure in a manner similar to $1.12/H(\alpha)$ in Equation 3.20. Therefore, the proposed model could predict the rupture of geometrically similar specimens in a manner similar to Type 2 SEL. A detailed comparison of the proposed model and Type 2 SEL is presented in Section 3.3.2.

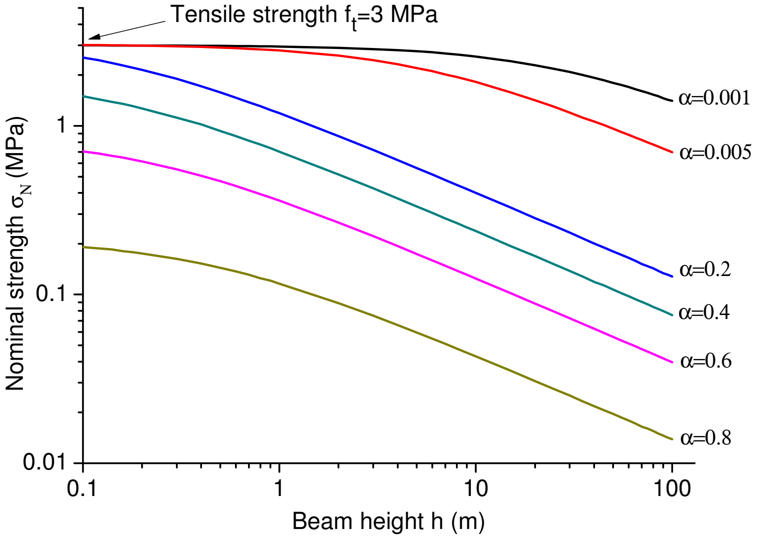

Figure 3.14: Nominal strengths versus beam height for various crack to height ratios.

Figure 3.14 presents an example of the nominal strengths with respect to beam heights for various crack to height ratios. The material parameters are identical as the parameters adopted in Figure 3.13. By using Equation 3.15 or 3.20, the nominal strength could be predicted for both geometrically similar specimens (Figure 3.14) and certain beam sizes with different crack to height ratios α (Figure 3.13). However, the proposed model of Equations 3.15 and 3.20 differs from the Type 1 SEL as it could not predict the size effect of crack initiation from the free surface. This is because it calculates the same nominal strength for different specimen sizes.

3.3 Comparison of the proposed model with existing models

3.3.1 Comparison of proposed model with BEM

Based on the boundary effect and using an equivalent crack length, Hu and Duan [17, 40] proposed a Boundary Effect Model (BEM) that could be used to predict the nominal strengths of finite or infinite width specimens with different crack sizes. It may be recalled that the boundary effect model for the rupture of finite size specimen is as follows:

$$\sigma_N = B(\alpha) f_t \left(1 + \frac{a_{e1}}{a_t}\right)^{-1/2}, \tag{3.21}$$

where $B(\alpha) = (1-\alpha)^2$ for cracked three point bending beam. Additionally, a_{e1} denotes the equivalent crack length in boundary effect model, and its value depends on the specimen geometry and crack length as follows:

$$a_{e1} = \left[\frac{B(\alpha) \times A(\alpha)}{1.12}\right]^2. \tag{3.22}$$

Equation 3.21 and Equation 3.15 correspond to crack size based models that estimate the effect of crack length on the nominal strength. Figure 3.15 shows the variation of equivalent crack length with respect to the real crack length a (beam height $h = 1\,m$). With respect to the same crack length, the equivalent crack length a_e in the proposed model exceeds the definition of equivalent crack length a_{e1} in the boundary effect model. The transition crack length a_t shares the same definition in both models. Thus, the higher equivalent crack length

a_e (higher a_e/a_t) in the proposed model indicates that the use of the proposed model lead to the domination of the rupture of the beam with a wider range of the crack length a by the energy criterion.

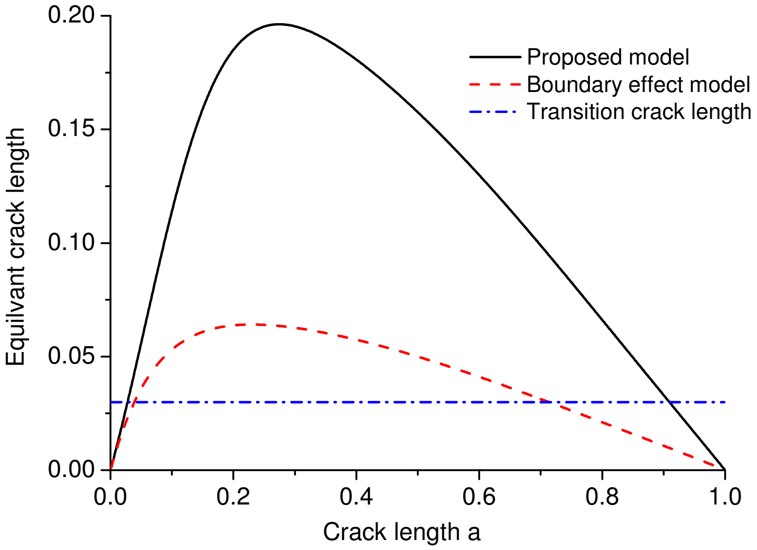

Figure 3.15: Equivalent crack length in the boundary effect model and the proposed model.

The nominal strength given by the strength mechanism $\sigma_N^{strength}$ in boundary effect model corresponds to $B(\alpha)f_t$. In contrast, in the proposed model, it is assumed that the strength mechanism is characterized better by the derivative of the energy release rate. Figure 3.16 presents the nominal strength predicted by strength mechanism to tensile strength ratios $\sigma_N^{strength}/f_t$ for various crack to height ratios α. The derivative of the energy release rate provides a nominal strength $\sigma_N^{strength}$ that exceeds that in the boundary effect model for the same crack to height ratio α. Conversely, with respect to the energy mechanism, both models results in the same nominal strength σ_N^{energy} because a simple energy criterion is used in both the models.

The difference in the nominal strength given by the strength mechanism $\sigma_N^{strength}$ finally lead to the prediction of different nominal strengths by the boundary effect model and proposed model. Figure 3.17 shows the nominal strength predicted by boundary effect model and proposed model relative to the tensile strength ratios σ_N/f_t for various crack to height ratios. As shown in the figure, the proposed model results in a nominal strength that exceeds that in the boundary effect model.

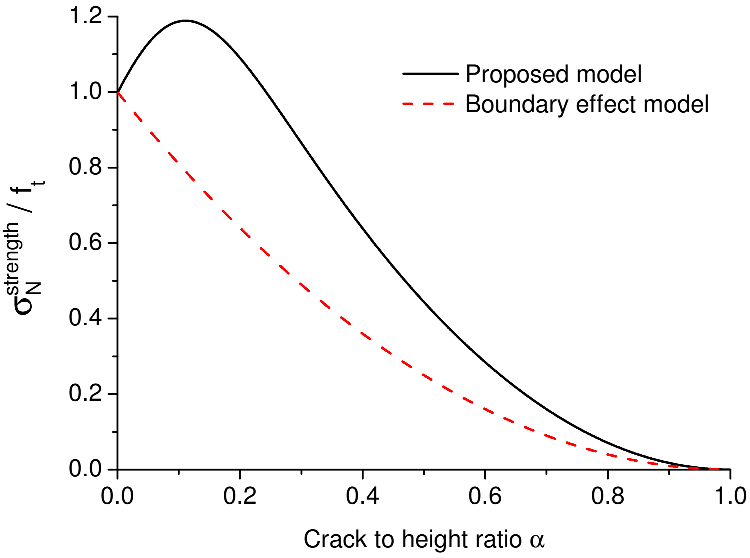

Figure 3.16: The ratio of nominal strength predicted by strength mechanism and tensile strength $\sigma_N^{strength}/f_t$ for various crack to height ratios.

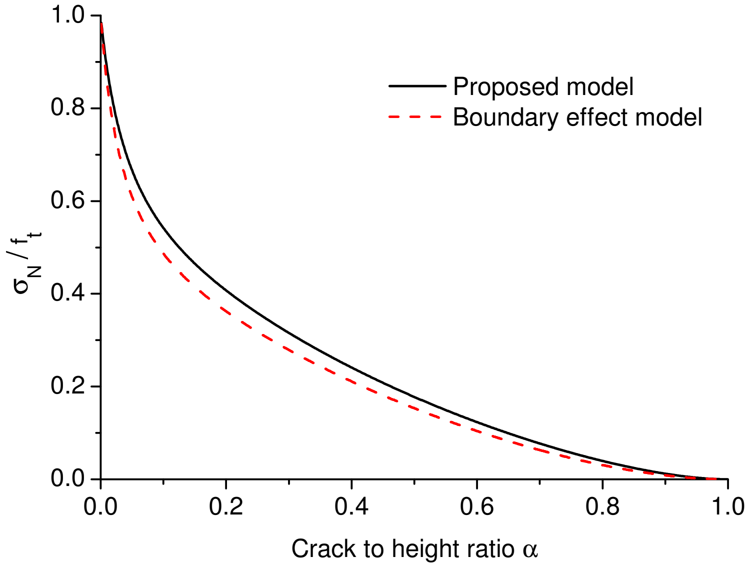

Figure 3.17: The ratio of nominal strength predicted by BEM and proposed model and tensile strength σ_N/f_t for different crack to height ratios.

Figure 3.18 shows the percentages of differences in the nominal strength calculated by the boundary effect model and proposed model. The difference in the nominal strengths calculated by the two models increased with increases in crack length (fixed beam height) and could exceed 40% when α approached 1.

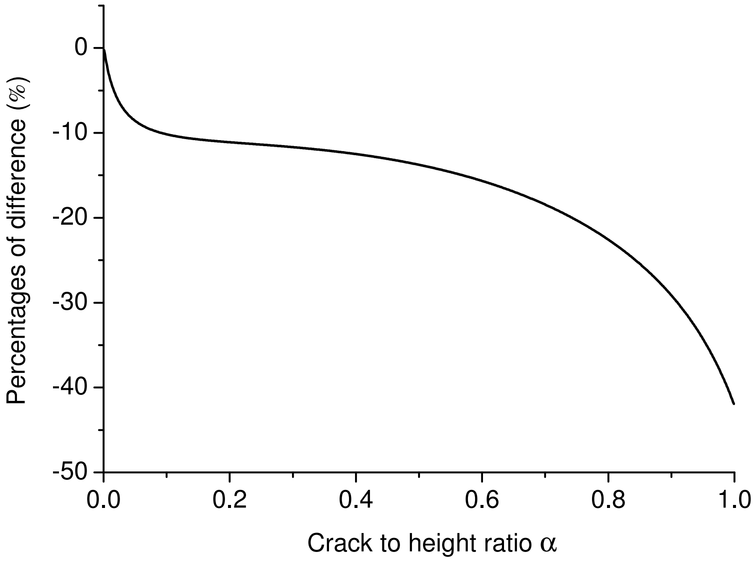

Figure 3.18: Percentages of differences in the nominal strengths calculated by boundary effect model and proposed model.

In a manner similar to the proposed model, BEM could also identify the material information from the test results. By setting $Y' = 1/(\sigma_N^2)$, Equation 3.21 gives a linear regression plot $Y' = J'X' + C'$, with $X = a_{e1}$, $J' = 1/[a_t(B(\alpha)f_t)^2]$, and $C' = 1/[(B(\alpha)f_t)^2$. Hence, transition crack length $a_t = C'/J'$, material tensile strength $f_t = \sqrt{1/C'}/B(\alpha)$, and fracture toughness $Kc = (1.12f_t)\sqrt{a_t\pi}$.

3.3.2 Comparison of the proposed model with Type 2 SEL

In the expression for the Type 2 SEL, h_0 denotes a constant proportional to Irwin's characteristic length l_{ch}, and $\hat{B}$ denotes a dimensionless constant characterizing the structure geometry. The expressions of the fore-mentioned two values are given as follows [78]:

$$h_0 = \frac{c_f g'(\alpha)}{g(\alpha)} \tag{3.23}$$

$$\hat{B}f_t = \sqrt{\frac{EG_c}{g'(\alpha)c_f}} \tag{3.24}$$

where $g(\alpha) = K_I^2(\alpha)h(t/F)^2 = A^2(\alpha)\pi\alpha$ denotes the dimensionless energy release function of linear elastic fracture mechanics. Additionally, c_f denotes the effective size of the fracture process zone that is proportional to the characteristic length l_{ch} and transition crack length a_t. It corresponds to the total crack length that either results in the same (according to LEFM) specimen compliance as the actual crack with its process zone minus the initial crack length or traction free crack length [78], or it is approximately equal to half length of FPZ [79]. Normally, c_f is identified from the tests results of geometrically similar specimens in conjunction with the transitional size h_0. It should be noted that when c_f is known, Type 2 SEL can be applied to structures or specimens that are not geometrically similar.

Given the definition of the correction factor for the derivative of the energy release rate $H(\alpha)$ (Equation 3.9), $g'(\alpha)$ can be simplified as follows:

$$g'(\alpha) = H^2(\alpha)\pi \tag{3.25}$$

After substituting Equations 2.21, 3.13, 3.23, 3.24 into Equation 2.41, calculations are performed to result in the following expression:

$$\sigma_N = \frac{1.12 f_t \sqrt{a_t/c_f}}{H(\alpha)} \left(1 + \frac{a_e}{c_f}\right)^{-1/2}, \tag{3.26}$$

When $c_f = a_t$, the proposed failure model shown in Equations 3.15 and 3.20 and Type 2 SEL are identical. However, the proposed model is presented in two different forms. However, c_f is a fitted parameter from the test results, and it is not guaranteed as equal to the transition crack length a_t [45]. This implies that the two models will provide different nominal strength predictions when $c_f \neq a_t$. It should be noted that a_t can also be identified from the test results, as opposed to calculating the same from the material tensile strength f_t and fracture energy G_c. In such cases, the proposed model and Type 2 SEL provided the same nominal strengths, but the material properties (f_t and G_c) fitted from the test results could be different.

3.4 Model validations

3.4.1 Concrete experiments

Bažant et al. [18, 19] conducted a series of experiments with cracked three point bending beam specimens with similar geometries to investigate the size effects in concrete specimens. Specifically, 8 specimens exhibited identical crack to height ratios $\alpha = 0.33$, identical span to height ratios $S/h = 4$, and a fixed thickness $t = 25.4\ mm$. The concrete presents the following mechanical properties: average tensile strength $f_t = 3.0\ MPa$ and fracture toughness $K_c = \sqrt{G_c E} = 1.23\ MPa\sqrt{m}$. The corresponding transition crack length $a_t = 42.66\ mm$. Two correction factors $A(\alpha)$ and $H(\alpha)$ correspond to 1.08 and 1.42 respectively, and thus the equivalent crack length a_e for each beam could be calculated accordingly.

The beam dimensions, equivalent crack length a_e, failure loads F_{max} and the nominal strengths σ_N for the 8 specimens are listed in Table 3.1. The nominal strengths σ_N for the cracked three-point bending beam specimen are defined as follows:

$$\sigma_N = \frac{3F_{max}S}{2h^2t}. \tag{3.27}$$

Table 3.1: Concrete specimen and test results.

Specimen dimensions (mm) [18]	a_e (mm)	F_{max} (N) [18]	σ_N (MPa)
$152.4 \times 38.1 \times 25.4$	7.32	366.53	2.27
$304.8 \times 76.2 \times 25.4$	14.63	721.28	2.24
$609.6 \times 152.4 \times 25.4$	29.27	1065.79	1.65
$914.4 \times 228.6 \times 25.4$	43.90	1759.72	1.82
$1219.2 \times 304.8 \times 25.4$	58.53	2179.63	1.69
$1524 \times 381 \times 25.4$	73.16	2288.61	1.42
$1828.8 \times 457.2 \times 25.4$	87.80	2470.99	1.28
$2133.6 \times 533.4 \times 25.4$	102.43	3113.76	1.38

Given the geometrical information and mechanical parameters, the failure load F_{max} is calculated by Equations 3.15 and 3.27. The predicted failure loads are plotted in Figure 3.19 and illustrate a good agreement with the test results and the predictions of Type 2 SEL. $\hat{B}f_t$ and h_0 in Type 2 SEL are obtained from the linear regression, and thus the predictions of the Type 2 SEL deviate slightly from the predictions of the proposed model. However, if the length parameter c_f in Type 2 SEL corresponds to the transition crack length a_t and the material tensile strength f_t is known, then without necessitating any experimental work, the Type 2 SEL and the proposed model provide identical predictions of the failure loads. With respect to the given material parameters, the boundary effect model results in predictions that are consistently smaller than the test results and the predictions of proposed model and Type 2 SEL. This implies that the boundary effect model could underestimate the load bearing capacity of the cracked structure if the material parameters used in the model, including the tensile strength f_t and fracture toughness K_c, were measured from standard tests.

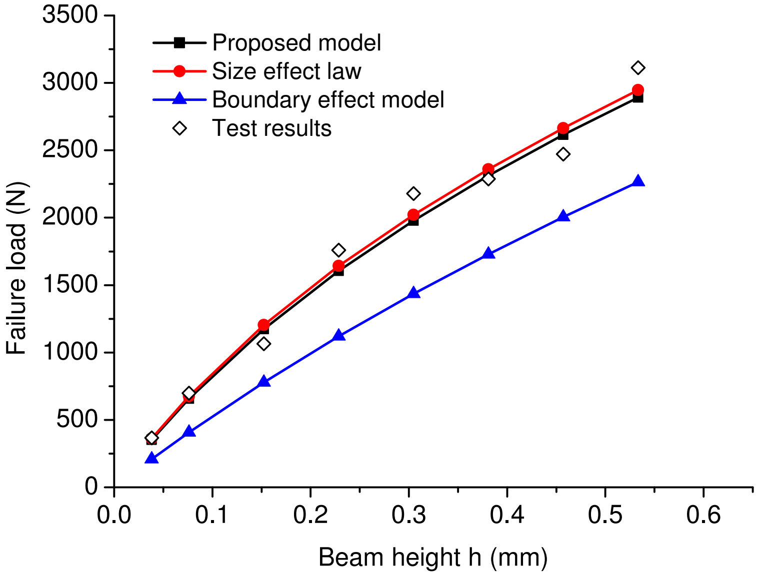

Figure 3.19: Model predictions of failure load versus beam height comparing with Type 2 SEL predictions, Boundary effect model predictions and test results of concrete.

With respect to geometrically similar specimens, the mechanical properties could be identified from the test results. Figure 3.20 shows the fitted linear curve with slope $J = [H(\alpha)/(1.12f_t)]^2/a_t = 4.04 \times 10^{-3}$ and intercept $C = [H(\alpha)/(1.12f_t)]^2 = 1.72 \times 10^{-1}$. The calculated values are: transition crack length $a_t = 42.70\ mm$, tensile strength $f_t = 3.06\ MPa$, and fracture toughness $K_c = \sqrt{G_c E} = 1.21\ MPa\sqrt{m}$. All the fore-mentioned values are extremely close to the experimental measurements. With respect to the Type 2 SEL, the transitional height $h_0 = 22.24mm$ is obtained by the best fit that included information with respect to the length parameter $c_f = h_0 A^2(\alpha)\alpha/H^2(\alpha) = 42.70\ mm$. The measured transition crack length $a_t = 42.66\,mm \approx c_f$, and thus, the predictions given by the proposed model and Type 2 SEL are almost identical. In terms of the boundary effect model, in order to obtain the optimal fit for the test results, the fitted material parameters correspond to $f_t = 5.42\ MPa$, $K_c = 1.26\ MPa\sqrt{m}$, and $a_t = 13.61\ mm$. The fitted tensile strength considerably exceeds the direct measurement, and this indicates that the predictions of the strength mechanism in the boundary effect model are not necessarily accurate.

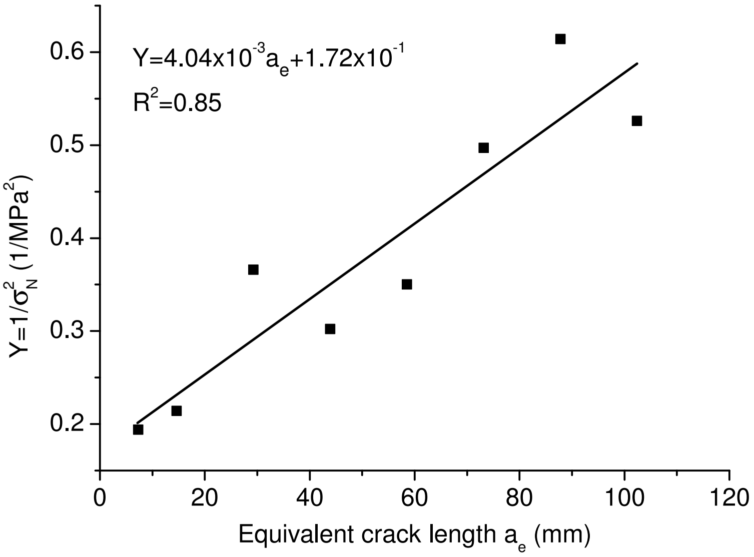

Figure 3.20: Linear regression of the test results of concrete.

3.4.2 Limestone experiments

Bažant et al. [80] tested 4 different sizes of the cracked three point bending beam specimens made of Indiana limestone to investigate the size effect. The specimens possessed identical crack to height ratio $\alpha = 0.4$, identical span to height ratio $S/h = 4$, and a fixed thickness $t = 13\ mm$. The measured fracture toughness corresponded to $K_c = \sqrt{G_c E} = 0.97\ MPa\sqrt{m}$. The tensile strength f_t exhibited different values, since Bažant obtained a value of 3.45 MPa with splitting tensile test, Jenq and Shah [81] obtained a value of 5.0 MPa from a large double edge cracked direct tensile test, and Schmidt obtained [82] a value of 5.38 MPa by 6 ”direct pull” tests on ”dog-bone specimens”.

The two geometrical correction factors $A(\alpha)$ and $H(\alpha)$ correspond to 1.18 and 1.72 respectively. The beam dimensions, equivalent crack length a_e, failure loads F_{max}, and the nominal strengths σ_N are listed in Table 3.2.

In order to obtain reasonable materials tensile strength f_t, the linear regression plot as shown by the solid line in Figure 3.21 provides the slope $J = [H(\alpha)/(1.12 f_t)]^2/a_t = 1.08 \times 10^{-2}$ and intercept $C = [H(\alpha)/(1.12 f_t)]^2 =$

Table 3.2: Limestone specimens and test results.

Specimen dimensions (mm) [80]	a_e (mm)	F_{max} (N) [80]	σ_N (MPa)
$52 \times 13 \times 13$	2.35	78	2.77
		82	2.91
		85	3.02
$100 \times 25 \times 13$	4.52	134	2.47
		140	2.58
		140	2.58
$204 \times 51 \times 13$	9.22	238	2.15
		243	2.20
		243	2.20
$408 \times 102 \times 13$	18.44	394	1.78
		405	1.83
		418	1.89

1.02×10^{-1}. The calculated transition crack length $a_t = 9.39\ mm$ and the tensile strength $f_t = 4.91\ MPa$ are within the range of the measured results. The calculated fracture toughness $K_c = \sqrt{G_c E} = 0.99\ MPa\sqrt{m}$ is extremely close to the experimental measurement of $0.97\ MPa\sqrt{m}$. With respect to the boundary effect model, the fitted material parameters correspond to $f_t = 8.72\ MPa$, $K_c = 0.95\ MPa\sqrt{m}$ and $a_t = 29.83\ mm$. Tensile strength f_t is not close to or within the range of the measured values from the standard tests.

With respect to the transition crack length a_t and tensile strength f_t obtained from the linear regression of the proposed model, the failure loads F_{max} could then be estimated and compared with the experimental results, predictions of Type 2 SEL, and the boundary effect model as shown in Figure 3.22. In keeping with expectations, the proposed model provides predictions that are almost identical to those of the Type 2 SEL because in Equation 3.20, the fitted h_t and $(1.12 f_t)/H(\alpha)$ are identical to the h_0 and $\hat{B} f_t$ in Equation 2.41.

3.4.3 Hardened Cement Paste Experiments

Karihaloo et al. [83] performed the C-TPB tests on cracked beams composed of hardened cement paste with a span to height ratio of $S/h = 4$. The heights of the beams corresponded to 50 mm, 100 mm, and 200 mm, respectively, and the

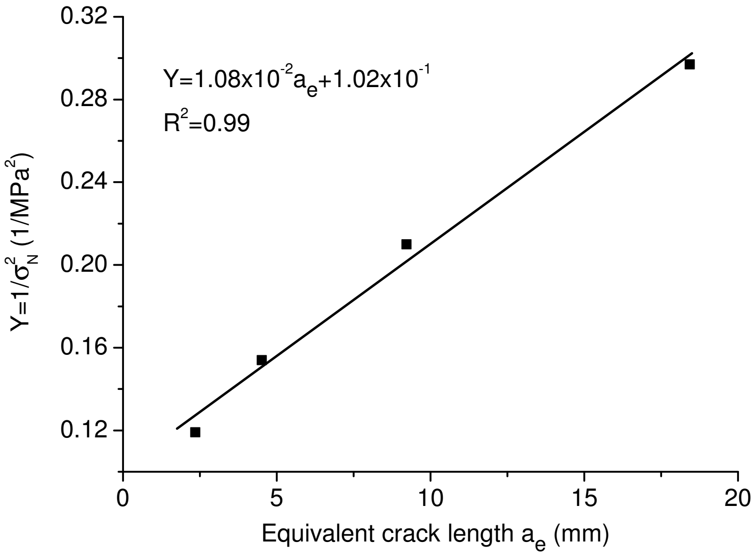

Figure 3.21: Linear regression on the test results of limestone.

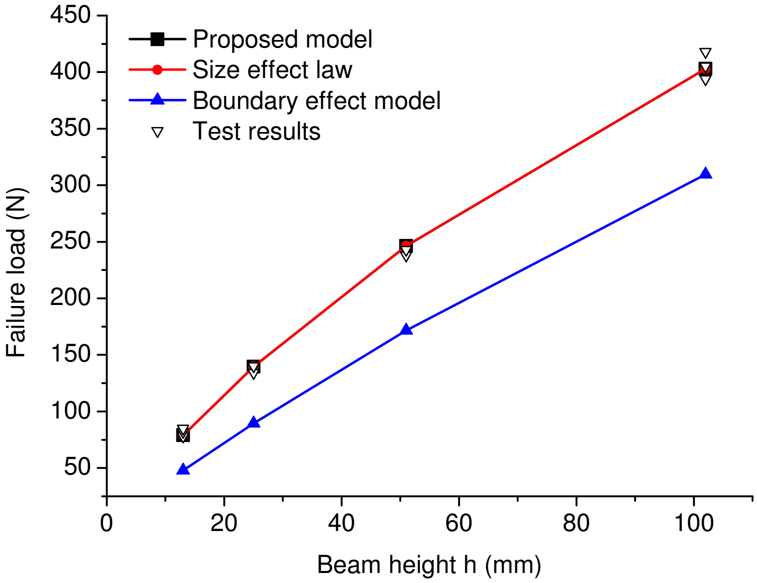

Figure 3.22: Model predictions of failure load relative to beam height when comparing Type 2 SEL predictions and test results of limestone.

thickness $t = 100$ mm was fixed for all the specimens. The crack to height ratios α corresponded to 0.1, 0.3, and 0.5. The hardened cement paste exhibited the following mechanical properties: averaged tensile strength $f_t = 3.53$ MPa, Young's modulus $E = 20.8$ GPa, and fracture energy $G_c = 13.5$ N/m, that is calculated by Equation 3.1 based on the measured failure load of the largest specimen. The corresponding transition crack length $a_t = 5.72$ mm. The predicted failure loads given by the proposed model, Type 2 SEL and the boundary effect model, and the test results are plotted in Figure 3.23. As shown in the figure, all the models are capable of predicting acceptable results albeit with different accuracies.

The Type 2 SEL parameters were provided by Yu et al. [49] and were calibrated for $a/h = 0.3$. The fracture energy $G_c = 18.1$ N/m, length scale $c_f = 7.2$ mm, $\hat{B}f_t$, and transition size h_0 in Equation 2.41 are calculated by Equation 3.23 and Equation 3.24 for crack to height ratios $\alpha = 0.1$, $\alpha = 0.3$, and $\alpha = 0.5$, respectively. With respect to the SEL, the results for small crack to height ratios $\alpha = 0.1$ are worse than the predictions of the proposed model and the boundary effect model. This is because the Type 2 SEL is not recommended for such small crack to height ratios as it belongs to the transition of Type 1 SEL to Type 2 SEL. It should be noted that the results for small crack to height ratios $\alpha \leq 0.1$ should be properly fitted by the universal size effect law that can describe this transition albeit with considerably complicated formulas [47, 49]. In contrast to Type 2 SEL, the proposed model is easier to implement and acceptable model predictions could be obtained for large crack to height ratios as well as small ratio, for which the Type 2 SEL is not recommended.

In terms of the boundary effect model, the material parameters $G_c = 18.2$ N/m and $f_t = 4.58$ MPa are obtained by the optimal fit. As shown in Figure 3.23, the proposed model works better than the boundary effect model for $\alpha = 0.1$. A smaller tensile strength $f_t \approx 3.50$ MPa, which is almost equal to Karihaloo's direct measurement is required to better fit the test results for $\alpha = 0.1$. However, if this tensile strength is adopted, then the predictions given by the boundary effect model for larger α values deviate more from the test results than the predictions given by the proposed model and Type 2 SEL. The boundary effect model is easy to implement in a manner similar to the proposed model. However, a higher material tensile strength is required (for example 29.7%) than the measured result for the hardened cement paste experiments examined in this section.

3.5 Conclusions of the chapter

This chapter presented a new failure model to investigate the size effect and boundary effect in quasi-brittle materials. The model adopted the derivative of energy release rate G' to predict the failure of the strength mechanism and the

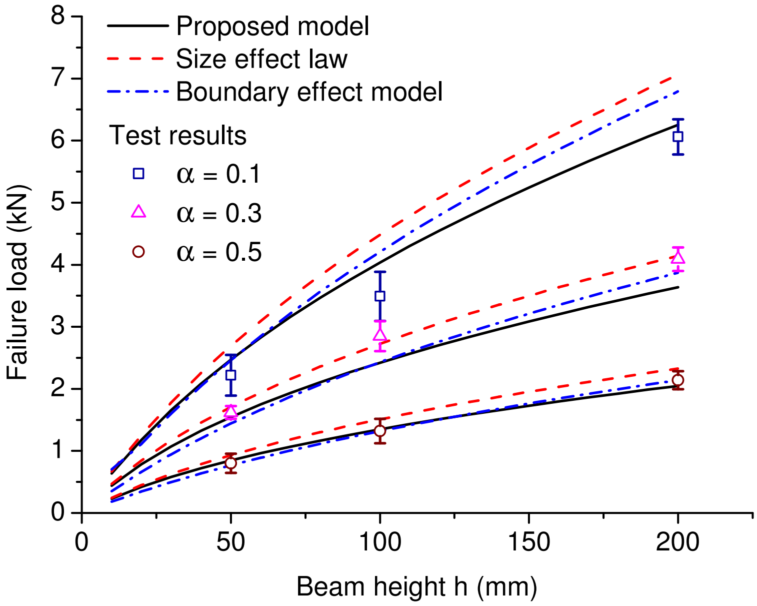

Figure 3.23: Model predictions of failure load relative to beam height when comparing with Type 2 SEL predictions, boundary effect model predictions, and test results of hardened cement paste. The error bars indicate the standard deviations of the experimental results.

energy criterion for the failure of the energy mechanism. An asymptotic model was proposed to capture the effect of all crack sizes on the nominal strength σ_N. Additionally, its expression for geometrically similar specimens was also established, and this could characterize the size effect induced by the specimen size.

The proposed model was compared with the boundary effect model and Type 2 SEL. The first expression (Equation 3.15) of the proposed model was similar to the boundary effect model that effectively captured the boundary effect. However, the two models were fundamentally different because of the different assumptions for the strength mechanisms. The strength mechanism is better characterized by the derivative of energy release rate than the linear assumption in the Boundary effect model. An alternative expression (Equation 3.20) of the proposed model for geometrically similar specimens was established and then compared with the Type 2 SEL. The results indicated that both models resulted in the same predictions when the length scale parameters in the proposed model and Type 2 SEL were identical. In contrast to the Type 2 SEL, the proposed model possessed an advantage as the length parameter could be directly calculated from the measured material parameters of the standard tests as opposed to being fitted from geometrically similar tests. The model could be used for both geometrically similar specimens in a manner similar to the Type 2 SEL as well as for the finite width specimen including different crack sizes. Furthermore, the proposed model also provided good predictions for small crack to height ratios ($\alpha \leq 0.1$) in cases where the Type 2 SEL was not recommended and much considerably complicated formulas of USEL were required. Therefore, the scope of Type 2 SEL was extended. However, the proposed model is not a universal model like USEL, since it is unable to predict all the size effects. For example, it could not predict the size effect observed in uncracked geometrically similar specimen tests. That is, the crack initiation from the free surface.

In order to validate the proposed model, three sets of experimental results were used from extant research for limestone, concrete and hardened cement paste. The results indicated that the predictions of the nominal strengths obtained from the proposed model were in very good agreement with the experimental results.

The proposed model was established based on two local quantities (the energy release rate and its derivative), which has been proved that it can work very well for the nominal strength predictions of cracked structures made of quasi-brittle materials. The defects other than the crack, which present the stress singularity weaker than a crack (v-notches) or only the stress concentrations (circular holes), are very common in the real structures. The structures contain such defects also presents size effects, therefore, the special analytic models are needed for the nominal strength predictions. Due to local feature of the proposed failure model, it may be possible to generalize the model to study the quasi-brittle failure for both singular and regular stress conditions. These will be discussed in the next chapter.

The following paper summarizes the main results of this chapter:
X. Gao, G. Koval, and C. Chazallon. A size and boundary effects model for quasi-brittle fracture. Materials, 9(12):1-20, 2016 [84].

Chapter 4

Generalization of the quasi-brittle rupture model

Contents

4.1 Introduction

The stress and energy release are basic elements found in most of rupture criteria where the failure is characterized by the initiation and propagation of cracks. A literature review suggests that intermediate situations, such as the rupture of a small cracked specimen or structures presenting “imperfections” other than cracks (e.g. heterogeneities, complex shaped notches, etc.) are not well described by either of these two criteria. These difficulties have given rise to different approaches in order to predict the rupture behavior of quasi-brittle materials.

The Critical Distance Theories (CDTs) are still the effective ways to predict the nominal strength of the intermediate situations. Based on the stress criteria, Novozhilov [85] proposed a simple failure criterion based on the average normal stress along the anticipated path of the crack formation. This model has been expanded by Seweryn [22,86–88] to study both regular and singular stress concentrations under mode I or mixed mode loading. Leguillon [13] proposed a criterion for failure initiation at a sharp v-notch under mode I loading, which requires the stress condition and energy condition to be fulfilled simultaneously. This criterion was compared with several known failure initiation criteria and validated in [13, 89] for mode I loading. It was improved by Leguillon and Yosibash [90] by introducing a correction due to the small notch tip radius, later extended by Yosibash *et al.* [91] to mixed mode loading and validated by experimental observations. The concept of Finite Fracture Mechanics was used in Leguillon’s criterion, which assumes the instantaneous formation of cracks of finite size at initiation [92]. Instead of the point-wise stress criterion adopted in Leguillon’s criterion, Cornetti *et al.* [14] proposed a similar criterion, based on the evaluation of stresses prior to fracture averaged over the crack. These coupled criterion allows for the general analysis of arbitrary stress concentrations [20, 24, 93], and has been used by many researchers to establish general failure criteria for a wide range of engineering problems in the last 14 years [92].

The cohesive zone models [94–96] simulate the damage that occurs in the process zone located ahead of the crack tip. This approach, which involves nonlinear constitutive laws that are described by a displacement jump and corresponding traction along the interfaces, provides a phenomenological model with which to simulate complex fracture behavior, such as crack nucleation, initiation and propagation [7]. The extension of the classical cohesive model to quasi-brittle materials usually shows fractal patterns in the failure process. This fractal approach leads to a scale-invariant cohesive crack model which is able to predict the size effects even in tests where the classical approach fails, e.g. the direct tension test [97].

Most of the methods are associated with a length scale that is usually proportional to Irwin's [2] characteristic length l_{ch}, which depends on the properties of the material, such as the stiffness, strength and fracture toughness. However, for certain building materials (such as concrete, rocks, some types of ceramics, etc.), the value of the characteristic length scale can become too large when compared to the specimen size (as already discussed in Chapters 2 and 3), which makes the direct implementation of these approaches impossible [15]. In the discrete element methods, the materials are organized into assemblies of particles in contact. Initially developed by Cundall [72] for modelling granular and particulate systems, these methods were further adapted to study the fracture of quasi-brittle materials, such as concrete [98, 99] and rocks [100]. Despite the simple (and physical) local point of view of ruptures, the intrinsic scale effects related to the particle size and characteristic length l_{ch}) also affect the response of the model to quasi-brittle rupture [28, 75, 76].

This chapter presents an alternative description of quasi-brittle failure based only on local quantities that are related to the energy release rate G, which can be regarded as a generalization of the proposed failure model presented in Chapter 3 for more complex defects (other than cracks) or boundary conditions and different materials. The model is compared to experimental results in the literature in the opening mode for: cracked three-point bending beams, v-notched tensile and bending samples, and plates with a circular hole in tension.

4.2 Local approach

4.2.1 Model

Equation 3.15 is developed for characterizing the size and boundary effects on fracture of a finite width plate with an edge crack. In this section, a more general form of Equation 3.15 is used to provide a more concise representation of the failure behavior:

$$\sigma_N = \frac{1.12 f_t}{H(\alpha)} \left[1 + \left(\frac{a_e}{a_t} \right)^r \right]^{-1/2r}, \tag{4.1}$$

where r is a parameter that describes the transition between a failure that is defined by the material strength ($a \to 0$) and one defined by LEFM ($a \gg a_t$). The effect of this parameter is presented in Figure 4.1a and traduces some complex consequences of the microstructure of the material such as granulometry, voids, etc. Lower values of r lead to smoother transitions between the two mechanisms, which are related to lower rupture values for cracked structures. As already discussed in Chapter 3, Equation 4.1 is identical to Type 2 Size Effect Law when the same r value is introduced in Type 2 SEL and transition crack length a_t is equal to the length scale parameter c_f in Type 2 SEL.

After substituting Equations 3.13 and 2.21 into Equation 4.1 and some algebraic work, the crack size dependence in Equation 4.1 can be as the contribution of two mechanisms:

$$\left[\frac{H(\alpha)\sigma_N}{1.12 f_t} \right]^{2r} + \left(\frac{G}{G_c} \right)^r = 1, \tag{4.2}$$

The ratio σ_N / f_t denotes the activation of the material strength, while G/G_c is related to the fracture mechanics. Hence, the rupture of a quasi-brittle material (represented by Equation 4.1) is rewritten as the contribution of the two mechanisms.

It is noticed that ratio of the local quantities $G'/\bar{G}_c$ can be used to replace the non-local quantity $[H(\alpha)\sigma_N/1.12 f_t]^2$ in Equation 4.2. Then, similar to the simple asymptotic model proposed for infinite plate (Equation 3.5), the failure criterion (Equation 4.2) may be finally rewritten as:

$$\left(\frac{G'}{\bar{G}_c} \right)^r + \left(\frac{G}{G_c} \right)^r = 1, \tag{4.3}$$

which is a function of quantities obtained exclusively at the crack tip and the parameters of the material. This failure criterion (Equation 4.3) is identical to the one (Equation 3.15) presented in the previous chapter when $r = 1$. The advantage of the new variable r is to give more liberty defining the transition between each mechanism (as shown in Figure 4.1a). This is shown necessary to describe more complex problems as it will be seen during the chapter. For the complex boundary and loading conditions, the explicit expression for the gradient of energy release rate G' is not always available, so that a numerical calculation like modified crack closure method (see Appendix B) of crack extension da from the tip of the defect may be required.

The values of $(G'/\bar{G}_c)^r$ and $(G/G_c)^r$ depend on the crack size, as shown in Figure 4.1b. The ratio $(G'/\bar{G}_c)^r$ dominates the failure behavior for very small cracks ($a \rightarrow 0$), which is in the region where fracture mechanics is not adapted for quasi-brittle materials; however its effects diminish for longer cracks. By definition, Equation 4.3 predicts the initiation of a crack under nominal stresses reaching the tensile strength f_t and crack propagation $G = G_c$ for long cracks. The transition between these two mechanisms occurs at $a = a_t$, which is the transition crack size.

The main advantage of Equation 4.3 is that it is independent of geometrical parameters. The values of G and its derivative G' can be quantified for defects that induce stress singularities, such as cracks or v-notches, or do not induce stress singularities, such as holes, as shown in Section 4.3.

4.2.2 Failure load for elastic structures

The relation represented by Equation 4.3 is defined for a failure load F_N. If a different load F_0 is applied, the equation becomes

$$\left(\frac{G_0'}{\bar{G}_c}\right)^r + \left(\frac{G_0}{G_c}\right)^r = \mu_0, \tag{4.4}$$

where G_0 and G_0' are the corresponding energy release rate and its derivative at the crack tip under the loading F_0. Considering that F_0 is a fraction of the failure loading ($F_N = \rho F_0$), by linearity, $G = \rho^2 G_0$ and $G' = \rho^2 G_0'$. The value of $\rho = \mu_0^{-1/(2r)}$ can be obtained by substituting the relation for G, G', and Equation 4.4 into Equation 4.3. Finally, the failure load F_N can be calculated based on the results of any given load F_0 based on the expression

$$F_N = \mu_0^{-1/(2r)} F_0. \tag{4.5}$$

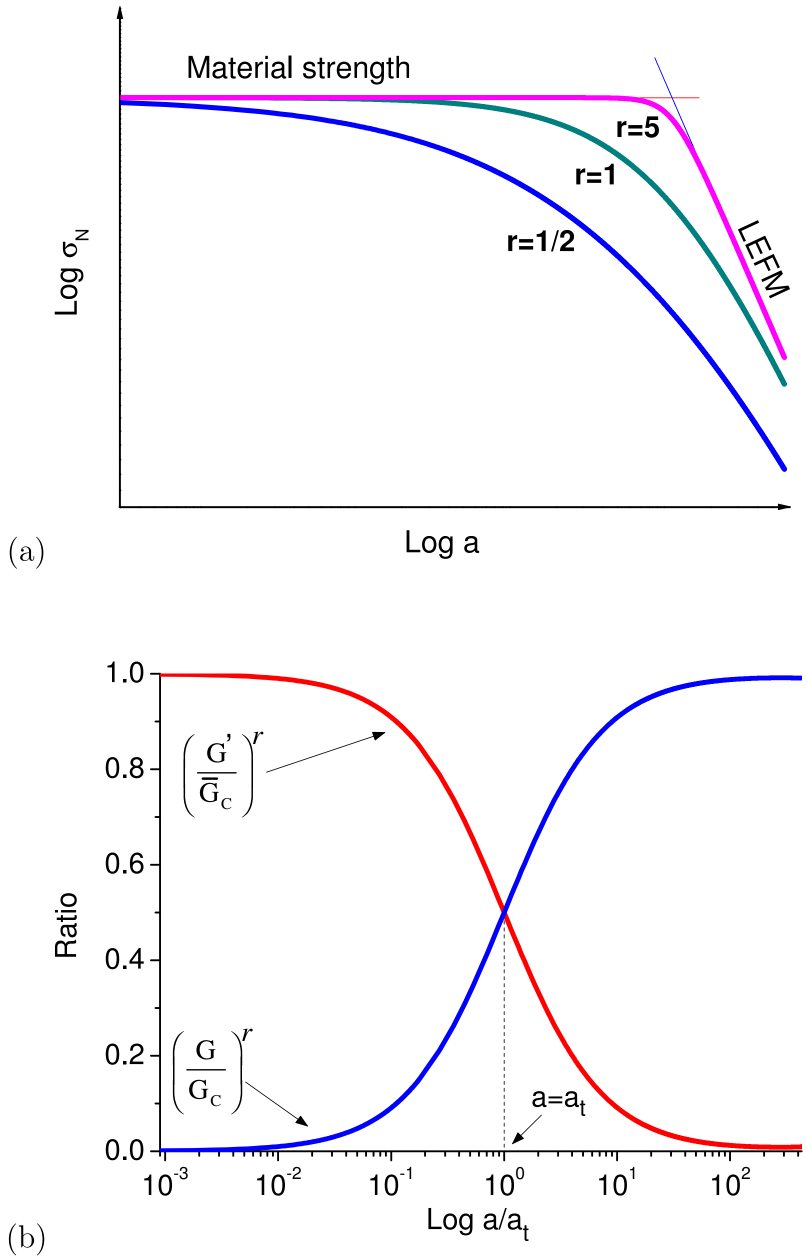

Figure 4.1: (a) Nominal strength σ_N as a function of crack length a for different r, and (b) evolution of the ratios $(G/G_c)^r$ and $(G'/\bar{G}_c)^r$ as functions of the crack length a/a_t(r = 1).

4.3 Comparison to experimental results from the literature

The failure criterion proposed in Equation 4.3 was compared to the experimental results given in the following section. The tensile strength f_t and fracture energy G_c adopted in the predictions are associated to measured values. However, the parameter r is adjusted in order to minimize the error between predictions and experimental results. The size and boundary effects were clearly visible on the three-point bending tests presented first. The generality of the proposed formulation was then analyzed using the results of the rupture tests of v-notched samples in different configurations. Finally, the crack initiation under a local stress gradient was verified in the tensile tests of samples with circular holes of different sizes.

4.3.1 Cracked Three-point Bending (C-TPB) tests

4.3.1.1 Evaluation of G and G'

The stress intensity factor K_0 of the Cracked Three-point Bending (C-TPB) specimen can be directly calculated by

$$K_0 = \frac{3F_0S}{2h^2t}\sqrt{\pi a}A_2, \tag{4.6}$$

where F_0 is the applied load, S, h, and t are the span, height, and thickness of the beam respectively, and a is the crack length (see Figure 4.2a). The function A_2 adopted in this Chapter is an approximation with high accuracy derived by Pastor [101–103], which is applicable to an arbitrary height to span ratio:

$$A_2 = \frac{P_{Sh}}{\sqrt{\pi}(1+2\alpha)(1-\alpha)^{3/2}}, \tag{4.7}$$

where P_{Sh} depends on the height to span ratio h/S and crack to height ratio α, which reads:

$$P_{Sh} = P_\infty + \frac{4h}{S}(P_4 - P_\infty), \tag{4.8}$$

with

$$P_4 = 1.9 - \alpha[-0.089 + 0.603(1-\alpha) - 0.441(1-\alpha)^2 + 1.223(1-\alpha)^3], \qquad (4.9)$$

$$P_\infty = 1.989 - \alpha(1-\alpha)[0.448 - 0.458(1-\alpha) + 1.226(1-\alpha)^2]. \qquad (4.10)$$

Once the height to span ratio h/S is fixed, $A_2(\alpha)$ is only dependent on the crack to height ratio α. A comparison of Equation 4.7 and Equation presented in [104] for any h/S ratio, with the empirical expressions presented in [36] for certain h/S ratio is performed and presented in Appendix A. The value of the energy release rate was obtained from the LEFM relation for plane stress $G_0 = K_0^2/E$, and G_0' was calculated by deriving G_0 with respect to the crack size a. These values are related to the material fracture energy G_c and material strength f_t, as shown in Section 4.2.2, and characterize the failure of the structure.

4.3.1.2 Birchall's experiments

Figure 4.2 illustrates the nominal strength results ($\sigma_N = 1.5F_NS/(h^2t)$) predicted by the proposed model and compared to the test results of the C-TPB specimens tested by Birchall *et al.* [105] that had a span to height ratio of $S/h = 4$ and were made of Portland cement paste. In the figure, the model results were obtained for a beam with dimensions of $h = 1\,m$, $t = 1\,m$, and $S = 4\,m$. The material parameters were measured by Birchall *et al.* [105]. The mean tensile strength $f_t = 10.5\,MPa$ and mean fracture energy $G_c = 23.8\,N/m$ were calculated by measuring the failure loads of uncracked and cracked specimens, respectively, which resulted in a transition crack size of $a_t = 1.1\,mm$. The transition between the failure mechanism associated with the material strength and that due to the fracture mechanics (visible in Figure 4.2b) is quite sharply delineated, which is well described by a high value of the parameter r ($r = 10$ in this case).

4.3.1.3 Karihaloo's experiments

The C-TPB tests performed by Karihaloo *et al.* [83] were conducted on cracked beams made of hardened cement paste with a span to height ratio of $S/h = 4$. The geometrical information and mechanical properties of the specimens have

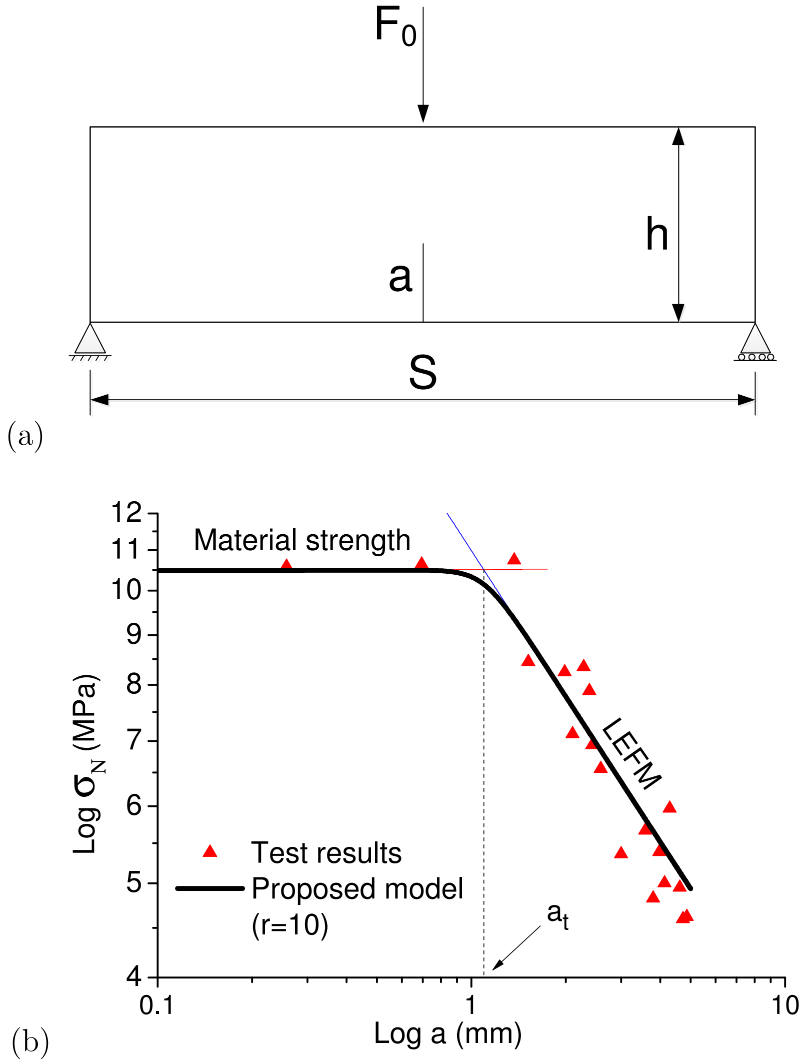

Figure 4.2: The nominal strength σ_N versus the crack length a for C-TPB specimens [105].

already presented in Section 3.4 (Chapter 3). The predicted failure loads given by the proposed model and Bažant's Type 2 Size Effect Law (Equation 2.41), and test results are plotted in Figure 4.3a as a function of the crack to height ratio α. In this example, the value of $r = 1$ seems adequate, which indicates a smooth transition between the mechanisms of failure based on fracture mechanics and material strength. In fact, Equation 3.15 presented in Chapter 3 and Equation 4.3 in this chapter are equivalent when $r = 1$. r parameter is important considering the range of crack sizes a ($5\,mm < a < 100\,mm$). The model parameters of Type 2 SEL $G_c = 18.1\,N/m$ and the length scale $c_f = 7.2\,mm$ were calibrated for $\alpha = 0.3$ [49].

4.3.1.4 Higgins' experiments

Higgins and Bailey [106] tested C-TPB specimens of a hardened cement paste with heights h that varied from $5\,mm$ to $110\,mm$, and a crack to height ratio α that varied from 0.02 to 0.5. The span to height ratio was equal to $S/h = 5$ for all beams, and the thickness was equal to $t = 25\,mm$. Figure 4.3b shows the comparison between the test results and the predicted failure loads obtained by the proposed model and by the Boundary Effect Model (BEM) [17] as functions of the crack to height ratio α. The proposed model and boundary effect model are both able to characterize size and boundary effects in this example. The mechanical properties obtained by optimizing the rupture model (for $r = 0.5$) were: tensile strength $f_t = 12\,MPa$ and fracture toughness $\sqrt{G_c E} = 0.83\,MPa\sqrt{m}$ (the Young's modulus E was not provided), resulting in a transition crack size $a_t = 1.21\,mm$. These results are consistent with the values obtained by the authors. The highest value of strength obtained in direct tensile tests on uncracked specimens was $12.5\,MPa$, associated with an estimated fracture toughness of $0.8\,MPa\sqrt{m}$. The material parameters adopted by Duan *et al.* [17] in BEM model were: tensile strength $f_t = 10.29\,MPa$ and fracture toughness $K_c = 0.65\,MPa\sqrt{m}$.

4.3.2 V-Notched tests

The results for the failure of the C-TPB specimens (Section 4.3.1) indicates the ability of Equation 4.3 to locally characterize the strength of structures displaying cracks of different sizes. In the following section, the failure of structures associated with other imperfections that induce singular stresses is analyzed. The experiments of v-notched plate performed by Seweryn *et al.* [22], and v-notched three point bending specimen performed by Dunn *et al.* [21] subjected to mode I loading are adopted as the reference, to validate the proposed model for the nominal strength prediction when the stress singularity factor is differ from 1/2.

4.3.2.1 Evaluation of G and G'

The vertical stress along the x-axis (see Figure 4.4) in the vicinity of the notch tip can be expressed as $\sigma_y(x) = (K_0^N)/(2\pi x)^{1-\lambda}$ [20], where λ is the order of the

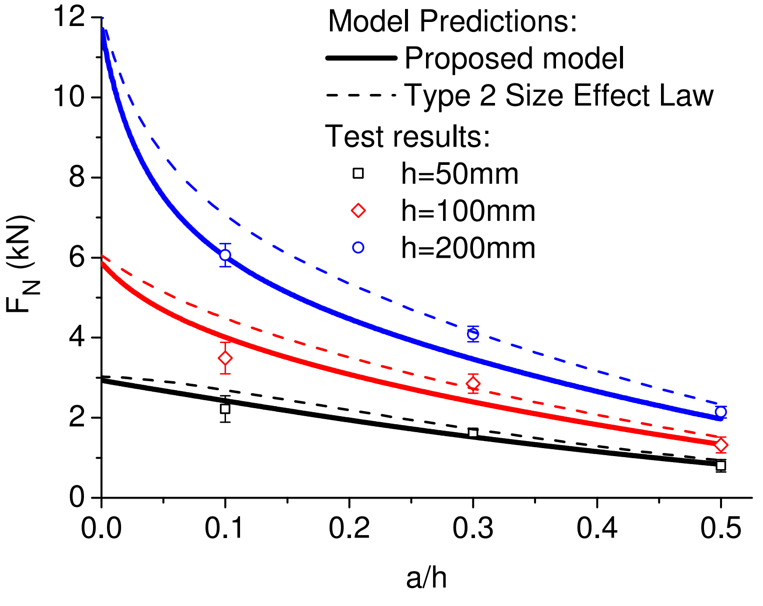

(a)

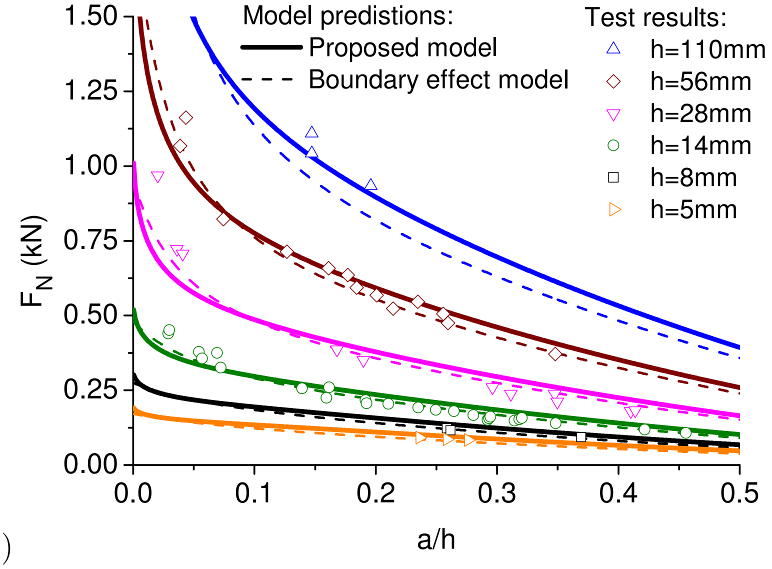

(b)

Figure 4.3: Failure loads F_N versus crack to height ratio α for various specimen sizes in the experiments of (a) Karihaloo *et al.* [83], and (b) Higgins and Bailey [106]. The error bars in (a) indicate the standard deviations of the experimental results.

stress singularity, which depends on the notch opening angle γ. λ is equal to $1/2$ for $\gamma = 0°$ (crack) and 1 for $\gamma = \pi$ (straight edge). The λ values for different notch opening angles are tabulated in Table 4.1. K_0^N is the Generalized Stress Intensity Factor (GSIF) whose physical dimensions depend on the notch opening angle γ.

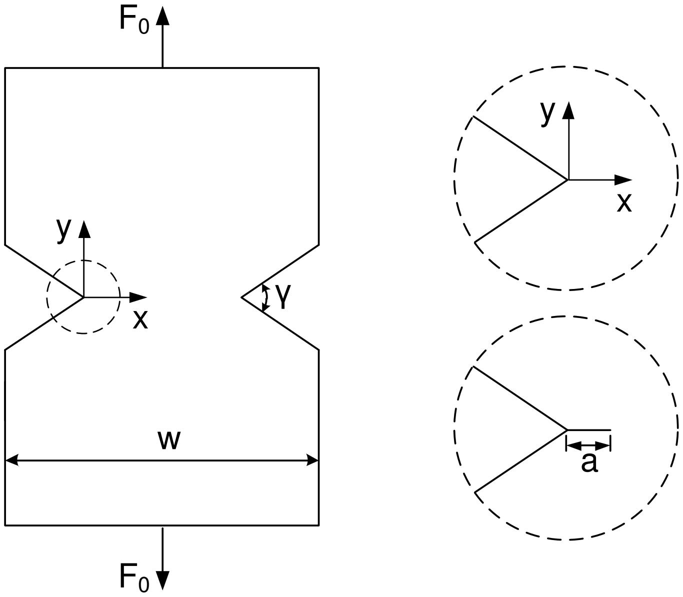

Figure 4.4: V-notched plate under tension loading and the corresponding emanating crack.

The stress intensity factor K_0 corresponding to a short crack emanating from the notch tip depends on the generalized stress intensity factor K_0^N, notch opening angle γ, and crack length a [107]. The relation between the two stress intensities and the crack length is given by [108] for cracks that are much shorter than the notch depth, which reads

$$K_0 = \Lambda(\gamma)\sqrt{\pi}\frac{K_0^N}{(2\pi)^{1-\lambda}}a^{\lambda-1/2}, \tag{4.11}$$

where Λ is plotted and tabulated in [108]. It should be noted that there is a difference of $1/(2\pi)^{1-\lambda}$ between Equation 4.11 and the original equation presented in [108] due to the different formal definition of generalized stress intensity factor.

The substitution of Equation 4.11 into the well-known Irwin's relation in plane stress ($E^* = E$) and plane strain ($E^* = E/(1-\nu^2)$) yields:

$$G_0 = \eta\frac{\left(K_0^N\right)^2}{E^*}a^{2\lambda-1}, \tag{4.12}$$

where $\eta = \Lambda^2(\gamma)\pi/(2\pi)^{2-2\lambda}$ is a dimensionless parameter that depends only on the notch opening angle γ [108], which can be calculated based on the highly accurate Λ values given by Philipps *et al.* [108] for the mode I case.

The generalized stress intensity factor K_0^N is related to the remote loading F_0 by $K_0^N = \xi F_0$, where the coefficient ξ for different specimens can be obtained numerically. The values of ξ for v-notched plates with different notch opening angles γ are tabulated in [88]. For v-notched beams, ξ values are calculated from the values of $K_c^N/(2\pi)^{1-\lambda}$ and σ_{max} tabulated in [21] ($\xi = K_c^N/[\sigma_{max}2h^2t/(3S)]$, where h, t, and S are the height, thickness, and span of the beams, respectively). Table 4.1 presents the values of λ, ξ, Λ and η for different notch opening angles for v-notched plates and beams. The unit of ξ is $Pa \cdot m^{1-\lambda}/N$.

Based on the known values of λ, ξ, Λ and η for different notch opening angles, the energy release rate G_0 corresponding to a short crack emanating from the notch tip can be calculated by Equation 4.12. The value of $G_0' = \eta(2\lambda-1)(K_0^N)^2a^{2\lambda-2}/E^*$ is obtained by derivation of Equation 4.12 with respect to the emanated crack length a.

Table 4.1: Parameters λ, ξ, Λ and η for v-notched plates and beams. The values with * were not originally tabulated but have been calculated by linear interpolation.

γ	λ [21,88,109]	ξ of plates [88]	ξ of beams [21]	Λ [108]	η
0	0.5	613.3	n/a	1.414	1.000
20	0.5004	616.6	n/a	1.417*	1.005
30	0.5015	n/a	n/a	1.418	1.011
40	0.5035	632.3	n/a	1.414*	1.013
60	0.5122	667.3	2335.5	1.407	1.035
80	0.5304	735.0	n/a	1.389*	1.079
90	0.5445	n/a	2964.6	1.380	1.121
100	0.5628	853.7	n/a	1.362*	1.168
120	0.6157	1057.6	4703.8	1.327	1.347
140	0.6972	1424.6	n/a	1.270*	1.665
150	0.7520	n/a	n/a	1.241	1.944
160	0.8187	2153.5	n/a	1.201*	2.327
180	1	6314.6	n/a	1.120	3.941

4.3.2.2 Failure identification

At the notch tip ($a = 0$), the value of the energy release rate G_0 tends to zero, as indicated by Equation 4.12, while its derivative G'_0 tends to infinity. According to Equations 4.4 and 4.5, in these conditions, the failure load F_N tends to zero, as shown in Figure 4.5a. The propagation of the crack induces an increase of G_0 and a decrease of G'_0, which leads to the rapid growth of the F_N value. For very short propagation lengths, the rupture is dominated by the strength mechanism $\sigma_N^{strength} = \sigma_0\sqrt{\bar{G}_c/G'_0}$, as shown in Figure 4.5b. After a certain length, the fracture toughness of the material is mobilized and the rupture behavior follows the prediction of the LEFM, and depends only on the energy release rate. During the transition between the two mechanisms, a maximum value of the failure load F_{max} is observed, which defines the failure limit of the sample.

4.3.2.3 Seweryn's experiments

Seweryn *et al.* [22] carried out tensile experiments using symmetric v-notched polymethyl methacrylate (PMMA) specimens with the following mechanical properties: Young's modulus $E = 3.3\,GPa$, Poisson ratio $\nu = 0.35$, tensile strength $f_t = 102.8\,MPa$, and fracture energy $G_c = 437.82\,N/m$. The fracture energy G_c was calculated by Seweryn *et al.* based on the relation between the fracture toughness and critical generalized stress intensity factor K_c^N for notch opening angles $\gamma = 20°$, $40°$, and $60°$ [88]. Samples with v-notch opening angles γ of 20°, 40°, 60°, 80°, and 100° were studied, and their dimensions are indicated in Figure 4.6a with a thickness of $5\,mm$. The results for $\gamma = 180°$ were based on the tensile strength f_t as determined with a sample presenting a double semicircular indentation.

The predicted failure loads F_{max} with different notch opening angles are compared to the experimental results in Figure 4.6b. A more detailed description of the behavior between $100° < \gamma < 180°$ is provided by the predictions of the strain energy release criterion [88], which are also presented in Figure 4.6b. Good agreement with the complete set of results was observed for $r = 4$.

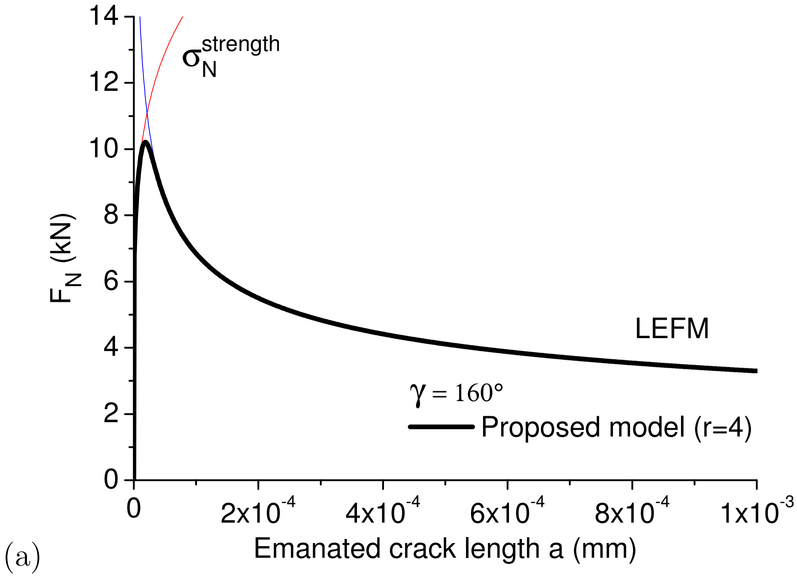

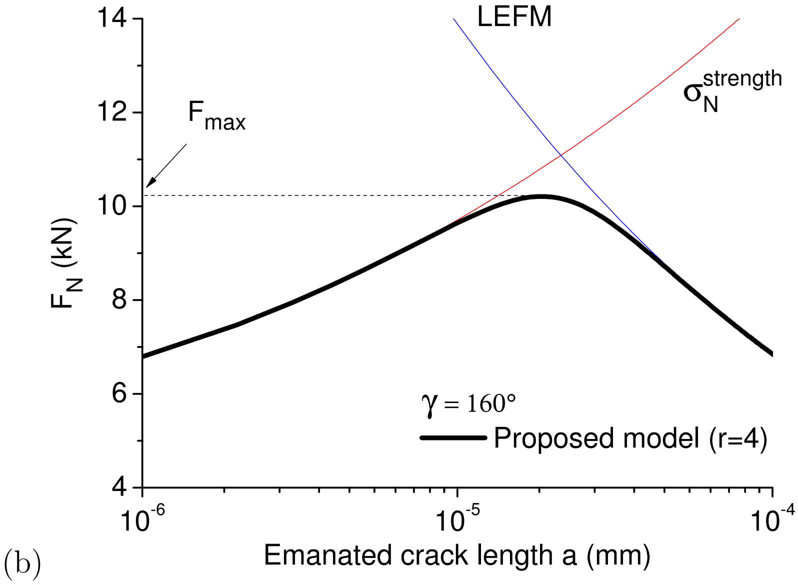

Figure 4.5: Failure load F_N during crack extension and the definition of the maximum failure load F_{max} for v-notches in (a) linear, and (b) semi-log scales.

4.3.2.4 Dunn's experiments

Dunn *et al.* [21] performed a series of three-point bending tests on notched specimens (N-TPB) in polymethyl methacrylate (PMMA) with dimensions of $L = 76.2\,mm$, $t = 12.7\,mm$, and $h = 17.8\,mm$, as indicated in Figure 4.7a. The

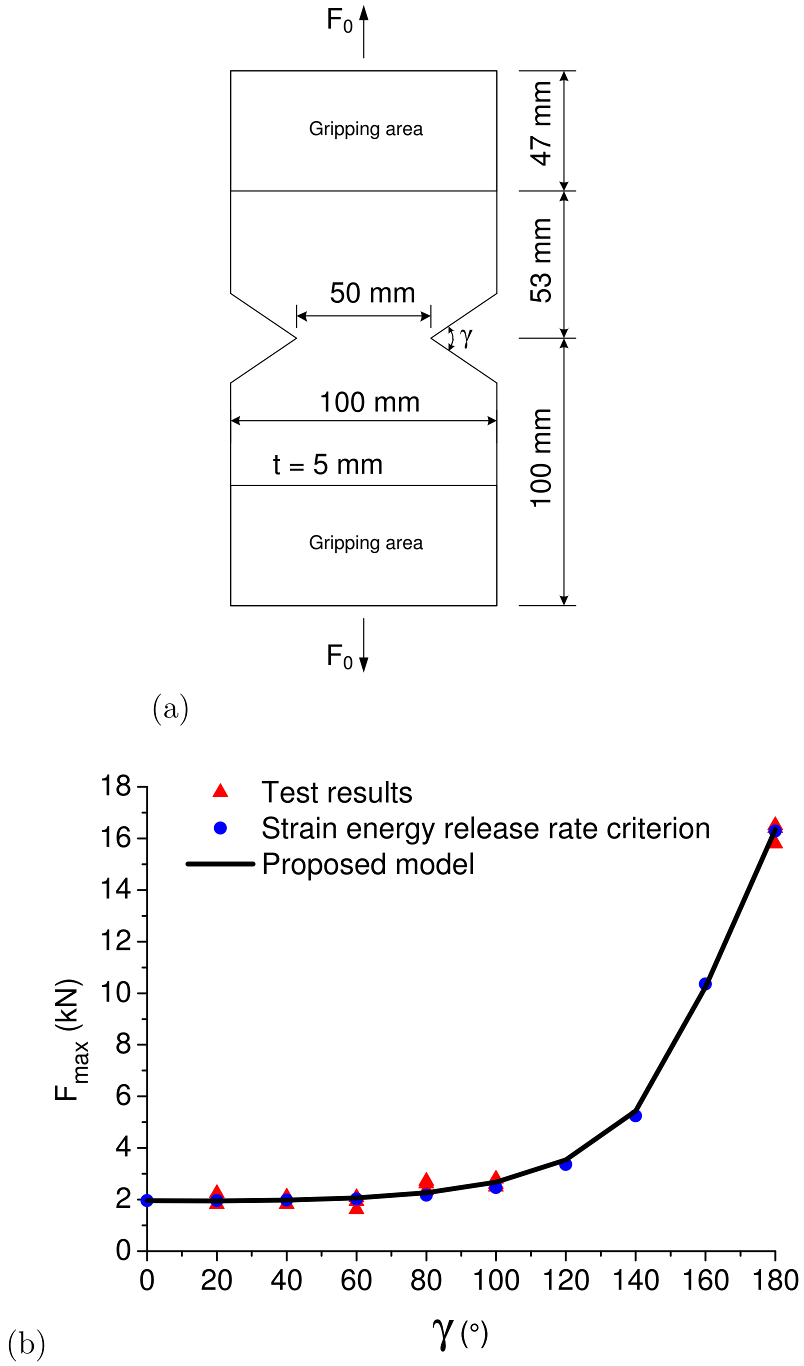

Figure 4.6: (a) Failure loads F_{max} for different notch opening angles γ. (b) The model prediction is compared to the results of references [22, 88].

tests were performed under plane strain conditions following the procedures outlined in ASTM E-399. The specimens were machined with three different notch opening angles γ: 60°, 90°, and 120°. For each notch opening angle, four notch depths c were used: $1.78\,mm$, $3.56\,mm$, $5.33\,mm$, and $7.11\,mm$. This choice of dimensions resulted in notch depth to height ratios c/h of 0.1, 0.2, 0.3, and 0.4, respectively. The PMMA had a Young's modulus $E = 2.3\,GPa$, Poisson ratio $\nu = 0.36$. The average failure stress $f_t = 124\,MPa$ was based on the bending tests of unnotched specimens. The fracture toughness $K_c = 1.25\,MPa\sqrt{m}$ adopted in the model predictions was calculated based on the relation between this quantity and the critical generalized stress intensity factor for the notch opening angle $\gamma = 60°$, as proposed by Seweryn *et al.* This value was expected to be more precise than the results obtained from cracked three-point bending (C-TPB) specimens ($K_c = 1.02\,MPa\sqrt{m}$ with a standard deviation of $0.12\,MPa\sqrt{m}$) [86].

The comparison between the predicted failure load F_{max} (for $r = 4$) and the experimental data is presented in Figure 4.7b for different notch opening angles γ.

4.3.3 Crack initiation in a finite width plate with a circular hole

4.3.3.1 Geometry and failure mechanism

Green *et al.* [110] performed open-hole tensile tests using the quasi-isotropic carbon-epoxy laminate IM7-8552 with stacking sequence $[45/90/-45/0]4s$ (for laminates with a nominal thickness of $4\,mm$). Specimens presenting the same aspect ratio based on the hole diameters D ($3.175\,mm$, $6.35\,mm$, $12.7\,mm$, and $25.4\,mm$) were adopted (for widths $w = 5D$ and lengths $20D$, as shown Figure 4.8a). The tensile strength $f_t = 929\,MPa$ was measured in the unnotched tests, and the fracture toughness $\sqrt{G_cE} = 42.3\,MPa\sqrt{m}$ was estimated by Camanho *et al.* [24].

A post-rupture analysis showed that all specimens with the adopted stacking sequence failed due to fiber failure, which indicates that the effect of the laminate stiffness reduction caused by the progressive matrix failures on the ultimate strength of the laminate was insignificant. Hence, the rupture of these uncracked samples depended on the crack initiation and subsequent propagation thereof due to the stress concentration at the lateral edges of the holes. The failure scheme adopted in this case is presented in Figure 4.8b, and is consistent with the failure pattern observed experimentally by the authors.

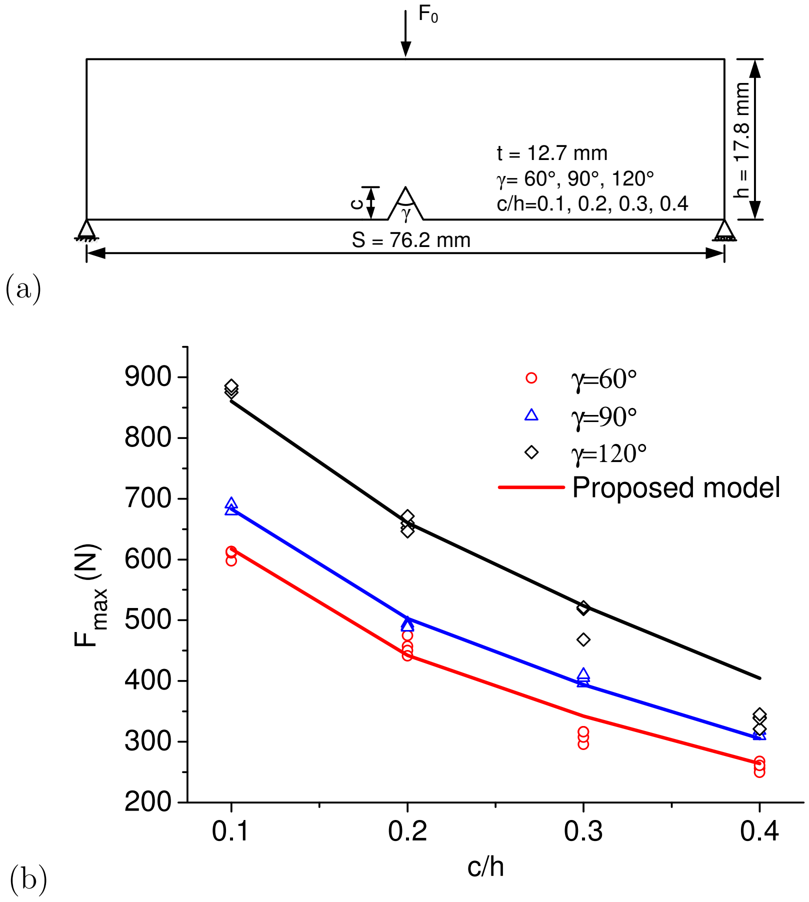

Figure 4.7: Model predictions of the failure load F_{max} compared to the experimental results of reference [21] as a function of the notch to height ratio c/h for various notch opening angles γ.

4.3.3.2 Evaluation of G and G'

The energy release rate corresponding to two symmetric cracks emanating from a plate with a central circular hole of radius R is given by [111] for an isotropic plate as

$$G_0 = \frac{\sigma_0^2 \pi a}{E} A_3^2 A_4^2, \tag{4.13}$$

where σ_0 is the applied stress, a is the extended crack length from the hole, and A_3 is the boundary correction factor for the circular hole. The equation for A_3 is

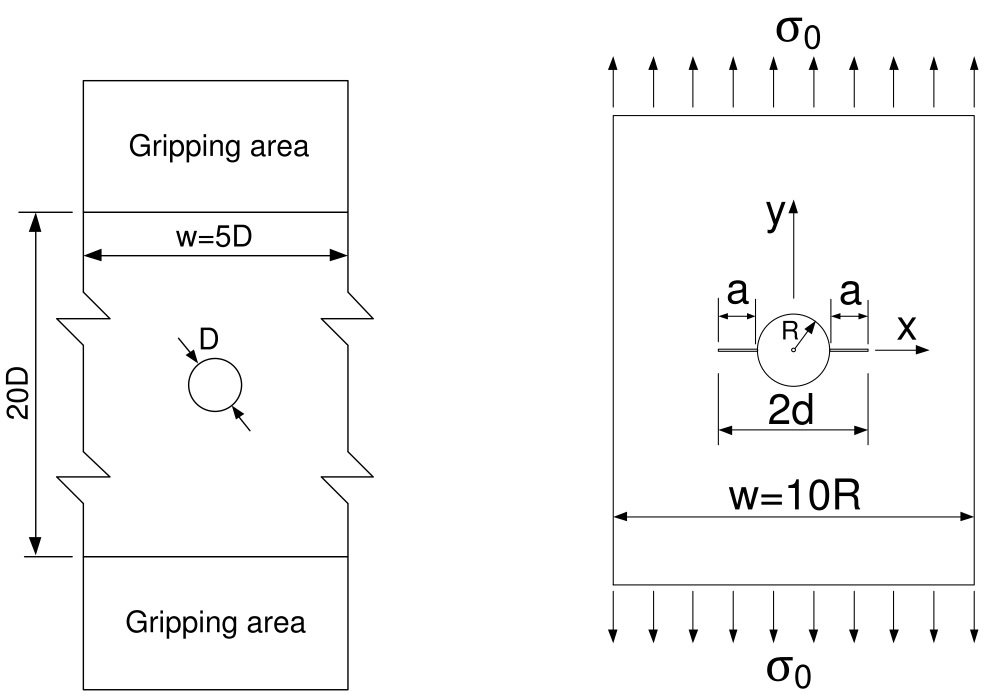

(a) (b)

Figure 4.8: (a) Geometry of the plates with circular holes (modified from the illustration by [110]), and (b) the corresponding failure mechanism (two symmetric cracks emanating from two sides of the hole).

$$A_3 = 1 + 0.358\left(\frac{R}{d}\right) + 1.425\left(\frac{R}{d}\right)^2 - 1.578\left(\frac{R}{d}\right)^3 + 2.156\left(\frac{R}{d}\right)^4, \tag{4.14}$$

with $d = a + R$ as indicated in Figure 4.8b. The quantity A_4 is the finite width correction factor and is equal to

$$A_4 = \sqrt{\sec\left(\frac{\pi R}{w}\right)\sec\left(\frac{\pi d}{w}\right)}. \tag{4.15}$$

The value of G' is obtained by derivation of the expression for G (Equation 4.13) with respect to a.

4.3.3.3 Failure identification

When the hole diameter is sufficiently large, two limit failure mechanisms may be observed when considering the rupture of the plate: one associated with the material strength ($d \to R, G \to 0$), and another associated with the fracture mechanics ($d \gg R$). The hole induces a stress concentration of $3\sigma_0$, which may be inferior to the tensile strength of the material f_t. Hence, in the absence of any cracks, the failure may occur for $\sigma_N = f_t/3$, which defines the initiation of the crack. On the other hand, after a relatively long crack propagation, the structure may behave as a simple middle-cracked plate of crack length $2(R+a)$ and be governed solely by the fracture mechanics ($G \leq G_c$). The transition between these two mechanisms is presented in Figure 4.9a. The individual prediction of the strength mechanism $\sigma_N^{strength} = \sigma_0\sqrt{\bar{G}_c/G_0'}$ tends to be almost independent of the extended crack size a, as is expected for a quasi-brittle material, until the transition to LEFM behavior.

For small diameters, the stress gradient near the edges of the holes affects the strength results [112,113]. This effect is described by Equation 4.3 as an increase in the load limit of the plate during crack initiation, following the trend of $\sigma_N^{strength}$ up to a maximum value before decreasing following the LEFM behavior, as shown in Figure 4.9b. This apparent nonphysical behavior is probably an “artifact” due to the simplicity of Equations 4.1 and 4.3. Consider the effect of the stress gradient that would theoretically prevent this increase in the sample strength. One may then predict a behavior similar to that shown in Figure 4.9a for any hole size, which is a stable failure stress for small cracks, and is followed by a decrease as predicted by LEFM. However, it seems much simpler to define the failure load based on the maximum value $\sigma_{max} = \max \sigma_N$ for all cases. The error associated with this simplification will be reduced in practical situations that concern relatively small crack sizes $a < a_t$ (e.g. $a_t \approx 0.5\,mm$ for the laminated sample used in this example).

4.3.3.4 Comparison to experimental results

The predictions of the proposed model for $r = 15$ are compared to experimental results and other model predictions in Figure 4.10. The theoretical results coincide with the predictions using the average stress method given by Green *et al.* [110] for the failure stress σ_{max}, as shown in Figure 4.10a. For the smallest hole

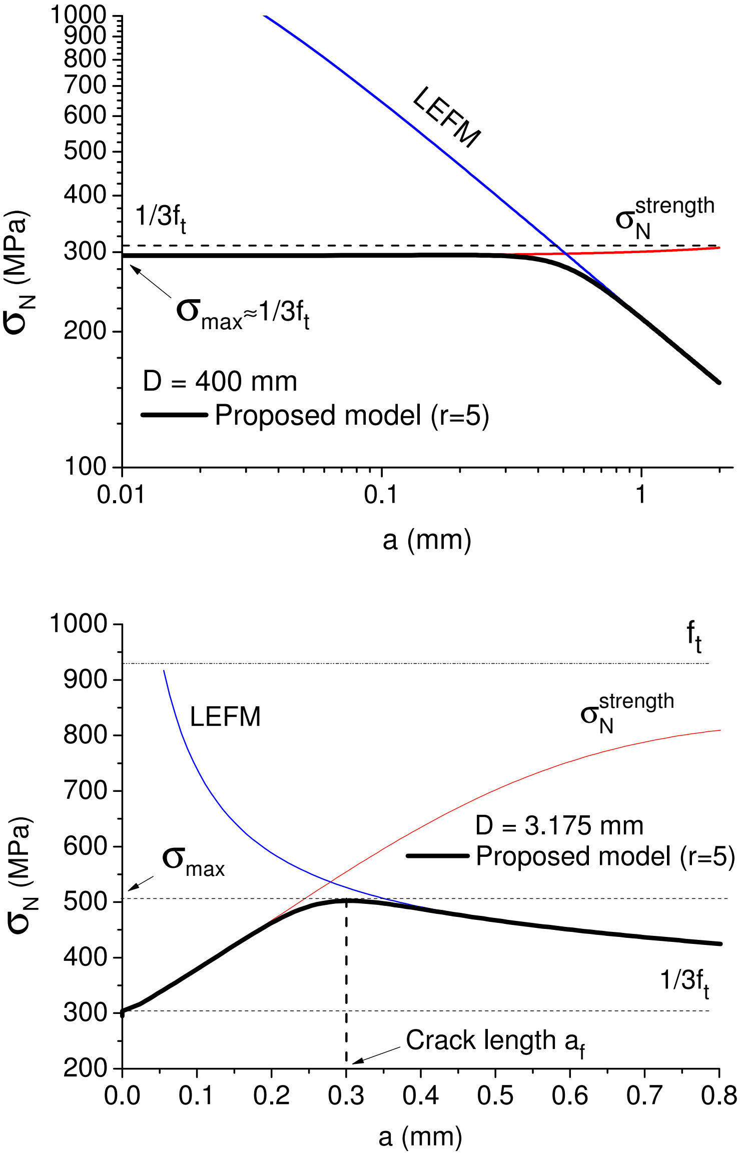

(a)

(b)

Figure 4.9: Nominal strength σ_N in a plate (a) with a big hole, and (b) with a small hole as function of the extended crack size a.

diameters D ($3.175\,mm$ and $6.35\,mm$), the failure mechanism was associated with the fiber pull-out across the width, which may explain the relative deviation of the results. It should be noted that this also happens with respect to the average stress criterion. The predictions of finite fracture mechanics given by Camanho *et al.* [24] also present an offset between the results of the smallest hole and the others.

Holes with bigger diameters induce a failure stress σ_{max} near $f_t/3$, as is expected due to the stress concentration of approximately $3\sigma_0$ at the edge of the holes. Figure 4.10b illustrates the difference between the predictions of the proposed model and the size effect law. Type 2 SEL fits well the test results, but predicts a failure stress σ_{max} which fades to zero for large holes. The extended size effect law [16, 114] corrects this trend for the holed specimens, which is also the case of the proposed model.

4.4 Failure process and length scales

The criterion represented by Equation 4.3 characterizes the rupture as continuous process. It defines the crack initiation and its propagation based on energetical quantities. In some cases, such as structures presenting weak singularities (e.g. v-notches) or stress concentrations (e.g. holes), the maximum value of the load F_N was obtained after a propagation length a_f. At this length scale, F_N is maximized, which means that a_f mathematically minimizes the quantity μ_0 (Equation 4.4) with respect to the crack length a. After some algebraic work, the equation $d\mu_0/da = 0$ can be rewritten as

$$\left[\frac{-(G_0)^{r-1}}{(G_0')^{r-2}G_0''}\right]^{1/r} = \frac{G_c}{\bar{G}_c} = \frac{l_{ch}}{1.12^2\pi}, \tag{4.16}$$

where $l_{ch} = G_c E/f_t^2$ is the characteristic length of the material. The length a_f, solution of Equation 4.16, is easily obtained for a v-notch plate ($a_f = 0.254 l_{ch}(2-2\lambda)^{1/r}(2\lambda-1)^{(1-1/r)}$). In Figure 4.11a, the value of a_f/l_{ch} is plotted as a function of the notch opening angle γ for $r = 4$. The ratio a_f/l_{ch} can be obtained numerically for a finite width plate with a circular hole. In Figure 4.11b, a_f/l_{ch} is presented for different hole diameters D ($r = 5$ and width $w = 5D$).

The analysis of the length $a_{vr} = \{-(G)^{r-1}/[(G')^{r-2}G'']\}^{1/r}$ (based on the left-hand side of Equation 4.16) can technically remedy the nonphysical increase of the failure load observed during crack initiation in v-notched (Figure 4.5) or holed plates (Figure 4.9). Only if $a_{vr} \geq l_{ch}/(1.12^2\pi)$, which corresponds to $a \geq a_f$, the failure load should be considered as physically consistent. Otherwise, the propagated crack a would only present a mathematical meaning on the crack initiation process. Consider a finite crack length absolutely bigger than a_f for the calculations, similar to finite fracture mechanics approaches [14, 24, 92] can also prevent any increase on the failure load.

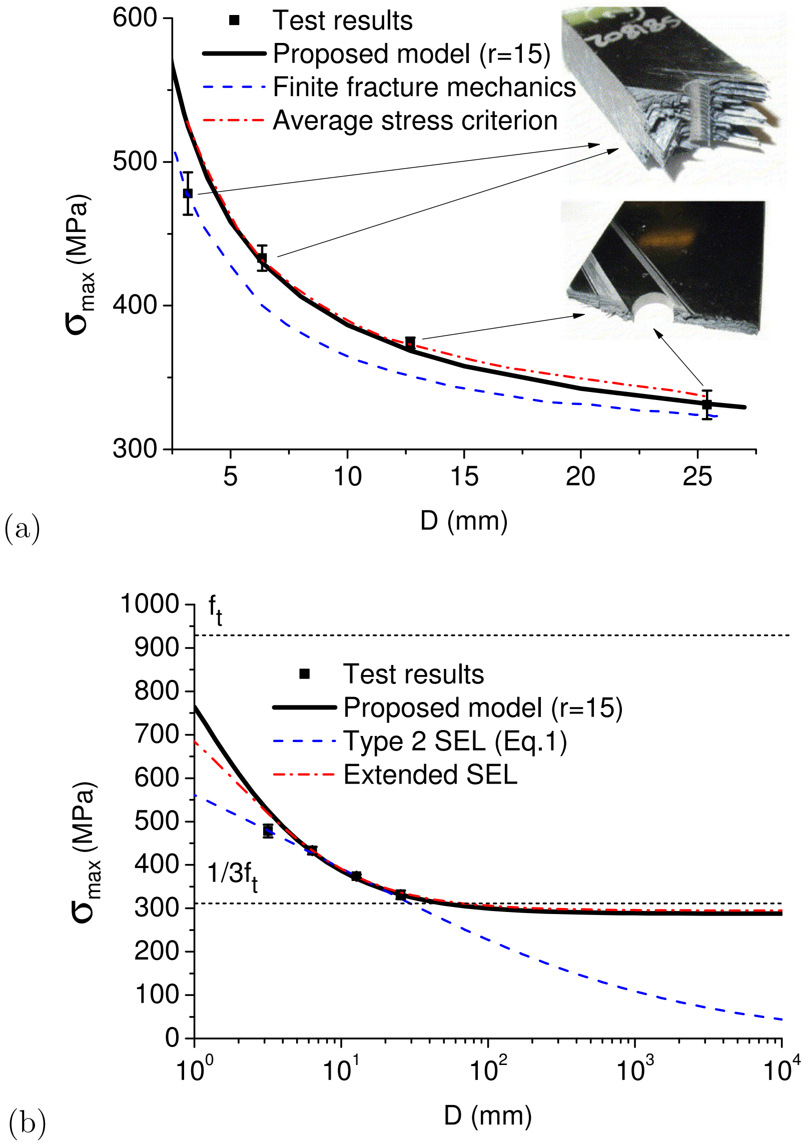

Figure 4.10: Prediction of the failure stress σ_{max} for various hole diameters D compared to the experimental [110] and model-based results. (a) Comparison between the proposed model, average stress criterion and finite fracture mechanics [24]. The insets depict the rupture patterns for different hole diameters. (b) Comparison between the proposed model and two versions of the size effect law (SEL).

Despite all possible approaches to avoid this apparent problem of the increase of the failure load, it should be noted that the length scale a_f is directly related to the characteristic length l_{ch}, usually associated to the size of the fracture process

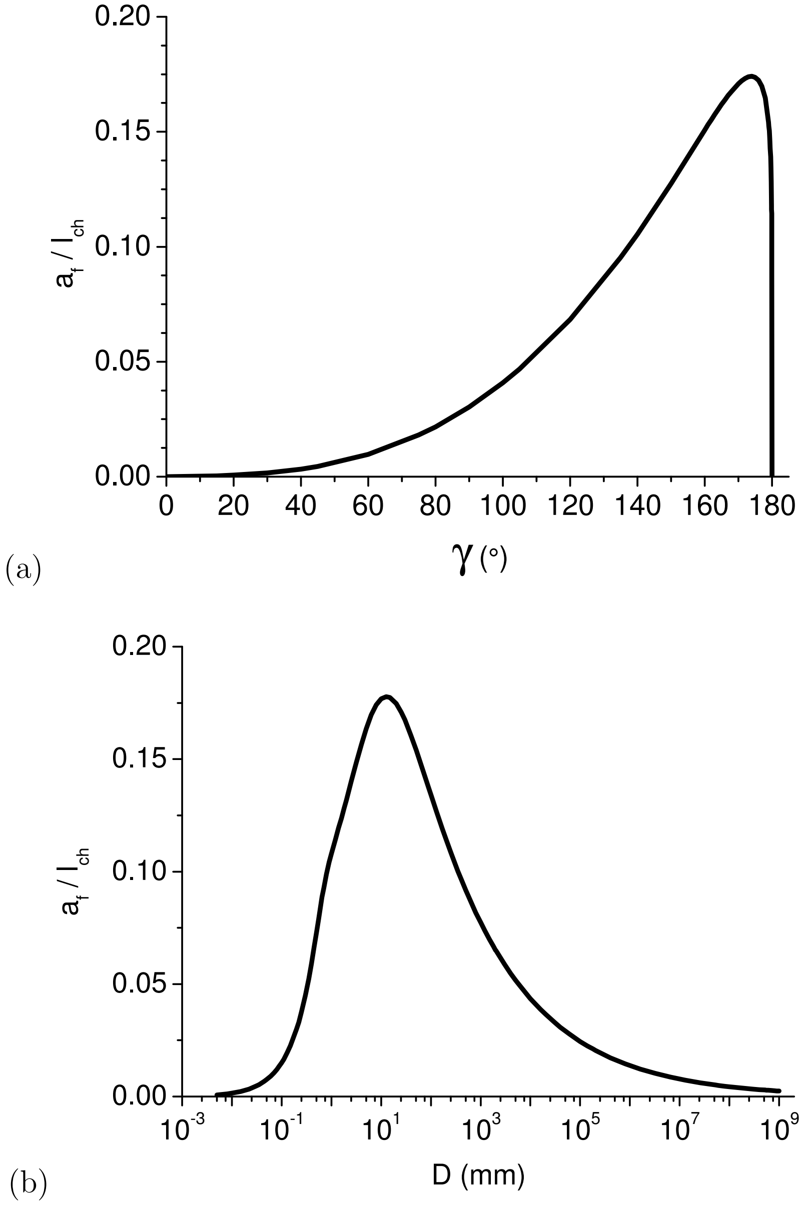

Figure 4.11: Ratio a_f/l_{ch} (a) versus notch opening angle γ for a v-notched plate and (b) as a function of the hole diameter D for a holed plate ($l_{ch} = 2.07\,mm$).

zone (FPZ), and the parameter r. The FPZ is an important element in many models [13, 14, 87], physically associated to a region containing micro-cracks near the crack tip. In small scales ($a \rightarrow 0$), the size effect behavior is particular and alternative models are proposed under these conditions [44, 47]. The improvement of Equation 4.3 based on these effects for $a_{vr} \leq l_{ch}/(1.12^2\pi)$ may provide a finer and more realistic description of the crack initiation.

4.5 Conclusions of the chapter

The local model proposed in this chapter consistently reflects the main rupture trends from crack initiation to crack propagation based on its agreement with the experimental results for different geometries. In all analyzed cases, the failure was induced by an opening mode wherein the value of the energy release rate G controlled the propagation of the crack, and its derivative with respect to the crack size G' controlled the crack initiation. The competition between these two quantities was related to the material parameters, namely, the fracture energy G_c, tensile strength f_t, and parameter r, which characterizes the transition between the crack initiation and propagation states. Despite the clear physical sense of r, only further testing with the same material and completely different geometries would definitively allow the association of this parameter exclusively to this material.

The principal feature of the model is to identify the effects of the nominal stress (a non-local quantity) through the evolution of the energy release rate G (in a local sense) specifically at the initiation of the crack. This leads to an alternative description of the rupture, which allows a relatively simple analysis of structures with any size of crack, or no cracks at all. For complex geometries and/or boundary conditions, a numerical implementation of the present formulation may produce convergent results with respect to the mesh sizes, depending only on the precision of the G and G' values. The scope of LEFM is extended to a certain extent, considering that neither plasticity nor damage are necessarily associated with the model to describe crack initiation.

Size effects caused by stress concentration (e.g. at the edges of the holes), were theoretically quantified using the value of G'. Despite the simplicity of Equation 4.3, the equation provides good insight into the competition between the failure mechanisms at a local level. Information regarding this point of view associated to the existing background may contribute to the improvement of rupture analysis.

The following paper summarizes the main results of this chapter:
X. Gao, G. Koval, and C. Chazallon. Energetical formulation of size effect law for quasi-brittle fracture. Engineering Fracture Mechanics, 2017. http://dx.doi.org/10.1016/j.engfracmech.2017.02.001. Article in press [115].

Chapter 5

Modeling of damage and fracture of asphalt concrete

Contents

5.1 Introduction

Besides the complexities in failures under monotonic loading condition, fatigue is also one of the most common yet complicated failures that can cause damage to mechanical structures [116]. The fatigue loading (repeated moving loads, cycles of temperature, etc.) applied to structures made of geo-materials (concrete, asphalt concrete, masonry, etc.), generates efforts that are far below the strength or the fracture toughness of the material. However, they are responsible of the degradation of the material properties and fatigue crack growth, which may lead to the final failure state of these structures. The number of cycles, of a specified character that a specimen sustains before failure of a specified nature occurs, is defined as the fatigue life. Fatigue life is very important for the structure design, however, its prediction is still an empirical science rather than a theoretical one [50].

The fatigue behavior can be studied experimentally and numerically. The experimental study is commonly expensive and time consuming and sometimes impossible in the case of huge structures, while the numerical study is time and cost efficient and can effectively enable researchers to optimise the experimental effort required [116]. A review of the literature (see Section 2.4) suggests that the continuum damage models are able to effectively characterize the fatigue life of the specimen without large cracks, including the stages of crack nucleation and short crack propagation. Once a large crack appears, the existence of a stress singularity at the crack tip leads the stress based or strain based continuum damage model to a fast and unreal propagation of the damaged zone, a representation of the crack. The non-local continuum damage models [54, 58] intend to solve this problem, however, these models are not able to indicate the damage or the evolution of the damage during the fatigue loading [64]. Therefore, the residual strength cannot be determined using these models. Moës *et al.* proposed an alternative non-local damage model called Thick Level Set (TLS) [117–120] approach and implemented it in extended finite element code to model the damage growth in solids. The undamaged zone and the damaged zone are separated by a level set, and in the damaged zone, the damage variable is an explicit function of the level set. The damage growth is expressed as a level set propagation [117]. This model can be considered as a continuous transition from damage to fracture [120], which is able to handle initiation, growth, branching and coalescence of crack-like patterns. Latif *et al.* [121] developed an interface damage model based on the Thick Level Set approach, for simulating fatigue-driven delamination in composite laminates using finite element method. It provides a link between damage mechanics and fracture mechanics through the non-local evaluation of the energy release rate, which is able to predict the fatigue crack growth rate and the delamination growth pattern accurately. Thick Level Set approach was compared with cohesive zone models in [122], which are the crack based models that deal with crack evolution in elastic materials. The cohesive zone models represent quasi-brittle behaviors with good accuracy but require extra equations to determine the crack path. These models were widely used to predict the fatigue crack growth [123–125], and also improved to study the damage initiation and evolution in the interconnects [116, 126–128].

Both continuous and discrete numerical methods have their own advantages and shortcomings. The extended finite element method (XFEM) was developed in 1999 by Belytschko and Black [129] and improved by Moës *et al.* [130], to help alleviate shortcomings of the finite element method (FEM) and has been used to model the propagation of various discontinuities. XFEM has been successfully adopted for simulation of various engineering problems, which have been reviewed in detail in [131]. Discrete element method (DEM) is particularly attractive for modelling geo-materials due to its ability to construct a mesh that is not completely continuous and homogeneous. Since the mesh is constructed by rigid elements that interact with each other at points of contact, the DEM mesh has the capability of easily constructing a medium with voids, imperfections and heterogeneities, which are commonly existing in rocks, concretes, asphalt mixtures, and other geo-materials [73]. The XFEM and DEM were compared in [132] for the simulations of crack initiation, propagation and coalescence in brittle materials. It shows that DEM yields the better results compared to the XFEM, which is able to predict the crack propagation and coalescence in good agreement with the test results, while XFEM failed to model the shear cracks and is difficult to generate the crack coalescence [132].

In this chapter, a discrete element approach is proposed, based on a local description of damage and fracture. Bodin's damage model is implemented in a discrete element code and verifies the theoretical prediction and is compared to test results. In Section 5.3, the continuum damage model is coupled with a fatigue crack growth model. This feature allows crack initiation to be induced by localized damage and a progressive transition to a fracture behavior with the crack propagation. Furthermore, independent parameters for the damage and the crack propagation laws are admitted without any previous calibration. Intact and pre-cracked samples are analyzed under fatigue loading to show the consistent coexistence of fractured and damaged zones in a single model. Finally, the numerical results are compared to theoretical predictions of fracture mechanics and experimental results of the literature.

5.2 Discrete element fatigue damage model

Most of fatigue laboratory tests of high number of cycles consist of applying a sinusoidal displacement (or force) with constant amplitude at the boundary of the sample. During testing, the variation of global stiffness is monitored, which is defined as the ratio between the amplitudes of the force and the displacement. In order to numerically model these time-consuming laboratory tests, Bodin *et al.* [54, 55] proposed a non-local damage model to predict the material behavior. The model was implemented in a finite-element code, along with a self-adaptive jump-in-cycle procedure for high cycle fatigue computations.

In this section, a local version of Bodin's damage model is implemented in a discrete element code. A close-packed assembly (regular hexagonal packing) is adopted, due to the direct relationship between the macroscopic parameters (Young's modulus E and Poisson ratio ν) and discrete elastic parameters (normal and tangential stiffness, k_n and k_t, respectively). During damage modeling, the Young's modulus of the material decreases as the evolution of damage value D, which can be characterized by the decrease of local contact stiffness.

5.2.1 Model implementation

The damage of all the contacts in the assembly are calculated in the same way and updated at the same time. The evaluation of the damage per contact can be summarized by the following operations:

(1) DEM elastic analysis and identification of the stress and strain fields (see Section 2.5.3). The contact forces N and T and contact displacements δ_n and δ_t are the direct values can be obtained from a discrete element analysis, based on these information, the stress and strain of each contact pair in the close-packed assembly (see Figure 2.24) can be calculated as follows:

$$\begin{cases} \overline{\sigma}_n = \left(N_{ik}\sqrt{3} + T_{ik} + N_{jk}\sqrt{3} - T_{jk}\right)/(2dt), \\ \\ \overline{\sigma}_t = \left(-N_{ik} + T_{ik}\sqrt{3} + N_{jk} + T_{jk}\sqrt{3}\right)/(2dt). \end{cases} \tag{5.1}$$

$$\begin{cases} \overline{\varepsilon}_{nn} = \dfrac{1}{4}\left(\delta_{nik}\sqrt{3} + \delta_{njk}\sqrt{3} + \delta_{tik} - \delta_{tjk}\right)\dfrac{2}{\sqrt{3}d}, \\ \\ \overline{\varepsilon}_{tt} = \dfrac{1}{2}\left(\delta_{nik} + \delta_{njk} - \delta_{tik}\sqrt{3} + \delta_{tjk}\sqrt{3}\right)\dfrac{1}{d}, \end{cases} \tag{5.2}$$

(2) Evaluation of the principal stresses (Equation 2.56). The stress tensor $\overline{\sigma}_n$ and $\overline{\sigma}_t$ (in two dimensions) can be defined by the value of the principal stresses $\overline{\sigma}_I$ and $\overline{\sigma}_{II}$, and their orientation as follows:

$$\begin{cases} \overline{\sigma}_I = \overline{\sigma}_n + \overline{\sigma}_t \tan\psi, \\ \\ \overline{\sigma}_{II} = \overline{\sigma}_n - \overline{\sigma}_t / \tan\psi, \end{cases} \tag{5.3}$$

with $\psi = -1/2 \arctan(2\overline{\sigma}_t/A)$ and $A = [E/(1-\nu)](\overline{\varepsilon}_{nn} + \overline{\varepsilon}_{tt}) - 2\overline{\sigma}_n$.

(3) Calculation of the equivalent strain (Equation 2.44) for each contact pair. The evolution of damage is controlled by the strain state of the material by a scalar equivalent strain, which can be written for 2D structure as follows:

$$\tilde{\varepsilon} = \sqrt{\left[\frac{\langle \sigma_I \rangle_+}{E_0(1-D)}\right]^2 + \left[\frac{\langle \sigma_{II} \rangle_+}{E_0(1-D)}\right]^2}. \tag{5.4}$$

(4) Local equivalent strain of the contact: average the equivalent strains of the contact pairs to contact points. Since damage is associated with the single contact, the mean equivalent strain of the contact pairs around a certain contact (calculated during the previous operation) is adopted as the local equivalent strain for the contact. Only the existing contact pairs of the scheme shown in Figure 5.1 are considered in the averaging.

(5) Evaluation of the damage growth (Equations 2.45, 2.46 and 2.47). The damage growth rate is defined as a function of local equivalent strain rate $\dot{\tilde{\varepsilon}}$:

$$\dot{D} = f(D)\tilde{\varepsilon}^{\beta} \left\langle \dot{\tilde{\varepsilon}} \right\rangle, \tag{5.5}$$

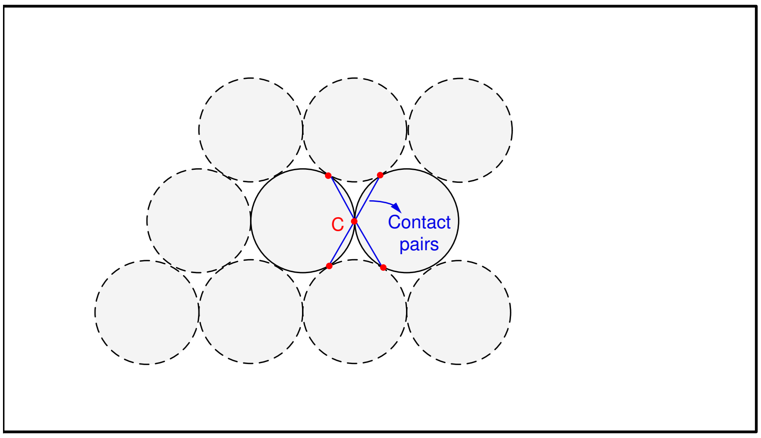

Figure 5.1: Contact pairs associated with the average of the equivalent strain of the contact C.

where $\dot{\tilde{\varepsilon}} = \tilde{\varepsilon}_{i+1} - \tilde{\varepsilon}_i$ is the increment of local equivalent strain from $t = i$ to $t = i + 1$; $f(D)$ is function of damage; β is a material parameter which can be calculated directly from the slope of the fatigue curve in log–log coordinates [64]. The damage functions $f(D)$ given by Paas [59] and Bodin [54] are:

$$Paas\ Law: \ f(D) = CD^{\alpha}, \tag{5.6}$$

$$Bodin\ L3R: \ f(D) = \frac{\alpha_2}{\alpha_1\alpha_3}\left(\frac{D}{\alpha_2}\right)^{1-\alpha_3} \exp\left(\frac{D}{\alpha_2}\right)^{\alpha_3}. \tag{5.7}$$

(6) Evaluation of the damage and update of the value of the Young's modulus ($E = E_0(1-D)$); and finally the update of the values of the normal and tangential stiffness (Equation 2.53):

$$\begin{cases} k_n = \dfrac{Et}{\sqrt{3}\,(1-\nu)}, \\ \\ k_t = \dfrac{1-3\nu}{1+\nu}k_n = \dfrac{1-3\nu}{\sqrt{3}\,(1-\nu^2)}Et. \end{cases} \tag{5.8}$$

5.2.2 Model verification

5.2.2.1 Damage of a plate under fatigue loading

Consider an un-cracked plate with dimensions $w = 80\,mm$ and $h = 117.8\,mm$ subjected to sinusoidal fatigue loading with amplitude $\varepsilon_0 = 1.25 \times 10^{-4}$ (Figure 5.2), the frequency of the loading $f = 25\,Hz$, the corresponding angular frequency $\omega = 2\pi f$. The material presents Young's modulus $E_0 = 30\,GPa$ and Poisson ratio $\nu = 1/3$. The damage function (Equation 5.6) proposed by Paas [59] is adopted in this analysis. The model parameters are $\alpha = -2.25$, $\beta = 4.0$ and $C = 5.0 \times 10^{16}$. The higher value of parameter C is adopted in order to ensure the fatigue life of applied loading condition is around 100 cycles ($E/E_0 = 0.5$ [133]), avoiding the jump in cycle procedure in this calculation.

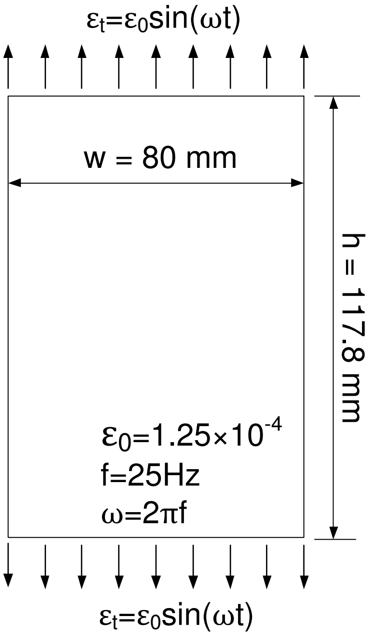

Figure 5.2: An un-cracked plate subjected to imposed sinusoidal strain.

The discrete element model is shown in Figure 5.3. The particle radius is $r = 1\,mm$, each row has 39 or 40 particles according to its position, and there are 69 rows in total. There are 2726 particles and 7961 contacts. For this discretization level, boundary effects are very reduced, therefore accurate stress and stain can be obtained in the whole geometry [74, 75]. According to Equation 5.8, the contact stiffness are calculated as $k_n = 5.2 \times 10^7\,N/m$ and $k_t = 5.2 \times 10^4\,N/m$. A time step $\Delta t = 5 \times 10^{-7}\,s$ and a low viscous damping $c_n = c_t = 0.0295\,Ns/m$ are

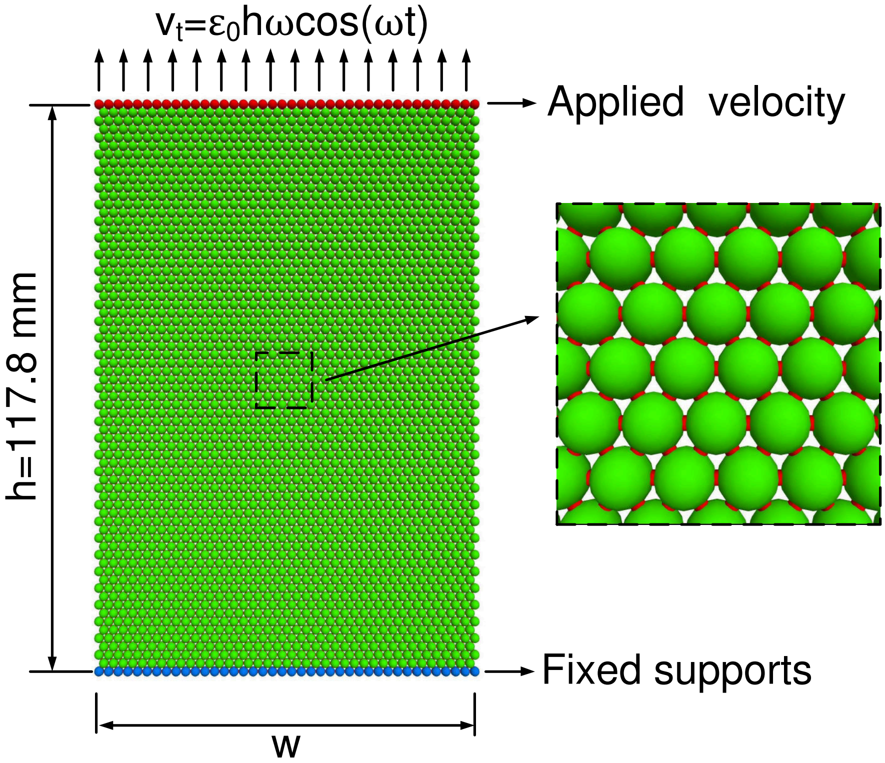

Figure 5.3: The discrete element model of an un-cracked plate subjected to imposed sinusoidal strain.

adopted in the simulations, to ensure stable calculations. The lower boundary is fixed at each particle center in vertical direction, and the sinusoidal velocity $v = \varepsilon_0 h\omega \cos(\omega t)$ is applied at the upper boundary. In order to apply the strain rate $\varepsilon_0 = 1.25 \times 10^{-4}$ during all cycles, the amplitude of the displacement of the upper boundary is constant and equal to $14.7\,mm$.

The numerical results are compared with damage model (Paas law) predictions, as shown in Figures 5.4 and 5.5. For an imposed strain condition, the global damamge increse and stiffness decrease are calculated from the decrease of the reaction force of the fixed support, which are in good agreement with the theoretical Paas law (Equation 5.6) prediction. No effects of the particle diameter are observed under homogenous conditions. According to the European fatigue standards [133], when the stiffness ratio reaches its critical value 0.5, the corresponding fatigue life $N_f = 105\,Cycles$ is identified.

The calculation speed of the discrete element modelling depends on the discretization level and computing power. This calculation was performed on an Intel Core i7-6700K 4.0 GHz with 4 cores and 8 threads running on a Windows 8.1 64 bit operation system. The calculation required around 48 hours, using parallel calculation with all 8 CPU threads, to run 350 fatigue loading cycles when the particle diameter is $d = 2\,mm$ (without jump in cycles procedure). More than 72 hours and around 12 hours were needed respectively, for $d = 1\,mm$ and $d = 4\,mm$. Hence, it is necessary to enhance the efficiency of the discrete element fatigue modelling, in order to perform large number of cycles with an appropriate discretization level.

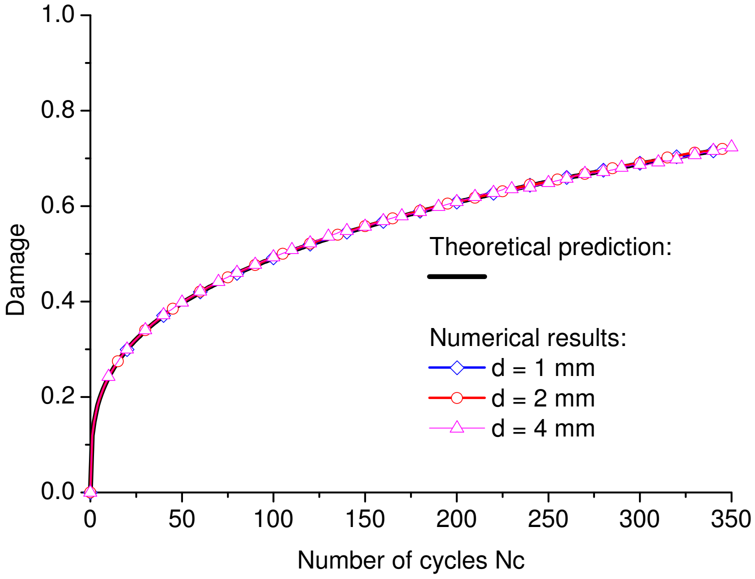

Figure 5.4: The theoretical and numerical predictions of the increase of damage for an un-cracked plate subjected to fatigue loading.

5.2.2.2 Damage of a four point bending beam under fatigue loading

In this section, the DEM damage calculations of four point bending beams made of asphalt concrete are performed. The predictions are compared with the test results and finite element results. A total of 36 fully reverse 4PB fatigue tests were performed by Arsenie *et al.* [57, 64, 65], with displacement control (constant strain), at 10°C with $f = 25\,Hz$. Among the 36 specimens, there were 18 non-reinforced specimens and 18 fiber glass grid reinforced specimens. The non-reinforced specimens, which are studied in this section, were loaded under three strain levels ($\varepsilon_0 = 150\,\mu m/m$, $\varepsilon_0 = 135\,\mu m/m$ and the range

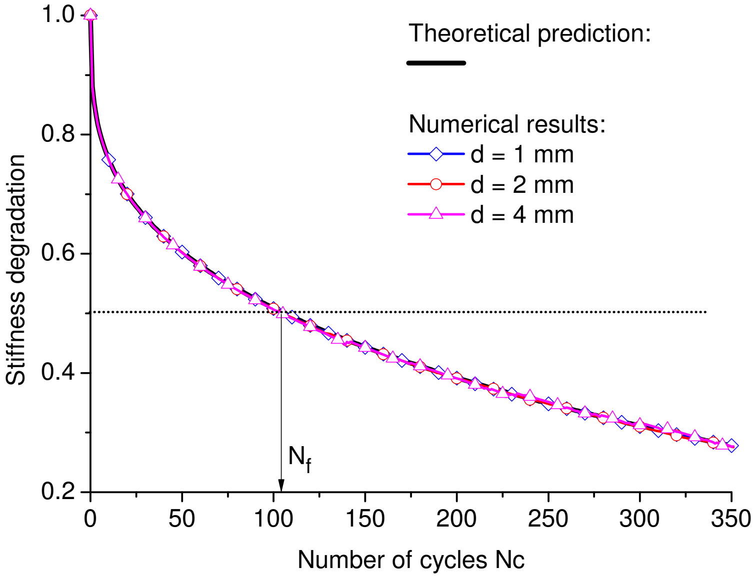

Figure 5.5: The theoretical and numerical predictions of the decrease of global stiffness for an un-cracked plate subjected to fatigue loading.

$\varepsilon_0 = (111, 116)\,\mu m/m)$ with six replicates per strain level. The geometry and boundary conditions are shown in Figure 5.6a. The span, height and thickness of the beam were $600\,mm$, $100\,mm$, $100\,mm$ receptively. The initial dynamic modulus $E_0 = 13.5\,GPa$ was obtained at $10°C$ and $25\,Hz$.

In Figure 5.6b, the half discrete element model is adopted due to the symmetry of the beam and applied loading. The particle radius is $r = 1.25\,mm$, each column has 39 or 40 particles according to its position, and there are 139 columns in total. In the model, there are 5491 particles and 16116 contacts. According to Equation 5.8, the contact stiffness are calculated as $k_n = 2.6 \times 10^7\,N/m$ and $k_t = 2.6 \times 10^3\,N/m$. A viscous damping $c_n = c_t = 0.065\,Ns/m$ and a time step $\Delta t = 5 \times 10^{-7}\,s$ are adopted in the simulations. The left boundary of the half structure is fixed at each particle center in horizontal direction, while the right boundary is fixed in vertical direction. The maximum applied displacement at $S/3$ of the beam $Z_0 = 2/3\varepsilon_0$, where ε_0 is the applied strain rate measured at the bottom of mid-span, which are $\varepsilon_0 = 150\,\mu m/m$, $\varepsilon_0 = 135\,\mu m/m$ and $\varepsilon_0 = 115\,\mu m/m$ [57] in the numerical calculations. The corresponding maximum applied displacements at $S/3$ are $Z_0 = 100.0\,\mu m$, $Z_0 = 90.0\,\mu m$ and $Z_0 = 76.7\,\mu m$, respectively. The loading is only applied on a certain range $(h/4)$ of the particles at $S/3$ of the beam, as shown in Figure 5.6b. This differs from Bodin's calculation [54], who applied loading on the full length between the two loading points in a non-local finite element model. This loading condition is used here to avoid the possible damage concentrations appeared near the loading points in a local discrete element model.

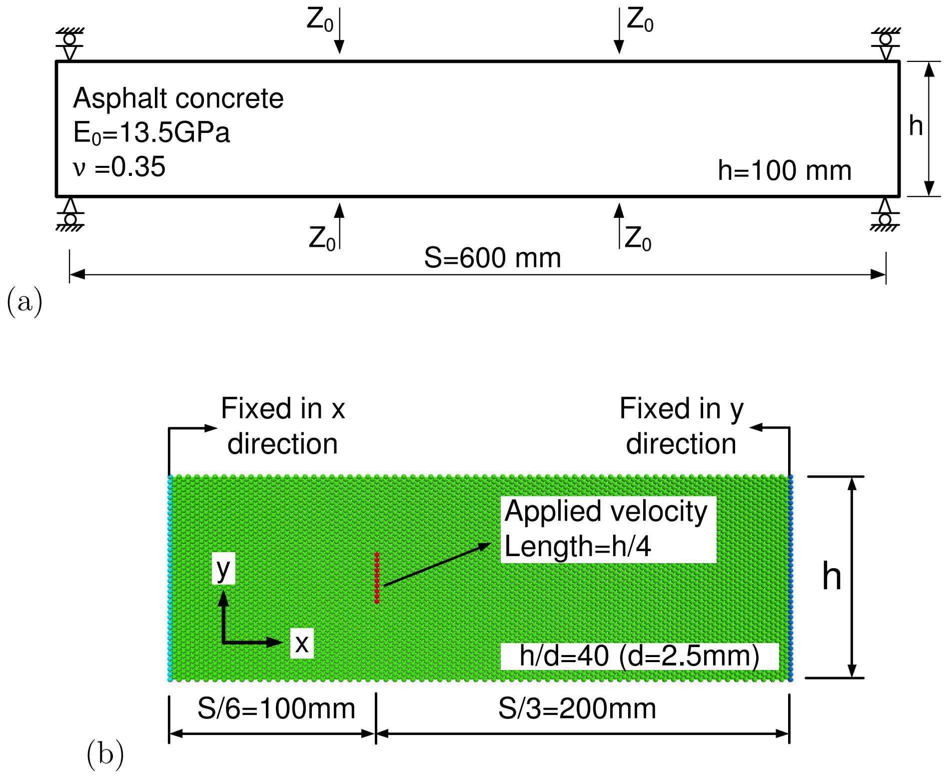

Figure 5.6: (a) Four point bending beam subjected to imposed sinusoidal displacement and (b) the half structure of discrete element model.

Like Arsenie *et al.* [57,64,65], the damage evolution law (Equations 5.5 and 5.7) proposed by Bodin is adopted in the four point bending simulations. The model parameters are $\alpha_1 = 8.0 \times 10^{-16}$, $\alpha_2 = 1.9$ $\alpha_3 = 1.6$ and $\beta = 4.3$. β value is calculated directly from the slope of the fatigue curve in log–log coordinates [64], while α_1, α_2 and α_3 are obtained by the best fit. The jump in cycles procedure, which has been introduced in Section 2.4.2.3, is implemented in the code in order of simulate the large number of cycles.

The discrete element results are compared with the experimental results and finite element predictions given by Arsenie *et al.*, which are plotted in Figures 5.7, 5.8 and 5.9 for three strain levels $\varepsilon_0 = 150\,\mu m/m$, $\varepsilon_0 = 135\,\mu m/m$ and $\varepsilon_0 = 115\,\mu m/m$, respectively. It is not surprising that the local continuum damage model provides a fast drop of the global stiffness due to the stress concentration induced by the reduction of the effective cross section. The non-local finite element parameters, defined in the original version of the Bodin's model [54] are $\alpha_1 = 1.6 \times 10^{-16}$, $\alpha_2 = 0.95$, $\alpha_3 = 1.6$, $\beta = 4.3$, and the internal length of the non-local continuum $l_c = 30\,mm$ is chosen to calculate the average equivalent strain. α_1, α_2 and α_3 values were calibrated for $\varepsilon = 135\,\mu m/m$ based on the experiments performed by Arsenie [57, 64]. Before the global stiffness is below 0.85 of its initial value, the discrete element results coincide with the finite element predictions for all of the three strain levels. In Figure 5.7, it shows that the numerical results are close to the average test result for $\varepsilon = 150\,\mu m/m$. However, it should be pointed out that for $\varepsilon = 115\,\mu m/m$, the discrete element and finite element predictions all deviate from the test results. Although the non-local finite element model can provide a fatigue life close to the test results, the evolution of the global stiffness matches neither of the test curves. This may indicate that the model needs to be further improved.

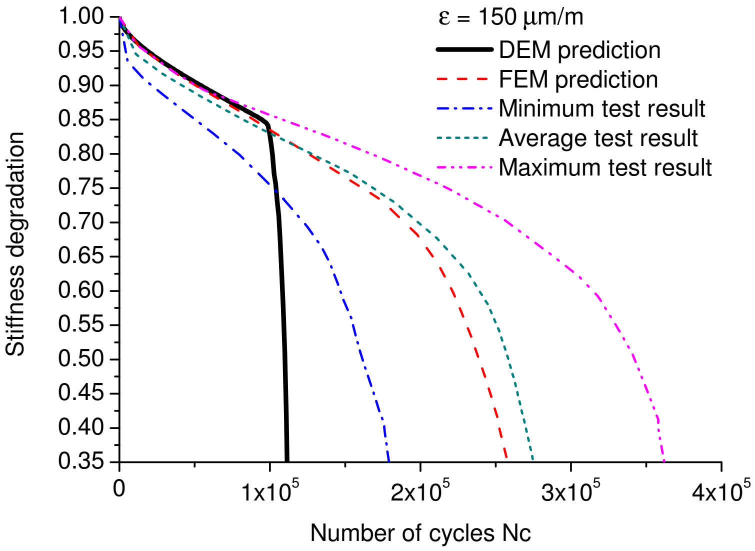

Figure 5.7: Numerical fatigue curves of the non-reinforced four point bending beam versus experimental fatigue damage curves (minimum, average and maximum) under applied strain $\varepsilon = 150\,\mu m/m$.

The effect of discretization level on the numerical fatigue curves of the non-reinforced four point bending beam under applied strain $\varepsilon = 150\,\mu m/m$ is illustrated in Figure 5.10. For similar fatigue parameters, the decrease of the particle diameter d induces a shorter fatigue life of the sample. It can be explained by the fact that, in DEM, the efforts are averaged over a particle diameter; under stress gradients, it means higher stresses for smaller particles. Consequently, a higher value of stress leads to more damage per cycle, which accelerates the degradation

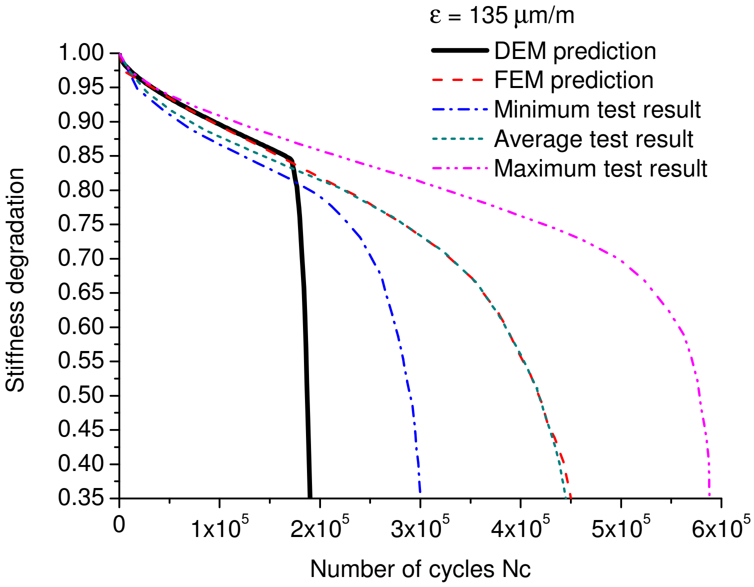

Figure 5.8: Numerical fatigue curves of the non-reinforced four point bending beam versus experimental fatigue damage curves (minimum, average and maximum) under applied strain $\varepsilon = 135\,\mu m/m$.

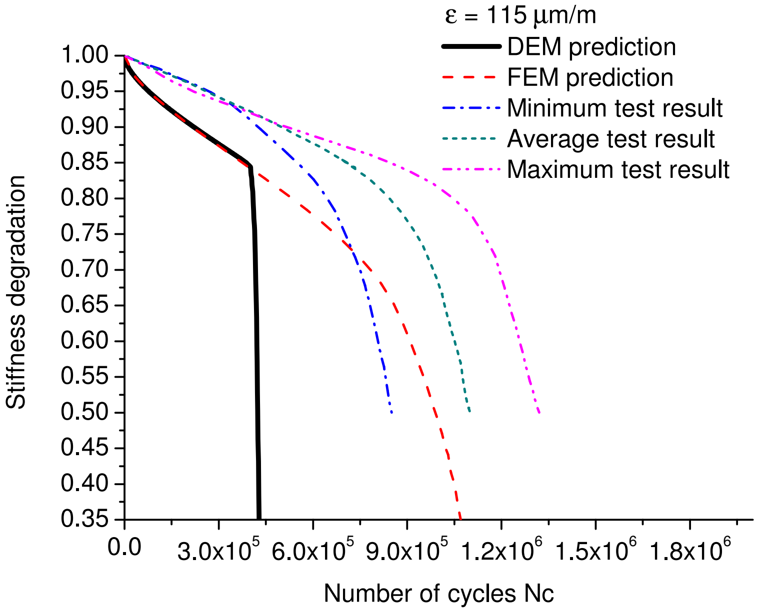

Figure 5.9: Numerical fatigue curves of the non-reinforced four point bending beam versus experimental fatigue damage curves (minimum, average and maximum) under applied strain $\varepsilon = 115\,\mu m/m$.

of the stiffness of the sample.

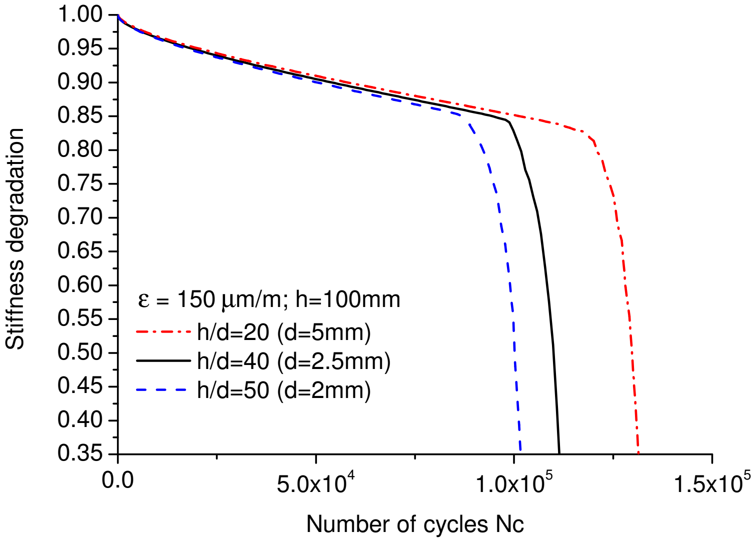

Figure 5.10: Effect of discretization level on the numerical fatigue curves of the non-reinforced four point bending beam under applied strain $\varepsilon = 150\,\mu m/m$.

In contrast to the non-local finite element modelling, the failure pattern of the local discrete element model seems more realistic, suggesting the effect of a clear middle crack, observed during the calculation, as shown in Figure 5.11. While for non-local finite element model, as the number of cycles increases, two large zones where damage $D = 1$ appear instead of a crack (see Figure 2.20).

5.3 Coupled DEM model for damage and fatigue crack growth

In view of the crack initiation and propagation, the failure modes of geo-materials subjected to fatigue loading can be described by four stages, including crack nucleation (Stage I), short crack growth (Stage II), large crack growth (Stage III), and ultimate failure (Stage IV)(see Figure 5.12). In the beginning of the lifetime, the material presents only inner defects (micro cracks, voids, etc.). Due to the effect of the cyclic loading, these small defects tend to grow in size and quantity which damage the material, reducing its stiffness. When the inner defects become short cracks, the failure process turns into its second stage of short crack growth. With a relatively high number of cycles, these growing short cracks become large

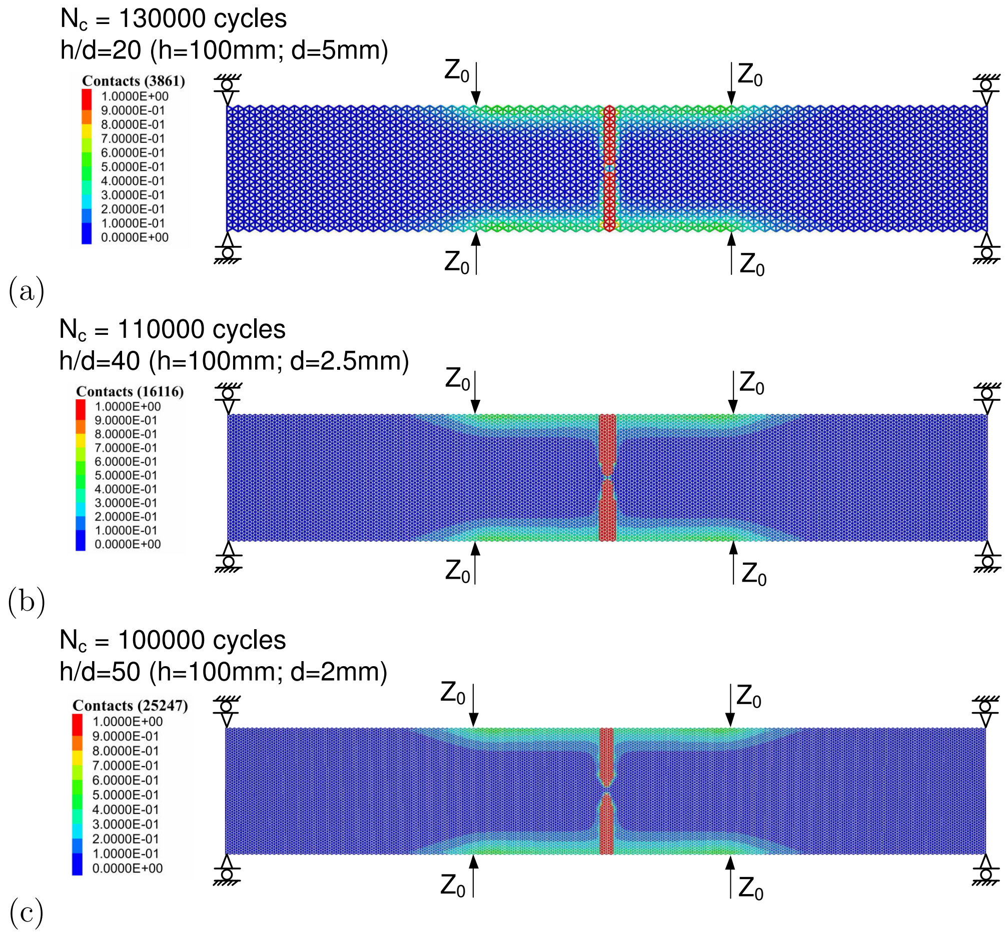

Figure 5.11: Damage distribution of a non-reinforced four point bending beam under applied strain $\varepsilon = 150\,\mu m/m$ for particle diameter (a) $d = 5\,mm$, (b) $d = 2.5\,mm$ and (c) $d = 2\,mm$.

cracks, which characterize the fracture behavior.

In Section 5.2.2.2, the crack nucleation stage and most of the short crack growth stage were shown to be well described by the continuum damage model. However, as the crack length increases, the decrease in the global stiffness becomes dominated by crack propagation. At this point, the continuum damage model failed, resulting in fast propagation due to the stress singularity at the crack tip. Hence, it is necessary to adopt a fatigue crack growth model (e.g. Paris' law) to better estimate the fracture behavior during the end of stage II, as well as stages III and IV.

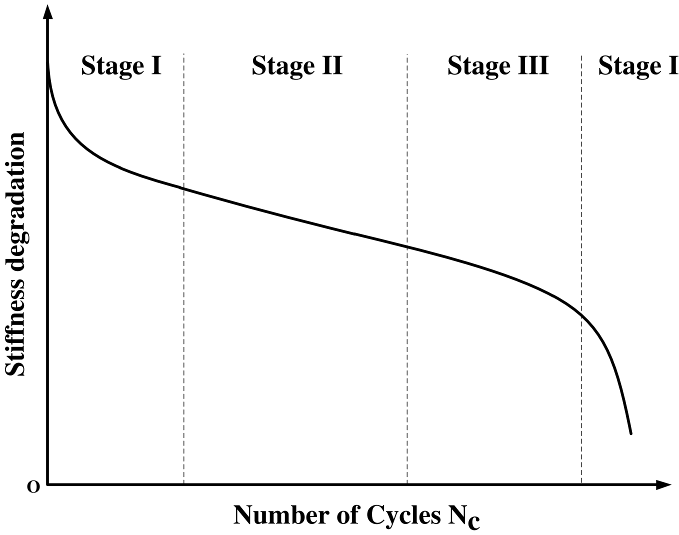

Figure 5.12: The four stages of the fatigue failure process.

5.3.1 Model implementation

Damage models (see Section 2.4.2) describe the effect of distributed (micro) defects over a certain region. The rupture is caused by the coalescence of these defects, giving rise to cracks which subsequently propagate. This phenomenon is not well described by standard fatigue models, which suffer from discretization effects due to the stress gradients.

In the present work, a damage approach (see Section 2.4.2) is adopted to describe the behavior before contact rupture. The rupture of a contact resulting in crack propagation is limited by a crack growth criterion (see Section 2.4.3).

5.3.1.1 Local identification of the position of crack tips

The propagation of a crack can be analyzed as the creation or extension of the boundaries of a given geometry. In fracture mechanics, this transformation is usually controlled by the energy release during the process. Despite the different existing criteria of crack propagation, roughly a crack may be created or propagated where the stress (and/or strain) are maximized (see Figure 5.13).

In an elastic system, a simple verification of the local maximum value of the principal stress may be enough to identify potential localization of crack tips.

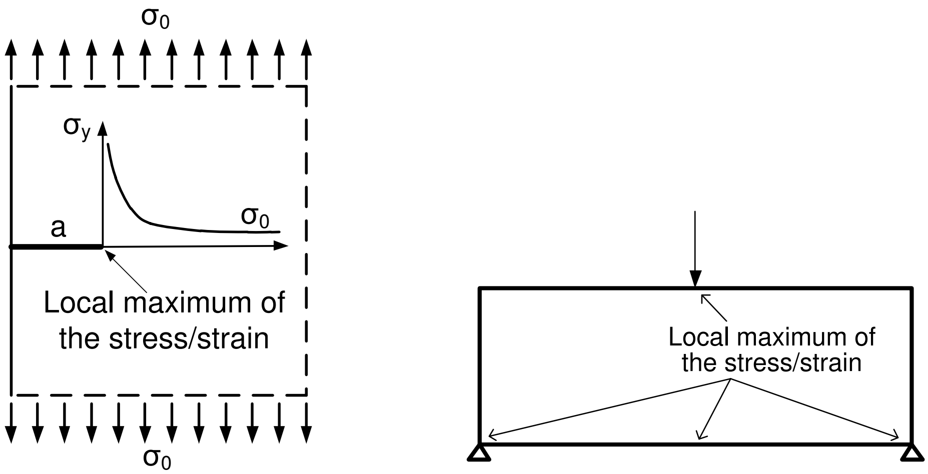

(a) (b)

Figure 5.13: Localization of the local maxima of the stress/strain for (a) a cracked plate and (b) a simply supported beam.

However, during fatigue, the value of the stress tends to decrease due to the degradation of elastic properties of the material where the stress is concentrated. A better indicator, in this case, is shown to be the damage increment per cycle dD/dN_c, which depends on the stress value but also on damage itself, and can be calculated numerically (see Section 2.4.2.2). Figure 5.14 shows an example of damage increment per cycle obtained from DEM simulation for a center cracked plate subjected to sinusoidal fatigue loading. The maximum dD/dN_c in Figure 5.14 is located at the crack tip.

In the present model, the possibility of crack propagation will be only considered on contacts which locally maximizes the damage increment per cycle, as shown in Figure 5.14. For these two contacts at the crack tip, when the damage reaches $D = 1$, indicating the total degradation of the stiffness, the energy release rate is calculated as shown in Section 5.3.1.2.

5.3.1.2 Evaluation of the range of the energy release rate ΔG

A damage value $D = 1$ indicates the possibility of crack propagation, if it happens at a crack tip (as described in Section 5.3.1.1, or indicates an overestimated damage value. This is usually the case at the neighborhood of crack tips, for example, where the damage grows until unrealistic values due to the stress concentration.

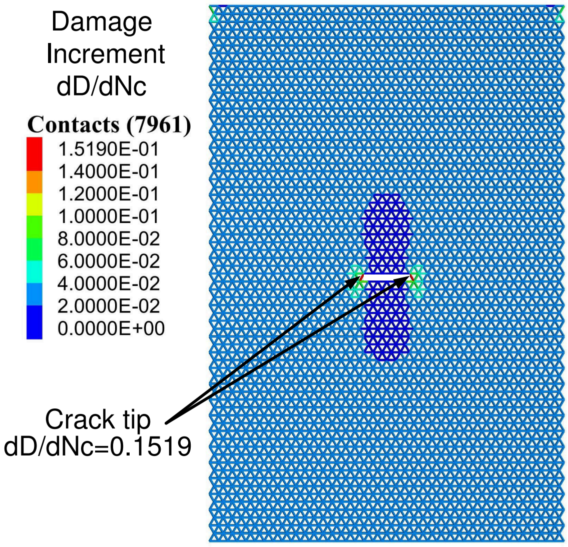

Figure 5.14: Damage increment per cycle of a center cracked plate.

In crack growth models, the energy release is considered to be localized exclusively at the crack tip. An over damaged zone near a crack tip, leads automatically to inconsistent evaluations of the energy release rates at the crack tip. In order to avoid these disturb due to un-physical damage values, if damage reaches $D = 1$ in a contact not identified as a crack tip, the value of D is automatically set to zero until this point eventually becomes a crack tip. Mathematically, this point is treated as an intact point, considering that it recovers its initial elastic properties. Physically, it indicates a scale decrease on the rupture process due to the proximity with a crack (see Section 2.3.4.3). As suggested in Figure 5.15a, damage is defined as the effect of certain number of defects inside a certain zone; however, in a smaller scale, there is only intact material. In Figure 5.15b, the damage value reaches $D = 1$ in contact C_1, a crack tip. The energy release rate is evaluated and a potential crack extension is identified.

The principal components of the contact forces N and T, and contact displacements δ_n and δ_t, can be written as Equations 5.9 and 5.10. For a certain contact, when it is the first contact (defined clockwise) in a pair of contacts (see Figure 5.16a), the principal components can be obtained by Equation 5.9, and when it is the second contact in a pair (see Figure 5.16b), Equation 5.10 should be used to calculate the principal components.

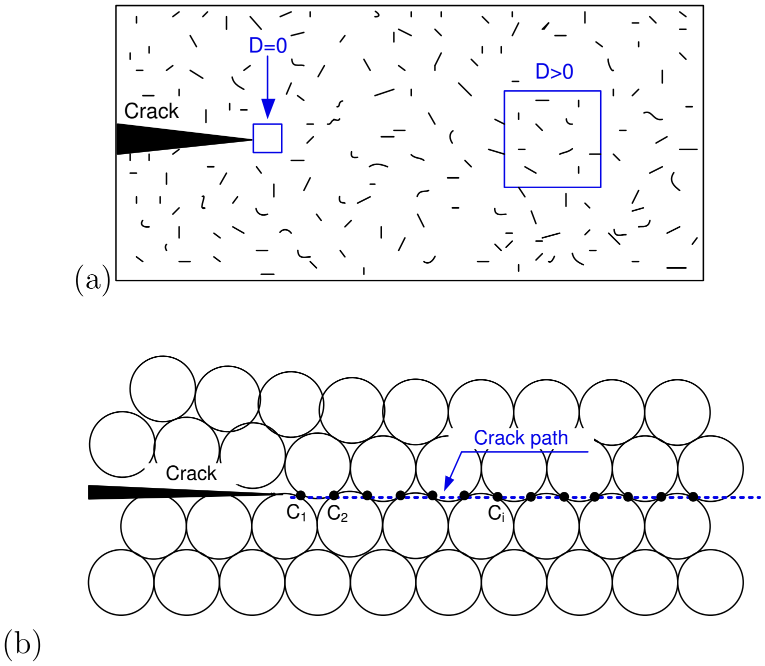

Figure 5.15: (a) Scale effect on the damage value and (b) contact points in the potential crack path.

$$\begin{cases} F_I = N\sin\left(\pi/3+\psi\right) - T\cos\left(\pi/3+\psi\right) \\ \delta_I = \delta_n\sin\left(\pi/3+\psi\right) - \delta_t\cos\left(\pi/3+\psi\right), \end{cases} \tag{5.9}$$

$$\begin{cases} F_I = N\sin\left(\pi/3-\psi\right) + T\cos\left(\pi/3-\psi\right) \\ \delta_I = \delta_n\sin\left(\pi/3-\psi\right) + \delta_t\cos\left(\pi/3-\psi\right), \end{cases} \tag{5.10}$$

where ψ is defined as the angle between $(n;\, t)$ and the coordinate system associated to the principal stresses (Figure 2.24c). During a fatigue test, F_I and δ_I oscillates between a minimum and a maximum level, which depends on the shape of the cyclic loading. For a sinusoidal loading centered at zero stress, the positive values of F_I and δ_I naturally vary from 0 to $\max F_I$ and $\max\delta_I$, respectively. In this case, the damage of a contact induces a maximum energy release rate [10] G_{max}. The minimal energy release rate G_{min} is equal to zero; consequently, the variation of the energy release rate is simply defined as

$$\Delta G = \frac{\sum_1^{N_{cD}} g_i}{d^2\cos\psi/2}, \tag{5.11}$$

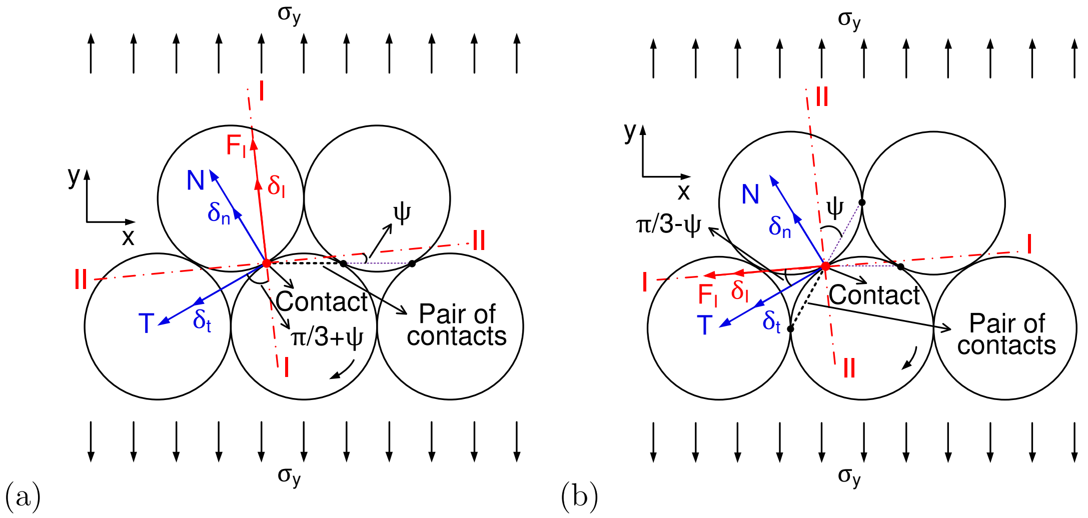

Figure 5.16: Principal components of force and displacement for a certain contact being (a) the first contact (defined clockwise) in a pair and (b) the second contact in a pair.

where N_{cD} is the number of cycles to reach $D = 1$ (total release of the contact energy), g_i is the surface of the triangle formed by the points $(0, 0)$, $(\max \delta_{I(i-1)}, \max F_{I(i-1)})$ and $(\max \delta_{I(i)}, \max F_{I(i)})$ as shown in Figures 5.17.

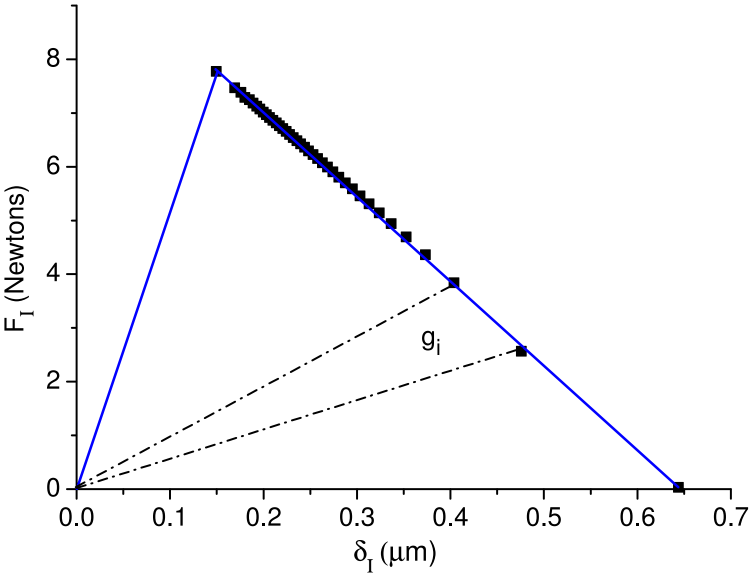

Figure 5.17: Evaluation of the energy release at the crack tip (contact C_1) during a fatigue test.

The second contact C_2 is not identified as a crack tip. The degradation of the elastic properties of the contact C_1 induces an increase of the contact force in C_2, in spite of the own damage of this contact as shown in Figure 5.15. After contact C_1 is totally released, in the case of a crack propagation, contact C_2 becomes the new crack tip. The value of the damage of C_2 is set back to zero $D = 0$ and the value of the number of cycles N_{cD} starts to be incremented. Once $D = 1$ for contact C_2, the surface of the full triangle can then be computed, which is substituted into Equation 5.11 to estimate the range of energy release rate. Following the same principle, the range of the energy release rate can be obtained systematically at the crack tip during crack propagation (discussed in Section 5.3.1.3).

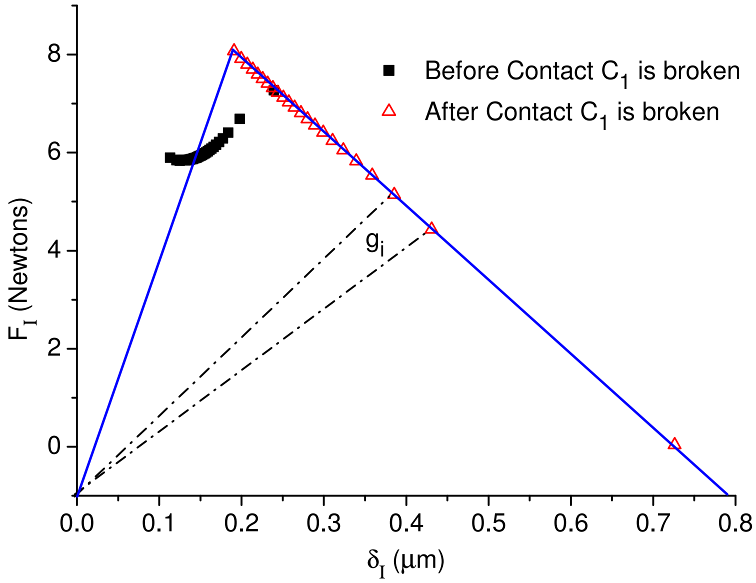

Figure 5.18: Evaluation of the energy release at the second contact close to the crack tip during a fatigue test.

Based on the relation between the energy release rate and the stress intensity factor in plane stress [10], the stress intensity range is simply defined as $\Delta K = E\sqrt{\Delta G}$.

5.3.1.3 Crack initiation and propagation

The evolution of the damage variable D characterizes the weakening of a contact before rupture. The rupture, associated with the propagation of a crack is defined by the value of da/dN_c (Equation 2.52):

$$\frac{da}{dN_c} = c\Delta K^m. \tag{5.12}$$

A contact which presents $D = 1$, is definitely broken (and ceases to exist) only if

$$\frac{da}{dN_c} N_c \geq \frac{d\cos\psi}{2}, \tag{5.13}$$

which represents a crack growth da equals to $d\cos\psi/2$ for one contact break. Otherwise, D is set to 0, and the fatigue loading continues, until the number of cycles N_c increases sufficiently to fulfill the rupture condition. This rupture criterion prevent deviations from the crack growth criterion induced by the damage model (Section 2.4.2) in conditions of a stress singularity at the crack tip.

5.3.2 Numerical modeling results for a center cracked plate

5.3.2.1 Geometry, loading and material properties

A center cracked plate with dimensions $w = 80\,mm$ and $L = 120\,mm$ (as indicated in Figure 5.19) is tested under sinusoidal fatigue loading with an amplitude $\sigma_0 = 1.25\,MPa$ and frequency $f = 25\,Hz$. The material presents Young's modulus $E_0 = 30\,GPa$ and Poisson ratio $\nu = 1/3$. A viscous damping $c_n = c_t = 0.0295\,Ns/m$ and a time step $\Delta t = 5 \times 10^{-7}\,s$ are adopted in the simulations. The damage model parameters are $\alpha = -2.25$, $\beta = 4.0$ and $\gamma = 5.0 \times 10^{16}$; the fatigue crack growth model parameters are $c = 3.0 \times 10^{-10}\,m/cycle[(Pa\sqrt{m})^m]$ and $m = 1.03$. Negligible effects of the frequency indicate very low dynamic effects (quasi-static regime) on the presented results.

5.3.2.2 Evaluation of the stress intensity range ΔK

In Figure 5.20, the numerical evaluation of the stress intensity range ΔK is compared to the theoretical result for different particle diameters d. Deviations are observed only for very large cracks ($2a > 50\,mm$) and tend to decrease for smaller values of d, which indicates a convergence of the data.

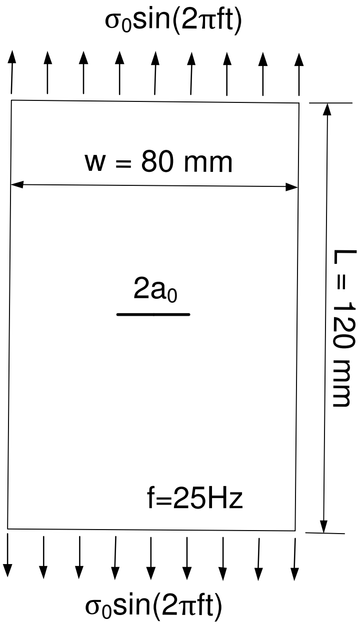

Figure 5.19: Center cracked plate subjected to imposed sinusoidal stress.

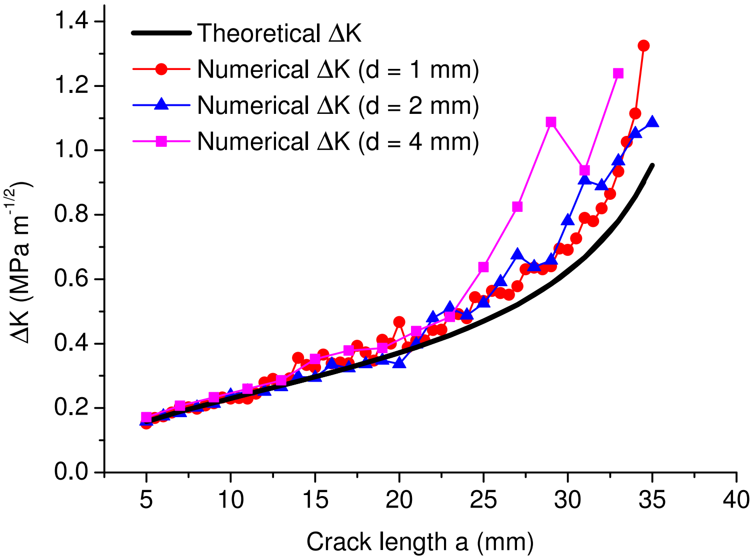

Figure 5.20: Comparison of the range of stress intensity factor ΔK calculated using numerical and theoretical methods for different crack lengths a ($a_0 = 5\,mm$) and particle diameters d.

5.3.2.3 Stiffness degradation

The amplitude of the displacements at the edges of the sample tends to increase during a fatigue test with constant amplitude of the imposed stress. This behavior is due to the damage of the material and the propagation of the crack which decrease the stiffness of the sample. The stiffness degradation can be quantified by the ratio between the initial amplitude of the displacements and its instantaneous value at a time during the test (which is a function of the number of cycle N_c). In Figure 5.21 the degradation of the fatigue stiffness obtained for plates with different initial crack sizes a_0 is compared to theoretical predictions. For the uncracked plate, the numerical solution accurately follows the theoretical damage prediction. When the plate present a long crack, e.g. $a_0 = 10\,mm$, the numerical results behave according to prediction of Paris' law. However, a smaller crack ($a_0 = 2\,mm$) deviates from Paris' law because of the additional contribution of the material damage on the stiffness degradation.

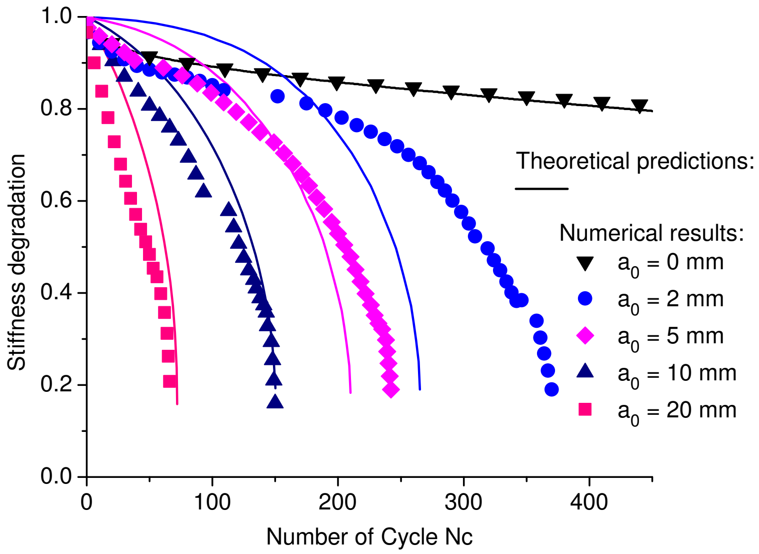

Figure 5.21: Stiffness degradation as a function of number of cycles N_c for different initial crack sizes.

5.3.2.4 Damage field

Figure 5.22 illustrates the damage distribution of a pre-cracked plate with an initial crack length $a_0 = 5\,mm$ after 166 fatigue loading cycles. The red values correspond to $D = 1$, and indicates the propagation of the crack. The deep blue correspond to very low values of damage, which happens near the initial crack surface, where the stresses (and strains) are low during the whole test. Far from the crack, the damage value tends to be homogeneous, excepting two points on the top of the sample, due to boundary effects. The damage tends naturally to be higher near the crack path, induced by the increase of the stresses (and strains). However, very close to crack tip, an undamaged zone ($D = 0$) is observed. The value itself should not be considered as damage quantity, but it indicates where the damage model fails to describe the material behavior, leading to unrealistic fast rupture. It can be associated to a fracture process zone (FPZ) [78,79], acting as a bridging zone between cracked region and un-cracked region.

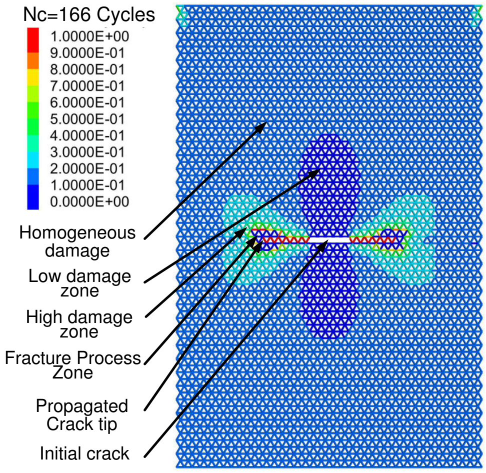

Figure 5.22: Damage distribution and crack propagation of a pre-cracked plate with initial crack length $a_0 = 5\,mm$ after 166 fatigue loading cycles.

The increase of the number of cycles, causes the evolution of the high damage zone due to the extension of the fatigue crack, as shown in Figure 5.23. The size of the fracture process zone seems to depend on the crack size.

The reduction of the global stiffness of the structure (Figure 5.21) is indeed controlled by the propagation of the crack associated to the damage of the un-cracked zone as shown in Figures 5.22 and 5.23.

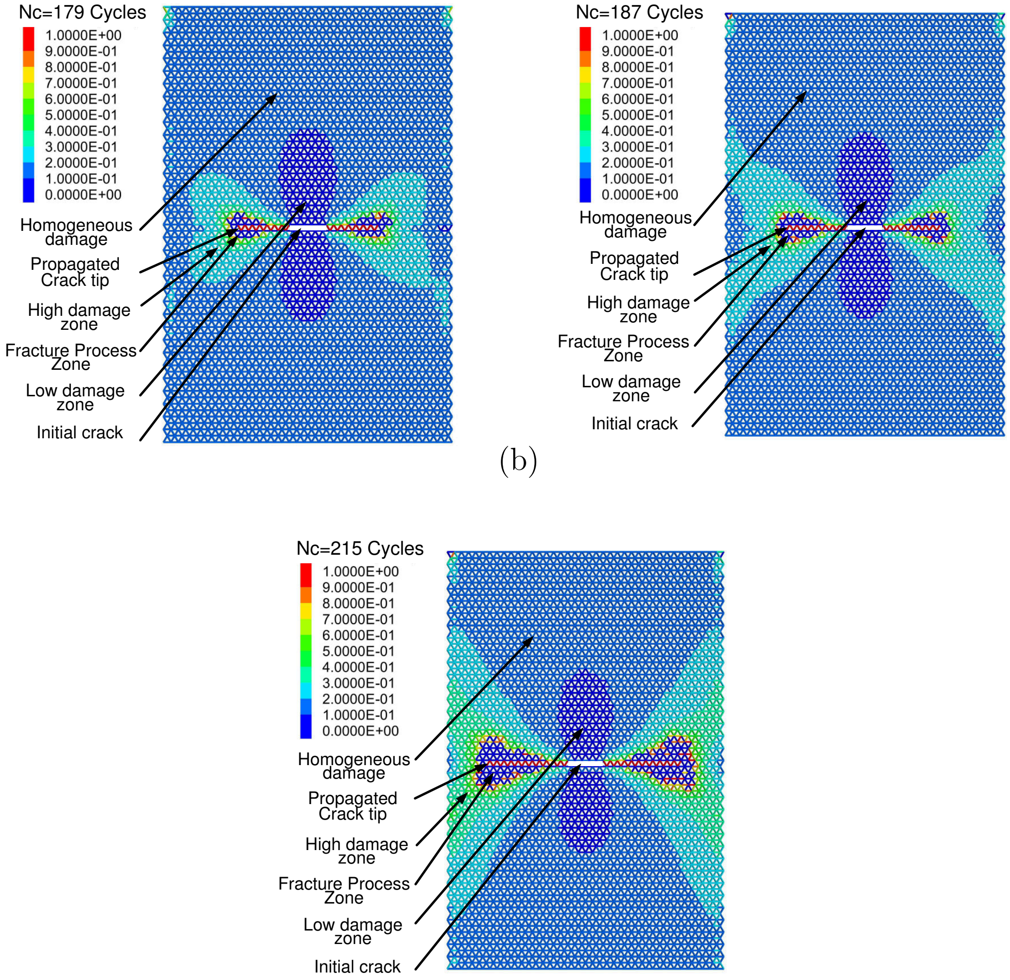

(a) (b)

(c)

Figure 5.23: Damage distribution and crack propagation of a pre-cracked plate with initial crack length $a_0 = 5\,mm$ after (a) 179, (b) 187 and (c) 215 fatigue loading cycles.

5.4 Conclusions of the chapter

Continuum damage model was implemented in the discrete element code and compared to the theoretical prediction showing good agreement under homogeneous stress conditions. A comparison of non-local and local approaches applied in four point bending test indicates the limits of each case. Non-local approaches may produce reasonable sample behavior, based on unrealistic material behavior. On the other hand, a pure local approach presents reasonable rupture patterns, but it is affected by mesh effects.

In order to reduce this limitation, a simple numerical scheme coupling damage and fracture mechanics in a discrete element environment was proposed. The association of these different mechanical formulations allows the reproduction of experimental evidences: before material rupture by damage models; during crack propagation by crack growth models. In parallel, important drawbacks of each approach are avoided, such as discretization effects, as shown by the convergent behavior of the results; and the nonphysical results of crack growth models for very short or simply no cracks.

The following paper summarizes the main results of this chapter:
X. Gao, G. Koval, and C. Chazallon. A discrete element model for damage and fracture of geomaterials under fatigue loading. Accepted by 8th International Conference on Micromechanics of Granular Media [134].

CHAPTER 6

Application to fiber glass reinforced asphalt concrete

Contents

6.1 Introduction

Fiber glass grids have been used as reinforcement materials in different pavement structures subjected to fatigue cracking since the late 1960s [57]. They are generally used for the rehabilitation of cracked pavements, such as semi-rigid, asphalt, and flexible pavements. Nowadays, they are also applied in new pavements as a result of the impressive pavement performance observed in the reinforced old pavements. The reinforcement can delay fatigue crack propagation in newly built pavements. For the reinforced old pavements, fiber glass grids are normally applied between the old pavement and new asphalt concrete overlay, which can prevent the crack propagation from the old pavement and improve the overall fatigue resistance [57, 64, 65]. However, the mechanism for the improved performance of pavements with fiber glass reinforcements is not well understood. Hence, it is necessary to quantify the benefits of fiber glass reinforcement, for the purpose of improving the structural design of pavements.

In this Chapter, the effect of fiber grid reinforcement on crack initiation and propagation of pavements is studied. The three dimensional (3D) fiber glass grid reinforced structures are simplified as two dimensional (2D) models. The crack positions in different asphalt concrete layers are considered, which represent either a new pavement or a reinforced old pavement. The effect of fiber quantity on the nominal strength of the reinforced material is then analyzed based on the failure model proposed in this study.

6.2 Effect of fiber glass grid reinforcement on crack initiation

In this section, the failure model presented in Chapter 3 is used to study the effect of fiber grid reinforcement on crack initiation and propagation in asphalt concrete. In a real reinforced structure, the fiber glass grid is implemented between the asphalt concrete layers, as shown in Figure 6.1a. In this study, an equivalent 2D model is adopted, in which the grid is treated as a continuous wire (see Figure 6.1b).

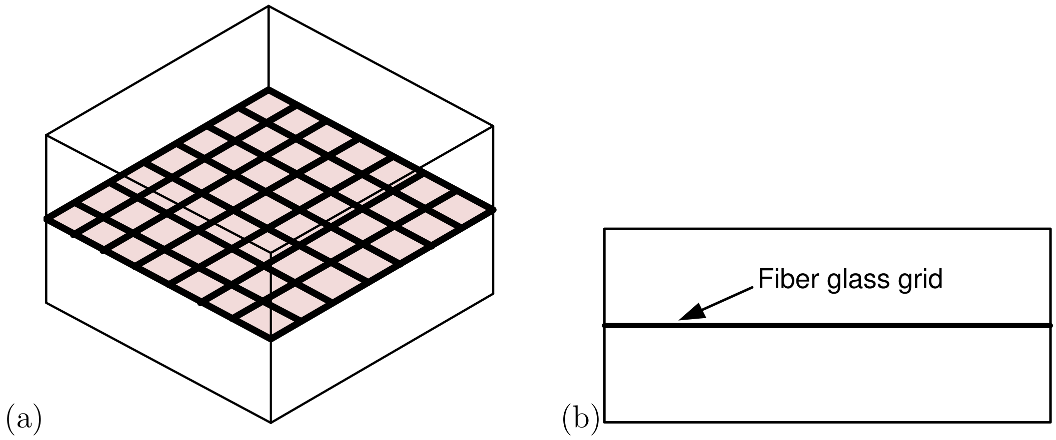

Figure 6.1: Schematic diagrams showing (a) the fiber reinforced structure and (b) its equivalent 2D model.

In a 2D model, the propagation of the crack across the fiber grid is not trivial, hence, two cases of problems are considered. The first are two new asphalt layers, shown in Figure 6.2a, which presents a crack that initiates from the bottom of the second asphalt concrete layer. The second is the reinforcement of an old pavement (second layer) by a new layer, shown in Figure 6.2b. In this case, a crack from the old layer crosses the fiber grid and affects the new layer.

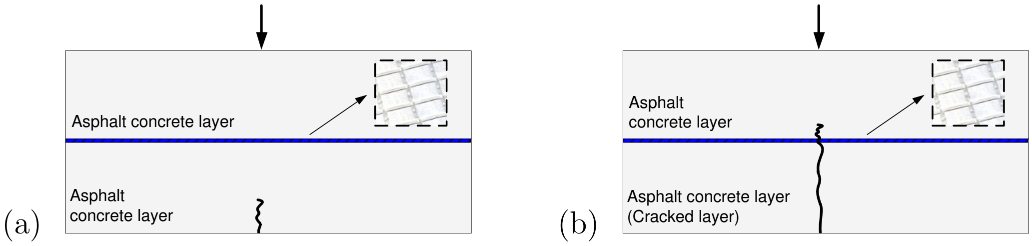

Figure 6.2: Crack initiates from the bottom of (a) the second layer and (b) the first layer.

In order to quantify the effect of fiber grid on the crack initiations from the bottom of the two asphalt concrete layers, case 1 and case 2 are further simplified as the reinforced plates subjected to uniform tensile loading (see Figure 6.3).

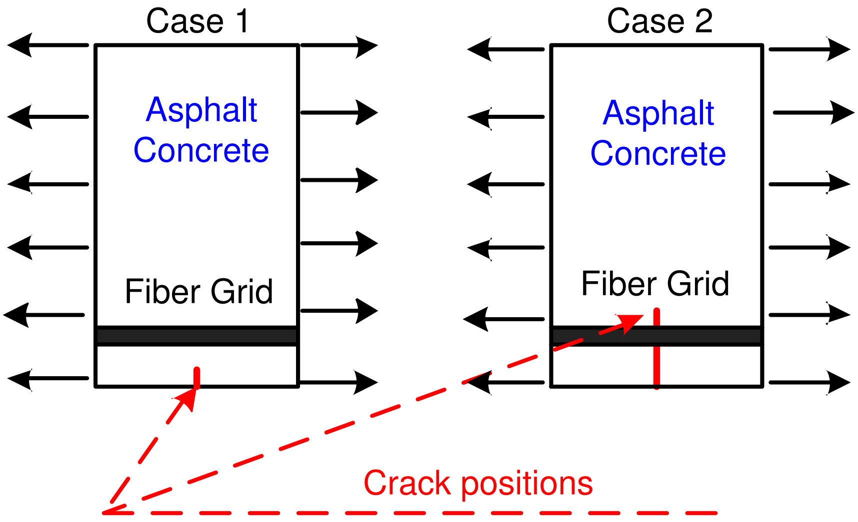

Figure 6.3: Crack initiates from the lower boundary of second asphalt concrete layer (case 1) and the bottom of the first asphalt concrete layer (case 2).

6.2.1 Non-reinforced plate

For the non-reinforce plate, the theoretical energy release rate expression is available in [36]:

$$G = \frac{[A(\alpha)\sigma]^2 \pi a}{E}. \tag{6.1}$$

The derivative of energy release rate with respect to the crack length a, as already discussed in Chapter 3, can be written as follows:

$$G' = \frac{[H(\alpha)\sigma]^2 \pi}{E}. \tag{6.2}$$

When $a \to 0$ for an edge crack in a large plate, the crack to width ratio $\alpha \to 0$ too, hence $H(\alpha) \to 1.12$ and the rupture is dominated only by the derivative of energy release rate G'. The expression of G' can be simplified as $G' = (H\sigma)^2\pi/E$, with $H = 1.12$ for an edge cracked non-reinforced plate. For a middle crack with same crack length a in a large plate, one can identify $H = 0.707$, hence, it is easier to initiate the same crack length a at the boundary than inside the material.

6.2.2 Reinforced plates

For the fiber grid reinforced plate, the analytic solution for the energy release rate is not available in the literature. In this Section, the plane stress models are calculated with finite element method. The values of energy release rate are obtained by the crack closure method, a local method based on the release of a small segment at the crack tip [10], which has been introduced in Appendix B. Several segments are released to obtain an evolution curve of energy release rate with respect to crack length a. The derivative of energy release rate G' is the slope of the energy release rate curve and H then can be computed by $H = \sqrt{G'E/\pi}/\sigma$, as well as the nominal strength for the crack initiation at different positions (see Figure 6.3). The effect of the cross section of the fiber quantity S_f (m^2/m) is studied, and generalized by $S_f E_f / E_{ac}$, where E_f and E_{ac} are the Young's modulus of the fiber and the asphalt concrete, respectively.

6.2.3 Numerical models

In the finite element calculation, only one half of the structure is modeled, due to the bilateral symmetry of the plate, as shown in Figure 6.4. The height of the plate is $h = 100\,mm$, the width of the plate is $w = 400\,mm$, and the unit thickness $t = 1\,m$ is adopted. The mesh size is chosen as $0.5\,mm$. The nodes at the right boundary are fixed in horizontal direction and can be released to calculate energy release rate. The applied strain is $\varepsilon = 1\,\mu m/m$. The mechanical properties of the asphalt concrete material are: Young's modulus $E_{ac} = 4.0\,GPa$ [135], Poisson ratio $\nu = 0.35$, tensile strength $\sigma_t = 2.7\,MPa$, fracture toughness $K_c = 0.12\,MPa\sqrt{m}$. The Poisson ratio of the fiber glass grid element is the same as the asphalt concrete, while Young's modulus E_f is chosen as a variable to model the different fiber quantities. The Young's modulus provided by Arsenie *et al.* is $E_f = 44\,GPa$ [65]. The cross section of the fiber glass element is fixed as $S_f = 0.15 \times 10^{-3}\,m^2/m$, so that the different ratios of $S_f E_f / E_{ac}$ represent the different fiber quantities.

Figure 6.4 presents the finite element model of the first case, a new pavement, where a crack initiates from the lower boundary of the second asphalt concrete layer and propagates towards the fiber glass.

The second case represents the rehabilitation of cracked pavements; that crack initiates from the lower boundary of the first asphalt concrete layer. This case can be separated in two different configurations, namely case 2.1 and case 2.2, according to the different conditions of the cracked layer. If there is only one crack is presented in the second layer, an extreme condition may be consider the fiber grid perfectly bonded to the asphalt layers, which can be represented by a fixed support at the level of the fiber grid, as shown in Figure 6.5a (case 2.1). In case 2.2, as shown in Figure 6.5b, the second layer is totally cracked, which means, that the fiber grid tends to be under uniform strain ε and under a tension force $F = \varepsilon E_f A_f$.

6.2.4 Numerical results

6.2.4.1 Energy release rate G

For case 1, the energy release rate G versus the crack length a for crack initiation from the lower boundary of the second asphalt concrete layer is plotted in Fig-

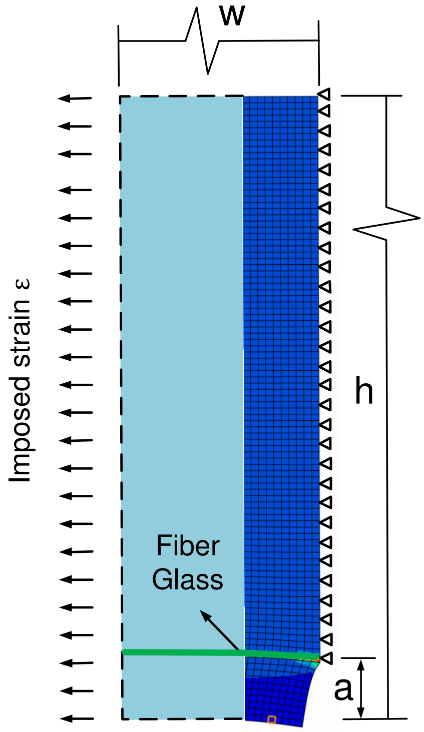

Figure 6.4: Crack initiation from the lower boundary of the second asphalt concrete layer (case 1).

ure 6.6. The energy release rate G increase linearly as the increase of the crack length. The derivative of the energy release rate is the slope of the linear curve, equals to $G' = 0.0139\, N/m^2$ in Figure 6.6. A further study on the effect of fiber quantity $S_f E_f / E_{ac}$ on the derivative of energy release rate indicates that, for case 1, the derivative of energy release is almost invariant with respect to the fiber quantity. It can be concluded that the effect of fiber glass on the crack initiation from the lower boundary of the second asphalt concrete is insignificant.

Considering case 2, the energy release rate versus the crack length for crack initiation from the lower boundary of the first asphalt concrete layer for various fiber quantities are plotted in Figures 6.7 and 6.8. In both cases (2.1 and 2.2), an improvement of the fiber quantity induces a decrease of the derivative of the energy release rate G', which corresponds to a lower correction factor H and a higher nominal strength (see Equation 3.11).

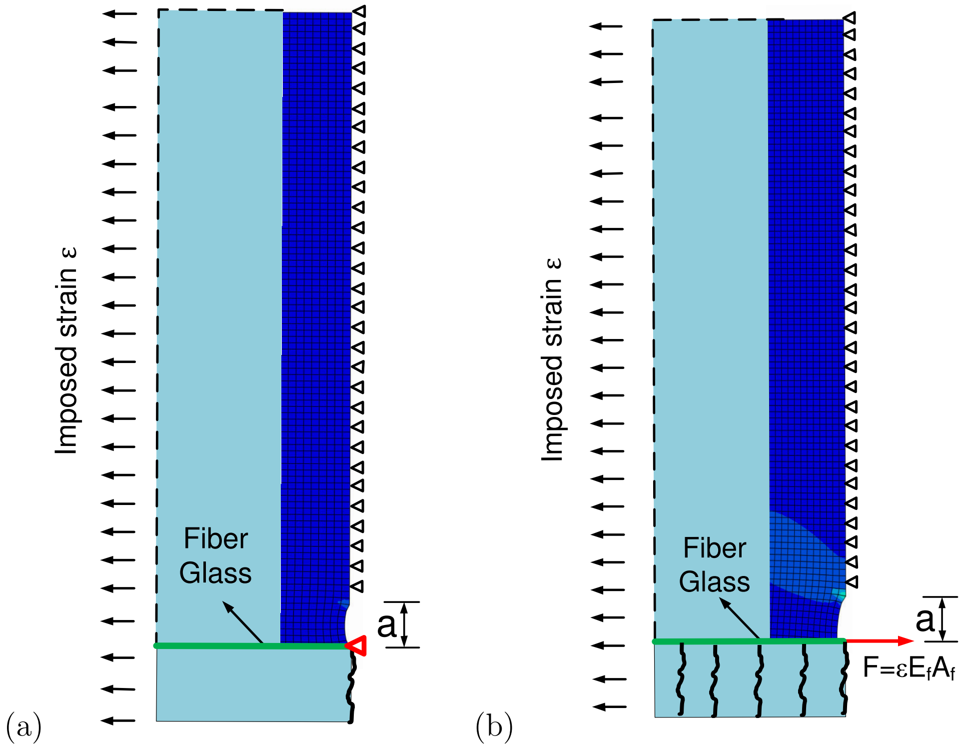

Figure 6.5: Crack initiation from the lower boundary of the first concrete layer for (a) fixed displacement (case 2.1) and (b) imposed force (case 2.2).

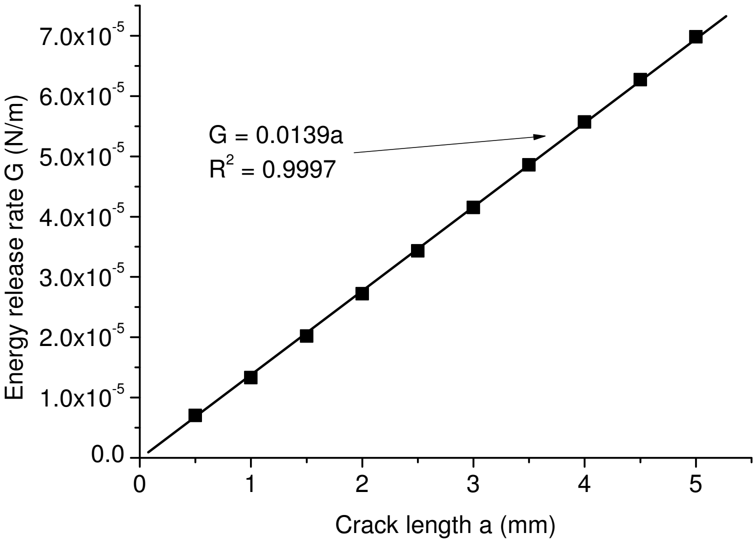

Figure 6.6: G versus a for crack initiation from the lower boundary of the second asphalt concrete layer (case 1).

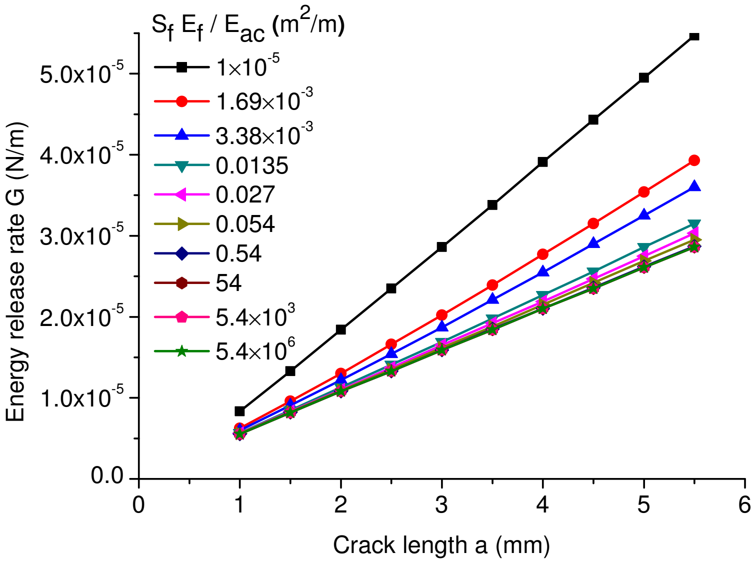

Figure 6.7: G versus a for crack initiation from the lower boundary of the first asphalt concrete layer for various fiber quantities when the displacement at the end of fiber grid element is fixed (case 2.1).

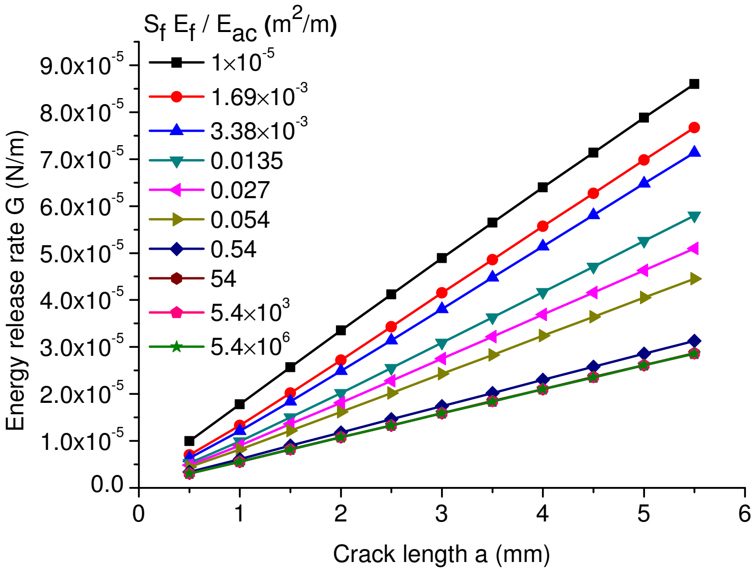

Figure 6.8: G versus a for crack initiation from the lower boundary of the first asphalt concrete layer for various fiber quantities when a concentrated force is imposed at the end of fiber (case 2.2).

6.2.4.2 Interpretation

The geometrical correction factor for the derivative of energy release rate H is plotted with respect to the fiber quantities $S_f E_f / E_{ac}$ for different cases in Figure 6.9. According to the simulations, the crack initiation on the lower boundary of the second layer (case 1), the value of $H \approx 1.12$ seems independent on the fiber quantity, which suggests a low effect of the fiber reinforcement against crack initiation. On the second case, the propagation of a longer crack beyond the fiber grid is studied. Two different contributions of the fiber against the crack opening are presented: as an imposed force and as a fixed displacement; the first underestimate the effect of the fiber and the second overestimate it. The real behavior is inside these two bounds but cannot be obtained without a tridimensional representation of the crack and the grid. In any case, the increase of the reinforcement quantity $S_f E_f / E_{ac}$ leads to a decrease of the value of H, and a consequent improvement on the local strength against crack initiation. The value of H is limited at 0.64 for very high quantities of fiber. However, $H = 1/\sqrt{2} \approx 0.71$ corresponds to the value obtained for a crack initiated at any point far from the boundaries; beyond this value, the cracks may initiate (relatively) far from the reinforcement (independently on the fiber quantity).

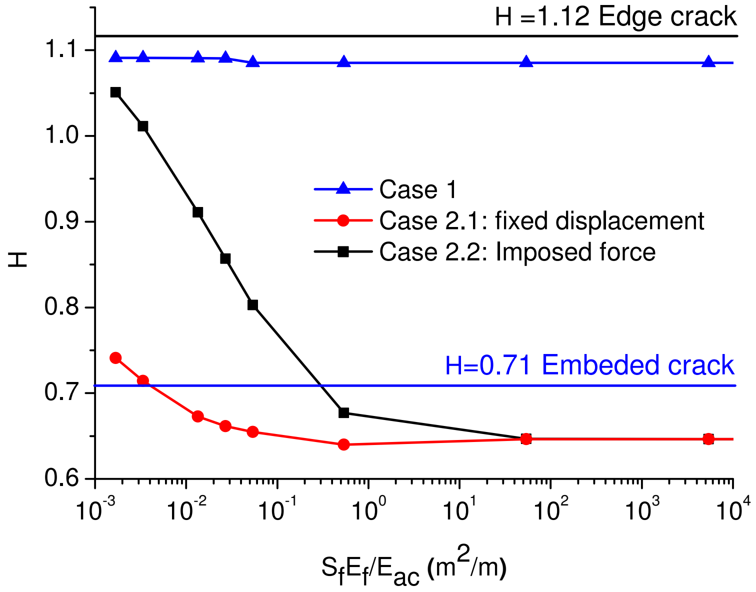

Figure 6.9: Geometrical correction factor H with respect to the fiber quantities $S_f E_f / E_{ac}$ for different cases.

6.3 Conclusions of the chapter

A bi-dimensional analysis was adopted to quantify the contribution of fiber grid reinforcement near a boundary. Low effect of the fibers was observed against crack initiation while the cracks are far from the reinforcement under imposed strain. However, the protective effect of the reinforcements is clear against cracks crossing the fiber glass grid. The effectiveness of the grid reinforcement (described by the evolution of the parameter H) seems to depend quasi-logarithmically on the fiber cross section S_f, its Young's modulus E_f and the Young's modulus of the asphalt concrete E_{ac} (through the relation $S_f E_f / E_{ac}$). This trend stabilizes for high quantities of fiber; however the fact that cracks may appear elsewhere (for $H < 0.71$), and not at the boundaries of the asphalt sample, imposes a practical limit for the fiber quantity. Considering these results, the usual quantities of fiber grid reinforcement $0 < S_f E_f / E_{ac} < 0.003$ [64] are technically inside the effectiveness range identified in these tests.

The following paper summarizes the main results of this chapter:
X. Gao, G. Koval, and C. Chazallon. Effect of fiber grid reinforcement on crack initiation and propagation in asphalt concrete. In 8th RILEM International Conference on Mechanisms of Cracking and Debonding in Pavements, pages 55-60. Springer, 2016 [136].

Chapter 7

Conclusions and perspectives

Contents

7.1 Conclusions

Building materials such as concrete, masonry, etc. are usually assemblies of different components of different size (aggregates, asphalt, cement hydrates, sand, clay, etc.). The mechanical behavior of these composite materials is naturally dependent on the size and shape of the structures where they are employed. These effects are generally referred as *size effects*. These size effects are not only important for the transposition of the results of laboratory tests (small scale) to real structures (large scale), but may appear on the interaction of the material with other elements of the structure such as localized reinforcements (steel bars, fiber grids, etc.), supports, connections, etc. The prediction of the behavior of a structure considering the type of loading (monotonic, cyclic, dynamic, etc.) during its life time depends necessarily on a precise understanding of the material behavior in different scales.

The degradation of the characteristics of a structural element, such as stiffness and strength, depends strongly on the rupture process. The propagation of intrinsic micro-defects of the material leading to the coalescence of bigger cracks, in the case of quasi-brittle materials, is often associated to different theoretical perspectives which are not always automatically compatible (i.e. properties like strength and toughness; rupture mechanisms like damage and fracture). This conceptual difficulty is also due to the scale difference associated to each phenomenon.

A theoretical solution adopted by many authors in order to bridge multiple approaches is to consider that the rupture of the material is related to the behavior of a limited amount of matter by means of a characteristic dimension. This non-local principle is physically consistent with the existence of a limited representative element volume necessary to characterize a composite material. However, this characteristic dimension can reach some centimeters in the case of building materials, which limits considerably the analysis of laboratory tests, or the behavior of structural components such as some type of reinforcements, often presenting centimetric dimensions.

The drawbacks associated to non-local theoretical approaches, outlined in Chapter 2, such as non-physical damage distributions under stress gradients or the complexity to handle crack initiation (specially at the proximity of different materials), motivated the study of local solutions to describe the failure process.

The hardest conceptual problem of most of local rupture approaches is the sensitivity of the results with respect to the discretization. The average of quantities, such as stress and strain, over the scale of a finite or discrete element affects directly the results, especially under strong gradients. The solution was to base the rupture criteria on the energy release rate, a punctual quantity, in order to obtain convergent results for finer discretization. Two cases were analyzed during this work: monotonic and fatigue loading.

In Chapter 3, size (and boundary) effects were examined in quasi-brittle rupture of pre-cracked samples. The basic ingredients of the proposed local model are the contribution of the material toughness and tensile strength on the failure load. The relation between toughness and the energy release rate G at the rupture is similar to typical linear elastic fracture mechanics criterion. However, an important feature of the model is to identify the effects of the nominal stress (a non-local quantity) by means of the evolution of the energy release rate G (in a local sense). This leads to an energetic definition of the tensile strength, which allows a relatively simple analysis of structures with any size of crack, or no cracks at all. A comparison of the proposed local formulation with boundary and size effect models (non-local approaches by definition) put the capabilities of the model into context, which are confirmed by the successful confrontation with experimental results.

Hence, the presented energetic relation was generalized to compose a simple local criterion of rupture in Chapter 4. A finer description of the transition between strength and fracture mechanisms (by means of the additional parameter r) was shown to be necessary to locally relate the material behavior to structural size effects. The initiation and propagation of cracks was analyzed in structures containing different types of defects such as cracks, v-notches and holes, where the obtained failure load was consistent with a series of experimental results. The scope of LEFM was somewhat extended, considering that neither plasticity nor damage were necessarily associated with the model to describe crack initiation in monotonic case. However, an apparent non-physical increase on the strength of the specimens was observed during this rupture phase, explained by the fact that for very short cracks, different size effects are relevant under localized stress gradients.

Fatigue loading is characterized by very low intensity efforts that are repeated for a large number of cycles. Neither strength, nor toughness is in fact mobilized. However, the material behavior presents different aspects depending on the stress/strain distribution. Under homogenous stress/strain, a global reduction of the material stiffness can be experimentally observed due to the effect of distributed micro cracks, which tends increase in number and propagate during cyclic efforts (damage). When these cracks become long enough or due to geometrical properties of a structural element, singular stress/strain distributions may be induced. In these conditions, concentrated effects are observed such as crack initiation or growth of pre-existing cracks (fatigue crack growth).

Three key elements were then considered in the proposed local fatigue model of Chapter 5: 1) before local rupture, the material is described by a damage behavior; 2) a localized rupture, characterized by crack initiation (or propagation), may occur only where stress (or strain) are locally maximized; 3) the energy release rate at a crack tip must obey a fatigue crack growth behavior. The total damage of a given point is conceptually equivalent to a contact rupture. It allows the evaluation of the energy release rate range, specially consistent under singular concentrations of stress, a fundamental parameter to any fatigue crack growth model. Considering all these conditions, a simple numerical scheme coupling Bodin's damage model to Paris' law in a discrete element environment could then be implemented. Simulations of cracked plates and four point bending beams compared to numerical and experimental results have shown the capabilities of the formulation in reproducing the structure response associated to consistent material behavior. The notion of fracture process zone, an intermediate space between cracked and un-cracked portions, is well distinguished and automatically generated during the simulation process. Furthermore, important individual drawbacks of each approach could be avoided, such as discretization effects, as shown by the convergence of the results; and the non-physical behavior of crack growth models for very short cracks (or simply no cracks).

The model presented in Chapter 4 is shown to be well adapted to analyze the monotonic rupture behavior near complex boundary conditions. Finally, a simple estimation of the protective effect of fiber grid reinforcements is discussed in Chapter 6. The values of the energy release rate and its derivative were calculated by finite element bi-dimensional simulations. Low effect of the fibers was observed against crack initiation when the cracks are far from the reinforcement under imposed strain. However, the protective effect of the reinforcements is clear against cracks crossing the fiber glass grid. The effectiveness of the grid reinforcement depends on the fiber cross section S_f, its Young's modulus E_f and the Young's modulus of the asphalt concrete E_{ac} (through the relation $S_f E_f / E_{ac}$). The numerical results suggest that the quantity of fiber grid should be limited in practice by the strength of the concrete, what imposes an effective range of $0 < S_f E_f / E_{ac} < 0.003$.

7.2 Perspectives

From a theoretical point of view, the proposed models present many possible extensions. The monotonic rupture model can be simply adapted to mixed mode if the direction of the potential crack initiation or extension is defined. One strategy is to combine the proposed model with other fracture criteria, such as maximum tensile stress criterion, minimum strain energy density criterion etc., which can predict the propagation angle. Another possibility is to define the direction of propagation as the one which minimizes the failure load.

The local model for monotonic loading was defined based on a formulation for size effects of the second type, which is associated to developed cracks. However, the trace of size effects of the first type could be visualized for v-notches and holes by means of an unnatural increase of the nominal strength, observed during crack initiation. Once the transition between both types of size effects was perfectly identified, a local expression for type 1 size effect law can be proposed, improving the characterization of crack initiation under stress gradients.

A tridimensional version of the fatigue model can be obtained by, at least, two ways. The first is to continue with a discrete element approach; nevertheless, a random particle distribution may decrease the necessary computation time. The second is to adapt the formulation to a finite element code, considering that the theory is founded on continuum mechanics.

From a practical point of view, many engineering applications can be envisaged. The local model for monotonic loading can replace complex structural analysis, if an expression of stress intensity factor is available. Size effects can be easily identified in standard laboratory tests, which allow a precise identification of material strength parameters even for small samples.

Fatigue tests are usually performed under heterogeneous stress conditions, which often demand a numerical analysis in order to identify the parameters of the material. A local model leads to a more reliable extrapolation to the structure behavior, undisturbed by scale limitations.

Appendix A

Comparison of different $A(\alpha)$ formulas for beams

A.1 Empirical Formulas in the literature

The empirical formulas are required to calculate the stress intensity factor analytically for the cracked three point bending beam specimen. Various formulas have been proposed, which have different accuracy for different beam span to height ratios S/h.

For pure bending condition ($S/h = \infty$), Tada *at al.* [36] derived the following expression for any α with accuracy better than 0.5%:

$$A(\alpha) = \sqrt{\frac{2}{\pi\alpha}\tan\frac{\pi\alpha}{2}}\,\frac{0.923 + 0.199\left(1 - \sin\frac{\pi\alpha}{2}\right)^4}{\cos\frac{\pi\alpha}{2}}. \tag{A.1}$$

Brown and Srawley [137] used the least square fitting method to derive an polynomial expression with 0.2% accuracy for $\alpha \leq 0.6$, which reads:

$$A(\alpha) = 1.122 - 1.40\alpha + 7.33\alpha^2 - 13.08\alpha^3 + 14.0\alpha^4. \tag{A.2}$$

For the beam cases with span to height ratio $S/h = 2.5$, the following expression was proposed by Gettu *et al.* [138], which was obtained by fitting the results of linear elastic finite element analysis:

$$A(\alpha) = \frac{6.647(1 - 2.5\alpha + 4.49\alpha^2 - 3.98\alpha^3 + 1.33\alpha^4)}{3.75\sqrt{\pi}(1-\alpha)^{3/2}}, \tag{A.3}$$

For span to height ratio equals to 4, Srawley [139] derived the empirical equation with 0.5% accuracy for any crack to height ratio α as follows:

$$A(\alpha) = \frac{1}{\sqrt{\pi}} \frac{1.99 - \alpha(1-\alpha)(2.15 - 3.93\alpha + 2.7\alpha^2)}{(1+2\alpha)(1-\alpha)^{3/2}}, \tag{A.4}$$

Brown and Srawley [137] utilized the least squares fitting method and proposed the expression for span to height ratio $S/h = 8$. The equation can provide 0.2% for $\alpha < 0.6$, which reads:

$$A(\alpha) = 1.106 - 1.552\alpha + 7.71\alpha^2 - 13.53\alpha^3 + 14.23\alpha^4. \tag{A.5}$$

In order to find a general expression for an arbitrary ratio of beam span S to span h, an approximation with high accuracy has been derived by Pastor, Guinea and their co-workers [101–103]:

$$A(\alpha) = \frac{P_{Sh}}{\sqrt{\pi}(1+2\alpha)(1-\alpha)^{3/2}}, \tag{A.6}$$

where P_{Sh} depends on the height to span ratio h/S and crack to height ratio α, which reads:

$$P_{Sh} = P_\infty + \frac{4h}{S}(P_4 - P_\infty), \tag{A.7}$$

with

$$P_4 = 1.9 - \alpha[-0.089 + 0.603(1-\alpha) - 0.441(1-\alpha)^2 + 1.223(1-\alpha)^3], \tag{A.8}$$

$$P_\infty = 1.989 - \alpha(1-\alpha)[0.448 - 0.458(1-\alpha) + 1.226(1-\alpha)^2]. \tag{A.9}$$

Based on Pastor's work, Guinea, Pastor and their co-workers [104] rewrote later a simple and general approximate closed-form expression for the geometrical correction factor. This result is claimed to be valid for any crack length and span to height ratios larger than 2.5:

$$A(\alpha) = \frac{P'_{Sh}}{\sqrt{\pi}(1+3\alpha)(1-\alpha)^{3/2}}, \tag{A.10}$$

where P'_{Sh} depends on the height to span ratio h/S and crack to height ratio α, which reads:

$$P'_{Sh} = P'_{\infty} + \frac{4h}{S}(P'_4 - P'_{\infty}), \tag{A.11}$$

with

$$P'_4 = 1.9 + 0.41\alpha + 0.51\alpha^2 - 0.17\alpha^3, \tag{A.12}$$

$$P'_{\infty} = 1.99 + 0.83\alpha - 0.31\alpha^2 + 0.14\alpha^3. \tag{A.13}$$

Although the previous two set of expressions are slightly different, they can provide the same correction factors for span to height ratios larger than 2.5. Hence, only Guinea' expressions are used for the comparison.

A.2 Comparison of different formulas

For pure bending condition, the formulas given by Tada *at al.* (Equation A.1), Brown and Srawley (Equation A.2) are compared with the one derived by Guinea *at al.* (Equation A.10). The values of $(1-\alpha)^{3/2}A(\alpha)$ are calculated based on the different formulas. These values are presented in Figure A.1, which confirms that Brown and Srawley's expression is only valid for $\alpha < 0.6$.

The percentages of difference with respect to Guinea's equation are plotted in Figure A.2. The difference is always below 2.5% between Tada *at al.*'s equation and Guinea's equation, while in the valid range of Brown and Srawley's expression, the difference with Guinea's equation is smaller than 1.0%.

The same comparison are performed for beam span to height ratio equals to 2.5, 4 and 8. Figure A.3 illustrates the values of $(1-\alpha)^{3/2}A(\alpha)$ calculated based on Equation A.3 and Equation A.10.

The differences of the finite element method results [104] and Equation A.3 with respect to the results of Equation A.10 are presented in Figure A.4, shows that Guinea's equation provides a better solution by comparing with the FEM results.

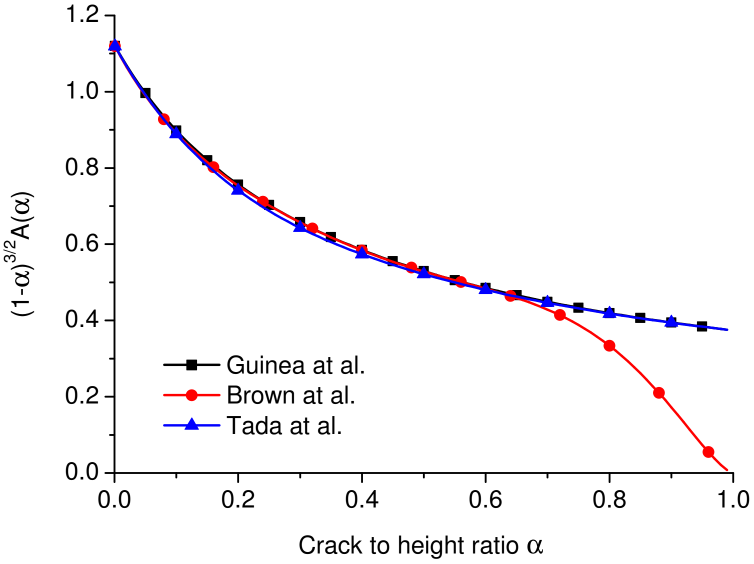

Figure A.1: $(1-\alpha)^{3/2}A(\alpha)$ calculated by different formulas for pure bending specimen.

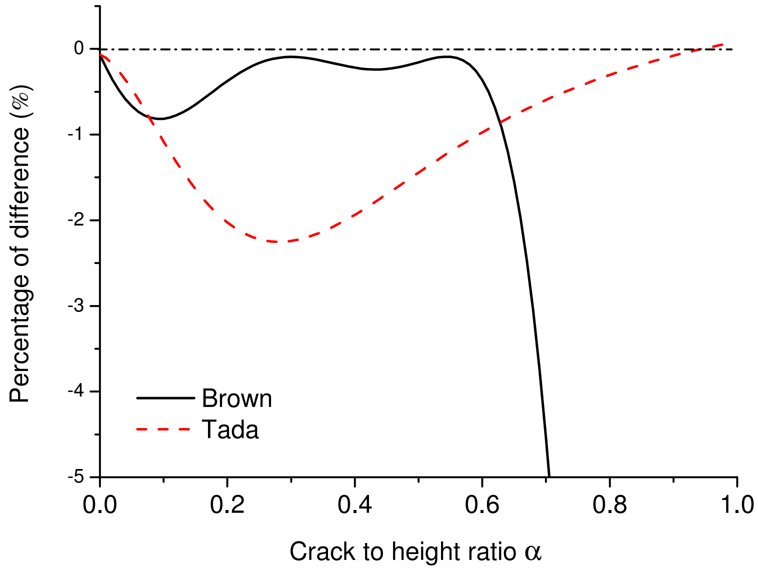

Figure A.2: Percentage of difference between the different formulas for pure bending specimen.

Figure A.5 shows the $(1-\alpha)^{3/2}A(\alpha)$ values calculated by Equation A.4 and Equation A.12. A slight difference is observed in the range of $\alpha < 0.1$. It can be concluded that Equation A.4 is better than Equation A.12, because it can provide the better values ($(1-\alpha)^{3/2}A(\alpha) \approx 1.12$) when $\alpha \to 0$.

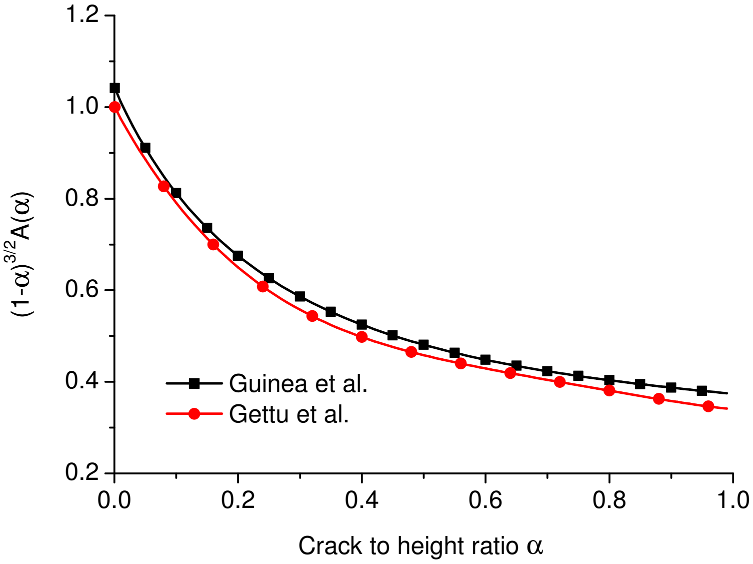

Figure A.3: $(1-\alpha)^{3/2}A(\alpha)$ calculated by different formulas for beams with $S/h = 2.5$.

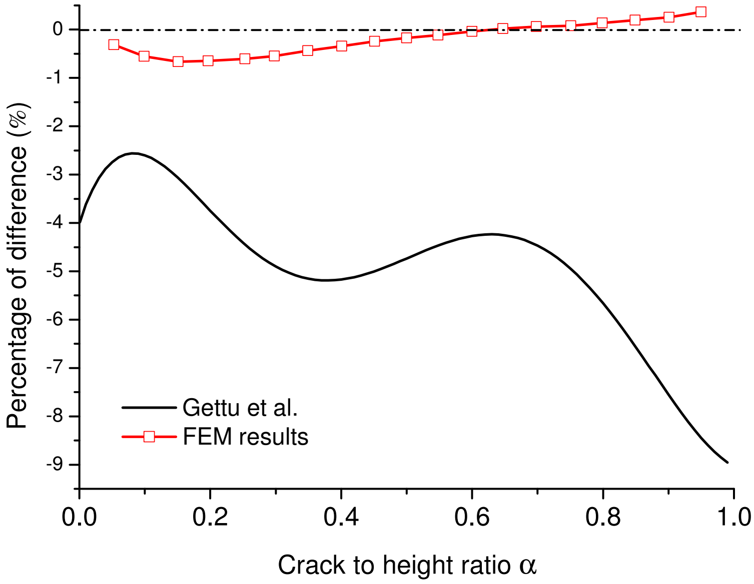

Figure A.4: Percentage of difference between the different formulas and FEM results for beam with $S/h = 2.5$.

For beam span to height equals to 8, Brown and Srawley's expression (Equation A.5) can provide the values of $(1-\alpha)^{3/2}A(\alpha)$ as good as Guinea et al.'s equation when α is in its valid range $\alpha < 0.6$. The difference is always below 1%. While for $\alpha > 0.6$, Guinea et al.'s equation can still provide the acceptable

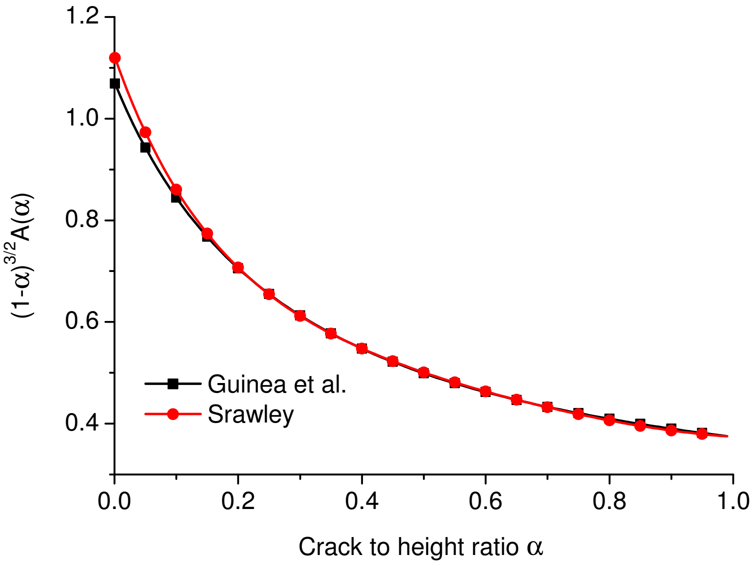

Figure A.5: $(1-\alpha)^{3/2}A(\alpha)$ calculated by different formulas for beams with $S/h = 4$.

correction factors.

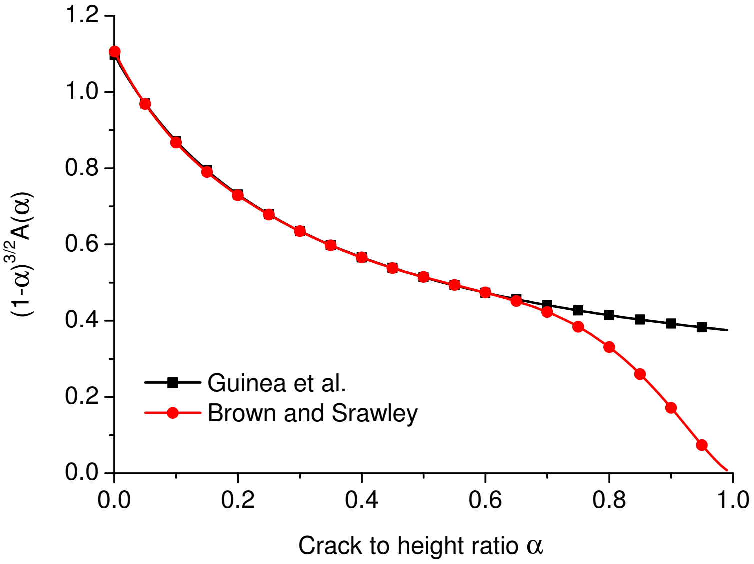

Figure A.6: $(1-\alpha)^{3/2}A(\alpha)$ calculated by different formulas for beams with $S/h = 8$.

The differences of the finite element method results [104] and Equation A.5 with respect to the results of Equation A.10 are presented in Figure A.7, shows that in their valid ranges, both equations provide very accurate results with respect to the FEM calculations.

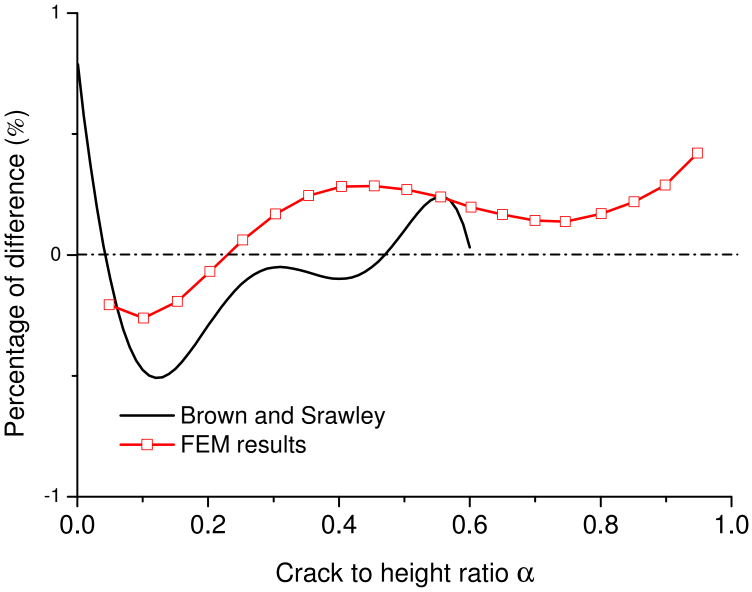

Figure A.7: Percentage of difference between the different formulas and FEM results for beam with $S/h = 8$.

A.3 Summary

In this appendix, a detained comparison of the different formulas of geometrical correction factor $A(\alpha)$ for stress intensity factor of cracked three point bending beam is performed. Guinea *et al.*'s formula is valid for any crack length and span to height ratios larger than 2.5. For $S/h = 4$, Srawley's equation is better than Guinea et al.'s formula when the crack to height ratio is small.

APPENDIX B

Numerical evaluation of energy release rate

When the geometries and/or boundary conditions are too complicated to compute the stress intensity factor K or energy release rate G analytically, an alternative way is to calculate them numerically. Finite element method is the most popular numerical method to calculate K and G. Based on the stress or displacement fields near the crack tip, the stress intensity factor can be obtained by stress extrapolation or displacement extrapolation based on the theoretical expressions in elasticity presented in Section 2.2.3. The stress or displacement extrapolation methods are conceptually simple, however, the accuracy of these methods is sensitive to the mesh size, therefore, an appropriate mesh size is required.

Another strategy is the use of the local information, including the nodal force at the crack tip and the nodal displacement after releasing this node (shown in Figure B.1), to calculate the energy release rate. This method is known as modified crack closure method, which has been proved to be insensitive with the mesh size. Following the nodal release algorithm [140], the energy release rate G_A is given by:

$$G_A = \frac{F^0_{yA} \Delta u^1_{yA}}{2t\ da}, \tag{B.1}$$

where F^0_{yA} is the nodal force at node A (at the crack tip) before releasing this node, Δu^1_{yA} is the opening displacement of node A after its release, da is the propagation length of the crack (directly associated to the mesh size) and t is the thickness of the structure (see Figure B.1).

A second value of the energy release rate G_B is obtained after a second nodal release:

$$G_B = \frac{F_{yB}^1 \Delta u_{yB}^2}{2t\ da}, \tag{B.2}$$

where F_{yB}^1 is the nodal force at node B (following notch tip) before releasing this node and Δu_{yB}^2 is the opening displacement of node B after its release. For a sufficiently small da: $G_0 \approx G_A$ and $G' \approx (G_B - G_A)/da$. The value of derivative of energy release rate G' can also be obtained as the slope of the linear curve of G with respect to crack length a, when the geometrical correction factor $H(\alpha)$ (Equation 3.9) for G' keeps almost constant.

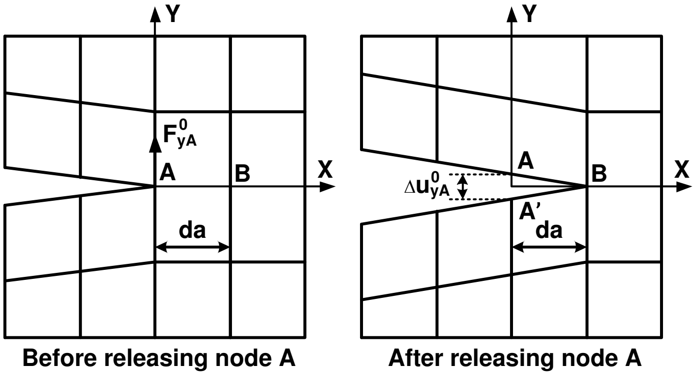

Figure B.1: Numerical evaluation of G.

Appendix C

Algorithm of DEM calculation

Discrete element method (DEM) is a numerical model capable of describing the mechanical behavior of assemblies of discs and spheres. It allows finite displacements and rotations of discrete particles, detects new contacts automatically as the calculation progresses, and solves the time evolution of this discrete system using an explicit dynamic solution to Newton's laws of motion. The fundamental elements for calculation are the dimensions of the particles, their spatial positions and properties.

Being a time-stepping formulation, as the simulation progresses, the model state is advanced in time by a series of calculation cycles. In each single calculation cycle, five operations are executed successively, including the timestep determination, law of motion, advance time, contact detection and force-displacement law, as shown in Figure C.1 [141].

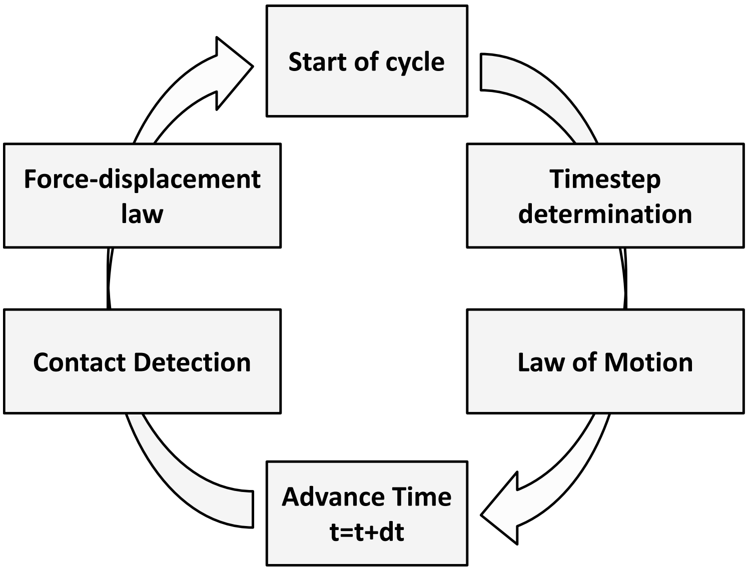

Figure C.1: Operations executed during each calculation cycle.

The detailed information about the operations are well described in the documentation of Particle Flow Code 5.0 and summarized as follows [141]:

1. Timestep determination: The DEM calculation requires a valid, finite timestep to ensure the numerical stability of the model. The critical timestep for one contact is $t_{crit} = \sqrt{m/k^{tran}}$ or $t_{crit} = \sqrt{I/k^{rot}}$, where m is the mass, I is the moment of inertia of the particle, k^{tran} and k^{rot} are the translational and rotational stiffnesses. The critical timesetp for the whole structure is decided by the smallest t_{crit} among all the contacts.

2. Law of motion: The position and velocity of each body is updated according to Newton's laws of motion using the current timestep and the forces calculated during the previous cycle.

3. Advance time: The model time is advanced by adding the current timestep to the previous model time.

4. Contact detection: Contacts are dynamically created/deleted based on the current particle positions.

5. Force-displacement law: The forces developing at each contact are updated by the appropriate contact model using the current state of the particles.

Bibliography

[1] A.A. Griffith. The phenomena of rupture and flow in solids. *Philosophical transactions of the royal society of london. Series A, containing papers of a mathematical or physical character*, 221:163–198, 1920. (Cited on pages 9 and 15.)

[2] G.R. Irwin. Analysis of stresses and strains near the end of a crack traversing a plate. *J. of Applied Mechanics*, 24:361–364, 1957. (Cited on pages 9, 19, 33 and 85.)

[3] G.P. Cherepanov. Crack propagation in continuous media. *Journal of Applied Mathematics and Mechanics*, 31(3):503 – 512, 1967. (Cited on page 9.)

[4] J.R. Rice. A path independent integral and the approximate analysis of strain concentration by notches and cracks. *Journal of applied mechanics*, 35(2):379–386, 1968. (Cited on page 9.)

[5] S. Li, M.D. Thouless, A.M. Waas, J.A. Schroeder, and P.D. Zavattieri. Use of a cohesive-zone model to analyze the fracture of a fiber-reinforced polymer–matrix composite. *Composites Science and Technology*, 65(3):537–549, 2005. (Cited on page 9.)

[6] G.I. Barenblatt. The mathematical theory of equilibrium cracks in brittle fracture. *Advances in applied mechanics*, 7:55–129, 1962. (Cited on page 9.)

[7] S.H. Song, G.H. Paulino, and W.G. Buttlar. Simulation of crack propagation in asphalt concrete using an intrinsic cohesive zone model. *Journal of Engineering Mechanics*, 132(11):1215–1223, 2006. (Cited on pages 9 and 84.)

[8] B.R. Lawn. *Fracture of brittle solids*. Cambridge solid state science series. Cambridge University Press, Cambridge ; New York, 2nd ed edition, 1993. (Cited on pages 10 and 11.)

[9] H.M. Westergaard. Bearing pressures and cracks. *SPIE MILESTONE SERIES MS*, 137:18–22, 1997. (Cited on page 10.)

[10] C.T. Sun and Z.H. Jin. *Fracture Mechanics*. Academic Press. Academic Press, 2012. (Cited on pages 10, 127, 129 and 140.)

[11] F. Erdogan and G.C. Sih. On the crack extension in plates under plane loading and transverse shear. *Journal of basic engineering*, 85(4):519–525, 1963. (Cited on pages 17 and 48.)

[12] G.C. Sih. Strain-energy-density factor applied to mixed mode crack problems. *International Journal of fracture*, 10(3):305–321, 1974. (Cited on page 18.)

[13] D. Leguillon. Strength or toughness? a criterion for crack onset at a notch. *European Journal of Mechanics-A/Solids*, 21(1):61–72, 2002. (Cited on pages 19, 30, 84 and 106.)

[14] P. Cornetti, N. Pugno, A. Carpinteri, and D. Taylor. Finite fracture mechanics: a coupled stress and energy failure criterion. *Engineering Fracture Mechanics*, 73(14):2021–2033, 2006. (Cited on pages 19, 29, 30, 84, 104 and 106.)

[15] D. Taylor. *The theory of critical distances: a new perspective in fracture mechanics*. Elsevier, 2007. (Cited on pages 19, 20, 21, 25, 28, 34, 53 and 85.)

[16] P. Maimí, E.V. González, N. Gascons, and L. Ripoll. Size effect law and critical distance theories to predict the nominal strength of quasibrittle structures. *Applied Mechanics Reviews*, 65(2):020803, 2013. (Cited on pages 19, 25, 30 and 104.)

[17] K. Duan, X.Z. Hu, and F.H. Wittmann. Scaling of quasi-brittle fracture: Boundary and size effect. *Mechanics of Materials*, 38(1):128–141, 2006. (Cited on pages 20, 31, 32, 52, 53, 60, 61, 69 and 92.)

[18] Z.P. Bažant, J.K. Kim, and P.A. Pfeiffer. Nonlinear fracture properties from size effect tests. *Journal of Structural Engineering*, 112(2):289–307, 1986. (Cited on pages 21, 22, 73 and 74.)

[19] Y.S. Jenq and S.P. Shah. Nonlinear fracture parameters for cement based composites: theory and experiments. In *Application of fracture mechanics to cementitious composites*, pages 319–359. Springer, 1985. (Cited on pages 21, 22 and 73.)

[20] A. Carpinteri, P. Cornetti, N. Pugno, A. Sapora, and D. Taylor. A finite fracture mechanics approach to structures with sharp v-notches. *Engineering Fracture Mechanics*, 75(7):1736–1752, 2008. (Cited on pages 21, 23, 84 and 92.)

[21] M.L. Dunn, W. Suwito, and S. Cunningham. Fracture initiation at sharp notches: correlation using critical stress intensities. *International Journal of Solids and Structures*, 34(29):3873–3883, 1997. (Cited on pages 21, 92, 95, 97 and 100.)

[22] A. Seweryn, S. Poskrobko, and Z. Mróz. Brittle fracture in plane elements with sharp notches under mixed-mode loading. *Journal of Engineering Mechanics*, 123(6):535–543, 1997. (Cited on pages 21, 84, 92, 96 and 98.)

[23] P. P. Camanho, P. Maimí, and C.G. Dávila. Prediction of size effects in notched laminates using continuum damage mechanics. *Composites Science and Technology*, 67(13):2715–2727, 2007. (Cited on page 23.)

[24] P.P. Camanho, G.H. Erçin, G. Catalanotti, S. Mahdi, and P. Linde. A finite fracture mechanics model for the prediction of the open-hole strength of composite laminates. *Composites Part A: Applied Science and Manufacturing*, 43(8):1219–1225, 2012. (Cited on pages 24, 27, 30, 84, 99, 103, 104 and 105.)

[25] Z.P. Bažant. Instability, ductility, and size effect in strain-softening concrete. *Journal of the engineering mechanics division*, 102(2):331–344, 1976. (Cited on page 24.)

[26] Z.P. Bažant and Cedolin L. Blunt crack band propagation in finite element analysis. *Journal of the engineering mechanics division*, 105:297–315, 1979. (Cited on page 24.)

[27] X.B. Zhang and J. Li. A failure criterion for brittle and quasi-brittle materials under any level of stress concentration. *Engineering Fracture Mechanics*, 75(17):4925–4932, 2008. (Cited on pages 24 and 25.)

[28] G. Koval, B.D. Le, and C. Chazallon. Discrete element model for quasi-brittle rupture under tensile and compressive loading. *International Journal for Numerical and Analytical Methods in Geomechanics*, 2016. (Cited on pages 25, 45 and 85.)

[29] H. Neuber. *Theory of Notch Stresses: Principles for Exact Calculation of Strength with Reference to Structural Form and Material.* Springer Verlag, Berlin, 1958. (Cited on page 25.)

[30] R.E. Peterson. Notch sensitivity. In *Metal fatigue*, pages 293–306. McGraw-Hill, New York, 1959. (Cited on page 25.)

[31] D. Taylor. Predicting the fracture strength of ceramic materials using the theory of critical distances. *Engineering Fracture Mechanics*, 71(16):2407–2416, 2004. (Cited on page 25.)

[32] A.J. Kinloch and J.G. Williams. Crack blunting mechanisms in polymers. *Journal of Materials Science*, 15(4):987–996, 1980. (Cited on page 25.)

[33] M.R. Wisnom, S.R. Hallett, and C. Soutis. Scaling effects in notched composites. *Journal of Composite Materials*, 44(2):195–210, 2010. (Cited on page 25.)

[34] M.E. Waddoups, J.R. Eisenmann, and B.E. Kaminski. Macroscopic fracture mechanics of advanced composite materials. *Journal of composite materials*, 5(4):446–454, 1971. (Cited on page 28.)

[35] M.H. El Haddad, K.N. Smith, and T.H. Topper. Fatigue crack propagation of short cracks. *Journal of Engineering Materials and Technology*, 101(1):42–46, 1979. (Cited on page 28.)

[36] H. Tada, P.C. Paris, and G.R. Irwin. *The Stress Analysis of Cracks Handbook*. Wiley, 2000. (Cited on pages 28, 54, 57, 62, 90, 140 and 153.)

[37] D. Taylor, P. Cornetti, and N. Pugno. The fracture mechanics of finite crack extension. *Engineering Fracture Mechanics*, 72(7):1021–1038, 2005. (Cited on page 29.)

[38] D. Leguillon, D. Quesada, C. Putot, and E. Martin. Prediction of crack initiation at blunt notches and cavities–size effects. *Engineering fracture mechanics*, 74(15):2420–2436, 2007. (Cited on page 30.)

[39] X. Hu and F. Wittmann. Size effect on toughness induced by crack close to free surface. *Engineering fracture mechanics*, 65(2):209–221, 2000. (Cited on pages 31 and 32.)

[40] X. Hu. An asymptotic approach to size effect on fracture toughness and fracture energy of composites. *Engineering Fracture Mechanics*, 69(5):555–564, 2002. (Cited on pages 31, 32 and 69.)

[41] Z.P. Bažant. Probabilistic modeling of quasibrittle fracture and size effect. In *Proc., 8th Int. Conf. on Structural Safety and Reliability (ICOSSAR)*, pages 1–23. Swets and Zeitinger, Balkema, 2001. (Cited on page 33.)

[42] Z.P. Bažant. Size effect in blunt fracture: concrete, rock, metal. *Journal of Engineering Mechanics*, 110(4):518–535, 1984. (Cited on page 33.)

[43] Z.P. Bažant and M.T. Kazemi. Size dependence of concrete fracture energy determined by rilem work-of-fracture method. *International Journal of Fracture*, 51(2):121–138, 1991. (Cited on page 33.)

[44] Z.P. Bažant and Z. Li. Zero-brittleness size-effect method for one-size fracture test of concrete. *Journal of engineering mechanics*, 122(5):458–468, 1996. (Cited on pages 33 and 106.)

[45] C.G. Hoover and Z.P. Bažant. Comparison of the hu-duan boundary effect model with the size-shape effect law for quasi-brittle fracture based on new comprehensive fracture tests. *Journal of Engineering Mechanics*, 140(3):480–486, 2014. (Cited on pages 33, 34 and 73.)

[46] Z.P. Bažant. Scaling of quasibrittle fracture: asymptotic analysis. *International Journal of Fracture*, 83(1):19–40, 1997. (Cited on page 34.)

[47] Z.P. Bažant and Q. Yu. Universal size effect law and effect of crack depth on quasi-brittle structure strength. *Journal of engineering mechanics*, 135(2):78–84, 2009. (Cited on pages 34, 52, 79 and 106.)

[48] C.G. Hoover and Z.P. Bažant. Universal size-shape effect law based on comprehensive concrete fracture tests. *Journal of Engineering Mechanics*, 140(3):473–479, 2014. (Cited on page 34.)

[49] Q. Yu, J. Le, C.G. Hoover, and Z.P. Bažant. Problems with hu-duan boundary effect model and its comparison to size-shape effect law for quasi-brittle fracture. *Journal of engineering mechanics*, 136(1):40–50, 2009. (Cited on pages 34, 53, 79 and 92.)

[50] N. Pugno, M. Ciavarella, P. Cornetti, and A. Carpinteri. A generalized paris' law for fatigue crack growth. *Journal of the Mechanics and Physics of Solids*, 54(7):1333–1349, 2006. (Cited on pages 36 and 110.)

[51] M. Castro and J.A. Sánchez. Estimation of asphalt concrete fatigue curves–a damage theory approach. *Construction and Building Materials*, 22(6):1232–1238, 2008. (Cited on page 37.)

[52] H. Di Benedetto, C. De La Roche, H. Baaj, A. Pronk, and R. Lundström. Fatigue of bituminous mixtures. *Materials and structures*, 37(3):202–216, 2004. (Cited on page 37.)

[53] H.J. Lee, J.S. Daniel, and Y.R. Kim. Continuum damage mechanics-based fatigue model of asphalt concrete. *Journal of Materials in Civil Engineering*, 12(2):105–112, 2000. (Cited on page 37.)

[54] D. Bodin. *Modèle d'endommagement par fatigue: application aux enrobés bitumineux*. PhD thesis, Nantes, 2002. (Cited on pages 37, 38, 40, 41, 110, 112, 114, 118 and 120.)

[55] D. Bodin, G. Pijaudier-Cabot, C. de La Roche, J.M. Piau, and A. Chabot. Continuum damage approach to asphalt concrete fatigue modeling. *Journal of Engineering Mechanics*, 130(6):700–708, 2004. (Cited on pages 37, 40, 41, 42 and 112.)

[56] R. Chkir, D. Bodin, G. Pijaudier-Cabot, G. Gauthier, and T. Gallet. An inverse analysis approach to determine fatigue performance of bituminous mixes. *Mechanics of Time-Dependent Materials*, 13(4):357–373, 2009. (Cited on pages 37 and 41.)

[57] I.M. Arsenie, C. Chazallon, J.L. Duchez, and S. Mouhoubi. Modelling of the fatigue damage of a geogrid-reinforced asphalt concrete. *Road Materials and Pavement Design*, pages 1–13, 2016. (Cited on pages 37, 41, 42, 117, 118, 119, 120, 137 and 138.)

[58] M. Jirásek and B. Patzák. Consistent tangent stiffness for nonlocal damage models. *Computers & structures*, 80(14):1279–1293, 2002. (Cited on pages 37 and 110.)

[59] M.H.J.W. Paas. *Continuum damage mechanics with an application to fatigue*. PhD thesis, Technishe Universiteit Eindhoven, 1990. (Cited on pages 37, 114 and 115.)

[60] J. Lemaitre. *A course on damage mechanics*. Springer Science & Business Media, 2012. (Cited on page 40.)

[61] R.H.J. Peerlings, W.A.M. Brekelmans, R. De Borst, and M.G.D. Geers. Gradient-enhanced damage modelling of high-cycle fatigue. *International Journal for Numerical Methods in Engineering*, 49(12):1547–1569, 2000. (Cited on page 40.)

[62] G. Pijaudier-Cabot, K. Haidar, and J.F. Dubé. Non-local damage model with evolving internal length. *International journal for numerical and analytical methods in geomechanics*, 28(7-8):633–652, 2004. (Cited on page 41.)

[63] Z.P. Bažant. Why continuum damage is nonlocal: micromechanics arguments. *Journal of Engineering Mechanics*, 117(5):1070–1087, 1991. (Cited on page 41.)

[64] I. M. Arsenie. *Etude et modélisation des renforcements de chaussées à l'aide de grilles en fibre de verre sous sollicitations de fatigue*. PhD thesis, Université de Strasbourg, 2013. (Cited on pages 41, 42, 110, 114, 117, 119, 120, 138 and 146.)

[65] I.M. Arsenie, C. Chazallon, J.L. Duchez, and P. Hornych. Laboratory characterisation of the fatigue behaviour of a glass fibre grid-reinforced asphalt concrete using 4pb tests. *Road Materials and Pavement Design*, pages 1–13, 2016. (Cited on pages 41, 42, 117, 119, 138 and 141.)

[66] C. Le Bellégo, J. F. Dubé, G. Pijaudier-Cabot, and B. Gérard. Calibration of nonlocal damage model from size effect tests. *European Journal of Mechanics-A/Solids*, 22(1):33–46, 2003. (Cited on page 42.)

[67] J. Carmeliet. Optimal estimation of gradient damage parameters from localization phenomena in quasi-brittle materials. *Mechanics of Cohesive-frictional Materials*, 4(1):1–16, 1999. (Cited on page 42.)

[68] P.C. Paris, M.P. Gomez, and W.E. Anderson. A rational analytic theory of fatigue. *The trend in engineering*, 13(1):9–14, 1961. (Cited on page 43.)

[69] Z.P. Bažant and K. Xu. Size effect in fatigue fracture of concrete. *ACI Mater. J*, 88(4):390–399, 1991. (Cited on page 43.)

[70] Z.P. Bažant and W.F. Schell. Fatigue fracture of high-strength concrete and size effect. *ACI Materials Journal*, 90:472–472, 1993. (Cited on page 43.)

[71] J. Le, J. Manning, and J.F. Labuz. Scaling of fatigue crack growth in rock. *International Journal of Rock Mechanics and Mining Sciences*, 72:71–79, 2014. (Cited on page 43.)

[72] P.A. Cundall and O.D. Strack. A discrete numerical model for granular assemblies. *Géotechnique*, 29(1):47–65, 1979. (Cited on pages 44 and 85.)

[73] F.A. Tavarez. *Discrete element method for modelling solid and particulate materials*. PhD thesis, University of Wisconsin–Madison, 2005. (Cited on pages 44, 45 and 111.)

[74] B.D. Le. *Modélisation discrète en mécanique de la rupture des matériaux fragiles*. PhD thesis, Université de Strasbourg, 2013. (Cited on pages 45, 46, 47, 48 and 115.)

[75] B.D. Le, G. Koval, and C. Chazallon. Discrete element approach in brittle fracture mechanics. *Engineering Computations*, 30(2):263–276, 2013. (Cited on pages 45, 85 and 115.)

[76] B.D. Le, G. Koval, and C. Chazallon. Discrete element model for crack propagation in brittle materials. *International Journal for Numerical and Analytical Methods in Geomechanics*, 40(4):583–595, 2016. (Cited on pages 45 and 85.)

[77] C. Liu, D.D. Pollard, and B. Shi. Analytical solutions and numerical tests of elastic and failure behaviors of close-packed lattice for brittle rocks and crystals. *Journal of Geophysical Research: Solid Earth*, 118(1):71–82, 2013. (Cited on page 45.)

[78] Z.P. Bažant. *Scaling of structural strength*. Butterworth-Heinemann, 2005. (Cited on pages 72, 73 and 133.)

[79] Z.P. Bažant. Scaling theory for quasibrittle structural failure. *Proceedings of the National Academy of Sciences of the United States of America*, 101(37):13400–13407, 2004. (Cited on pages 73 and 133.)

[80] Z.P. Bažant, R. Gettu, and M.T. Kazemi. Identification of nonlinear fracture properties from size effect tests and structural analysis based on geometry-dependent r-curves. In *International journal of rock mechanics and mining sciences & geomechanics abstracts*, volume 28, pages 43–51. Elsevier, 1991. (Cited on pages 76 and 77.)

[81] Y. Jenq and S.P. Shah. Two parameter fracture model for concrete. *Journal of engineering mechanics*, 111(10):1227–1241, 1985. (Cited on page 76.)

[82] R.A. Schmidt. Fracture-toughness testing of limestone. *Experimental Mechanics*, 16(5):161–167, 1976. (Cited on page 76.)

[83] B.L. Karihaloo, H.M. Abdalla, and Q.Z. Xiao. Size effect in concrete beams. *Engineering fracture mechanics*, 70(7):979–993, 2003. (Cited on pages 77, 90 and 93.)

[84] X. Gao, G. Koval, and C. Chazallon. A size and boundary effects model for quasi-brittle fracture. *Materials*, 9(12):1–20, 2016. (Cited on page 81.)

[85] V.V. Novozhilov. On a necessary and sufficient criterion for brittle strength. *Journal of Applied Mathematics and Mechanics*, 33(2):201 – 210, 1969. (Cited on page 84.)

[86] A. Seweryn. Brittle fracture criterion for structures with sharp notches. *Engineering Fracture Mechanics*, 47(5):673–681, 1994. (Cited on pages 84 and 99.)

[87] A. Seweryn and Z. Mróz. A non-local stress failure condition for structural elements under multiaxial loading. *Engineering Fracture Mechanics*, 51(6):955–973, 1995. (Cited on pages 84 and 106.)

[88] A. Seweryn and A. Łukaszewicz. Verification of brittle fracture criteria for elements with v-shaped notches. *Engineering Fracture Mechanics*, 69(13):1487–1510, 2002. (Cited on pages 84, 95, 96 and 98.)

[89] Z. Yosibash, A. Bussiba, and I. Gilad. Failure criteria for brittle elastic materials. *International Journal of Fracture*, 125(3-4):307–333, 2004. (Cited on page 84.)

[90] D. Leguillon and Z. Yosibash. Crack onset at a v-notch. influence of the notch tip radius. *International journal of fracture*, 122(1-2):1–21, 2003. (Cited on page 84.)

[91] Z. Yosibash, E. Priel, and D. Leguillon. A failure criterion for brittle elastic materials under mixed-mode loading. *International journal of fracture*, 141(1-2):291–312, 2006. (Cited on page 84.)

[92] P. Weißgraeber, D. Leguillon, and W. Becker. A review of finite fracture mechanics: crack initiation at singular and non-singular stress raisers. *Archive of Applied Mechanics*, 86(1-2):375–401, 2016. (Cited on pages 84 and 104.)

[93] P. Weißgraeber, J. Felger, D. Geipel, and W. Becker. Cracks at elliptical holes: stress intensity factor and finite fracture mechanics solution. *European Journal of Mechanics-A/Solids*, 55:192–198, 2016. (Cited on page 84.)

[94] G.I. Barenblatt. The formation of equilibrium cracks during brittle fracture. general ideas and hypotheses. axially-symmetric cracks. *Journal of Applied Mathematics and Mechanics*, 23(3):622–636, 1959. (Cited on page 84.)

[95] G.I. Barenblatt, R.L. Salganik, and G.P. Cherepanov. On the nonsteady motion of cracks. *PMM Applied Mathematics and Mechanics*, 26:469–477, 1962. (Cited on page 84.)

[96] D.S. Dugdale. Yielding of steel sheets containing slits. *Journal of the Mechanics and Physics of Solids*, 8(2):100–104, 1960. (Cited on page 84.)

[97] A. Carpinteri, P. Cornetti, F. Barpi, and S. Valente. Cohesive crack model description of ductile to brittle size-scale transition: dimensional analysis vs. renormalization group theory. *Engineering fracture mechanics*, 70(14):1809–1839, 2003. (Cited on page 85.)

[98] K. Meguro and M. Hakuno. Fracture analyses of concrete structures by the modified distinct element method. *Structural engineering/earthquake engineering*, 6(2):283–294, 1989. (Cited on page 85.)

[99] Y. Matsuda and Y. Iwase. Numerical simulation of rock fracture using three-dimensional extended discrete element method. *Earth, planets and space*, 54(4):367–378, 2002. (Cited on page 85.)

[100] D.O. Potyondy and P.A. Cundall. A bonded-particle model for rock. *International journal of rock mechanics and mining sciences*, 41(8):1329–1364, 2004. (Cited on page 85.)

[101] J.Y. Pastor, G. Guinea, J. Planas, and M. Elices. Nueva expresión del factor de intensidad de tensiones para la probeta de flexión en tres puntos. In *Anales de Mecánica de la Fractura*, volume 12, pages 85–90, 1995. (Cited on pages 89 and 154.)

[102] C.G. Hoover and Z.P. Bažant. Comprehensive concrete fracture tests: size effects of types 1 & 2, crack length effect and postpeak. *Engineering Fracture Mechanics*, 110:281–289, 2013. (Cited on pages 89 and 154.)

[103] K. Kirane and Z.P. Bažant. Size effect in paris law and fatigue lifetimes for quasibrittle materials: Modified theory, experiments and micro-modeling. *International Journal of Fatigue*, 83:209–220, 2016. (Cited on pages 89 and 154.)

[104] G.V. Guinea, J.Y. Pastor, J. Planas, and M. Elices. Stress intensity factor, compliance and cmod for a general three-point-bend beam. *International Journal of Fracture*, 89(2):103–116, 1998. (Cited on pages 90, 154, 155 and 158.)

[105] J.D. Birchall, A.J. Howard, and K. Kendall. Flexural strength and porosity of cements. 1981. (Cited on pages 90 and 91.)

[106] D.D. Higgins and J.E. Bailey. Fracture measurements on cement paste. *Journal of Materials Science*, 11(11):1995–2003, 1976. (Cited on pages 92 and 93.)

[107] P. Cornetti, A. Sapora, and A. Carpinteri. Mode mixity and size effect in v-notched structures. *International Journal of Solids and Structures*, 50(10):1562–1582, 2013. (Cited on page 94.)

[108] A.G. Philipps, S. Karuppanan, C.M. Churchman, and D.A. Hills. Crack tip stress intensity factors for a crack emanating from a sharp notch. *Engineering Fracture Mechanics*, 75(18):5134–5139, 2008. (Cited on pages 94 and 95.)

[109] A. Carpinteri, P. Cornetti, N. Pugno, and A. Sapora. On the most dangerous v-notch. *International Journal of Solids and Structures*, 47(7):887–893, 2010. (Cited on page 95.)

[110] B.G. Green, M.R. Wisnom, and S.R. Hallett. An experimental investigation into the tensile strength scaling of notched composites. *Composites Part A: Applied Science and Manufacturing*, 38(3):867–878, 2007. (Cited on pages 99, 101, 102 and 105.)

[111] J.C. Newman. A nonlinear fracture mechanics approach to the growth of small cracks. Technical report, DTIC Document, 1983. (Cited on page 100.)

[112] E.Z. Lajtai. Effect of tensile stress gradient on brittle fracture initiation. In *International Journal of Rock Mechanics and Mining Sciences & Geomechanics Abstracts*, volume 9, pages 569–578. Elsevier, 1972. (Cited on page 102.)

[113] B.J. Carter. Size and stress gradient effects on fracture around cavities. *Rock Mechanics and Rock Engineering*, 25(3):167–186, 1992. (Cited on page 102.)

[114] Z.P. Bažant. Asymptotic matching analysis of scaling of structural failure due to softening hinges. i: Theory. *Journal of engineering mechanics*, 129(6):641–650, 2003. (Cited on page 104.)

[115] X. Gao, G. Koval, and C. Chazallon. Energetical formulation of size effect law for quasi-brittle fracture. *Engineering Fracture Mechanics*, 2017. http://dx.doi.org/10.1016/j.engfracmech.2017.02.001. (Cited on page 107.)

[116] H. Khoramishad, A.D. Crocombe, K.B. Katnam, and I.A. Ashcroft. Predicting fatigue damage in adhesively bonded joints using a cohesive zone model. *International Journal of fatigue*, 32(7):1146–1158, 2010. (Cited on pages 110 and 111.)

[117] N. Moës, C. Stolz, P.E. Bernard, and N. Chevaugeon. A level set based model for damage growth: the thick level set approach. *International Journal for Numerical Methods in Engineering*, 86(3):358–380, 2011. (Cited on page 110.)

[118] P.E. Bernard, N. Moës, and N. Chevaugeon. Damage growth modeling using the thick level set (tls) approach: Efficient discretization for quasi-static loadings. *Computer Methods in Applied Mechanics and Engineering*, 233:11–27, 2012. (Cited on page 110.)

[119] C. Stolz and N. Moës. A new model of damage: a moving thick layer approach. *International journal of fracture*, 174(1):49–60, 2012. (Cited on page 110.)

[120] N. Moës, C. Stolz, and N. Chevaugeon. Coupling local and non-local damage evolutions with the thick level set model. *Advanced Modeling and Simulation in Engineering Sciences*, 1(1):1, 2014. (Cited on page 110.)

[121] M Latifi, FP Van der Meer, and LJ Sluys. A thick level set interface model for simulating fatigue-drive delamination in composites. In *Composites 2015: 5th ECCOMAS Thematic Conference on Mechanical Response of Composites, Bristol, UK, 7-9 September 2015*, 2015. (Cited on page 110.)

[122] A. Parrilla Gómez, N. Moës, and C. Stolz. Comparison between thick level set (tls) and cohesive zone models. *Advanced Modeling and Simulation in Engineering Sciences*, 2(1):1, 2015. (Cited on page 111.)

[123] B. Yang, S. Mall, and K. Ravi-Chandar. A cohesive zone model for fatigue crack growth in quasibrittle materials. *International Journal of Solids and Structures*, 38(22):3927–3944, 2001. (Cited on page 111.)

[124] K.L. Roe and T.h. Siegmund. An irreversible cohesive zone model for interface fatigue crack growth simulation. *Engineering fracture mechanics*, 70(2):209–232, 2003. (Cited on page 111.)

[125] J.L. Bouvard, J.L. Chaboche, F. Feyel, and F. Gallerneau. A cohesive zone model for fatigue and creep–fatigue crack growth in single crystal

superalloys. *International Journal of Fatigue*, 31(5):868–879, 2009. (Cited on page 111.)

[126] A. Abdul-Baqi, P.J.G. Schreurs, and M.G.D. Geers. Fatigue damage modeling in solder interconnects using a cohesive zone approach. *International Journal of Solids and Structures*, 42(3):927–942, 2005. (Cited on page 111.)

[127] Q.D. Yang and B. Cox. Cohesive models for damage evolution in laminated composites. *International Journal of Fracture*, 133(2):107–137, 2005. (Cited on page 111.)

[128] H. Khoramishad, A.D. Crocombe, K.B. Katnam, and I.A. Ashcroft. Fatigue damage modelling of adhesively bonded joints under variable amplitude loading using a cohesive zone model. *Engineering Fracture Mechanics*, 78(18):3212–3225, 2011. (Cited on page 111.)

[129] T. Belytschko and T. Black. Elastic crack growth in finite elements with minimal remeshing. *International journal for numerical methods in engineering*, 45(5):601–620, 1999. (Cited on page 111.)

[130] N. Moës and T. Belytschko. Extended finite element method for cohesive crack growth. *Engineering fracture mechanics*, 69(7):813–833, 2002. (Cited on page 111.)

[131] S. Mohammadi. *Extended finite element method: for fracture analysis of structures*. John Wiley & Sons, 2008. (Cited on page 111.)

[132] M. Sharafisafa and M. Nazem. Application of the distinct element method and the extended finite element method in modelling cracks and coalescence in brittle materials. *Computational Materials Science*, 91:102–121, 2014. (Cited on page 111.)

[133] European Committee for Standardization. *Bituminous mixtures. Test methods for hot mix asphalt. Resistance to fatigue*, 2012. (Cited on pages 115 and 116.)

[134] X. Gao, G. Koval, and C. Chazallon. A discrete element model for damage and fracture of geomaterials under fatigue loading. In *8th International Conference on Micromechanics of Granular Media*, accepted. (Cited on page 135.)

[135] G. Li, Y. Li, J.B. Metcalf, and S. Pang. Elastic modulus prediction of asphalt concrete. *Journal of Materials in Civil Engineering*, 11(3):236–241, 1999. (Cited on page 141.)

[136] X. Gao, G. Koval, and C. Chazallon. Effect of fiber grid reinforcement on crack initiation and propagation in asphalt concrete. In *8th RILEM International Conference on Mechanisms of Cracking and Debonding in Pavements*, pages 55–60. Springer, 2016. (Cited on page 146.)

[137] W. Brown and J. Srawley. Plane strain crack toughness testing of high strength metallic materials. In *Plane Strain Crack Toughness Testing of High Strength Metallic Materials*. ASTM International, 1966. (Cited on pages 153 and 154.)

[138] R. Gettu, Z.P. Bazant, and M.E. Karr. Fracture properties and brittleness of high-strength concrete. *ACI Materials Journal*, 87(6):608–618, 1990. (Cited on page 153.)

[139] J.E. Srawley. Wide range stress intensity factor expressions for astm e 399 standard fracture toughness specimens. *International Journal of Fracture*, 12(3):475–476, 1976. (Cited on page 153.)

[140] M.A. James. *A plane stress finite element model for elastic-plastic mode I/II crack growth*. PhD thesis, Kansas State University, 1998. (Cited on page 161.)

[141] Itasca Consulting Group Inc. *Particle Flow Code 5.0 documentation*, 2015. (Cited on pages 163 and 164.)

UNIVERSITÉ DE STRASBOURG

Xiaofeng GAO

CHINA SCHOLARSHIP COUNCIL

Modelling of nominal strength prediction for quasi-brittle materials. Application to discrete element modelling of damage and fracture of asphalt concrete under fatigue loading.

Résumé

L’estimation de la durée de vie et de la rupture de structures composées par des matériaux quasi-fragiles nécessite le développement de nouveaux modèles théoriques et numériques. Dans ce travail, la modélisation de l’apparition des fissures et leur propagation en chargement monotone est d'abord étudiée. Un modèle d'effet de taille pour les structures fissurées et sa forme généralisée pour les structures présentant des défauts plus complexes qu’une fissure sont développés. Les prédictions du modèle de rupture sont comparées à des résultats expérimentaux de la littérature pour divers spécimens composés de différents matériaux et de différentes tailles. Des échantillons présentant des défauts initiaux en forme de V et en forme de trou illustrent les capacités de la formulation. Ensuite, l’endommagement et la fissuration induite par des chargements cycliques en fatigue sont discutés. Un modèle local en éléments discrets est développé, qui permet de coupler les deux mécanismes (endommagement et fissuration). Les prédictions numériques sont comparées aux résultats théoriques et expérimentaux. À la fin, les applications associées au comportement du béton bitumineux renforcé par des grilles en fibres de verres sont analysées en détail.

Mots-clés: quasi-fragiles; résistance nominale; la durée de vie en fatigue; modélisation par éléments discrets

Abstract

The prediction of the fatigue life and the rupture of structures made of quasi-brittle materials requires the development of new theoretical and numerical models. In this work, the modelling of the crack initiation and propagation under monotonic loading is firstly investigated. A size effect model for cracked structures and its generalized form for structures with defects more complex than a crack are developed. The predictions of the proposed model are compared with experimental results from the literature for various specimens of different materials and sizes. Samples with initial V-shaped and hole-shaped defects exemplify the formulation's capabilities. Then, the damage and cracking induced by cyclic fatigue loads is discussed. A local model using discrete elements is developed, that allows the coupling of two mechanisms (damage and fatigue cracking). The numerical results are compared to those of experimental bending fatigue tests. Finally, applications associated with the behavior of fiber glass reinforced asphalt concrete are analyzed in detail.

Key words: quasi-brittle; nominal strength; fatigue life; discrete element modeling